

UNIVERSITY OF ASTON IN BIRMINGHAM

DEPARTMENT OF PHYSICS

STUDIES IN DEBLURRING, WITH SPECIAL REFERENCE  
TO COMPUTER SIMULATION.

9 MAY 1977

204627

535.42 DAV

A THESIS SUBMITTED FOR THE DEGREE  
OF DOCTOR OF PHILOSOPHY

BY

JEREMY CHARLES DAVIES

AUGUST 1976.

## ABSTRACT

The process of deconvolution is studied by coherent, non-coherent and numerical techniques. Computer simulations have been used to model the operation of coherent systems using different types of spatial filters, and the effects of Gaussian distributed random noise added to the amplitude and phase of the components are presented. This has led, via statistical analysis of the simulated recovered images, to a re-assessment of the LMSE optimum deconvolution filter. The effects of filter misregistration and the use of a filter mis-matched to the system convolute are also modelled by computer, and filter amplitude quantization errors are studied in terms of their impulse responses. Using a non-coherent optical system a new method of deconvolution is described and experimental results of the deconvolution of a dilute object and a Gaussian blurring function are presented.

### ACKNOWLEDGEMENTS

I would like to express my thanks to Prof. G.L.Rogers and Mrs.M.Pegg. The former for his guidance and sometimes obtuse but always stimulating suggestions, and the latter for her patience and skill in typing this thesis.

I also extend my thanks to Prof.S.E.Hunt in whose department this research has been conducted.



## CONTENTS

### CHAPTER 1 - THE ROLE OF COMPLEX SPATIAL FILTERS IN SIGNAL PROCESSING.

	<u>Page</u>
1.1 Introduction	1
1.2 Numerical Processing	3
1.3 Optical Processing	4
1.4 Techniques for Producing Coherent Spatial Filters	18
1.5 Computer Generated Holograms	21
1.6 Lohmann Binary Hologram	22
1.7 Lee Hologram	26
1.8 Bleached Filters	27
1.9 Parity Sequence Filters	28
1.10 ROACH (Referenceless-on-Axis Complex Hologram)	29
1.11 Dynamic Range	31

### CHAPTER 2 - AMPLITUDE AND PHASE VARIATIONS IN A COHERENT DECONVOLUTION SYSTEM

2.1 Introduction	32
2.2 Least-Mean-Square-Error Filter	34
2.3 Form of the LMSE Filter	35
2.4 Computer Simulation - Description of System	37
2.5 Deconvolution Results and Discussion	43



CHAPTER 3 - COMPUTER GENERATED HOLOGRAMS - ANALYSIS		Page
3.1	Introduction	111
3.2	Sampling Rate Limitations	113
3.3	Holographic Copying of Filters	117
3.4	Lohmann Binary Hologram - Diffraction Analysis	118
3.5	Spectrum Shaping with Parity Sequences	130
3.6	Parity Sequence Filters	135

#### CHAPTER 4 - COMPUTER SIMULATION OF COHERENT OPTICAL SPATIAL FILTERING SYSTEM

4.1	Introduction	149
4.2	Optical Transfer Function Error in Blur Extent	150
4.3	Results of Computer Simulation	156
4.4	Lateral Misregistration of the Filter Element	157
4.5	Quantization and Dynamic Range	161
4.6	Amplitude Quantization in a Deblurring Filter	163

#### CHAPTER 5 - NONCOHERENT DECONVOLUTION

5.1	Introduction	184
5.2	Image Formation as a Superposition of Young Fringes	185
5.3	Deconvolution of a Gaussian Function	189
5.4	The Noncoherent Deconvolution Mask	190

		Page
5.5	Construction and Operation of the Noncoherent Filter	191
5.6	Experimental Deconvolution Results	198
5.7	Discussion and Conclusions	201
CHAPTER 6 - CONCLUSIONS		205
REFERENCES		209

## ILLUSTRATIONS

<u>CHAPTER 1</u>		Page
1.1	Convolution of the Rectangle Functions	8
1.2	Diffraction Patterns of Figure 1.1	8
1.3	Bar Chart Object and Associated Diffraction Pattern	9
1.4	Blurred Bar Chart Object and Associated Diffraction Pattern	10
1.5	Spoke Target and a Blurred Spoke Target	11
1.6	Linear Motion Deblurring Filter	14
1.7	Coherent Spatial Filtering System	15
1.8	Lohmann and Conventional Hologram Cells	23
1.9	Detour Phase in a Diffraction Grating	24
1.10	ROACH - Referenceless-on-Axis-Complex- Hologram Scheme	30
 <u>CHAPTER 2</u>		
2.1	Block Diagram of Computer Simulation System	38
2.2	Dilute and Continuous Tone Objects	41
2.3	Blurred Dilute and Continuous Tone Objects	42
2.4	Kinoform Filter	44
2.5	Kinoform Recovery of Bar Chart Object	45
2.6	Ramp Filter Recoveries of Bar Chart Object	47
2.7	Ideal Filter	48
2.8	Optimum Bar Chart Recovery	49
2.9	Optimum Continuous Tone Recovery	50
2.10	Least Mean Square Error Filters	52
2.11	Amplitude and Phase Noise Schemes	54



2.12a	Ideal Filter Recoveries of Bar Chart in the Presence of Object Amplitude Noise a)	56
2.12b	As above b)	57, 58
2.13a	Ideal Filter Recoveries of Continuous Tone Object in the Presence of Object Amplitude Noise a)	59
2.14	LMSE Recoveries of Bar Chart Objects in to the Presence of Amplitude Noise a) and b)	
2.17	for Signal to Noise Ratios 1,000, 500, 100, 10	60-77
2.18	EMSE Recoveries of Continuous Tone Objects to in the Presence of Object Amplitude Noise a) and b) for Signal to Noise Ratios 1,000, 500, 100, 10	78-93
2.22	Calculated Standard Deviations of Recovered to Images in the Presence of Object Amplitude Noise a) and b)	94-97
2.24	Ideal Filter Recoveries in the Presence of Filter Amplitude Noise a) and b)	103-105
2.25	Kinoform Recoveries with Additive Phase Noise	107-108
2.26	Ideal Filters Recoveries with Additive Phase Noise	109,110

### CHAPTER 3

3.1	Sampling in Object, Fourier and Image Space	115
3.2	Pulse Code Modulation of a Complex Signal and Associated Spectrum	116
3.3	Holographic Copying of a Computer Generated Spatial Filter	119
3.4	Lohmann Binary Hologram Cell	120
3.5	Region of a Lohmann Filter Coded for First Order Operation, $J = 1$ $C = \frac{1}{2}$	126
3.6	Region of a Lohmann Filter Coded Identically to Fig.3.5 Coded for Second Order Operation, $J = 2$ , $C = \frac{1}{2}$	128
3.7	Scheme for Spectrum Levelling Parity Sequences	133

3.8	Dynamic Range Variations Across the Complex Plane of a Parity Sequence Filter	138
3.9	Linear Motion Deblurring Filter Produced by Microfilm Plotter, FR80, $J = 1$ , $C = \frac{1}{2}$ . (Full size and enlarged)	143
3.10	Linear Motion Deblurring Filter Produced by Graph Plotter, $J = 2$ , $C = \frac{1}{2}$ (Enlarged)	144
3.11	Impulse Response Generated by Filter of Figure 3.9	146

#### CHAPTER 4

4.1	Bar Chart Object Used in Simulations	151
4.2	Recoveries of Bar Chart Object with Blurs to Mismatched to Deconvolution Filter	152-155
4.5		
4.6	Graph of Variance of Recovered Images as a Function Blur Mismatch	158
4.7	Images Recovered with a Lateral to Misregistration of the Filter Element	159-160
4.8		
4.10	Quantized Filters and Associated Impulse to Responses for Dynamic Ranges 50, 20, 10 for	
4.27	Signal to Noise Ratios 1,000, 100, 10	164-181
4.28	Amplitude Quantization Errors $DR = 10$ $\beta = 1000$	181

#### CHAPTER 5

5.1	Formation of Young Fringes using a Lens	186
5.2	Noncoherent Addition of laterally Misregistered Young Fringes, showing Reduction in Visibility	188
5.3	Ideal and Realised Inverse Gaussian Noncoherent Filters	192
5.4	Enlarged Negative of Noncoherent Filter	194
5.5	Bar Chart and Gaussian Blurred Bar Chart Object Distributions	195
5.6	Enlarged Negatives of Bar Chart and to Gaussian Blurred Bar Chart Objects	196
5.7		



5.8	Diagram of Optical Deconvolution System	197
5.8a	Photograph of Optical Deconvolution System	197
5.9	Microdensitometer Traces of Gaussian Blurred Bar Chart and Deconvolved Image	199
Table 5.1	Peak Edge Angles and Peak Heights of Recovered Bar Chart Measured from Fig.5.9	200
Table 5.2	Inverse Gaussian Filter Solutions	200
5.10	Noncoherent Deconvolution of Gaussian Blurred Bar Chart (Enlarged)	203
5.11	Enlarged Deconvolution of Gaussian Blurred Bar Chart Showing Higher Order Images	204



CHAPTER 1

THE ROLE OF COMPLEX SPATIAL FILTERS IN SIGNAL  
PROCESSING

## 1.1 INTRODUCTION

The processing of optical data can involve the extraction of information from the data field by locating particular features (such as edges in the character recognition system) or it can involve the redistribution of the data into a more satisfactory form. It is impossible to increase the information content of a data field by any processing operations. Any apparent increase in information is a result of supplying an equivalent amount of information about the processing operation itself. The question which arises then is why should we perform such operations if they do not increase the total information content? The simple answer is that the processing operation may help us to recognise certain pieces of information. Although an out of focus photograph, plus details of how points on the photograph have suffered due to this misfocus, give us the same information as a photograph processed to correct the misfocus, we recognise more information when presented with the processed photograph.

Not all operations are specifically designed to increase



the amount of recognisable information in a data field. Although photographic film has a high storage density (typically  $10^{10}$  bits on a  $100 \times 100\text{mm}^2$  film) this cannot be utilised directly to record combined amplitude and phase information. In this case a processing operation must be used to encode the information in terms of the film's variable density or variable optical thickness. However, even for wholly real data advantages may be gained by such holographic encoding. For example, processing of such data into the form of a Fourier transform hologram increases the data record's resistance to local defects and for subsequent read-out makes the system insensitive to lateral misregistration of the record.

This type of data encoding, storage and read-out is analogous to coded data transmission schemes in the sense that both the encoding and decoding can be chosen to minimise the subsequent read-out error. This facility to operate before and after transmission (or storage) is a Shannon class of processing (Ref. 1). It is to be distinguished from the Wiener form which deals only with operations on data after transmission (Ref. 2.). In both cases, of course, the original data may be corrupted in various ways by noise or system distortions etc.



Processing in order to more easily recognise features in a data field can be carried out in a number of ways. Some success may be achieved by operating directly on the data although in many cases - particularly the deconvolution situation - this can be very inefficient. Commonly a transformation to frequency space produces an equivalent but more efficient operation. The processed data is then recovered by inverse transformation. Clearly there is a trade-off between how many operations are required in data space for the processing and how many operations are required to transform, process in transform space and retransform for the result.

## 1.2 NUMERICAL PROCESSING

Until 1965 the numerical Fourier transformation (in which space the convolution operation becomes a multiplication operation) was expensive to perform by digital computer. However, the Fast Fourier Transform Algorithm (F.F.T) due to Cooley and Tukey (Ref. 3) significantly reduced the number of operations in the ratio of  $N \log N/N^2$  for an  $N$  point data set and made the numerical "transform, operate, inverse transform" process more attractive. The Fourier transformation is based on the expansion of a function in terms of complete orthogonal sets of sines and cosines. There are many other complete sets in terms of which a

function can be expanded. Of these the Walsh functions (Ref. 4) form a set of particular interest for computer operations as, although taking only the values +1 and -1, they have many properties similar to the trigonometric sines (Ref. 5). A Fast Walsh Transform also exists. (Ref. 6).

Even so numerical processing is still inefficient being a sequential operation although some degree of parallel processing now seems feasible following a reduction in the cost of integrated circuit chips capable of performing the basic mathematical operations (Ref. 7).

### 1.3 OPTICAL PROCESSING

For a coherently illuminated system and with certain restrictions on their lateral extent (Ref. 8) the amplitude distribution in the front and back focal planes of a lens are related by a Fourier transformation. As a lens operates in parallel on an object distribution, if the required Fourier plane operation can be accomplished, a pair of lenses may be used to achieve a transform, operate, retransform type of system. The operating speed of such an optical computer depends on the time required to obtain a satisfactory back focal plane record as all components in the system being passive its overall transmission  $< 1$ . Unlike the equivalent numerical system



the speed of the optical systems operation is independent of the number of data points to be operated upon. The main difficulties to be overcome in a coherent optical processing system are the sensitivity to noise and the realising of the complex operating elements.

We shall restrict ourselves to processing in transform space and in particular in Fourier space to the techniques of deconvolution. Both numerical and optical Fourier space deconvolution are achieved by multiplying with a generally complex operator (or filter) which has been optimised in some way to minimise the effects of noise. In Chapter 2 we study the effects of noise at various stages of deconvolution using a computer simulation. Chapter 3 is devoted to a discussion of some of the most recent and efficient techniques of producing complex coherent optical elements, and the operation of these elements is simulated, again by a computer model, in Chapter 4. A completely different approach is taken in Chapter 5 in which a new noncoherent optical system for performing deconvolution is described. The system's operation is discussed and some results of the deconvolution of a Gaussian linear blur and a dilute object are presented.

The rest of this chapter is concerned with the deconvolution process and with a discussion of the basic requirements of an optical filter for its satisfactory operation. That the real space operation of convolution becomes a multiplication of the individual transformations in Fourier



space is described by the Convolution Theorem (Ref. 8 )  
 In one dimension if  $\otimes$  represents convolution, and, for  
 brevity,  $T$  and  $T^{-1}$  represent the operations of Fourier  
 transformation and inverse transformation, then

$$c(t) = g(x) \otimes s(x) = \int_{-\infty}^{+\infty} g(x) \cdot s(t-x) dx \quad 1.1$$

$$\begin{aligned} T[c(t)] \equiv C(H) &= T[g(x) \otimes s(x)] \\ &= T[g(x)] \cdot T[s(x)] \end{aligned}$$

$$\therefore C(H) = G(H) \cdot S(H) \quad 1.2$$

where capitals are used for Fourier space functions.

Hence, if an operator  $F(H)$  can be realised such that

$$F(H) \cdot S(H) = D \text{ where } D \text{ is a constant} \quad - 1.3$$

then by operating with  $F(H)$  on the spectrum,  $C(H)$ , of  
 the convolved functions and following with an inverse  
 Fourier transformation a recovered version of  $g(x)$  can  
 be obtained.

$$\text{That is } F(H) \cdot C(H) = D \cdot G(H) \quad - \quad 1.4$$

$$\text{and thus } i(x) = D \cdot g(x) \quad - \quad 1.5$$

where  $i(x)$  is the recovered image. In general the basic operation of spatial filtering described by equation 1.4 is a complex operation.

Physically the process of convolution produces a smoothing of sharp features which is exhibited in frequency space as a suppression of the high frequency components. This is shown in Figures 1.1 and 1.2, where the convolution of a pair of rectangle functions is shown, and in Figures 1.3 and 1.4 which are photographs of a bar chart before and after a linear blur together with their associated diffraction patterns.

Two further aspects of the convolution process are worthy of note. The first is that due to the complex nature of the operation convolution modifies the phases of the spatial frequency components as well as their magnitudes. For the case of a  $\text{rect}(x/\Delta x)$  blurring function which in frequency space has a  $\sin \theta/\theta$  form, the spectrum of the function operated upon suffers phase changes of  $\pi$  radians in the spatial frequency regions where  $\sin \theta/\theta$  is negative. This phase change can clearly be seen in the photograph of a spoke target taken under conditions of misfocus. In this case the frequency space operator describing the misfocus contains a Bessel function of the first kind and order one, and again has negative and positive regions, Figure 1.5. The phase changes produced by the misfocus emerge in the

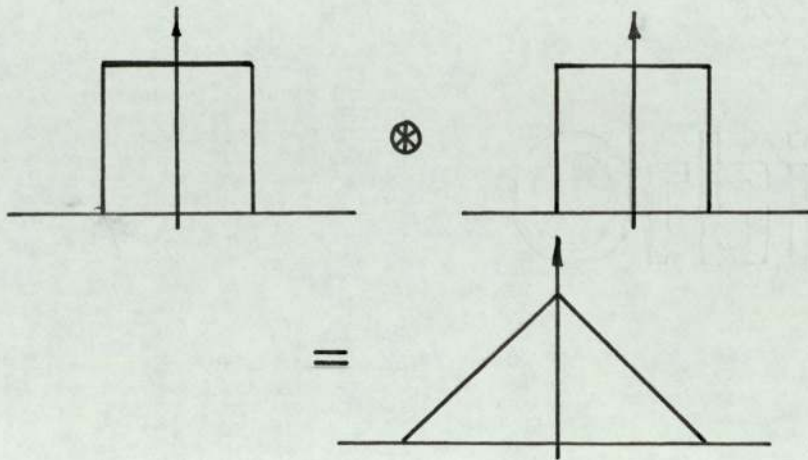
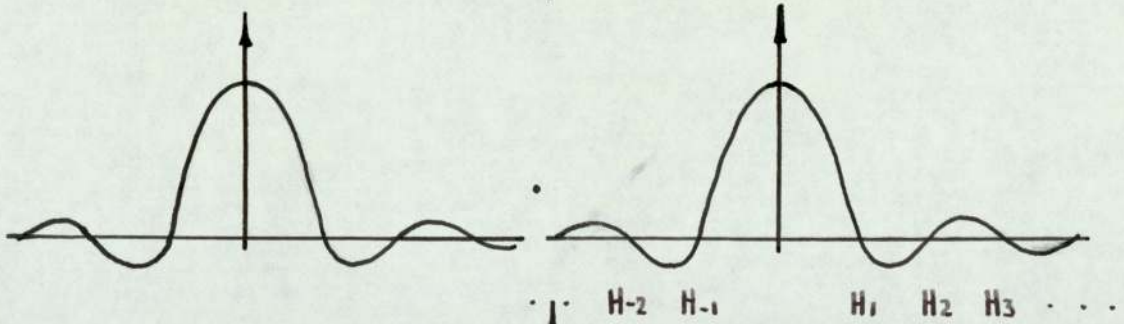


FIG 1.1



=

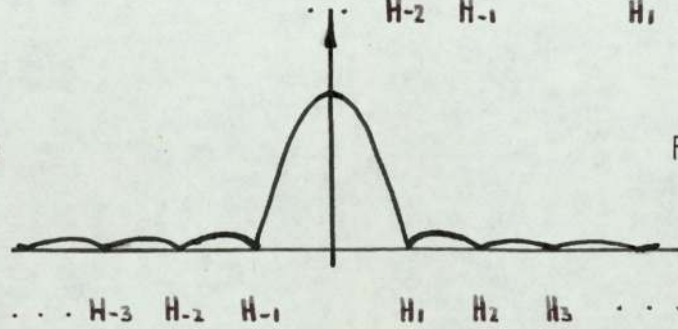


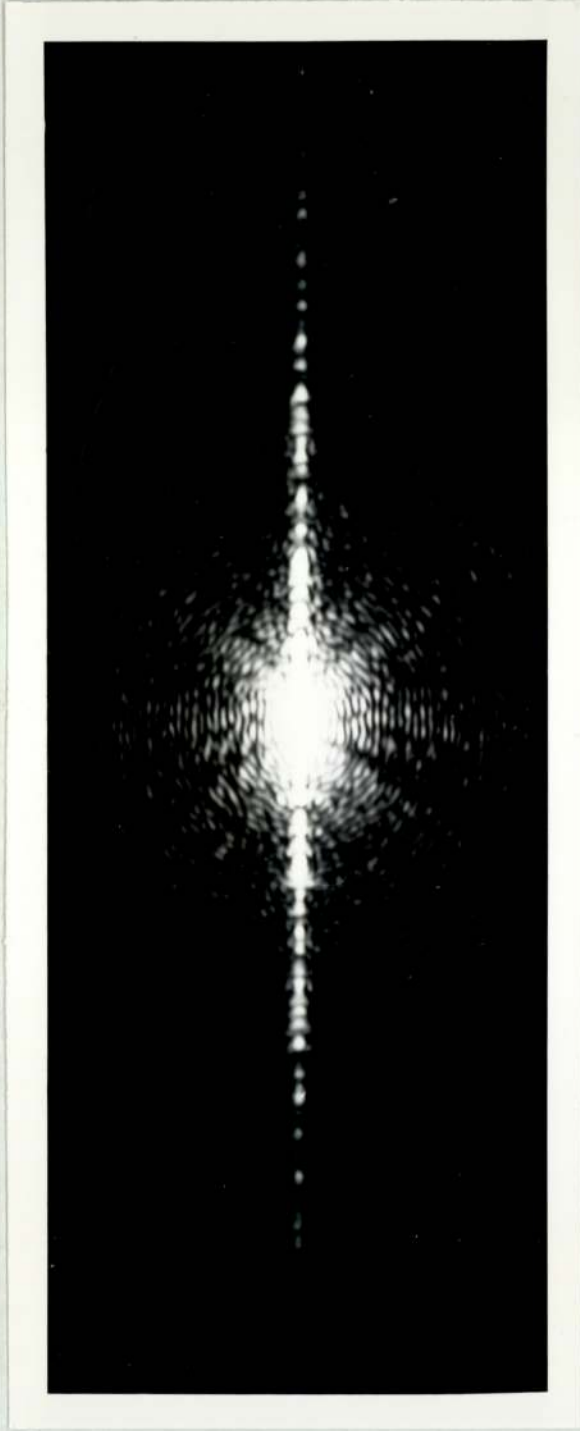
FIG 1.2





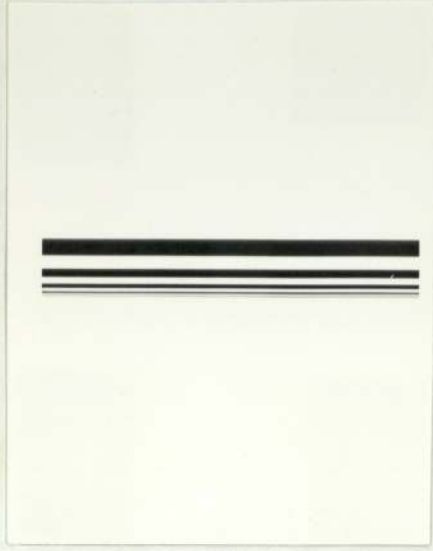
Bar Chart

FIG I.3



Diffraction Pattern Of Barchart Object

FIG 1.3



Blurred Bar Chart

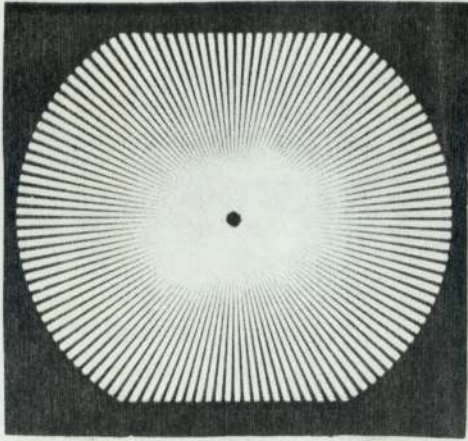
FIGI.4



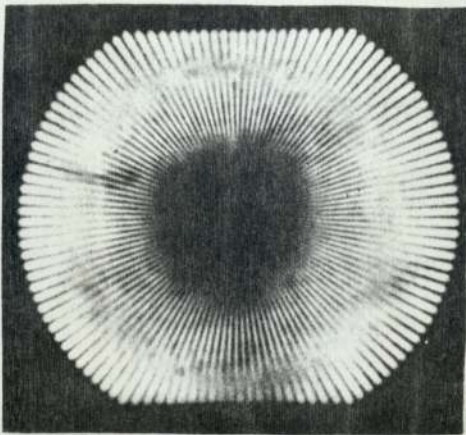


Diffraction Pattern Of Blurred Barchart Object

FIG 1.4



Spoke Target



Blurred Spoke Target  
(De focussed)

FIG 1.5

blurred image as lateral shifts of the various frequency regions of the spoke pattern.

The second important point is a consequence of the phase change of the blurring function as this also means that these frequencies at which the axis is crossed are suppressed to zero by the convolution process. This can be seen in Figure 1.2 at the frequencies  $H_{\pm 1}, H_{\pm 2}, \dots$ . The process of deconvolution by spatial frequency filtering (or any other method) can thus never be perfect as these absent frequencies represent information which has been irretrievably lost. This is emphasised by the form of the filter which is required to perform the deconvolution of a linear blur.

If the linear blur is represented by  $\text{rect}(x/\Delta x)$  where

$$\begin{aligned} \text{rect}(x/\Delta x) &= 1 && \text{for } |x| < \frac{\Delta x}{2} \\ &= \frac{1}{2} && \text{for } |x| = \frac{\Delta x}{2} \\ &= 0 && \text{for } |x| > \frac{\Delta x}{2} \end{aligned}$$

then as from 1.3

$$F(H) = \frac{D}{S(H)}$$

and as

$$S(H) = \int_{-\infty}^{+\infty} \text{rect}(x/\Delta x) e^{-2\pi i H x} dx$$



$$= \int_{-\frac{\Delta x}{2}}^{\frac{\Delta x}{2}} e^{-2\pi i H x} dx$$

then  $S(H) = \sin(\pi H \Delta x) / (\pi H)$

and  $F(H) = D \pi H / \sin(\pi H \Delta x)$  1.6

Clearly as  $\pi H \Delta x$  tends to  $n\pi$ , where  $n$  is integer, then  $F(H)$  tends to infinity and cannot be realised.

This is equivalent to requiring an infinite amount of energy to recover the information lost at the suppressed frequency points (or poles) of the filter. The form of the inverse sine filter is shown in Figure 1.6.

Numerically the process involves forming the two dimensional Fourier transform by F.F.T. and performing the  $2(N \times M)$  complex multiplications,  $F(H, K)$ , on the calculated spectrum before inverse transforming yields the  $(N \times M)$  filtered image intensities. At least two  $(N \times M)$  arrays have to be handled which can result in storage problems for large arrays.

For optical deconvolution the basic two lens system is shown in Figure 1.7.

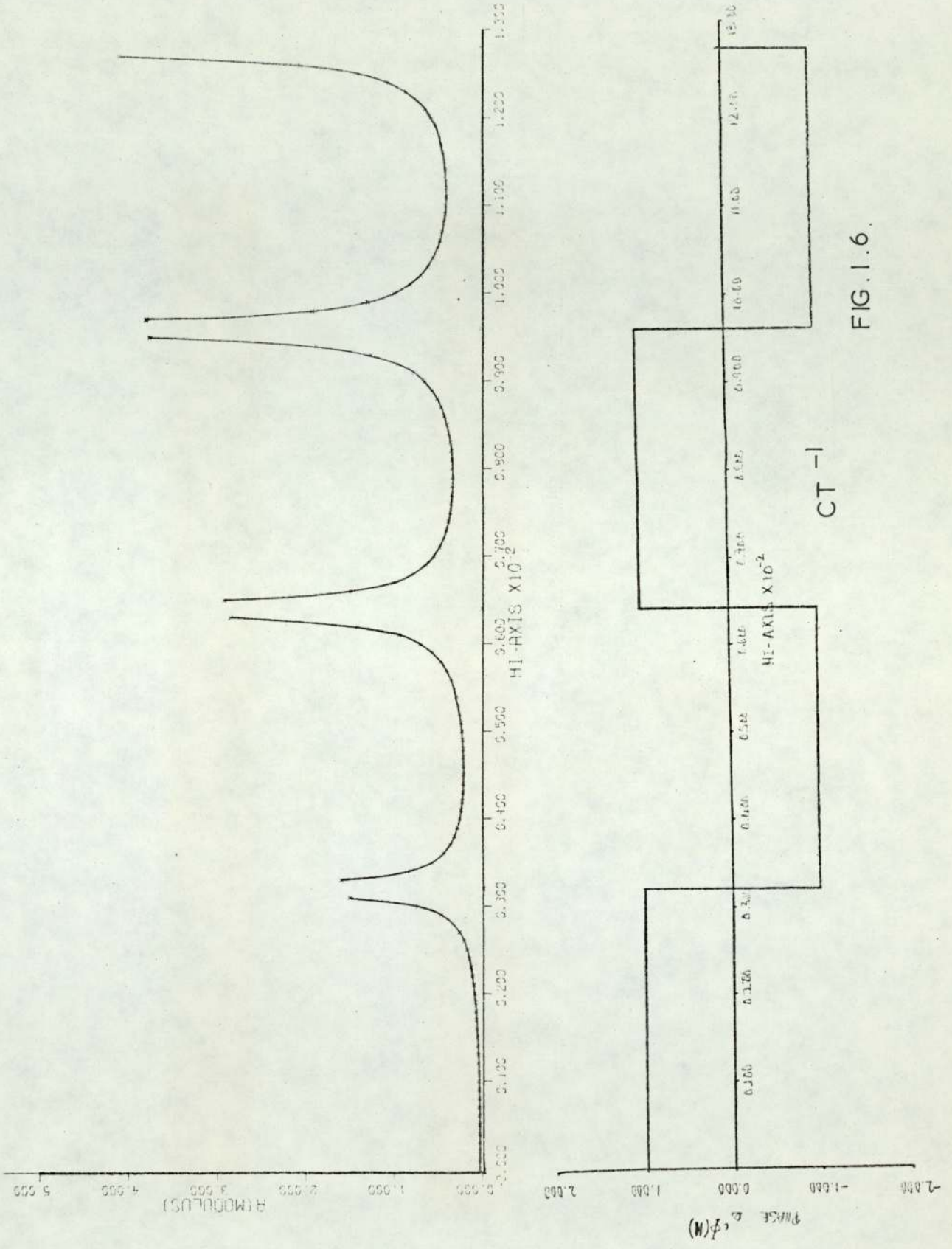
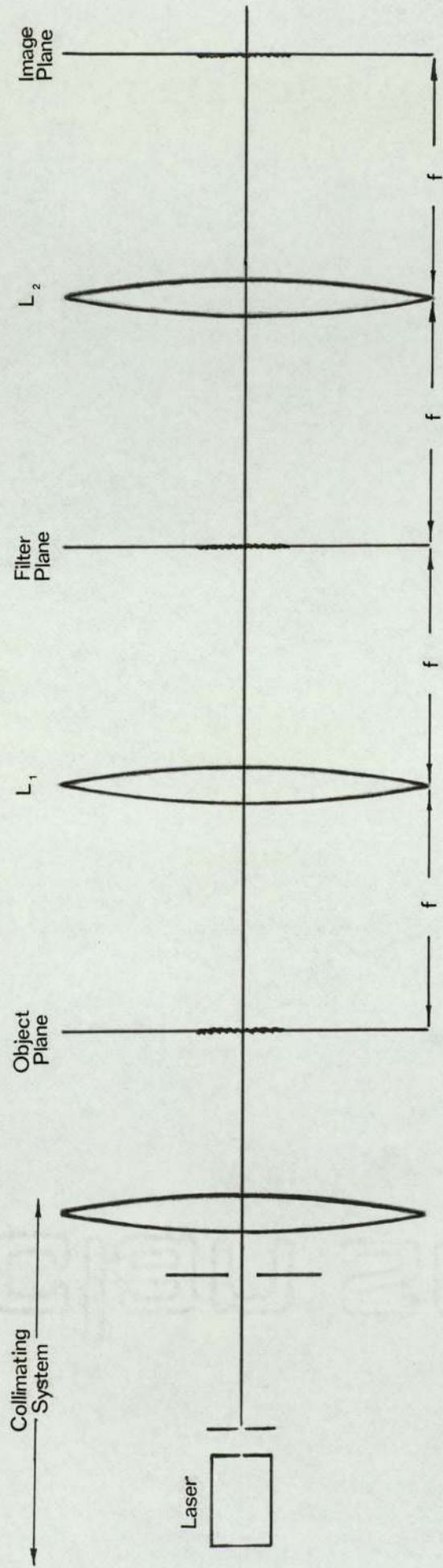


FIG. 1.6.

CT -1



Coherent Spatial Filtering System

FIG. 1.7



The coherent field distributions of the front and back focal planes of a converging lens are a Fourier transform pair. Hence, for an object distribution in the front focal plane of lens  $L_1$ , its complex spatial frequency distribution can be operated upon by a filter,  $F(H, K)$ , in the back focal plane of lens  $L_1$ . This modified complex spectrum, in the front focal plane of the second lens,  $L_2$ , is retransformed by this lens to give a filtered image in its back focal plane. For a wavelength,  $\lambda$ , illuminating an object distribution,  $o(x, y)$ , with lenses of focal lengths,  $f$ , we have

$$O(u, v) = A \overline{T} [ o(x, y) ] \quad 1.7$$

where  $A$  is a constant and  $u = \lambda f H_{\text{mm}}, v = \lambda f K_{\text{mm}}$ , the distance off axis of the frequency  $H$  lines  $\text{mm}^{-1}$ ,  $K$  lines  $\text{mm}^{-1}$ .

The complex amplitude after the filter element is then

$$O_F(u, v) = B \overline{T} [ o(x, y) ] \cdot F(u, v) \quad 1.8$$

which after a retransformation gives an image of

$$i_F(x, y) = C_1 \cdot o(x, y) \otimes f(x, y) \quad 1.9$$

where  $B$  and  $C_1$  are constants and

$$f(x, y) = \overline{T} [ F(u, v) ] \quad 1.10$$

The lenses can only perform a Fourier transformation

with the negative exponent denoting phase retardation so the inverse transformation is replaced by a second transformation which produces an inverted image. For convenience we shall assume the axes in image space in the opposite sense to those in object space and so avoid negative co-ordinates.

The complex nature of all the operations requires that the phases of all components are controlled. It is thus usual to put the object transparency and filter transparency in liquid gates to "back-off" any spurious optical thicknesses in the films.

Almost all spatial filtering involves an attenuation in intensity transmittance of  $10^{-2}$  to  $10^{-4}$ . This is due to the form of the optical transfer function which, for the case of the deblurring filter shown in Figure 1.6, has a maximum to minimum amplitude transmittance ratio of approximately 130. The intensity transmittance at zero frequency is thus down by a factor of about  $10^4$ , compared with its pre filter value. This means the light level of the deblurred image is very low. This is common to all spatial filtering devices which are inherently passive in operation. However, further attenuation may be introduced, the exact amount depending on the method used to construct the filter.

The need to realise the required maximum and minimum values of amplitude transmittance is also in itself a



serious constraint on the filters. We shall discuss this dynamic range constraint and the light efficiency requirements in the next section which is a review of current methods of producing spatial filters.

#### 1.4 TECHNIQUES FOR PRODUCING COHERENT SPATIAL FILTERS

Zernike (Ref. 9 ) used a phase contrast technique to improve the imaging of phase objects in 1935 although Abbe (Ref. 10 ) had realised the significance of spatial filtering as early as 1893. A major development was the advent of the highly coherent laser source. Marechal and Croce (Ref. 11 ) improved the contrast of a photographic image by purely attenuative filtering and Tsujiuchi (Ref. 12 ) constructed a complex deblurring filter to correct a known degree of defocus. The absorption part of this filter was produced by rotating a suitable painted disc and recording its transmittance on film. The phase control was due to a vacuum deposition on a thin film in suitable concentric zones. The final filter was a sandwich of these two components accurately aligned.

A significant step forward came when Vander Lugt (Ref. 13 ) constructed a complex filter holographically by exposing a photographic film simultaneously to the Fourier transform of the impulse response of the required filter and an oblique plane reference wave.



Writing the reference wave as  $A_0 \exp(-2\pi i u \sin \psi / \lambda)$ , where  $\psi$  is the angle between the wave vector and the normal to the film, then if the film is processed so that the resulting amplitude transmittance,  $T(u, v)$ , is proportional to the incident intensity we can write

$$T(u, v) \propto \left| F(u, v) + A_0 e^{-2\pi i B u} \right|^2 \quad 1.11$$

where  $B = \sin \psi / \lambda$ .

Expanding we have

$$T(u, v) \propto A_0^2 + |F(u, v)|^2 + A_0 F^*(u, v) e^{-2\pi i B u} + A_0 F(u, v) e^{2\pi i B u} \quad 1.12$$

The last term in the expression gives the required complex filter transmittance, its impulse response appearing a distance  $f \sin \psi$  off axis in the output plane of a subsequent spatial filtering system. The term  $A_0^2 + |F(u, v)|^2$  appears on axis and provided a large enough value of  $B$  is chosen there is negligible overlap of the adjacent orders. The complex conjugate of the filter function is also formed as the 3rd term and this makes the Vander Lugt filter useful for matched filtering. The complex information is held as an amplitude and phase modulation of the tilted reference wave which acts as a carrier. This is made clear by writing Equation 1.12 in cosine form,

$$T(u, v) \propto A_0^2 + |F(u, v)|^2 + 2A_0 F(u, v) \cos(2\pi u B + \theta(u, v)) \quad 1.12'$$

A deblurring filter to correct for defocus was realised by

Stroke and Zech (Ref. 14 ) and Lohmann and Wehrlich (Ref. 15 ) by sandwiching a Vander Lugt hologram with a purely alternating filter. The attenuating part is made by recording the intensity of the Fourier transform of the point spread function of the required filter and processing this with an overall gamma of 2 such that the resulting amplitude transmittance is  $\propto 1/|F(u,v)|^2$ . Using the same system, but adding a suitable reference wave the holographic part is formed, and the two are automatically of the same scale (unlike in the scheme due to Tsujiuchi (Ref. 12 )). When placed in series the resulting transmittance to one of the first image orders is

$$T(u,v) \propto F^*(u,v) \cdot \frac{1}{|F(u,v)|^2} \quad 1.13$$

$$\propto \frac{1}{F(u,v)}$$

Stroke and Halicoua (Ref. 16 ) also made a holographic sandwich filter but with an absorption part  $\propto 1/|F(u,v)|$ .

Brown and Lohmann (Ref. 17 ) defined light efficiency as the ratio of the intensity diffracted into the first order to the total light incident for the case of a simple regular grating. Considered as a hologram they studied different techniques of producing these gratings and compared their light efficiencies.

For a grey continuous tone hologram such as the Vander Lugt type the maximum efficiency is 6.25%. In practice,



the reference wave is usually two or three times larger in amplitude than the object wave, (to ensure the fringe contrast does not extend beyond the linear region of the transmission versus exposure curve of the photographic plate). The effect of this is to reduce the maximum light efficiency for a grey hologram to less than 2%. For a deblurring filter then, the overall intensity transmittance is likely to be reduced by more than  $10^4$ . In this case grain noise and scattered light can seriously reduce the image quality.

### 1.5 COMPUTER GENERATED HOLOGRAMS

All the techniques discussed so far require the impulse response of the filter to be available. A significant step forward in producing a general complex element was the development of computer generated holograms. The Fourier transform of the required filter's impulse response is calculated, the complex transmittance coded and displayed (typically on a graphplotter output or C.R.T. output device) and recorded photographically with suitable processing.

The earliest of these computer generated holograms was simply a model of Equation 1.12. As information is contained in the carrier wave term the zero order terms can be replaced by a constant to reduce the computation. Burch (Ref. 18 ) used the form,



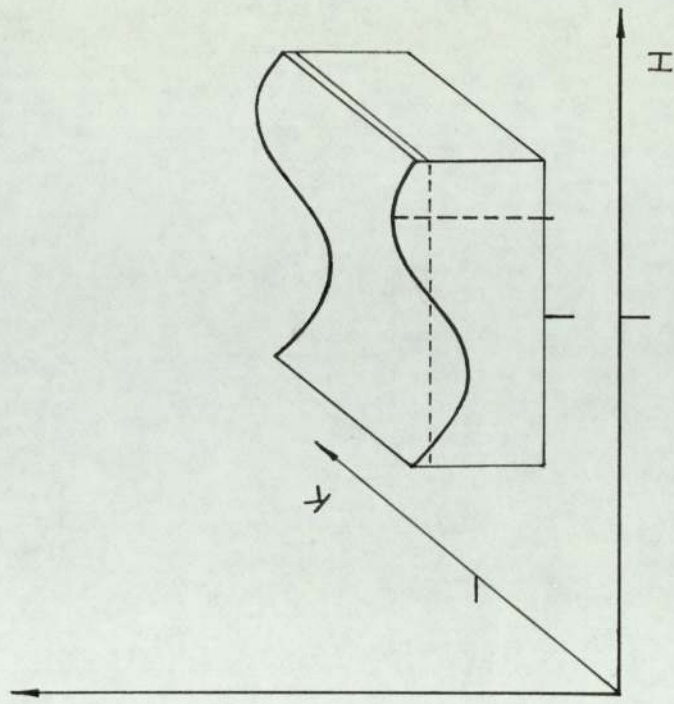
$$T(u,v) = \text{Constant} + 2A_0 G(u,v) \cos(2\pi u B + \theta(u,v)) \quad 1.12''$$

This technique requires a grey scale display and control of the subsequent grey tone processing. It is also inefficient in its use of the available computer display, as several display points are needed to produce a phase modulated cosine fringe.

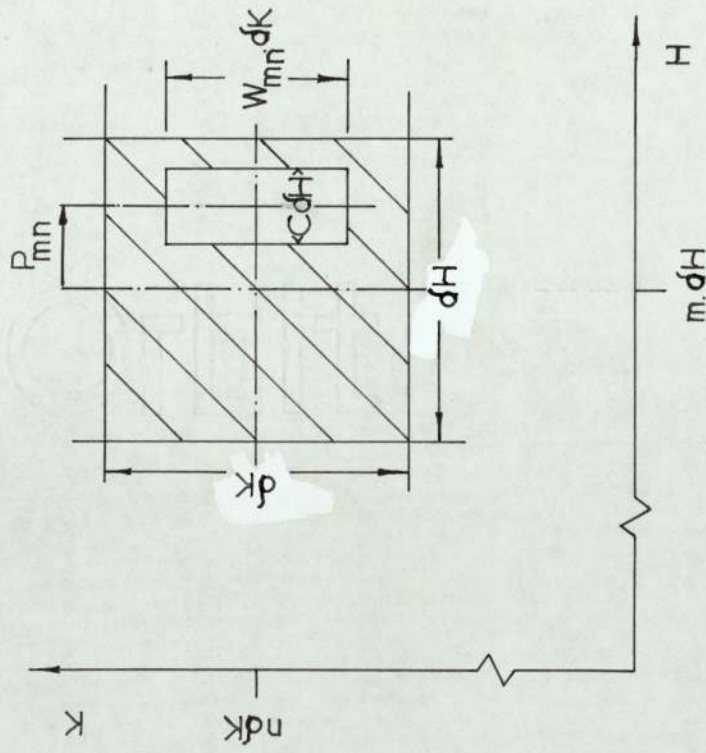
The real development in the computer generation of holograms came with the invention of the binary detour phase coding scheme by Lohmann (Ref. 19 and Ref. 20) although the hard clipped matched filter, due to Kozma and Kelly (Ref. 21) was the first binary transmittance computer generated spatial filter.

### 1.6 LOHMANN BINARY HOLOGRAM

To produce a Lohmann hologram the complex amplitude transmittance of the required filter is computed numerically by F.F.T. Computer limitations on storage, as discussed for the case of numerical filtering, restrict the number of calculated complex amplitudes to a finite number of sampling points,  $M \times N$ . Consequently a matrix of cells of size  $dHdK$  is established, over each of which the associated complex coefficient is assumed to be constant. If the calculated sampled value of the filter in the  $(m,n)^{\text{th}}$  cell is

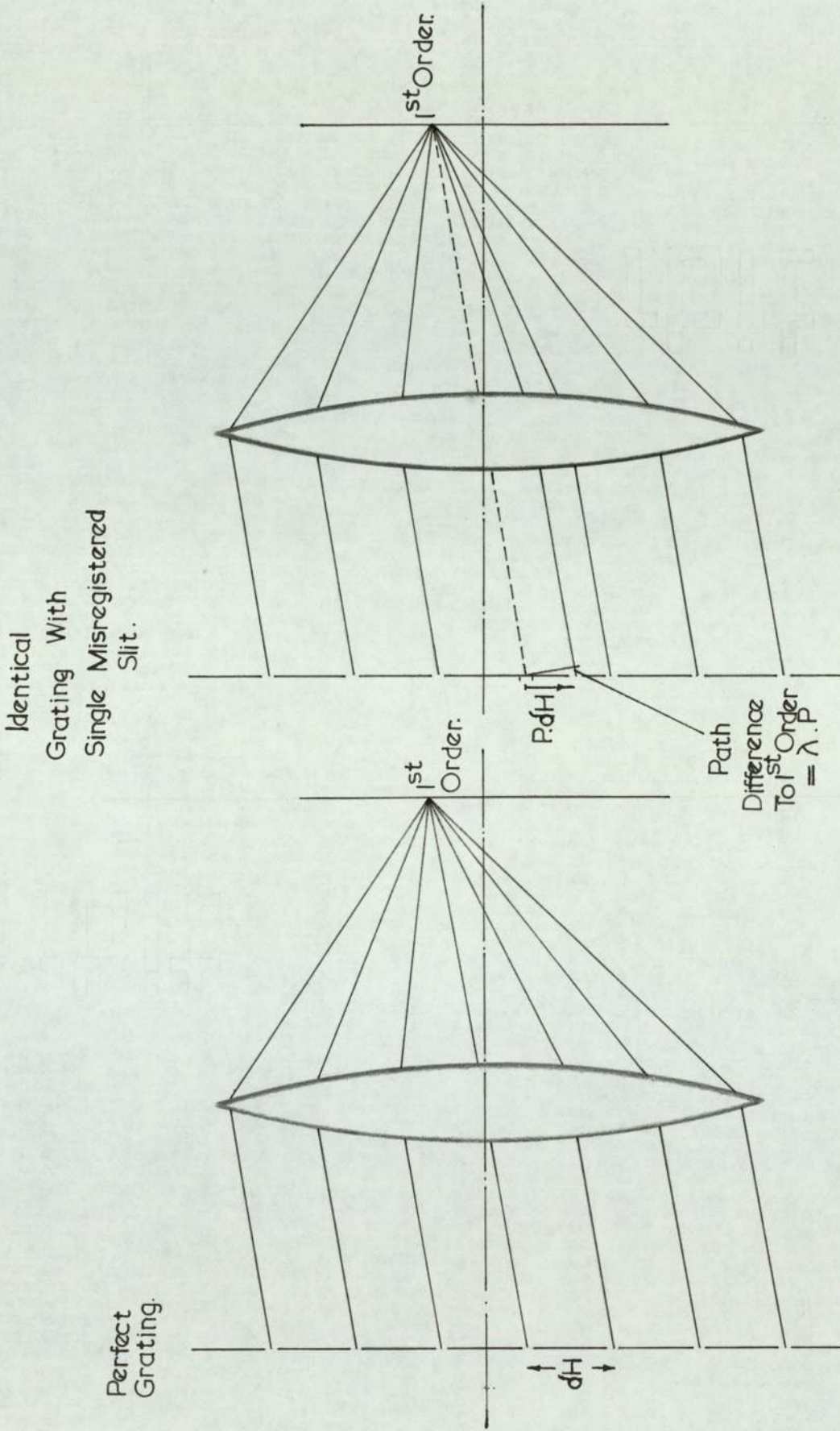


Conventional Hologram Cell



Lohmann Coded Hologram Cell





First Order Detour Phase For A Diffraction Grating With A Single Slit Laterally Displaced

FIG. 1.9



$$F(m\delta H, n\delta k) = |F(m\delta H, n\delta k)| e^{i\phi(m\delta H, n\delta k)} \quad 1.14$$

then the sampled filter's transfer function is

$$\hat{F}(u, v) = \sum_{m=0}^{M-1} \sum_{n=0}^{N-1} |F(m\delta H, n\delta k)| e^{i\phi(m\delta H, n\delta k)} \cdot \delta(u - m\delta H, v - n\delta k) \quad 1.15$$

where  $\delta(u, v)$  is a two dimensional delta function

To code the complex information of each sampled coefficient an aperture, of size controlled by the modulus of the amplitude, and position by the phase of the coefficient, is constructed in each cell, as shown in Figure 1.8. The detour phase, associated with the shift in aperture position, is used to code the phase. Lord Rayleigh noticed the detour phase effect, as the appearance of "ghosts" in the spectrum of a diffraction grating when slight dislocations were present in some of the slits of the grating. For a perfect grating, the path length difference from adjacent slits for wavelets reaching the 1st diffraction order, is exactly one wavelength. If one of the slits is displaced towards one of its neighbours, its path length difference will no longer be one wavelength with respect to the adjacent slits.

Hence, still seen from the first diffraction order, a lateral shift in a slit's position by a fraction,  $P$ , of a grating period will produce a detour phase of  $P \cdot 2\pi$  radians, as shown in Figure 1.9. When  $P = 1$  the shifted

slit is superimposed on its neighbour. In terms of the Lohmann coding scheme a shift of an aperture  $(m,n)$  by  $\pm d\lambda/2$  gives an X-direction, first-order detour phase of  $\pm\pi$  radians associated with the  $(m,n)^{\text{th}}$  coefficient.

As seen from the  $J^{\text{th}}$  diffraction order, into which regular adjacent slits diffract with  $J\cdot\lambda$  path difference, a shift of  $\pm P$  gives an associated detour phase of  $\pm J\cdot P\cdot 2\pi$  radians. A binary mask of suitably sized and positioned apertures can thus control the complex transmittance. The use of different diffraction orders has advantages which are discussed in Chapter 3 along with a more rigorous analysis of the Lohmann filter.

The maximum light efficiency of a binary Lohmann hologram is 10% which is the maximum diffraction efficiency of a square wave absorption grating (Ref. 18). In practice it is important to ensure that the hologram is truly binary as its loss will lower the light efficiency.

Of course, a binary hologram has high resistance to noise and the extra advantage of independence of photographic processing.

### 1.7 LEE HOLOGRAM

Another technique which utilises detour phase is that due to Lee (Ref. 22). Any complex number can be decomposed



into four positive numbers which are its components on the positive real, negative real, positive imaginary and negative imaginary axes,  $A^+$ ,  $A^-$ ,  $B^+$  and  $B^-$  respectively.

If every Fourier coefficient cell is divided into four equal parallel strips they will each transmit with a different detour phase. Adjacent strips will differ in phase, as seen from the  $J^{\text{th}}$  diffraction order, by  $J \cdot \pi/4$  and a complex amplitude can be simulated by weighting the transmittances, either by controlling the density or size of two of the component regions  $A^-$ ,  $B^-$ ,  $A^+$  and  $B^+$ .

The maximum transmittance occurs when two of the subcells are clear. In this case, like the Lohmann hologram, the light efficiency has a maximum value of 10%.

### 1.8 BLEACHED FILTERS

Any of the filters already discussed can be bleached in order to improve their diffraction efficiency (Ref.23 ). For a continuous tone hologram that is subsequently bleached the maximum light efficiency becomes 33.9% - the diffraction efficiency of a sine wave phase grating (Ref. 18 ). Bleached binary holograms have a maximum light efficiency of 41% - that of a square wave phase grating. On bleaching, however, the amplitude information is lost. In this sense these bleached holograms behave like a Kinoform (Ref. 24 ). This is a phase only computer

generated element in which it is assumed the modulus of the transmitted amplitude is unity. Under circumstances of a well diffused object this may be a fair assumption but in general this will not be the case and the resulting image will suffer a loss in fidelity due to this discarded amplitude information. The Kinoform, however, does have a maximum light efficiency of 100% when all the incident light is diverted to its single on axis image.

### 1.9 PARITY SEQUENCE FILTERS

One technique which offers high light efficiency but preserves fidelity is based on spectrum levelling by parity sequences (Ref. 25, Ref. 26). The parity terms form a sequence orthogonal to the required complex transmittance sequence from which they are calculated. A constraint is applied so that both the complex sum of and difference between the amplitude transmittance and its associated parity sequence term is unity. Thus if each amplitude and phase term is replaced by its associated pair of phase only terms, the modulus of the amplitude is levelled to a constant value of unity, and a high light efficiency element is the result.

Physically the parity sequence filter operates like a Kinoform except in terms of the loss of fidelity in the image. The parity elements ensure that the light is diffracted either into or away from image points so that

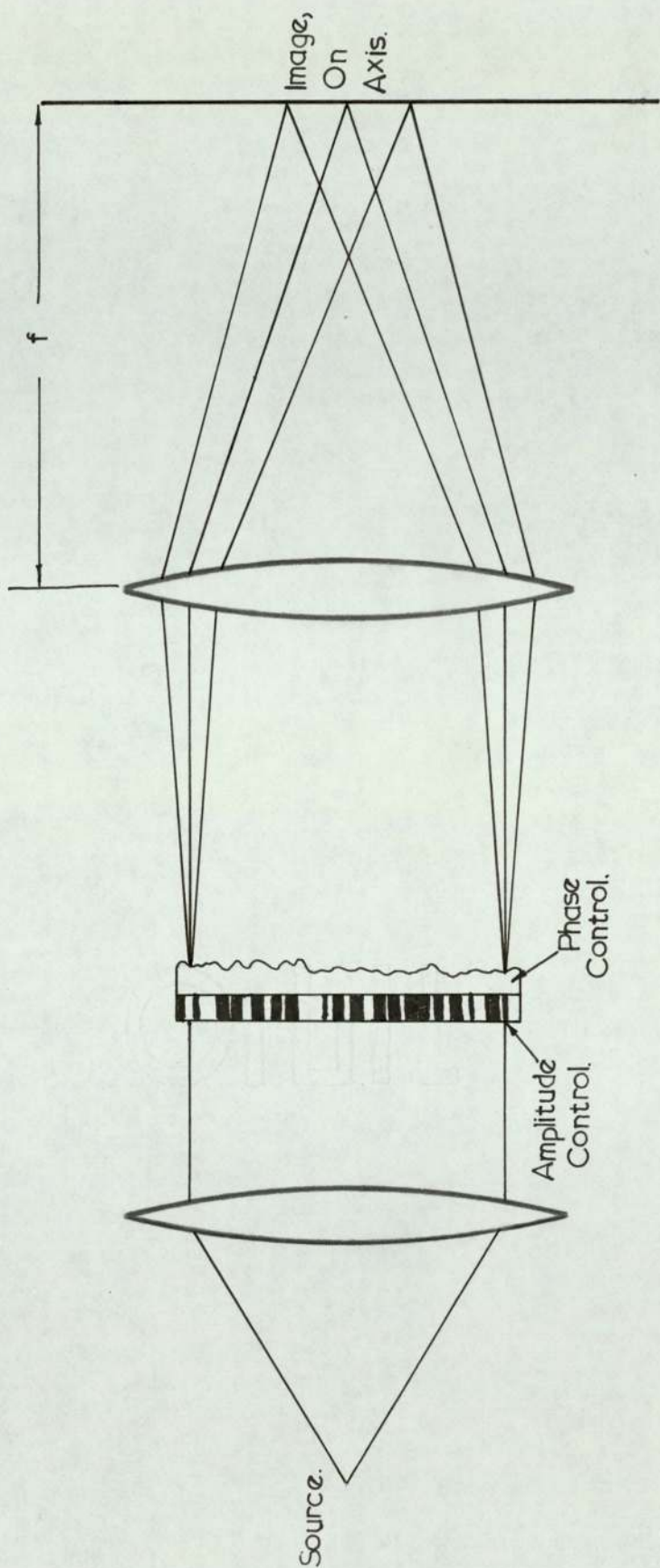


its fidelity is preserved. Like the Kinoform the parity sequence filter requires continuous phase control over  $2\pi$  radians which demands grey scale display and carefully controlled photographic processing.

The recent approach of binary phase filters (Ref. 27 ) avoids the continuous tone and processing requirements and involves filling each cell with an array of subcells in which the phase can take only two values.

#### 1.10 ROACH (REFERENCELESS-ON-AXIS COMPLEX HOLOGRAM)

The loss of fidelity of the Kinoform is not suffered by the Referenceless On Axis Complex Hologram (Ref. 28 ) which uses two different emulsions in a colour reversal film such as Kodachrome II to control the complex wavefront, see Figure 1.10. The emulsion which absorbs the colour of the reconstructing light is used to control the modulus of the complex transmittance. The phase is controlled by the other emulsions which do not attenuate at the reconstructing wavelength. The hologram is constructed by illuminating the colour film with the modulus and phase information independently through different colour filters. The light efficiency falls below the theoretical value of 100% because of the attenuation by the colour dyes and in practice the maximum light efficiency is 50% (Ref. 18 ). In effect ROACH is a sandwich filter with the construction and alignment difficulties avoided.



Referenceless - On - Axis - Complex - Hologram. - ROACH

FIG. 1.10



1.11 DYNAMIC RANGE

The dynamic range for grey tone holograms is limited by the finite film density range. For the computer generated binary holograms the dynamic range is limited by the number of available addressable points on the display. For the sandwich filters (including ROACH) the amplitude transmittance is related to film density by

$$T = 10^{-\frac{D}{2}} \quad 1.16$$

Typically the range of density over which transmittance is related to the inverse of the exposure linearly is 3. Hence, for the  $1/(F)$  type filter the dynamic range is about 30:1 while for the  $1/(F)^2$  type of attenuation the dynamic range is about  $\sqrt{30}$ :1. For the continuous tone Lee hologram the dynamic range is similarly about 30:1. The Lohmann binary hologram with  $(RxR)$  addressable points per cell has a dynamic range of  $(R+1)$ . The Kinoform, of course, has a dynamic range of 1. The Parity phase filters and Binary phase filters that will be discussed in more detail in a later chapter have more efficient coding than other forms of computer generated holograms and consequently have a higher dynamic range.

CHAPTER 2

AMPLITUDE AND PHASE VARIATIONS IN A COHERENT  
DECONVOLUTION SYSTEM



## 2.1 INTRODUCTION

In Chapter 1 some of the limitations of computer generated holograms were mentioned, in particular those related to the limited number of addresses in the display. These constraints will be considered in more depth in Chapter 3 and 4.

In practice the linear deburring filter will be different from the ideal form shown in Figure 1.6 for another quite different reason - the presence of noise in the system. Coherent optical systems are very sensitive to the presence of dust or other blemishes on the components. As we have already mentioned, the use of a Fourier transform system suppresses the effects of this coherent noise due to blemishes in the spatial filter. However, elsewhere in the system blemishes create unwanted diffraction rings in the image. Wolton and Redman (Ref. 29 ) have produced a system which suppresses this type of noise by introducing a continuous simultaneous movement of both the first

Fourier transforming lens and the filter element.

Also, as well as this coherent optical noise there is always some spatial noise,  $n(x)$ , in the data. For data in the form of a transparency the main source of spatial noise is the grain of the film. (This is also true for a numerical system which has to read the numerical data, typically by microdensitometer from a film record).

The blurred object distribution,  $c(x)$ , is thus modified to  $c^1(x)$  where

$$c^1(x) = g(x) \otimes s(x) + n(x) \quad 2.1$$

As we have seen, the perfect deblurring filter is highly amplifying at the pole regions. (Strictly, "amplifying" is an incorrect term for the action of a passive coherent filter. We shall use "amplifying" as meaning a transmittance of approximately unity).

As the spatial noise,  $n(x)$ , will contain frequencies far beyond those of the signal, an operation by the ideal restoring filter, Figure 1.6, on a spectrum of a noisy object distribution,  $C^1(H)$ , will result in a high amplification of the noise in the regions where the signal to noise ratio is small - at the poles of the filter.

There is clearly an optimum filter function the general form of which must be such that when the signal to noise power is large its operation is with the degree of



amplification of the perfect filter but when the signal to noise power is small a greatly reduced amplification results.

## 2.2 LEAST-MEAN-SQUARED-ERROR FILTER

When  $n(x)$  is unknown Equation 2.1 cannot be solved directly. The most that can be done is to produce an estimate,  $\hat{g}(x)$ , of the solution. If the object distribution and the noise are viewed as spatially stochastic processes, the best estimate is defined as one that maximises the posterior probability density of  $g(x)$ , given  $c^1(x)$ , as determined by Bayes's rule. The processes  $n(x)$  and  $g(x)$  are independent. If they were also Gaussian with zero means and known covariances, the posterior probability density would be greatest for the linear estimate

$$\hat{g}(x) = \int m(x^1) g(x-x^1) dx^1 \quad 2.2$$

in which the estimating kernel,  $m(x^1)$  is chosen to minimise the mean squared error,

$$\mathcal{E} = E(\hat{g}(x) - g(x))^2 \quad 2.3$$

between the true distribution and the estimate, where  $E$  denotes an expected value (Ref.30 )

Often the noise may at least approximately be considered to be a Gaussian process. However, this is rarely the case for the object to be restored. It is assumed that if the estimator is optimum for a class of Gaussian

processes that resemble in their structure the finest detail of the object to be restored, then it will be effective when applied to these objects as well.

For the case of optical data, photographic grain noise is mostly multiplicative and only for low contrast images can the additive noise model of Equation 2.1 be assumed, Huang (Ref. 31) and Yu (Ref. 32). In addition the human observer, frequently the last step in an optical system, adds a further complication to the determination of a filter superior to the linear least mean square error estimator defined by Equation 2.2.

Later in this chapter we demonstrate the failure of this LMSE criterion for the deconvolution of a linear motion blurred object by simulating a coherent optical system by computer. We also study, again by computer simulation, the effects of random noise processes on other parts of the system.

### 2.3 FORM OF THE LMSE FILTER

The estimating kernel,  $M(x)$ , of equation 2.2 is determined by the form of the blurring function,  $s(x)$  and the noise and object properties. These are completely characterised by their spatial covariance functions - or by the Fourier transform of these,  $\phi_n(H)$  and  $\phi_o(H)$ , which are the spatial spectral density functions of the noise and object processes



respectively.

The resulting LMSE filter, in the usual Wiener form (Ref. 2), is written as

$$F'(H) = F(H) \cdot \frac{\frac{\phi_o(H)}{\phi_n(H)}}{\left\{ \frac{\phi_o(H)}{\phi_n(H)} + |F(H)|^2 \right\}} \quad 2.4$$

where  $F(H)$  is the ideal filter for the noise free system.

The minimum mean square error attained by this estimator is then

$$E_{\min} = \int \frac{\phi_o(H) \cdot \phi_n(H) \cdot dH}{\left\{ |S(H)|^2 \cdot \phi_o(H) + \phi_n(H) \right\}} \quad 2.5$$

Wiener filtering does not, of course, increase the signal to noise ratio.

## 2.4 COMPUTER SIMULATION - DESCRIPTION OF SYSTEM

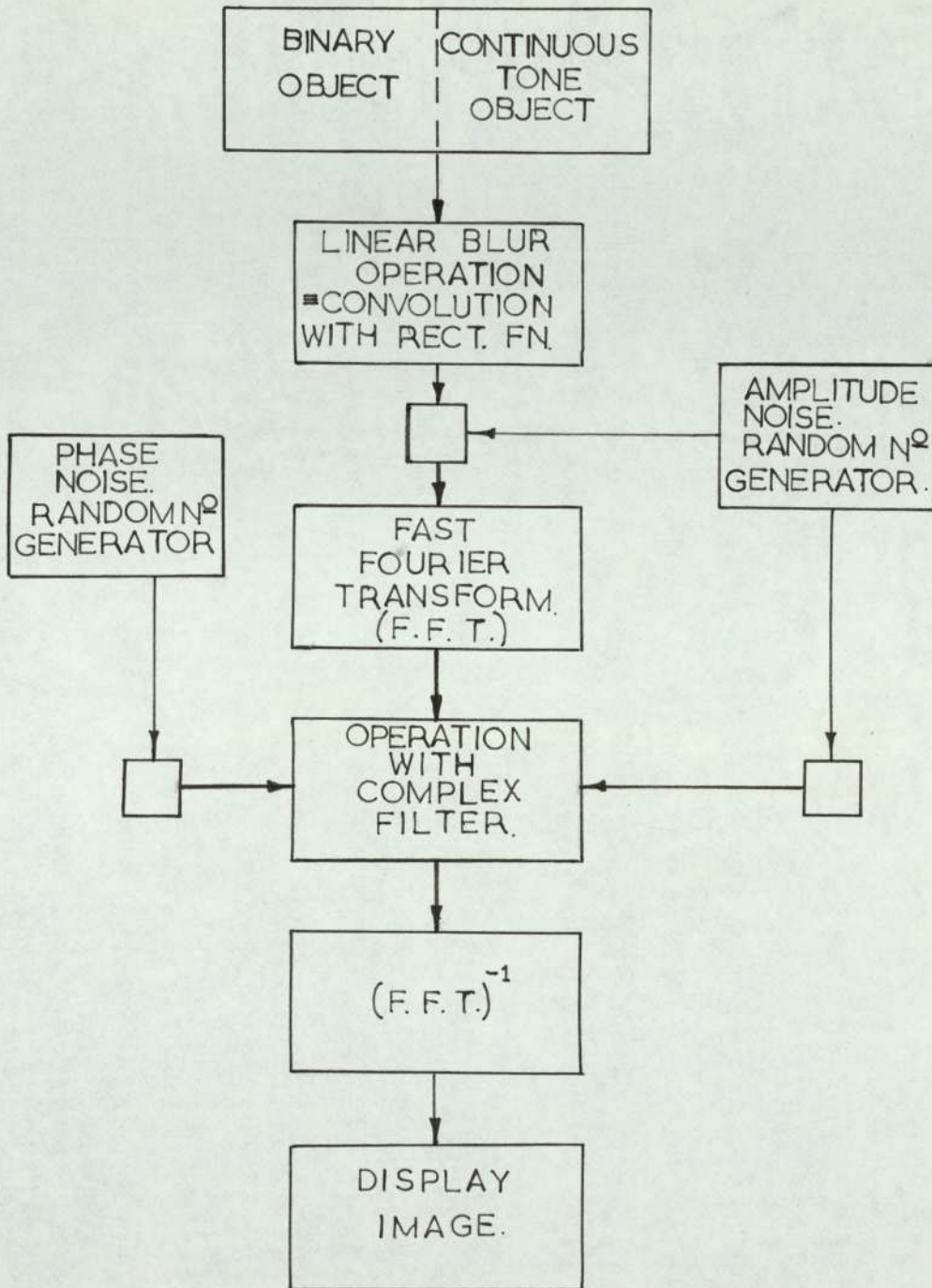
A block diagram, Figure 2.1, shows the computer model used to investigate the operation of a coherent deconvolution system. For convenience and speed it was restricted to one dimension and the convolution process considered was limited to a linear motion blur.

Data, after input, is first convolved with a rectangle function. At this stage a random variation can be produced in the blurred object amplitude by the addition of a sequence of computer generated normally distributed random numbers - scaled to simulate various degrees of noise in the object. This noisy object is then Fast Fourier Transformed to yield the complex spectrum. The transformation was performed using a standard Nottingham Algorithms Group Library procedure, CO6ABA.

### Fast Fourier Transformation

The requirement of having a data sequence with a number of terms,  $N$ , as a power of 2 was met by using 256 sampling points to represent the object. It is worth noting that in order to ensure perfect symmetry, from a computational point of view, between object and Fourier space, the calculated spectrum has only positive frequency terms. The transform is still capable of operating with complex data, however, as the spectrum extends from zero frequency to a frequency of  $2.N_q-1$ , where  $N_q$  is the Nyquist





Computer Simulation System.

frequency. That is, the upper half of the zero order and the lower half of the positive first order of the total periodic spectrum are used. The spectrum periodicity is a result of the finite sampling in data space. As the most efficient sampling criterion of Whittaker and Shannon is implicit in the Fast Fourier Transform procedure the zero order frequency terms and the first order frequency terms about exactly - see Chapter 3, section 3.2 and Figure 3.1. The first order terms are thus aliased frequencies of the negative half of the zero order period of the spectrum, and indeed are equivalent to these first order terms positively shifted by one frequency space period. As the central frequency of the first order of the spectrum is the alias of the zero frequency term (which already appears in the spectrum sequence) it is discarded. Hence, for  $N$  data points the spectrum extends from frequency 0 to  $(N-1)/\Delta X$ , where  $\Delta X$  is the object extent and  $dX = \Delta X/N$  is the separation of samples in the data.

The procedure CO6ABA can thus perform the operations

$$F(HZ) = \frac{1}{\sqrt{N}} \sum_{XZ=0}^{N-1} f(XZ) e^{-\frac{2\pi i HZ \cdot XZ}{N}} \text{ for } HZ=0,1,2,\dots,N-1 \quad 2.6$$

and

$$f(XZ) = \frac{1}{\sqrt{N}} \sum_{HZ=0}^{N-1} F(HZ) e^{\frac{2\pi i HZ \cdot XZ}{N}} \text{ for } XZ=0,1,\dots,N-1 \quad 2.7$$



where  $F(HI)$  and  $f(XI)$  are each a pair of one dimensional arrays containing real and imaginary terms.

### Object Data

Two different data sequences were used in the simulations:

- 1) A dilute binary variable frequency bar chart shown in Figure 2.2 having bars of sizes 64, 32, 16, 8, 4 and 2 samples, with gaps of 48, 24, 12, 6, 3 samples. A reduced version of this with the 5 smallest period bars was also used.
- 2) A continuous tone but dilute object formed by convolving the 5 point bar chart of Figure 2.2 with a Gaussian distributed function having a full width at half maximum height of 8 samples - Figure 2.2.

### Convolution Operation

In each case a linear convolution operation extending over 8 samples was performed to produce the blurred objects shown in Figures 2.3.

The bar chart periods which have frequencies within the negative regions of the optical transfer function of the blur will suffer lateral shifts of half their periods induced by the  $\pi$  radians phase change in frequency space. For the object considered, the bars with periods less than 4 units will be laterally shifted. This can be seen at the high frequency end of the bar chart

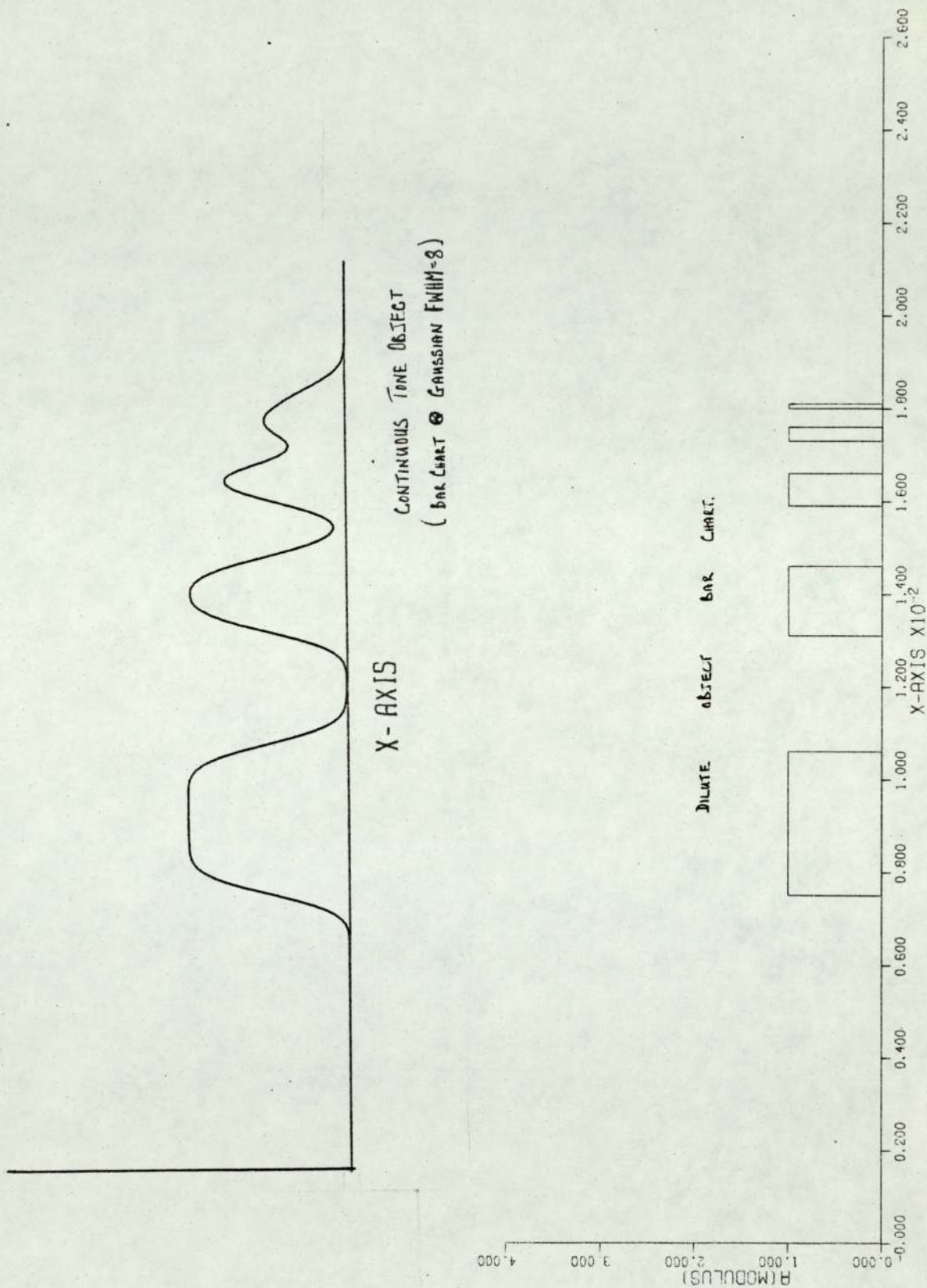


FIG. 2 . 2



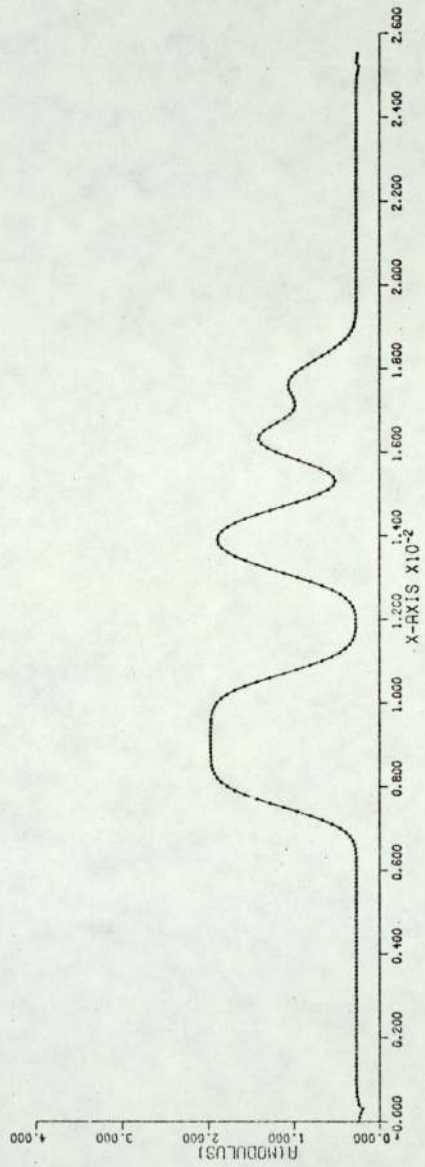
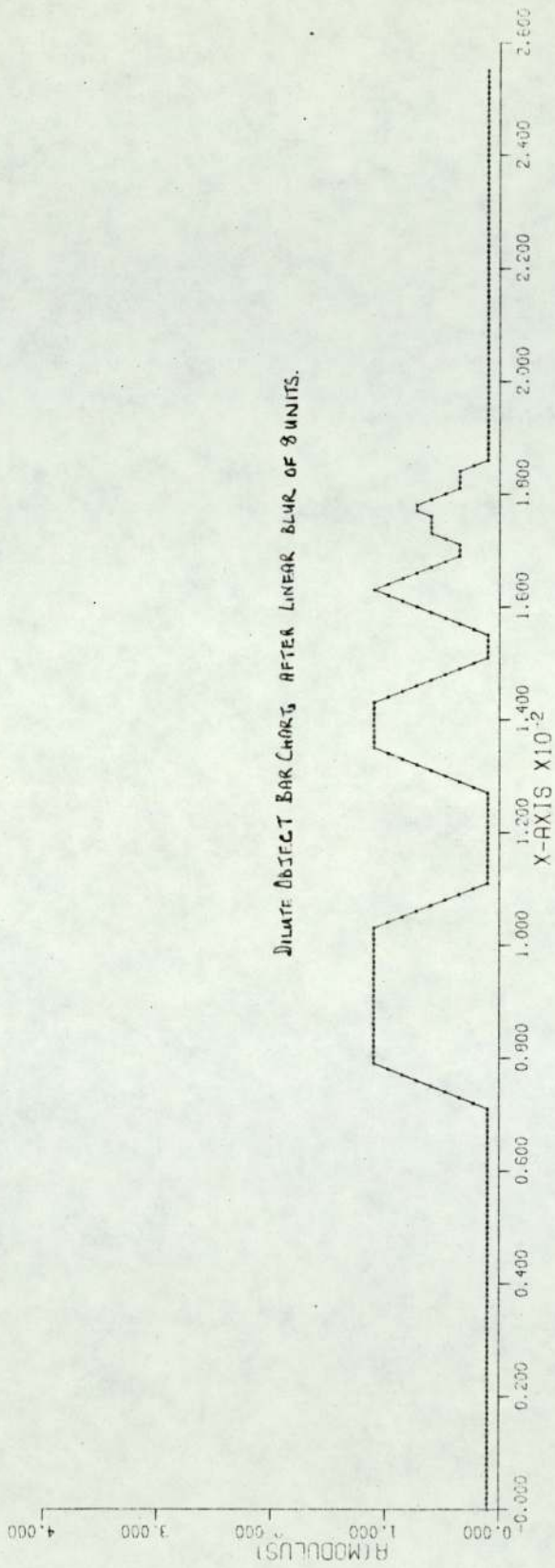


FIG 2.3

in Figure 2.3. The phase terms in the deblurring filter have to correct for this.

## 2.5 DECONVOLUTION RESULTS AND DISCUSSION

### Kinoform

The necessary phase correcting element is shown in Figure 2.4 as a square shaped function which oscillates between +1 and -1. If this element operates on the spectrum of the blurred bar chart and corrects its phase, an inverse transformation will result in the image of Figure 2.5. Over all this image does not look much more like the original bar chart than does the blurred version. However, the correction of the phases in Fourier space has had the important effect of correctly redistributing the peaks at the high frequency end of the bar chart. It is this real space shifting property of the Fourier space phase terms which makes phase control of paramount importance. The phase only element, used here as a crude deconvolution filter, is often called a Kinoform. Its impulse response is also shown in Figure 2.4. The general loss of fidelity of the image after deconvolution by a Kinoform is due to the Kinoform's inability to assign the correct weightings of the frequency components.



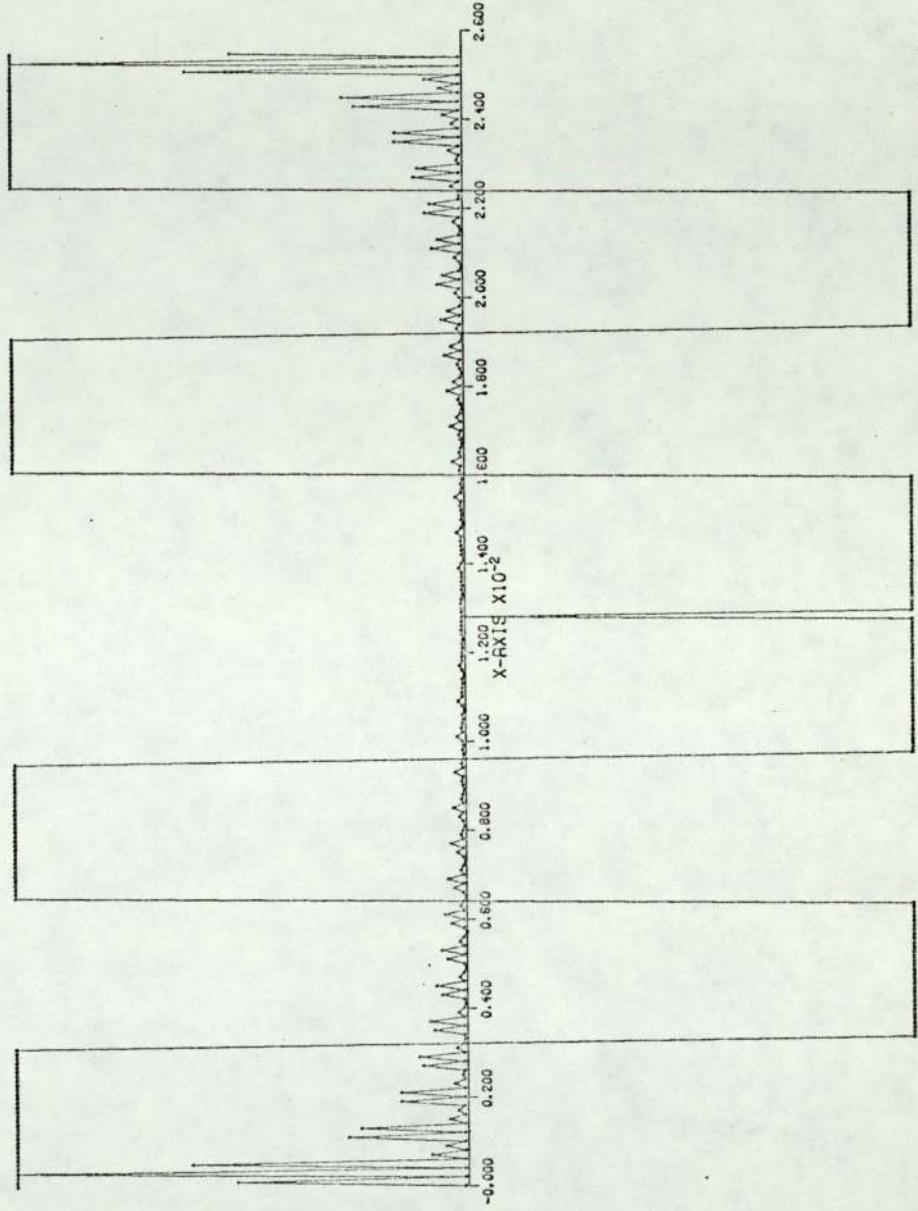


FIG. 2.4

Kinoforn Filter.

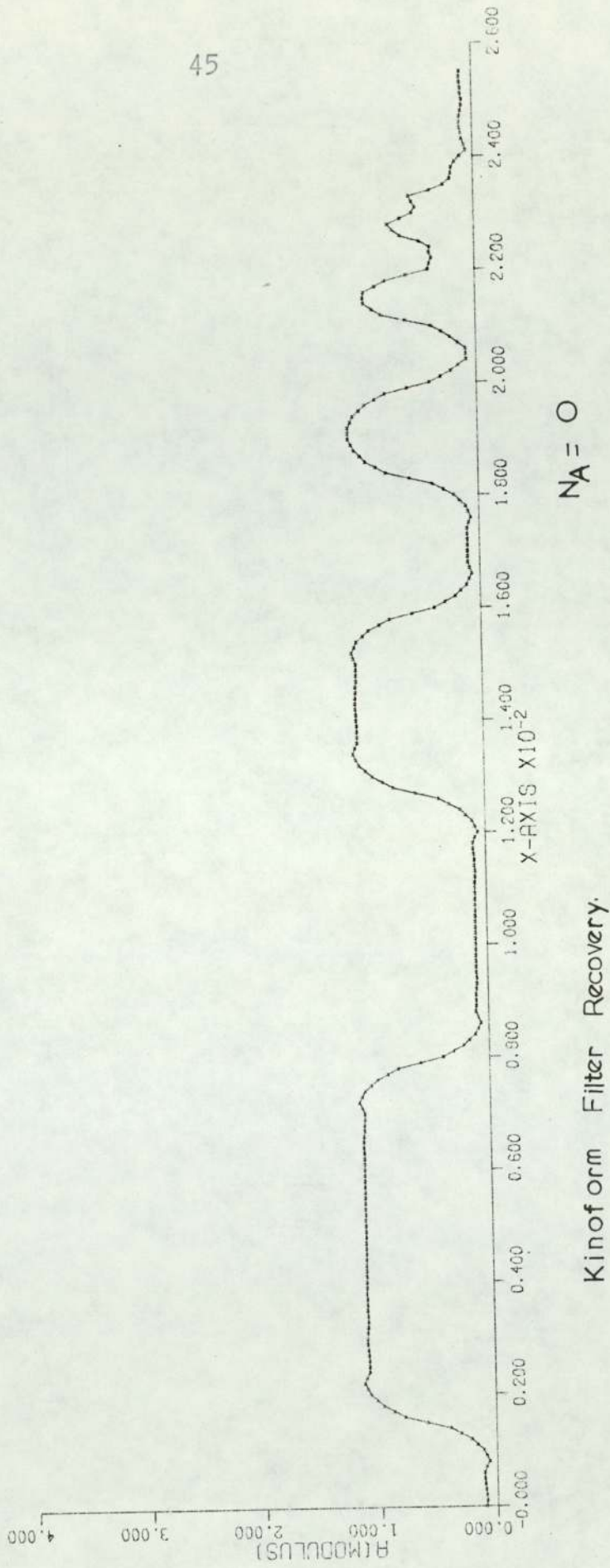


FIG. 2.5



### Ramp Filter

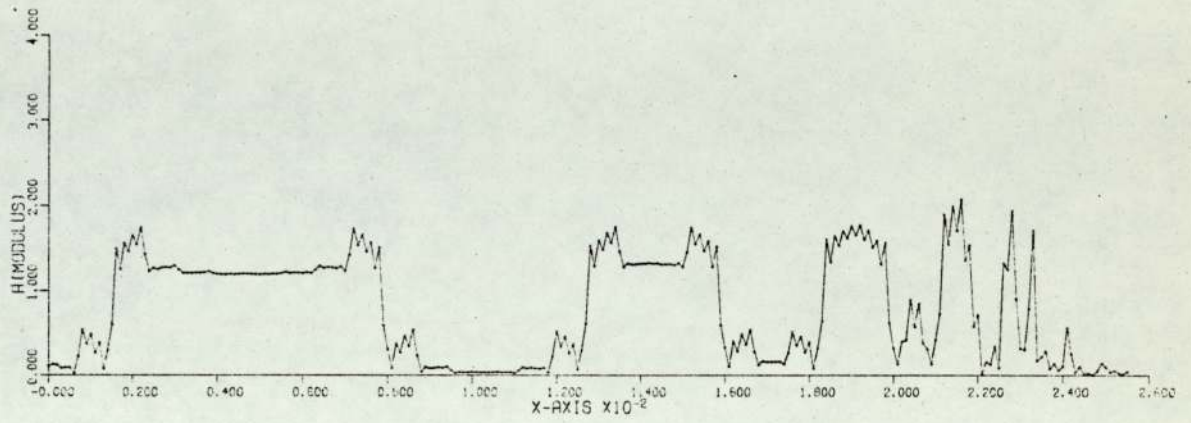
The simplest element which operates on both phase and amplitude and produces some degree of image sharpening is the ramp filter. This corrects the phase as a Kinoform, but also, amplifies the Fourier coefficients by a factor proportional to their frequencies. The larger the value of the constant which measure the slope of the filter's modulus across frequency space, the larger will be the ratio of high to low frequency amplification. Recovered images are shown in Figure 2.6. Although there is sharpening of the deconvolved images compared with the Kinoform recovery, there is considerable image noise due to the amplitude amplification errors of the filter.

### Ideal Filter

In the ideal case an element is required which operates on the amplitudes of the Fourier coefficients so as to correct them to their pre-convolution values.

The ideal filter, the inverse of the optical transfer function of the blur, is shown in Figure 2.7, along with its impulse response.

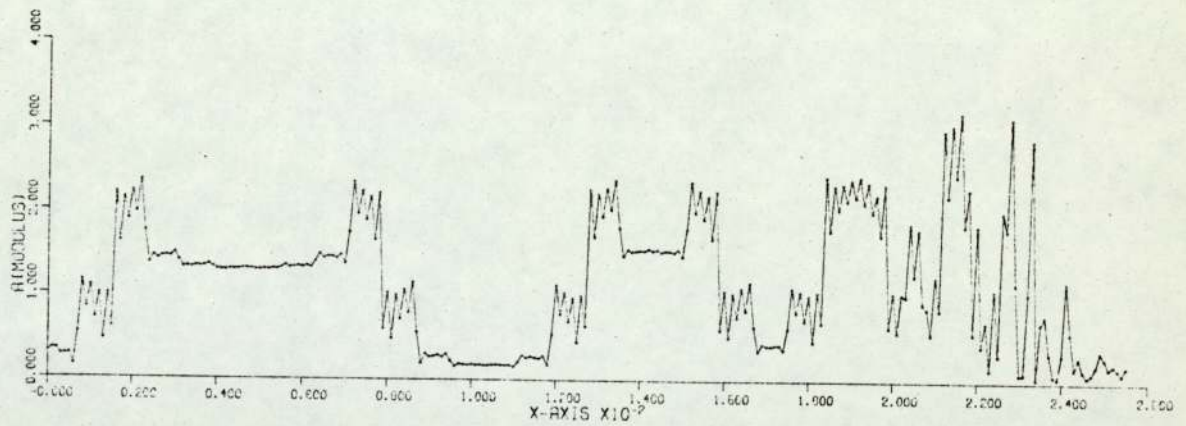
Operating with this filter on the blurred object distributions of Figure 2.3 results in the optimum recoveries of Figures 2.8 and 2.9. These represent the best recoveries possible, as in general the presence of noise will preclude



Ramp Filter Recovery

$$F = 1 + \frac{20}{128} HI$$

$$N_A = 0$$



Ramp Filter Recovery

$$F = 1 + \frac{40}{128} HI$$

$$N_A = 0$$

FIG. 2.6



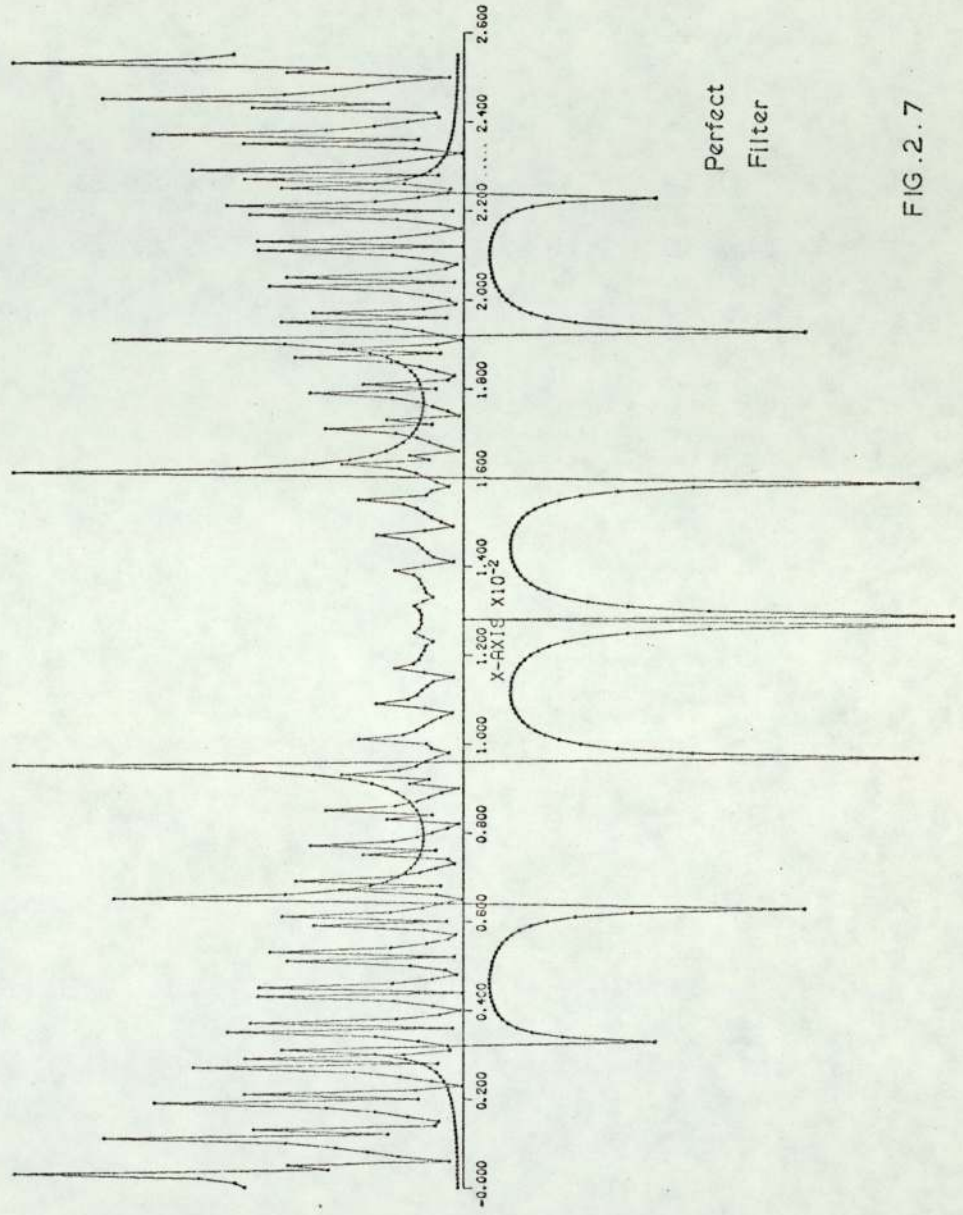
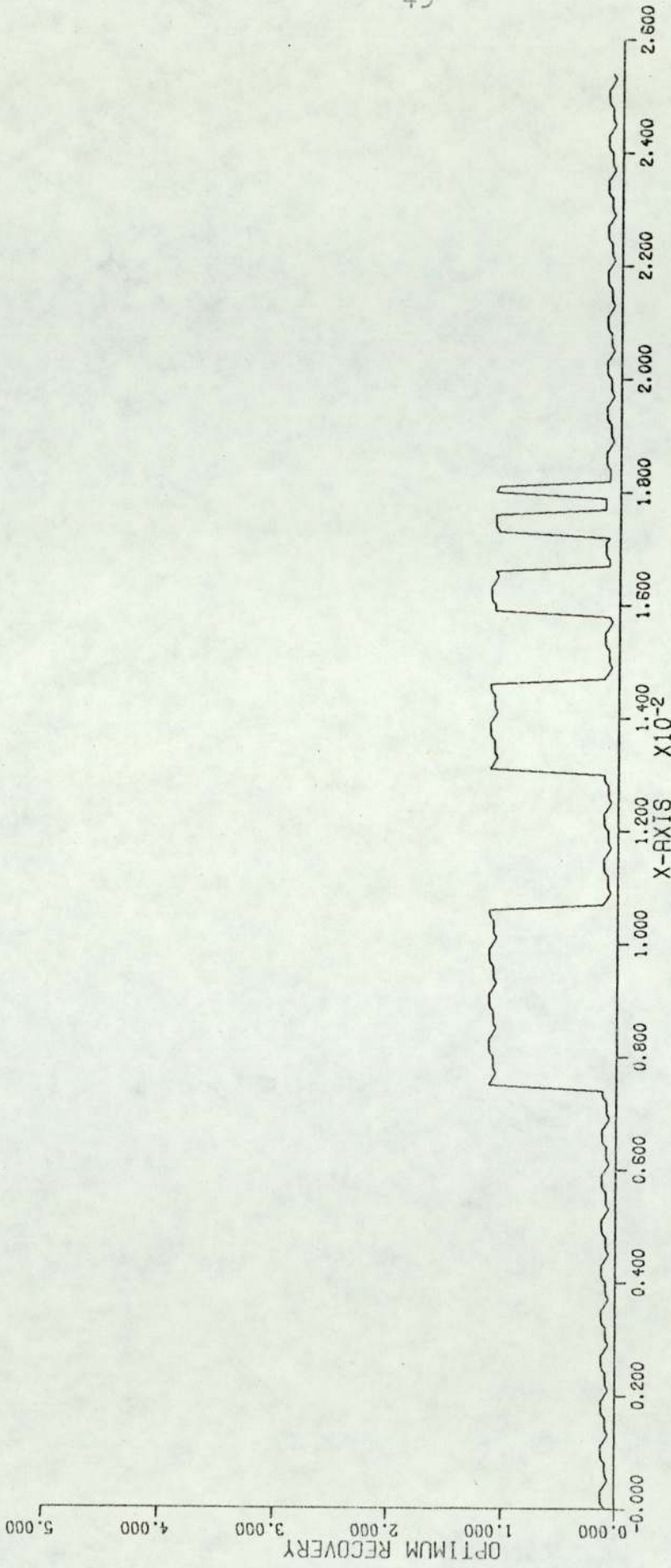


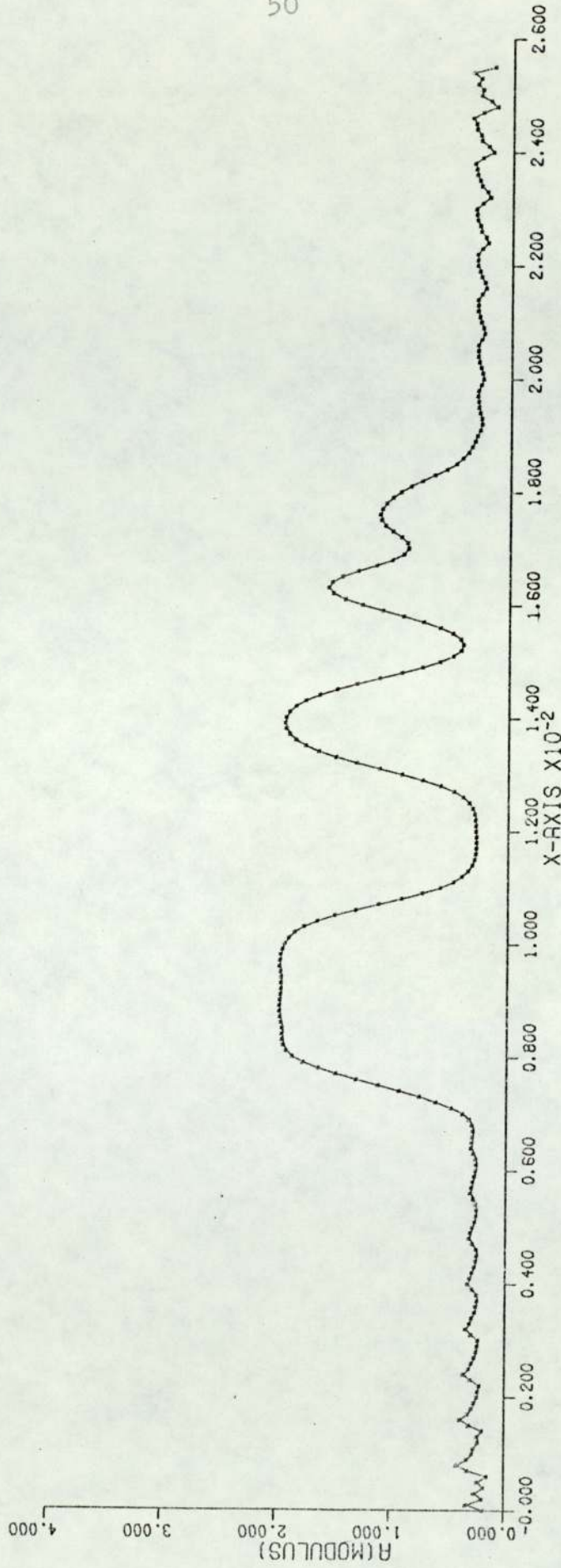
FIG. 2.7



Optimum Recovery.

FIG. 2.8





$N_A = 0$

Optimum Recovery, Continuous Tone Object.

FIG. 2.9

the use of this ideal filter function and necessitate the use of optimum, yet approximate filters.

### Least Mean Square Error (LMSE) Filter

The discussion of section 2.3 centred on the Wiener Least Mean Square Error Filter (LMSE) as an optimum recovery element. Figure 2.10 shows LMSE filters and their impulse responses for signal to noise power ratios,  $\beta = 10000, 1000, 100, 10$  and  $1$ .

### Amplitude Noise Simulation

Two schemes were considered for the simulation of random amplitude noise processes in the data and filter functions.

- a) The amplitude of the random noise was made independent of the local amplitudes, and had a maximum excursion that was simply a constant % of the maximum amplitude.
- b) The random noise was constrained to have a maximum excursion that was a constant percentage of the local object amplitude.

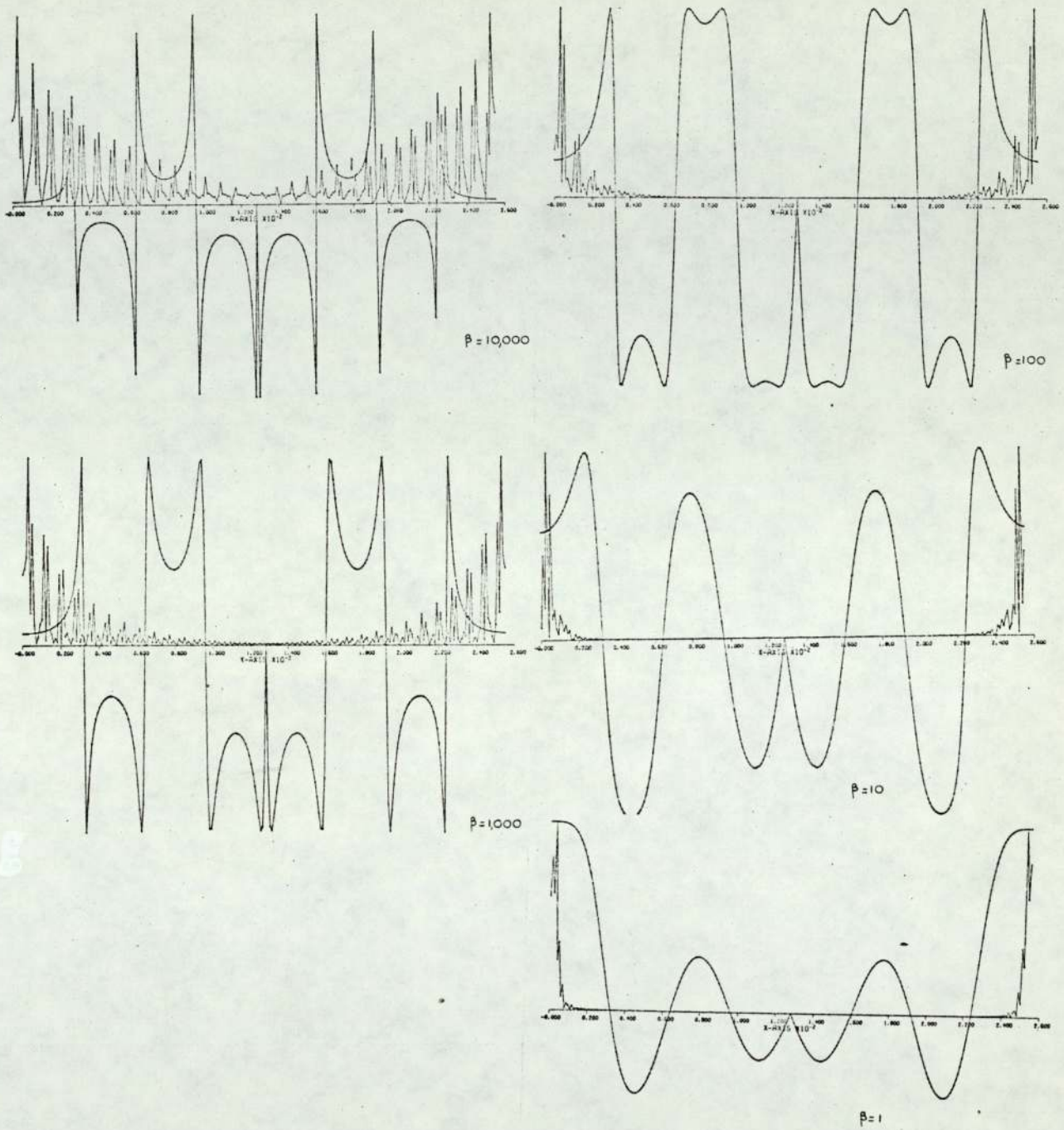
If the random numbers  $n(I)$  are normally distributed over the range 0 to 1, where  $I$  is in this case a counter for the 256 noise values required over the field, then

$$a) \quad C^1(x) = C(x) + n(I).D_1 \quad \text{for scheme a)} \quad 2.8$$

and

$$b) \quad C^1(x) = C(x) + n(I).C(x).D_2 \quad \text{for scheme b)} \quad 2.9$$





LMSE Filters And  
Impulse Responses.

FIG. 2.10

Where  $D_1$  and  $D_2$  are constants equal to the maximum percentage noise excursion being simulated.

Equation 2.8 produces a noisier object distribution as no suppression of the noise terms occurs for low values of  $C(x)$ . Equation 2.9 is more like a model of a grainy film, for a medium density range, as at low amplitude levels the noise is suppressed - see Figure 2.11.

### Phase Noise Simulation

Phase noise was also impressed upon the filter element by adding random fluctuations to the filter's phase components. The filter thus becomes

$$F^1(H) = F(H) \exp i (\phi(H) + n(I).D_3) \quad 2.10$$

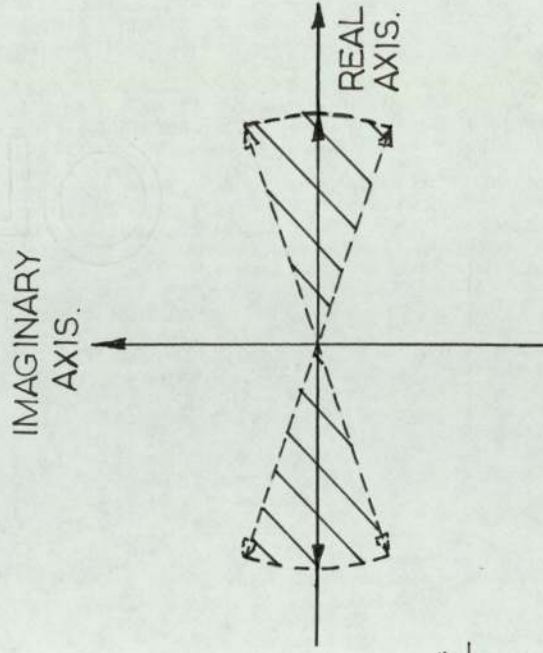
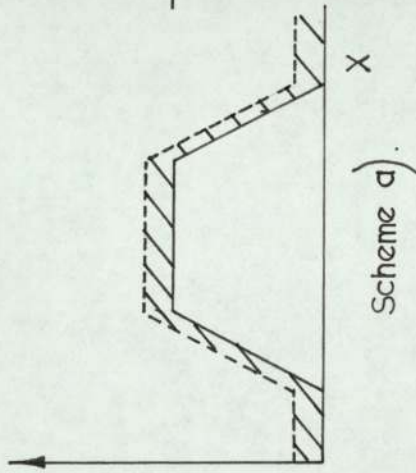
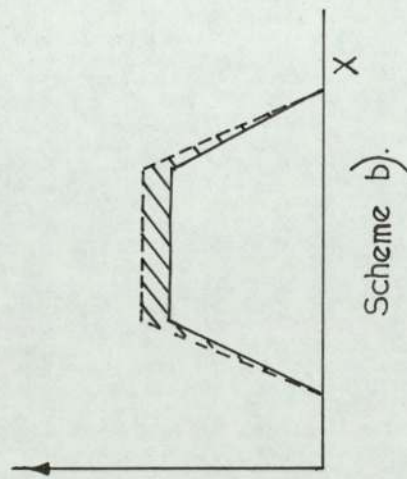
where  $n(I)$  is a random number distributed on the interval 0 to 1, and  $D_3$  is a constant equal to the maximum excursion of the random phase variation. This random phase factor converts the wholly real deblurring filter into a truly complex element - see Figure 2.11.

### Deconvolution in the Presence of Object Amplitude Noise

In this section the results of deconvolving both the blurred binary object and the blurred continuous tone object are presented. The noise value,  $\bar{N}$ , represent the average excursions of the noise process, as a percentage of the maximum object amplitude for a), and as a percentage of the local amplitude for b). The results are in terms



Random Excursions Constrained  
Within Shaded Regions.



Object Amplitude Noise.

Filter Phase Noise.

FIG 2.11

of the modulus of the recovered image amplitudes. The images recovered by an ideal filter for the blurred objects degraded by various levels of noise according to scheme a) are shown in Figures 2.12 a) for the binary object and 2.13 a) for the continuous tone object. The lack of noise suppression is apparent in the images which are severely affected by quite modest values of  $\bar{N}$ . For comparison, recovered images of the binary object, with noise added as scheme b), and deconvolved with an ideal filter, are shown in Figure 2.12 b). The ideal filter represents the case when the noise power,  $\Phi_n$ , is zero and as such the signal to noise power ratio,  $\beta$ , is infinity. It can be seen from the recoveries that scheme a) produces a more noisy image than scheme b), as would be expected.

The effects on the recoveries of using Least Mean Squared Error type filters can be judged from the deconvolved images of Figures 2.14 a); 2.15 a), b); 2.16 a), b); 2.17 a), b), for the binary object with signal to noise power ratios,  $\beta$ , of 1000, 500, 100 and 10 respectively for the noise schemes a) and b). Similarly, Figures 2.18 a), b) to 2.21 a), b) are deconvolutions with  $\beta$  of 1000, 500, 100 and 10 for noise schemes a) and b) but with the continuous tone object.



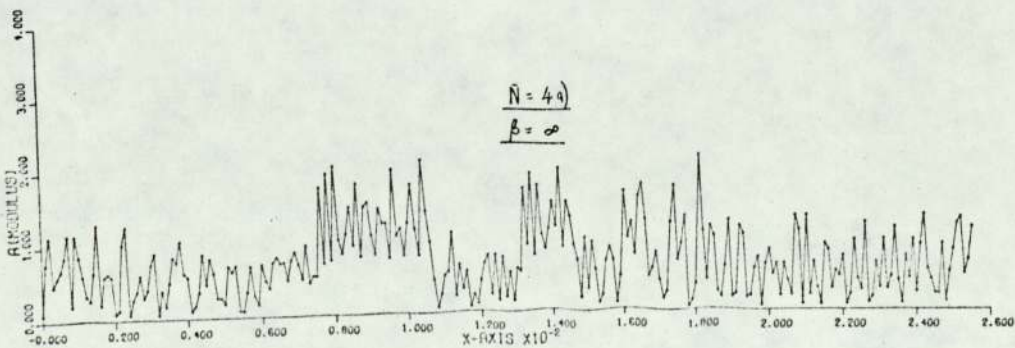
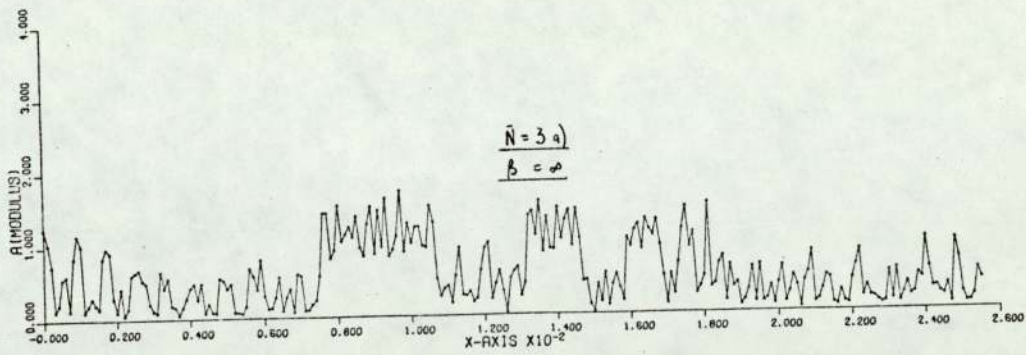
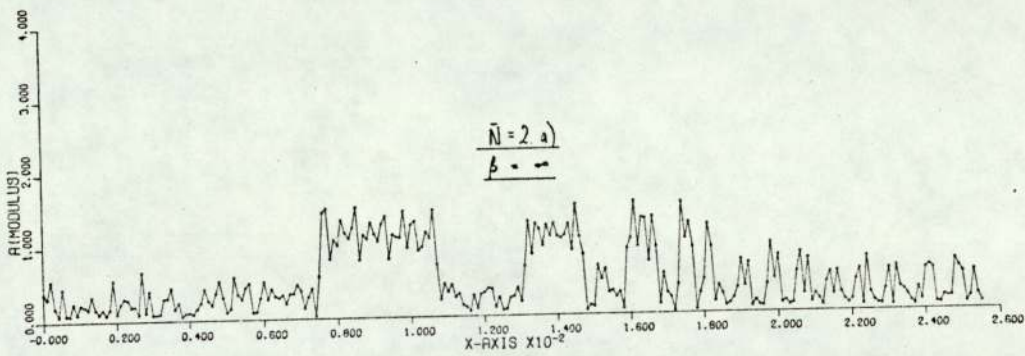
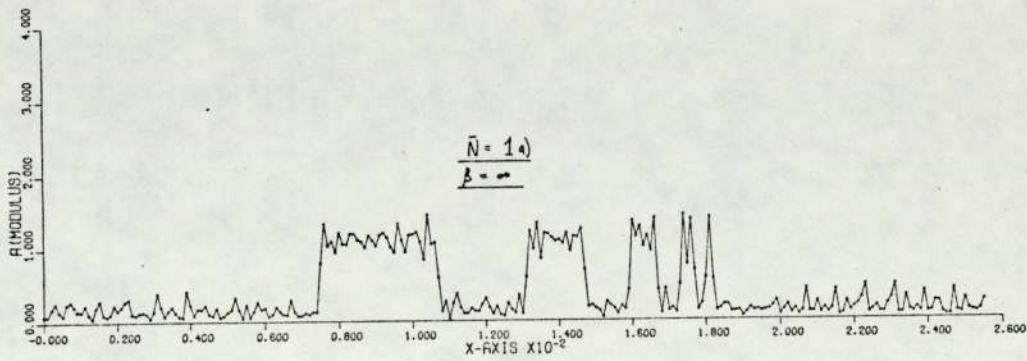
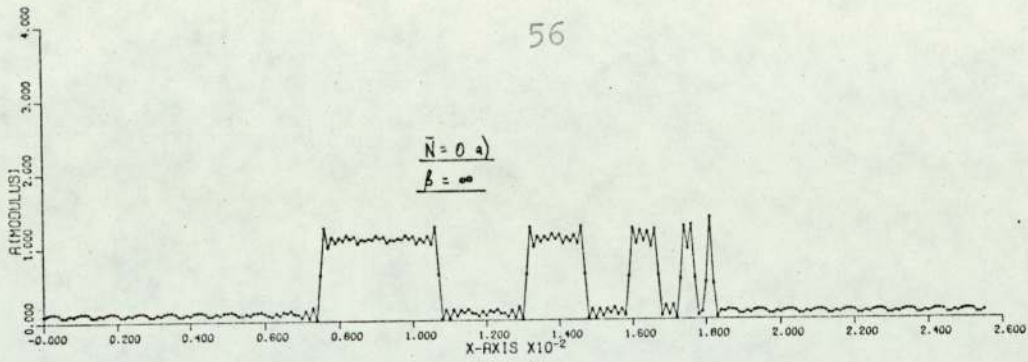


FIG.2.12 a

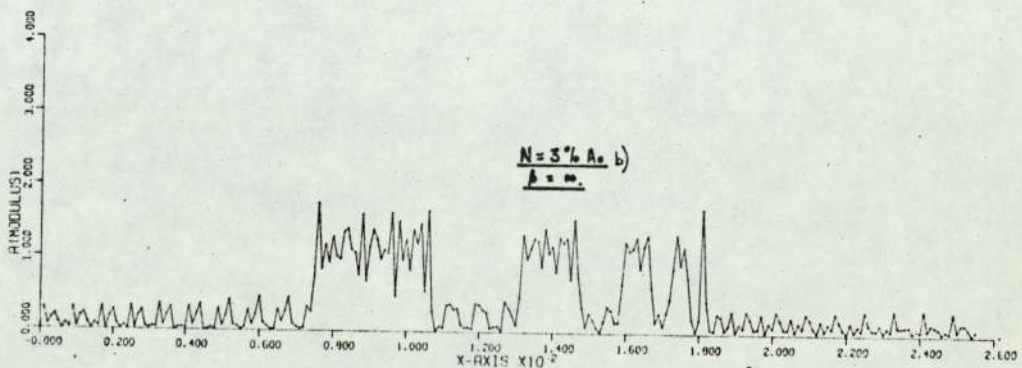
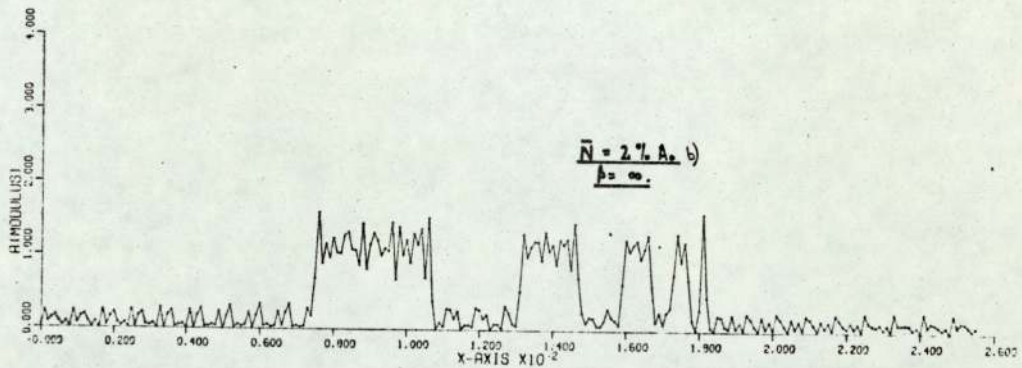
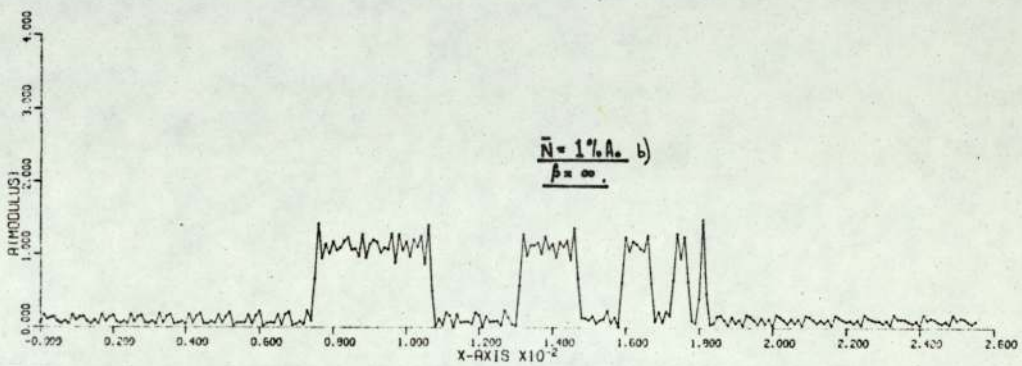
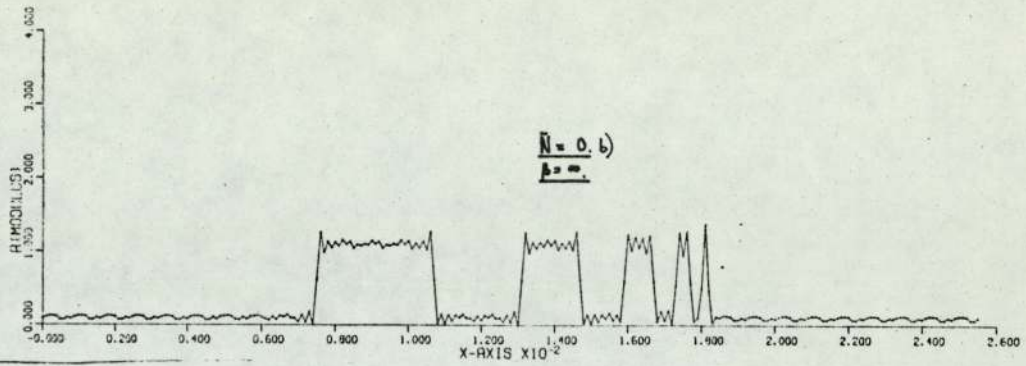


FIG. 2.12 b



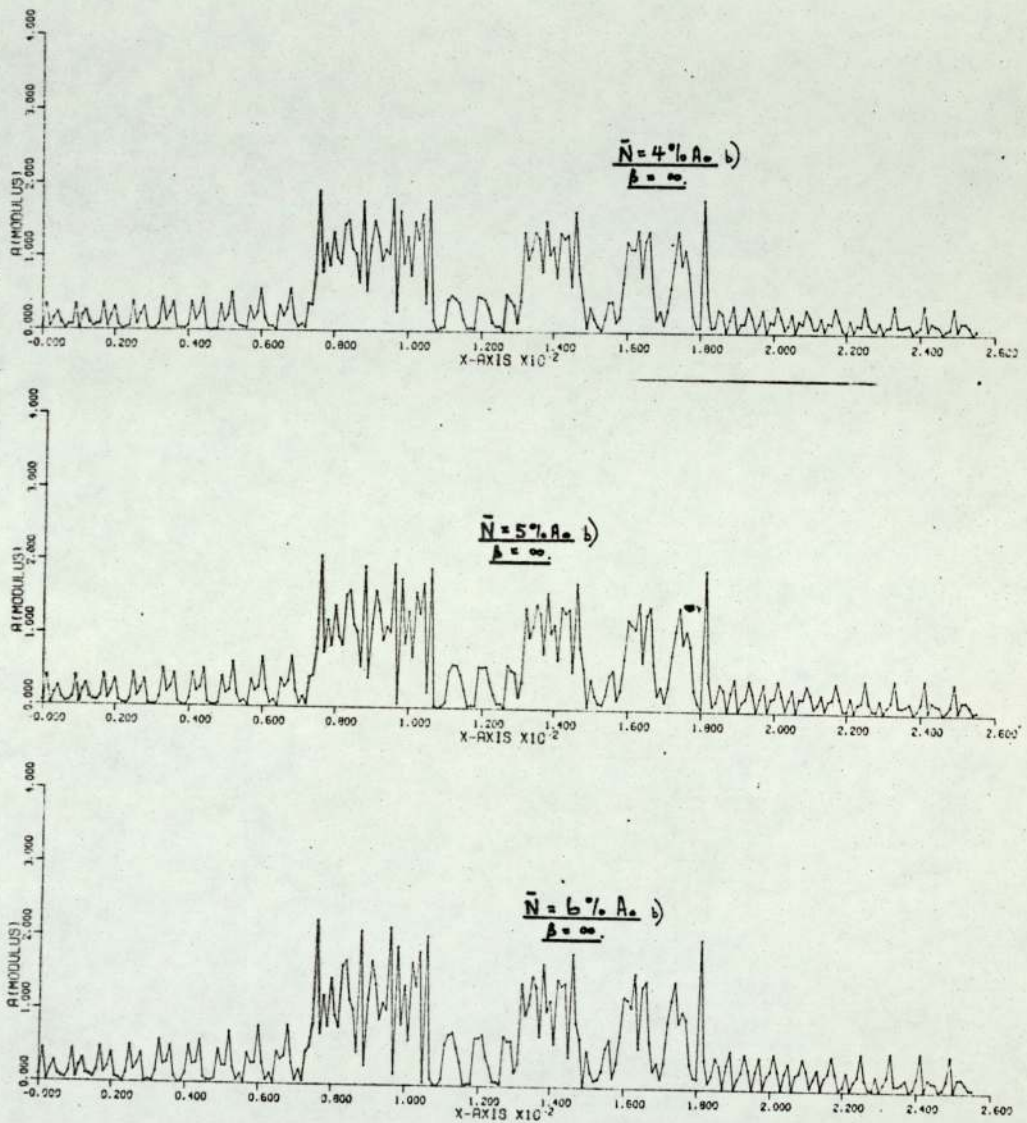


FIG. 2.12 b

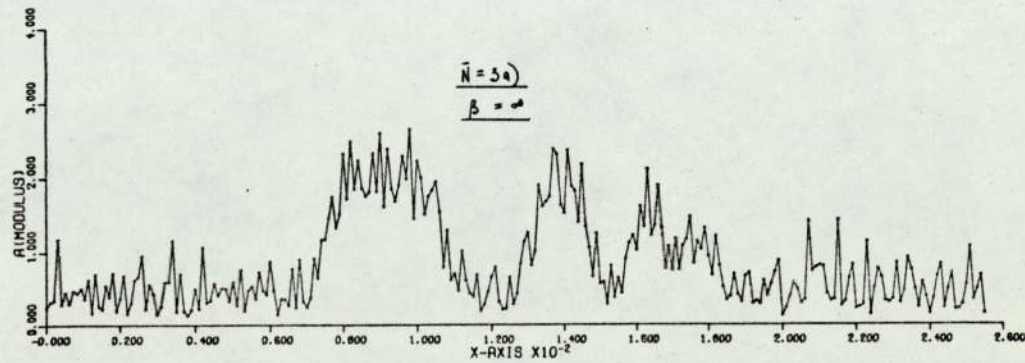
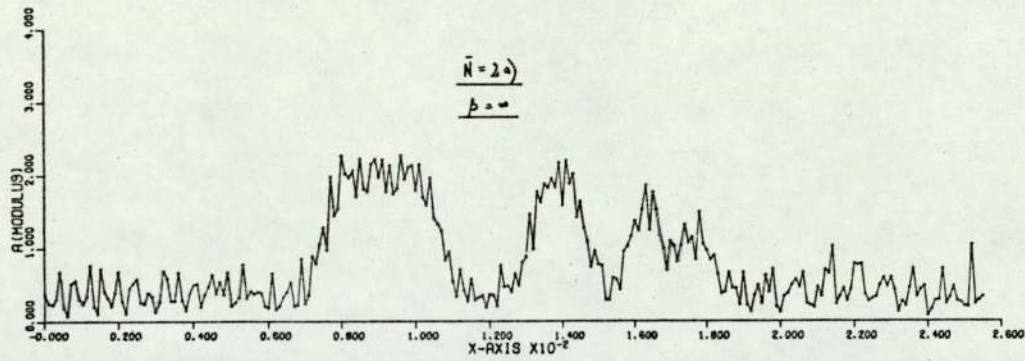
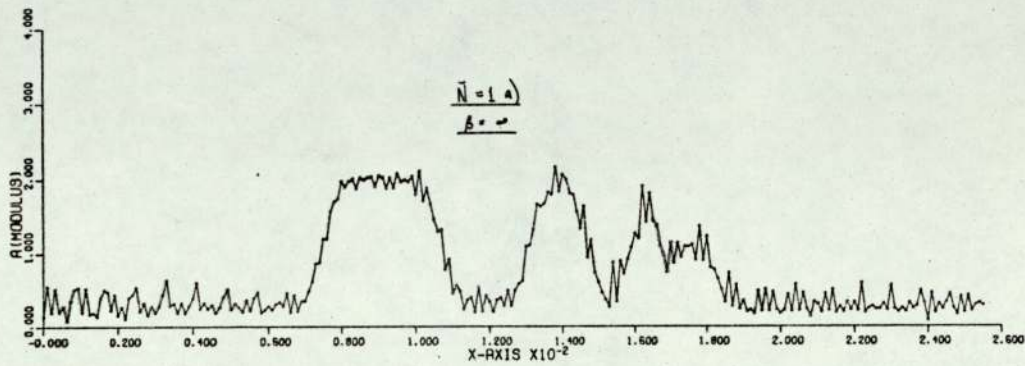
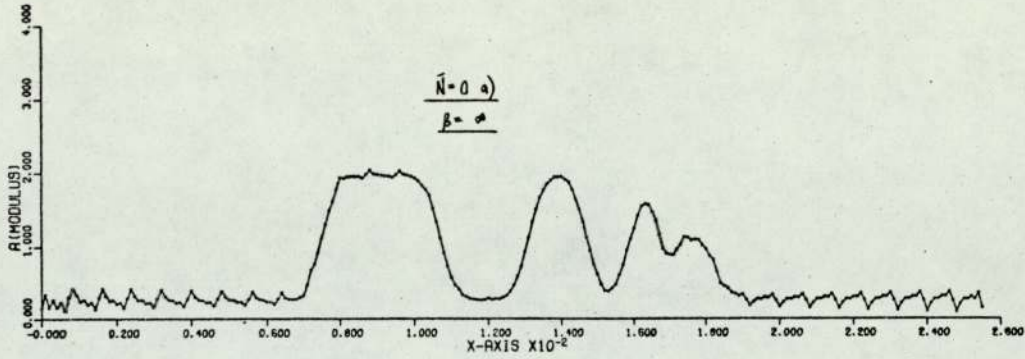


FIG. 2.13a



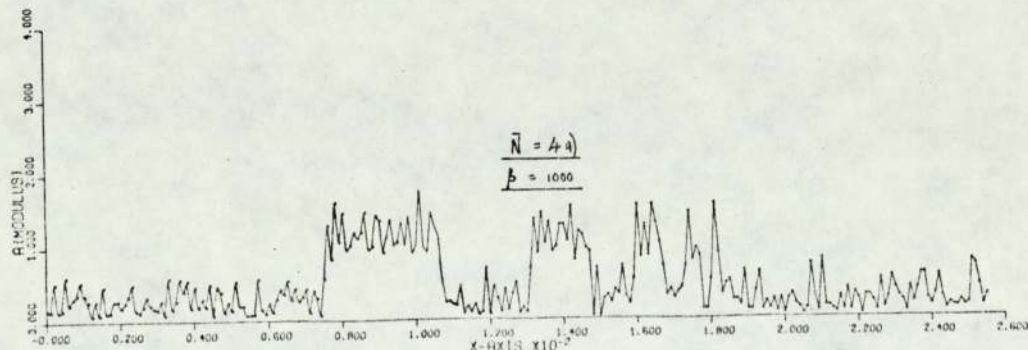
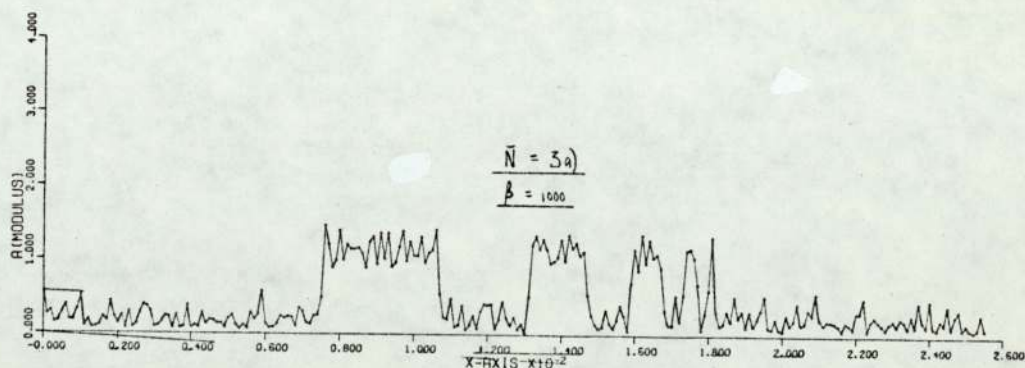
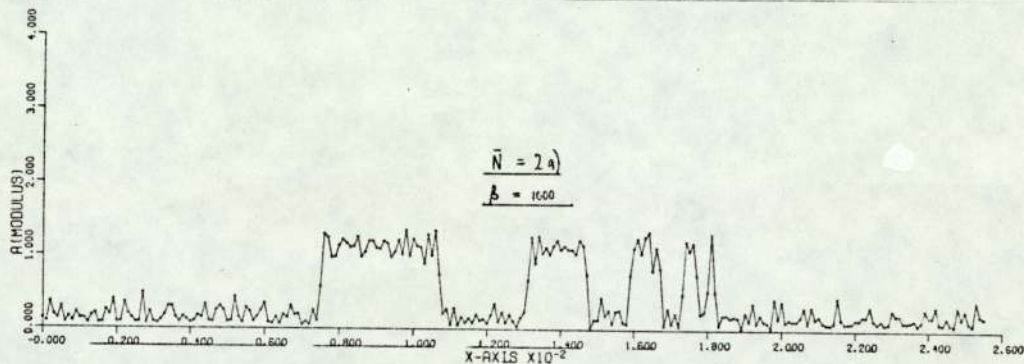
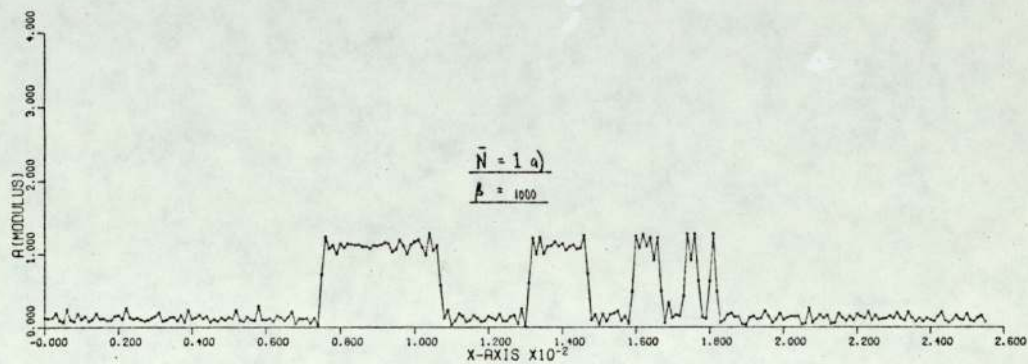
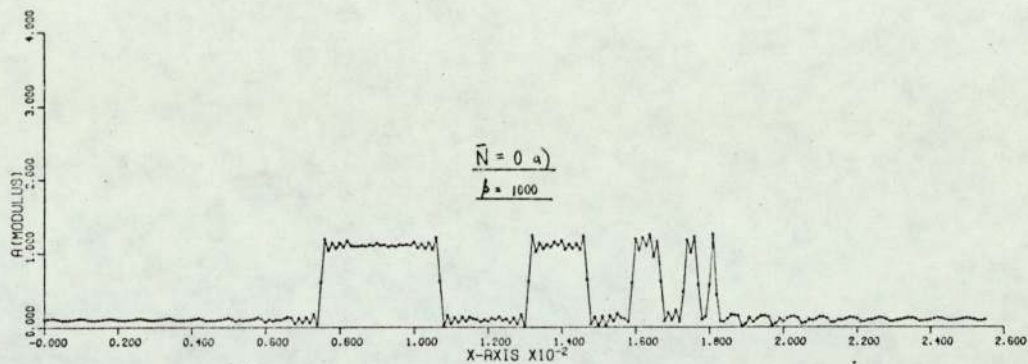


FIG. 2.14a

61

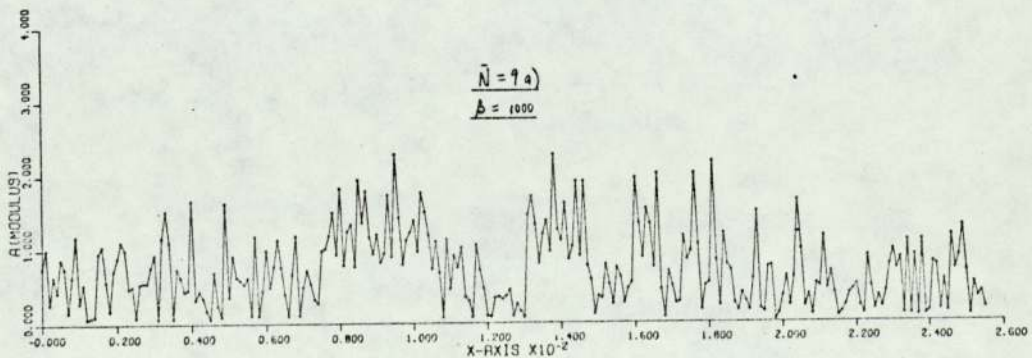
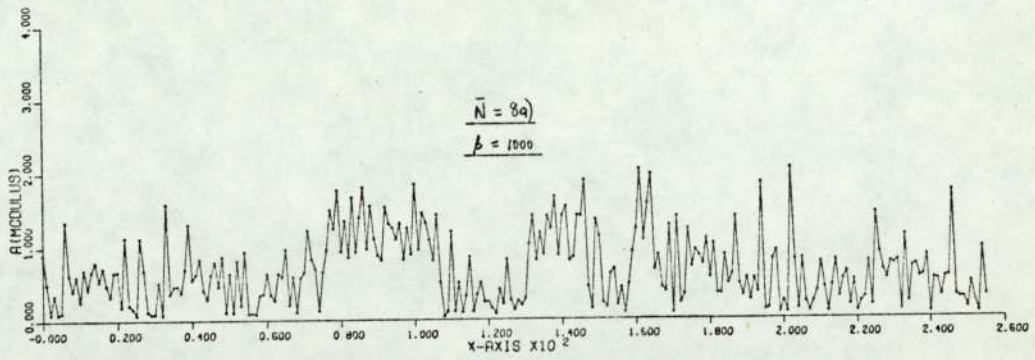
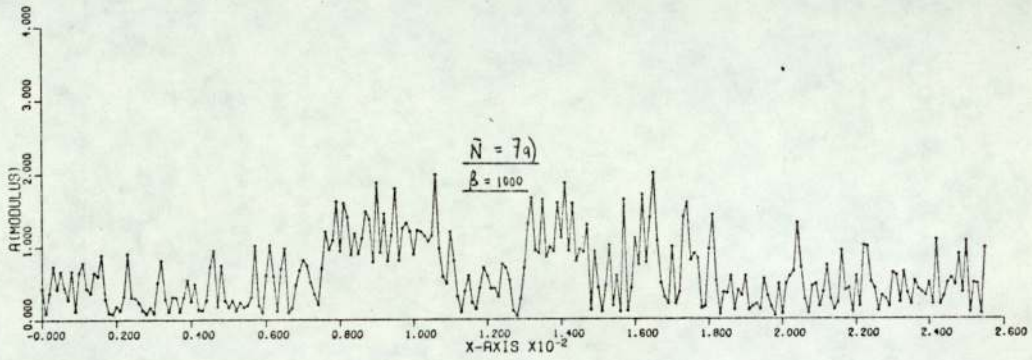
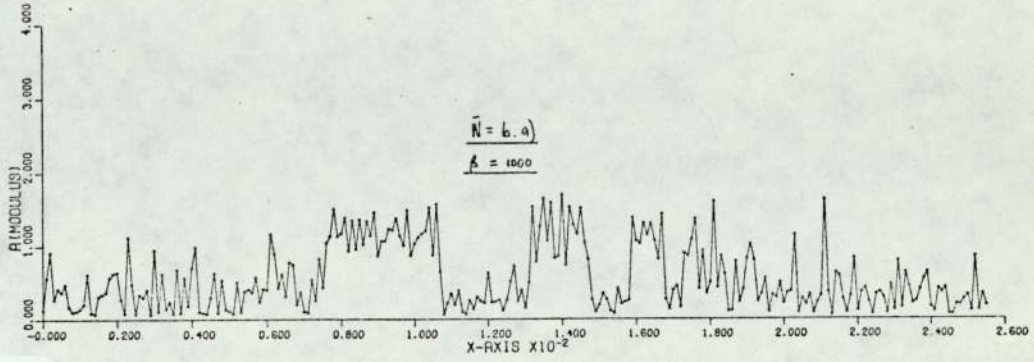
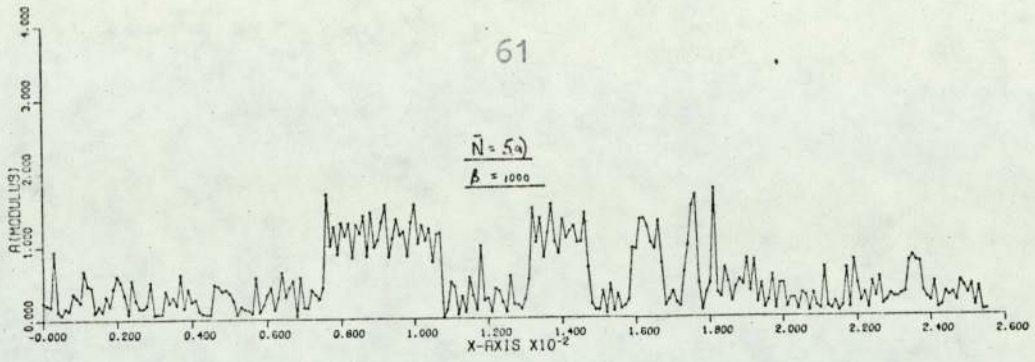
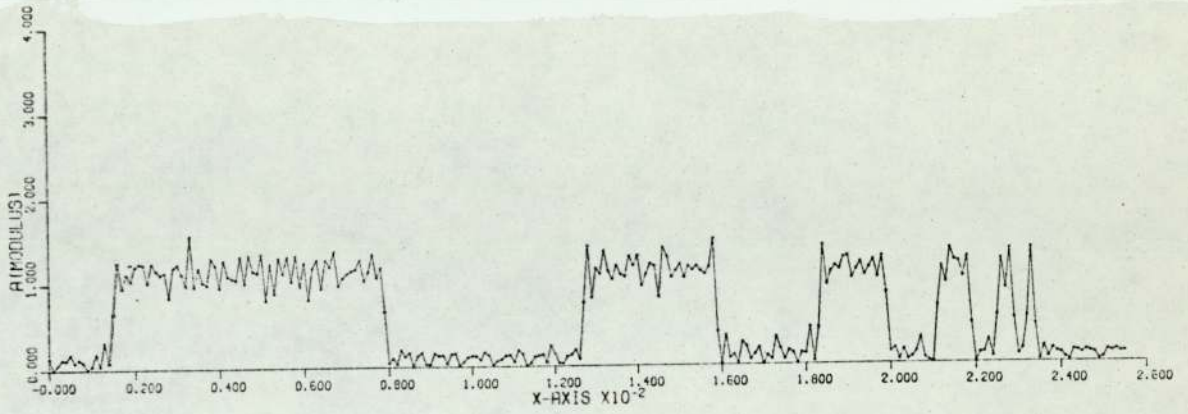


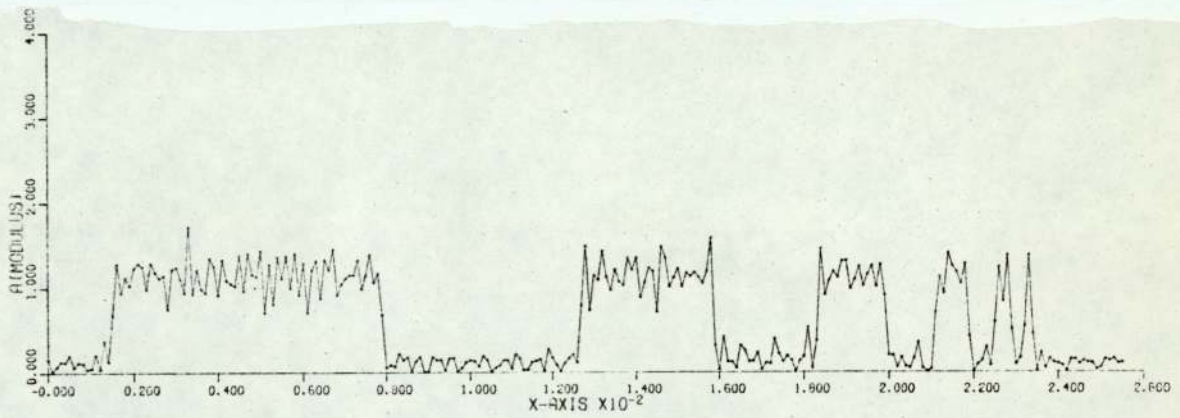
FIG.2.14a





$N_A = 3$  b).

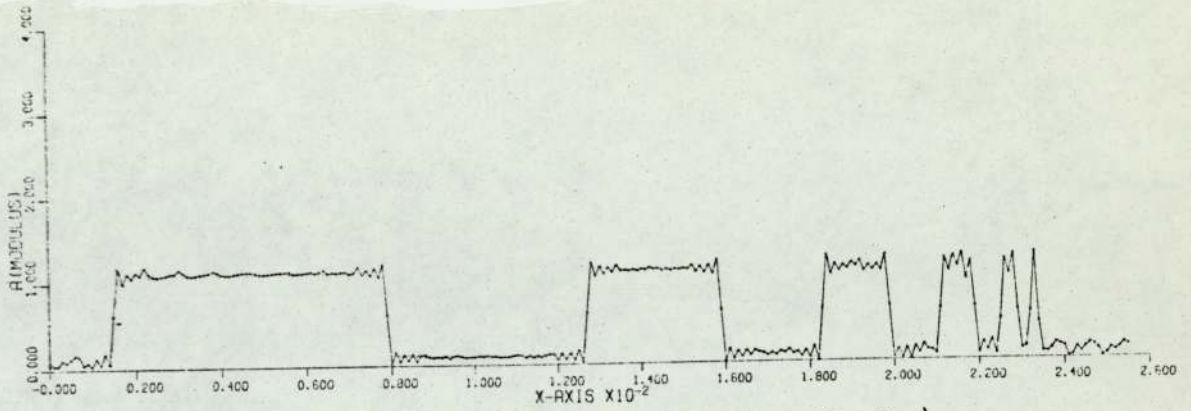
$\beta = 1000$



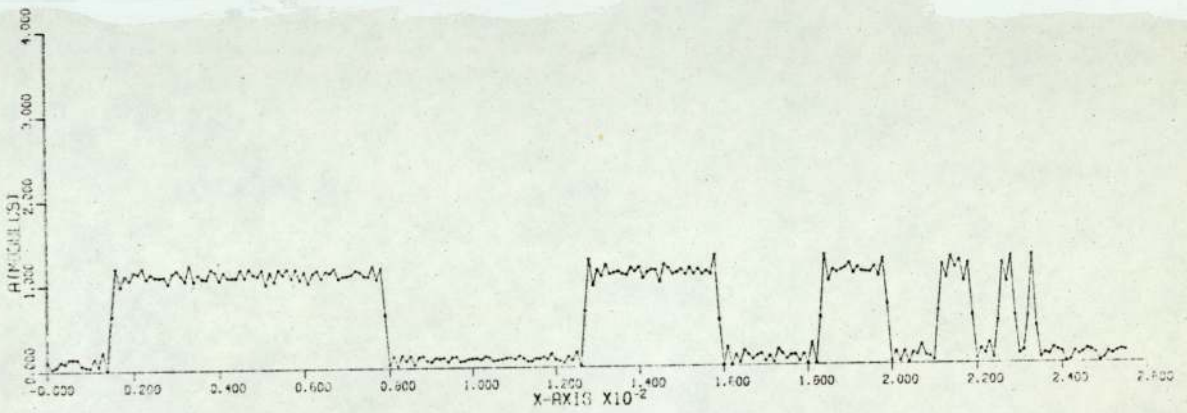
$N_A = 4$  b).

$\beta = 1000$

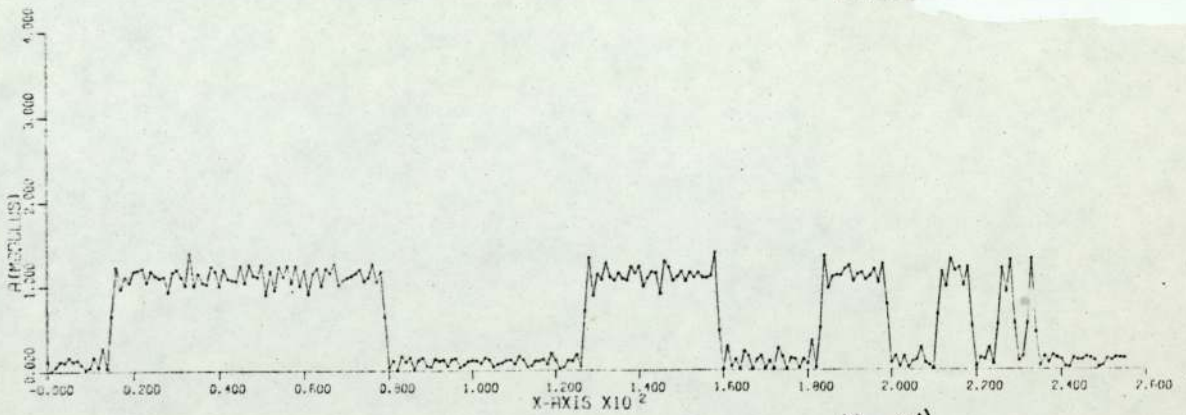
FIG. 2.14 b



$N_A = 0$  b)  
 $\beta = 1000$



$N_A = 1$  b)  
 $\beta = 1000$



$N_A = 2$  b)  
 $\beta = 1000$

FIG. 2.14 b



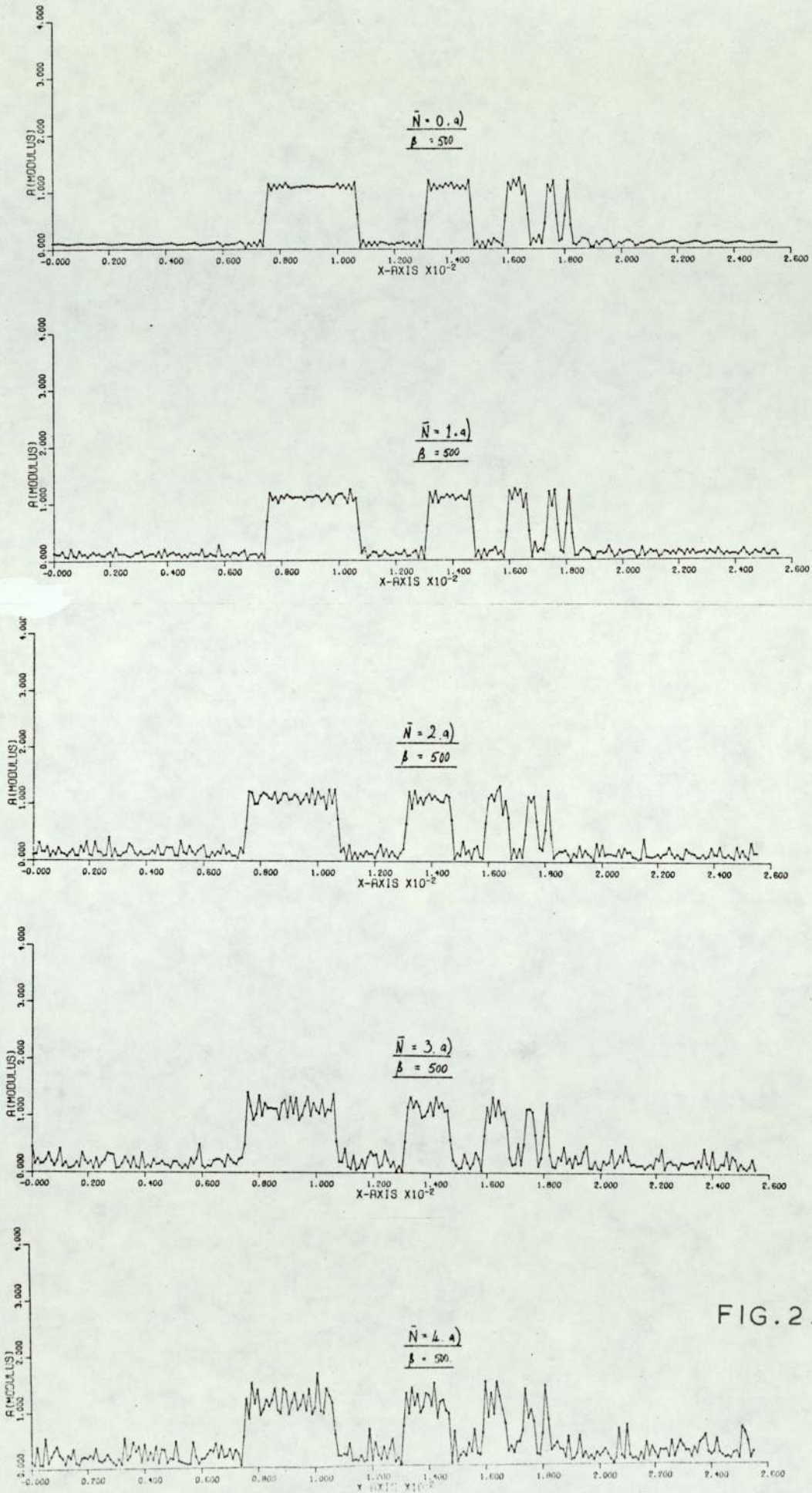


FIG. 2.15 a

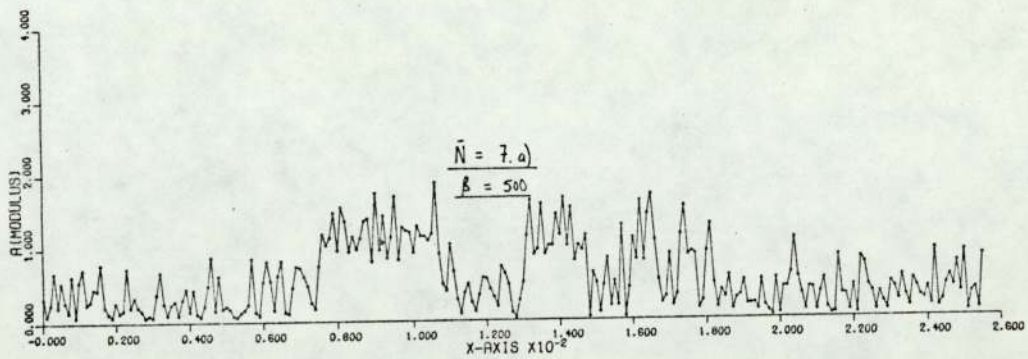
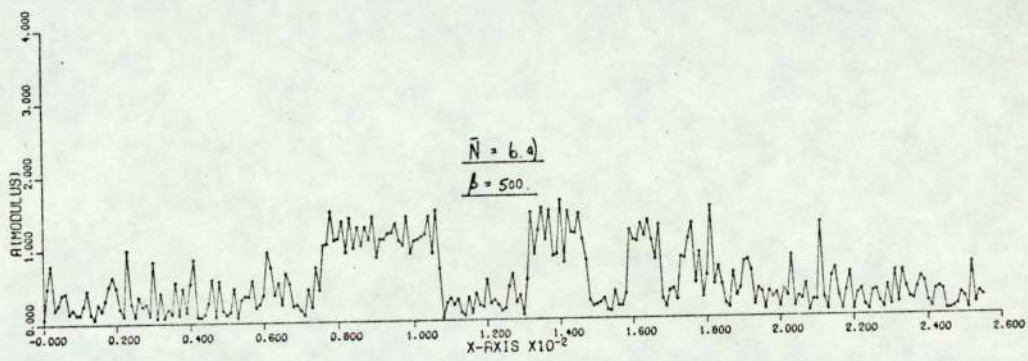
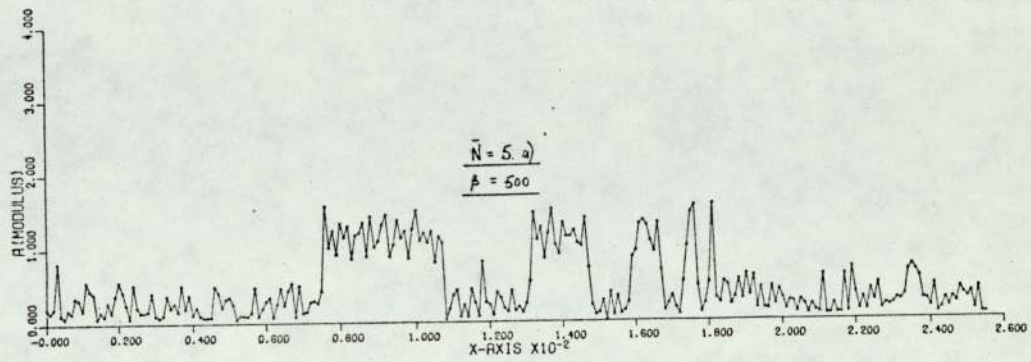


FIG. 2.15 a



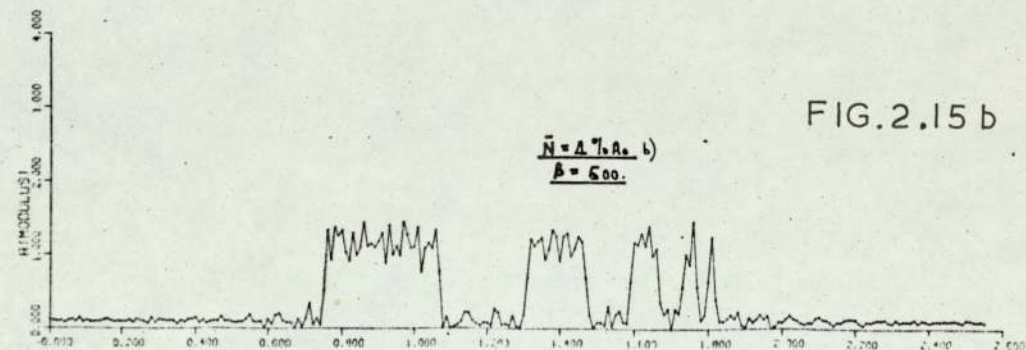
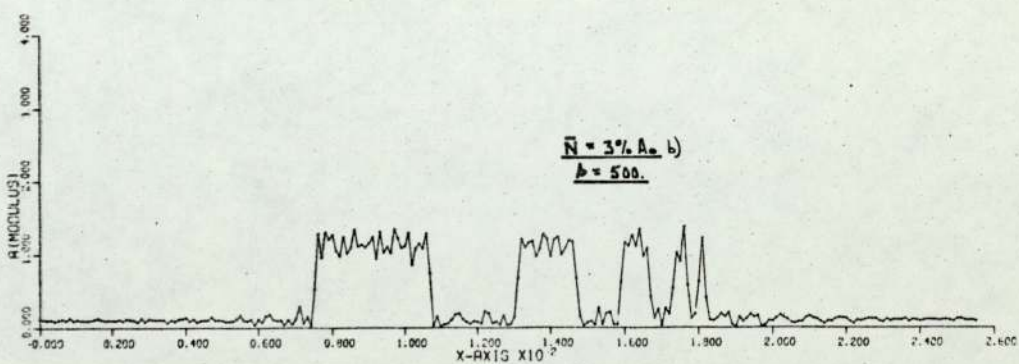
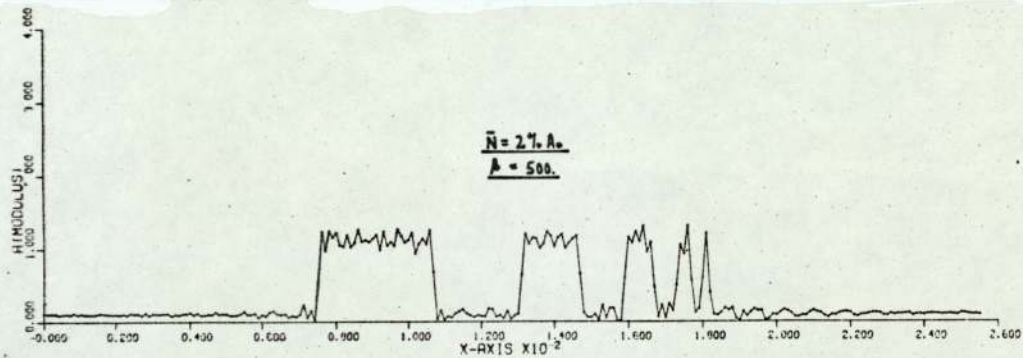
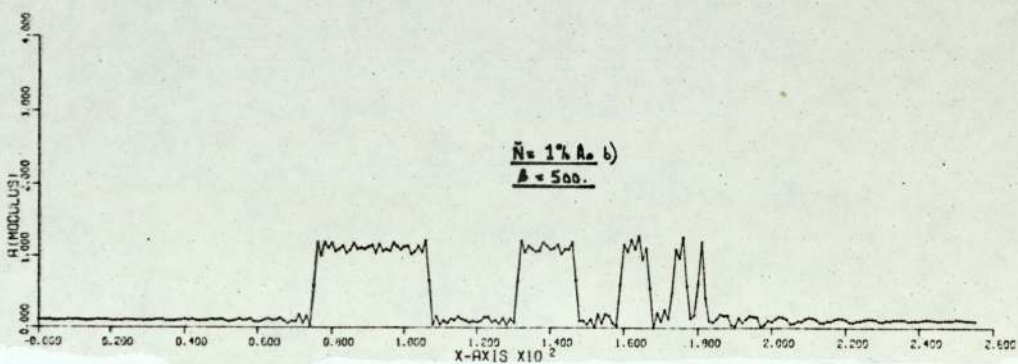
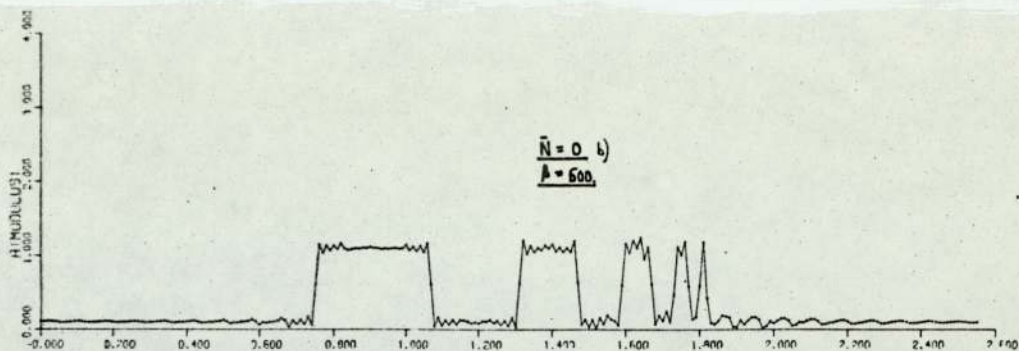


FIG.2.15 b

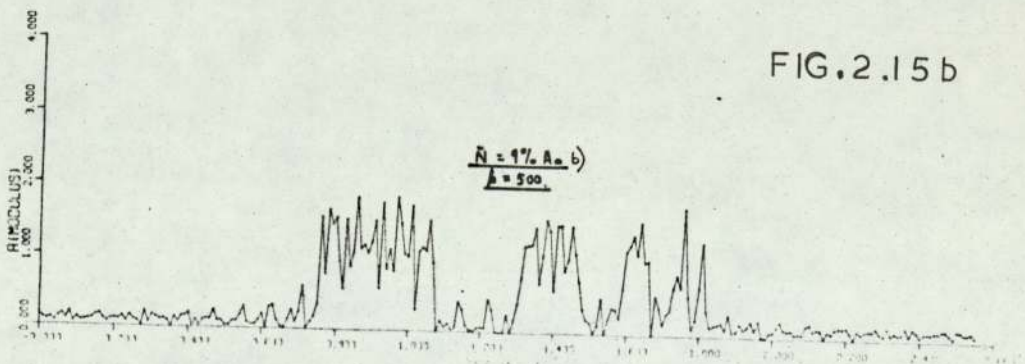
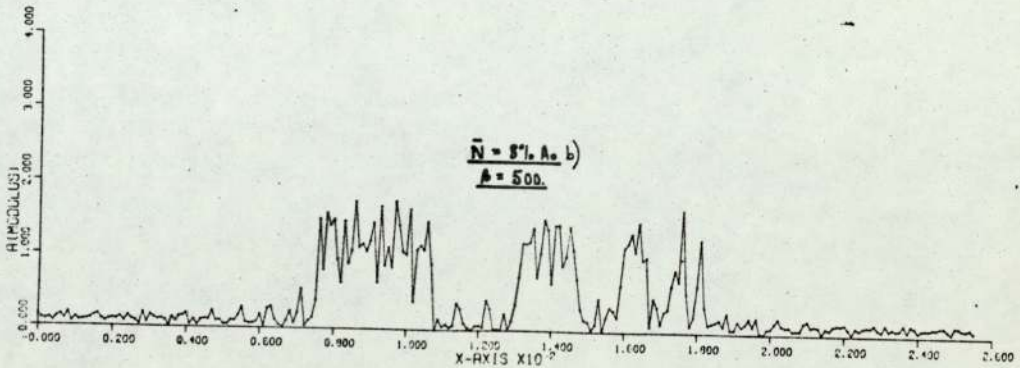
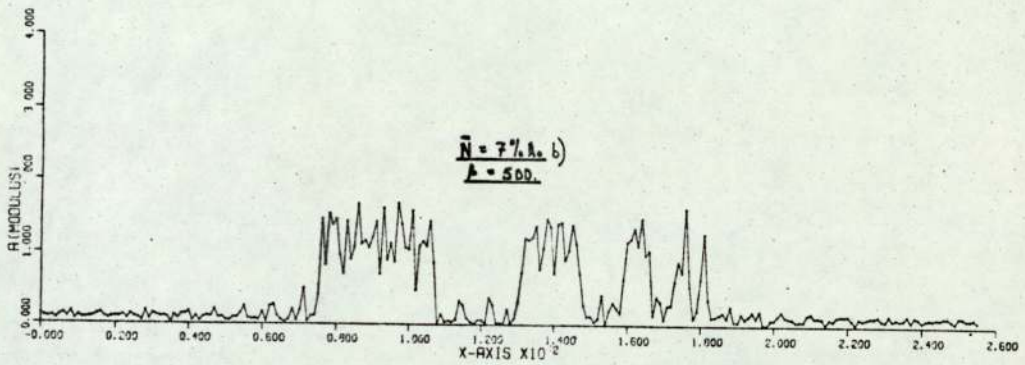
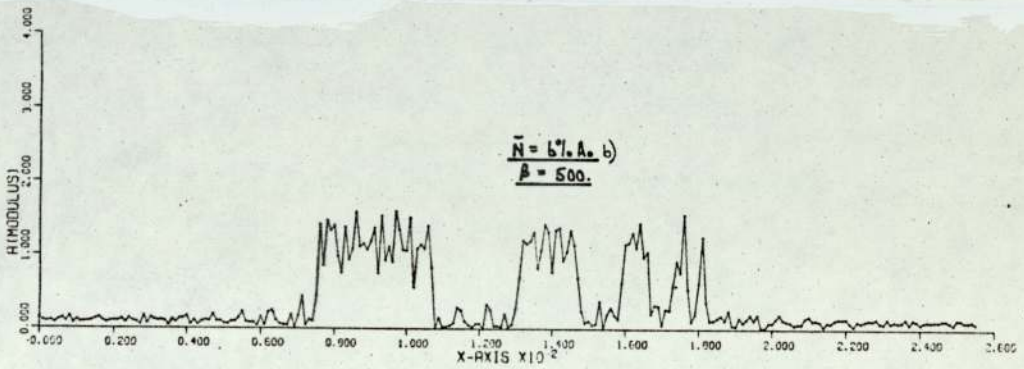
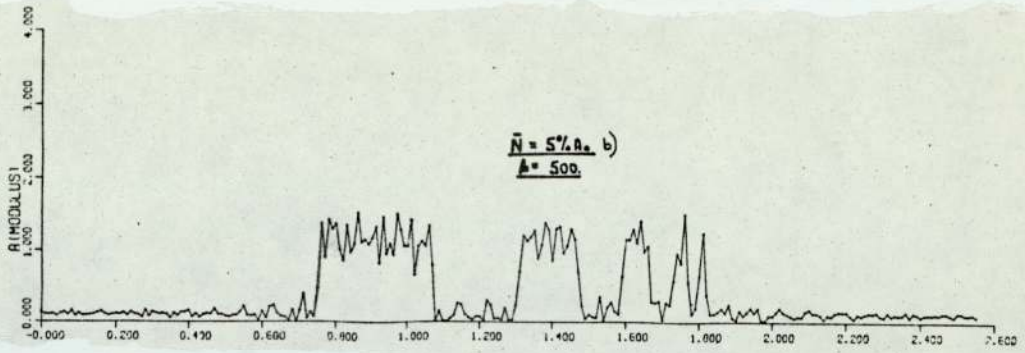


FIG. 2.15 b



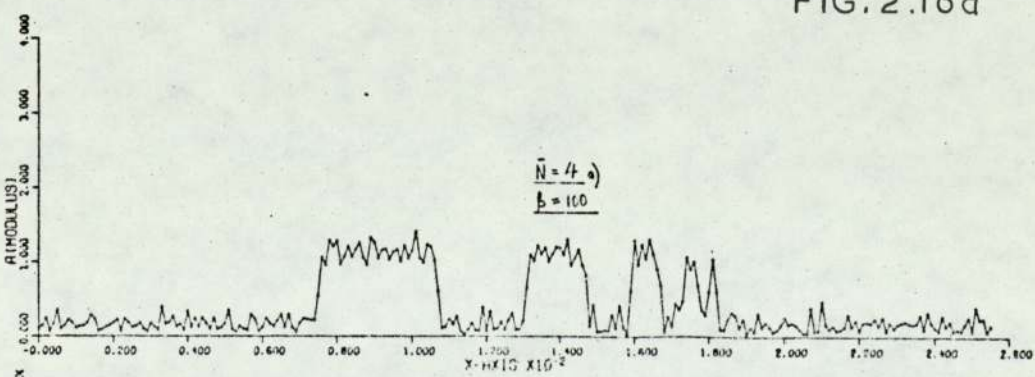
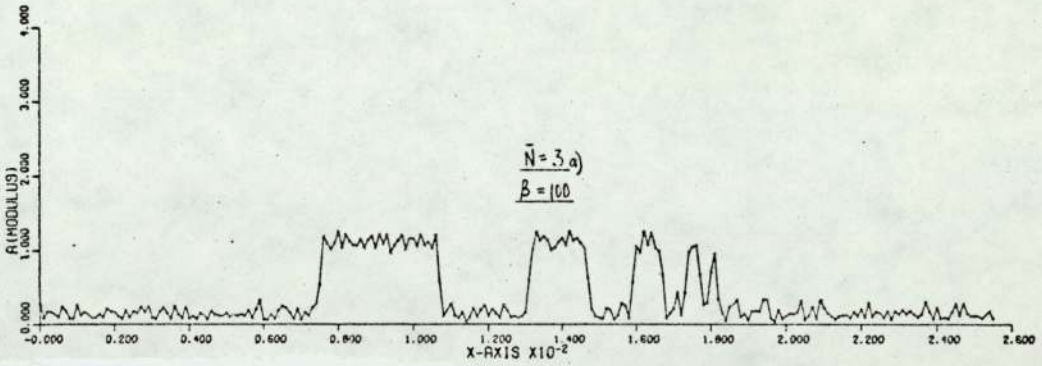
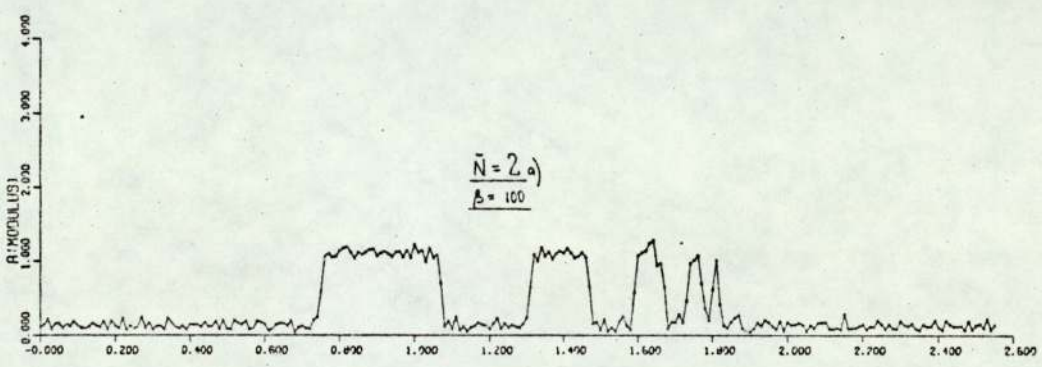
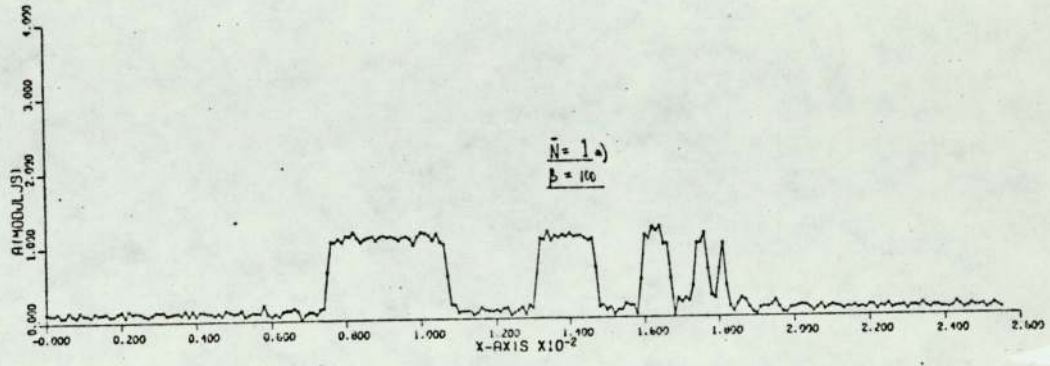
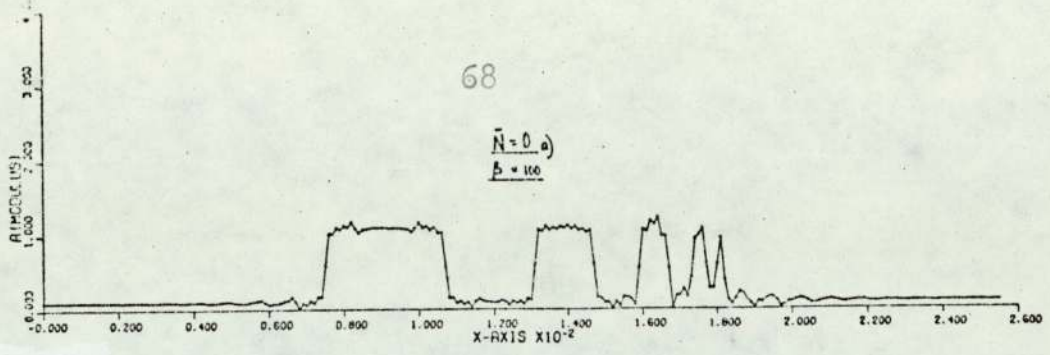
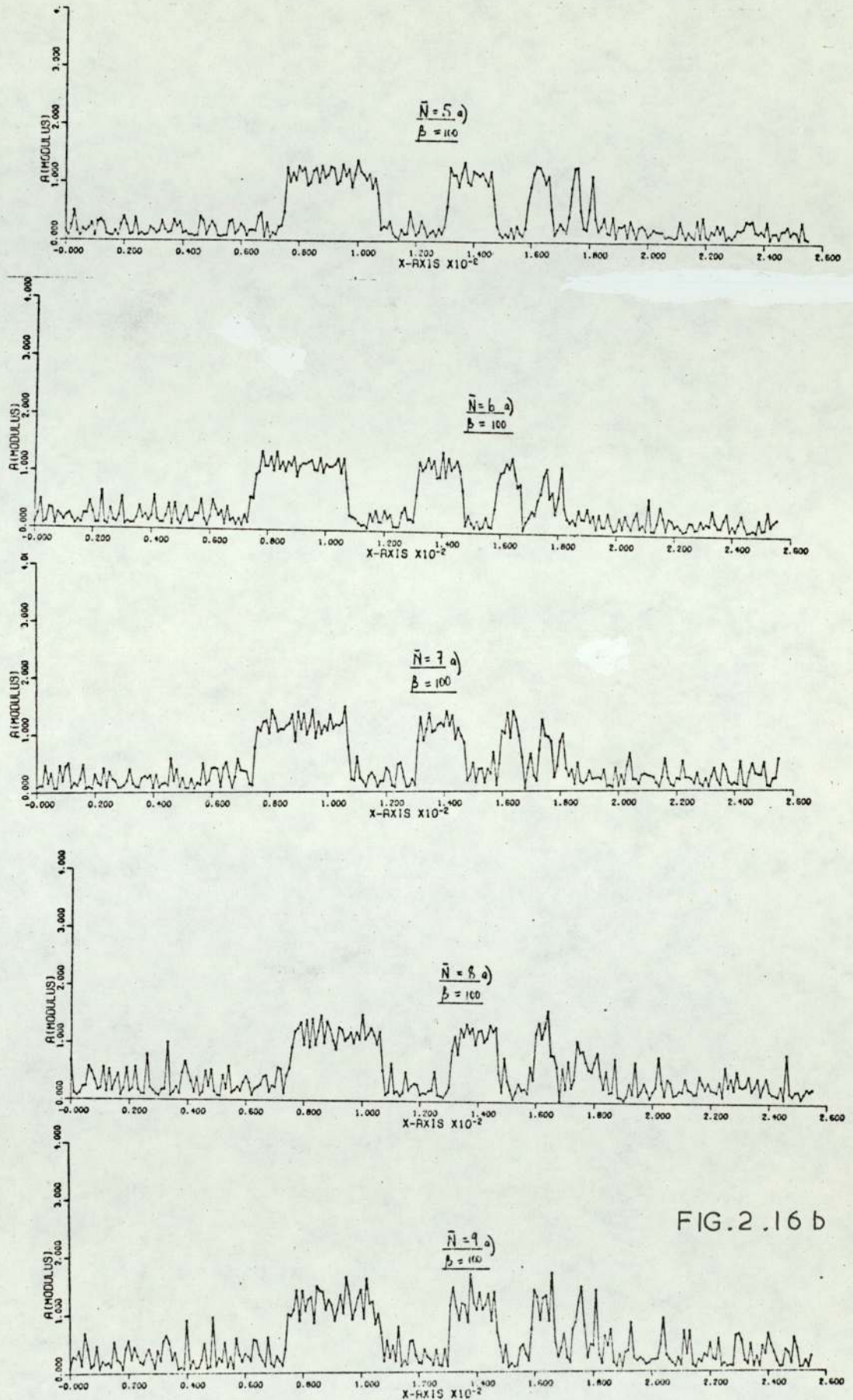
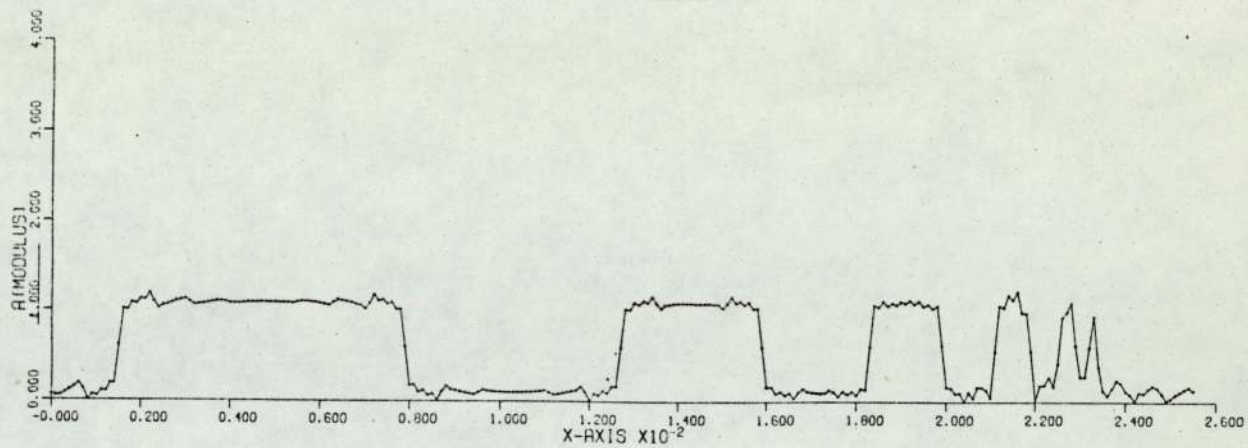


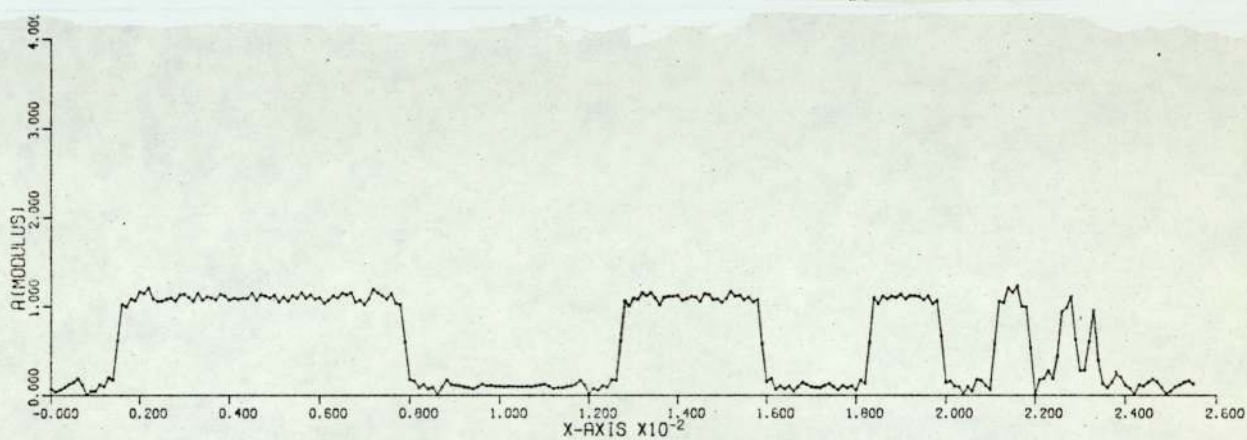
FIG. 2.16a



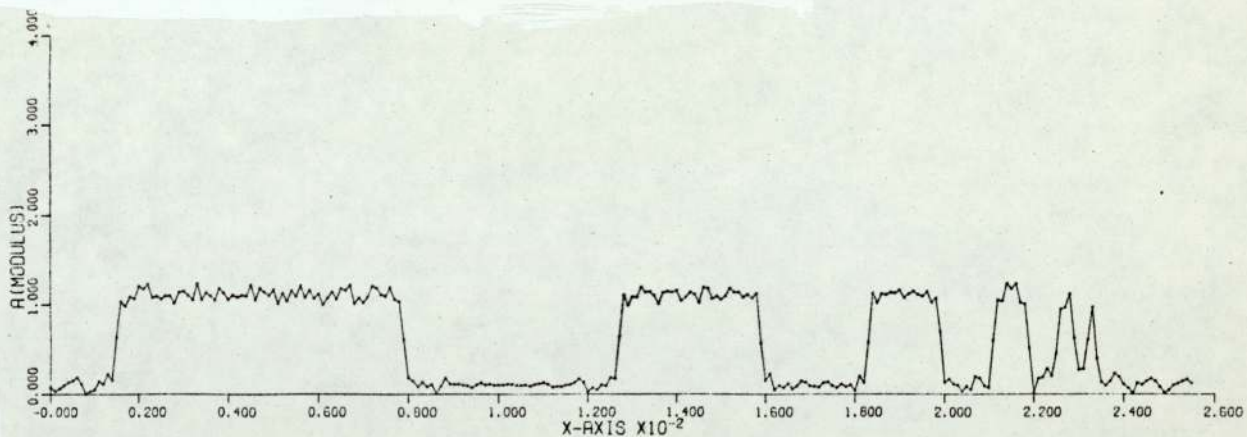




$N_A = 0$  b)  $\beta = 100$



$N_A = 1$  b)  $\beta = 100$



$N_A = 2$  b)  $\beta = 100$

FIG. 2.16 b

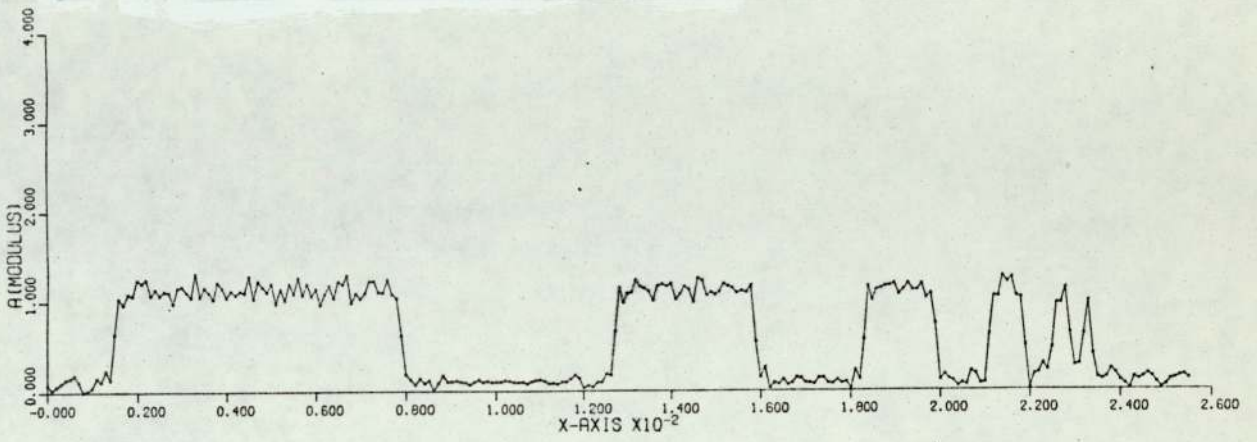
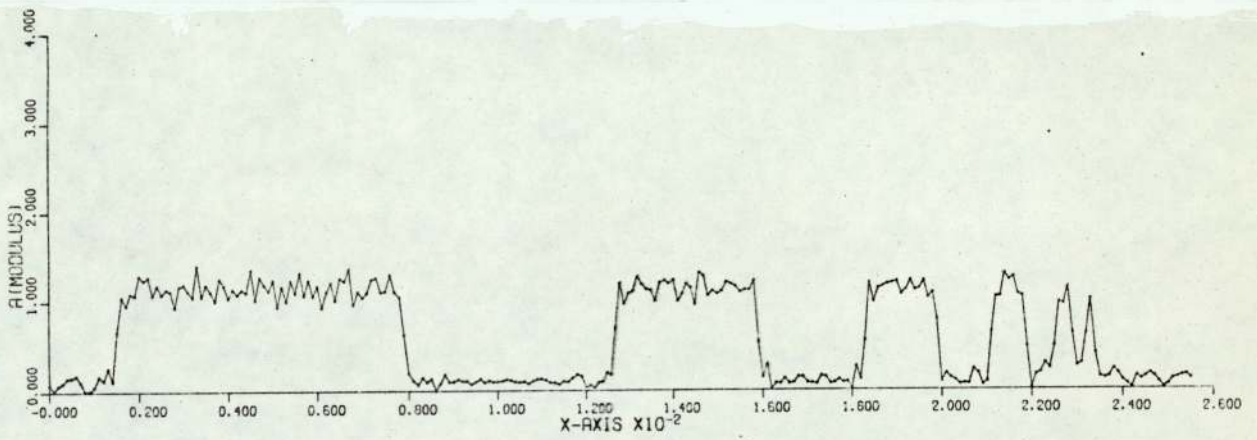
 $N_A = 3 \quad \beta = 100$  $N_A = 4 \quad \beta = 100$ 

FIG. 2.16 b



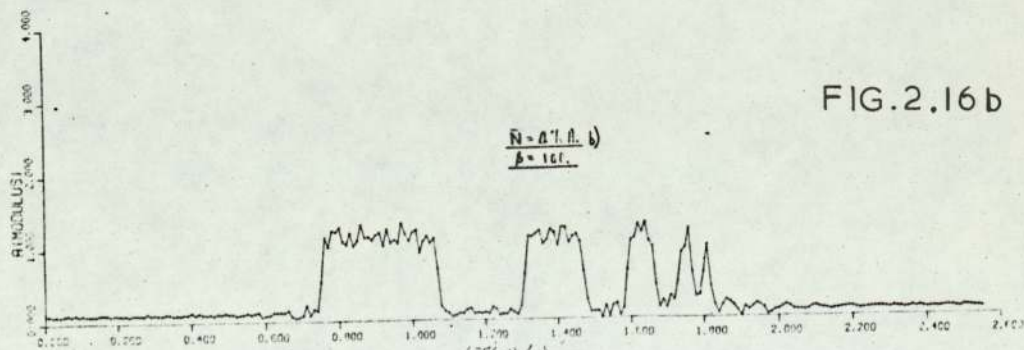
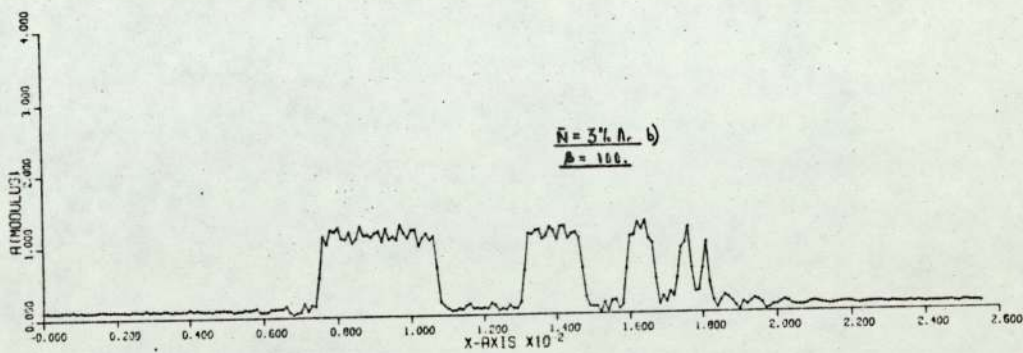
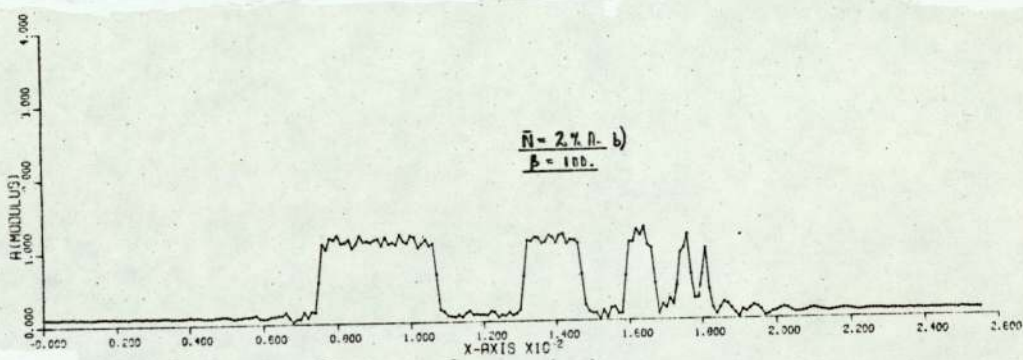
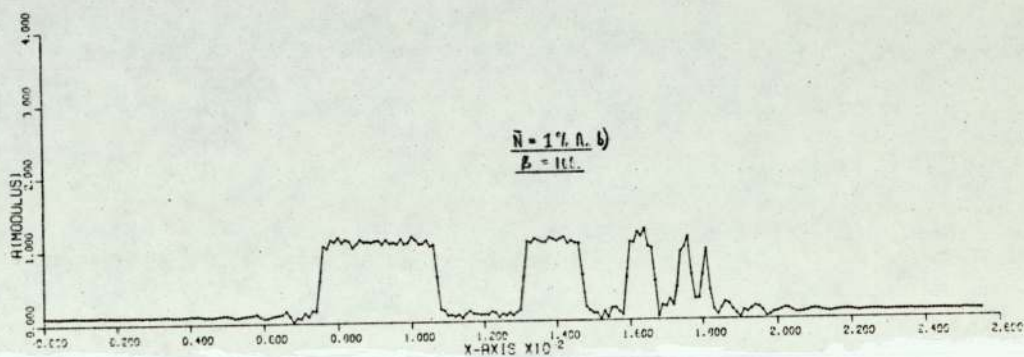
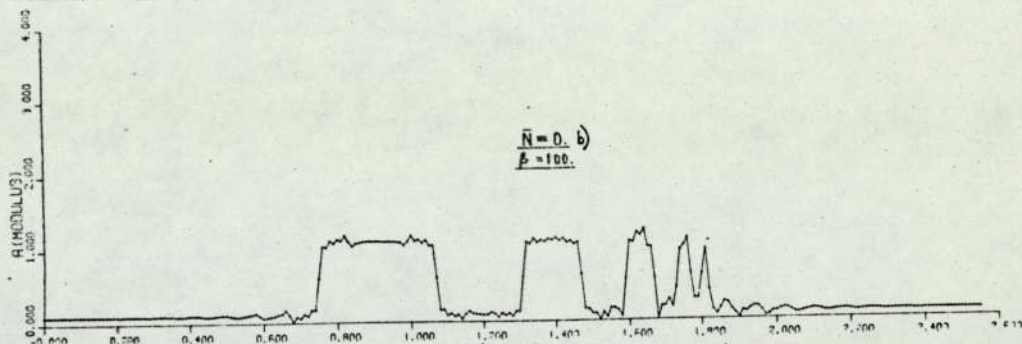


FIG. 2.16 b

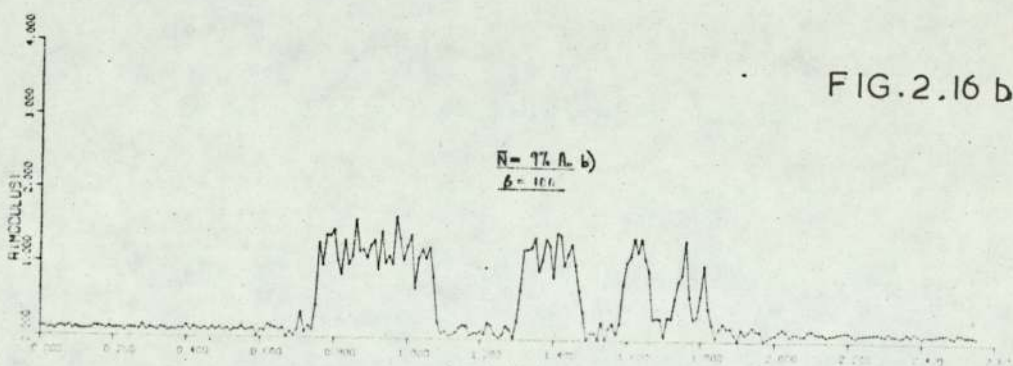
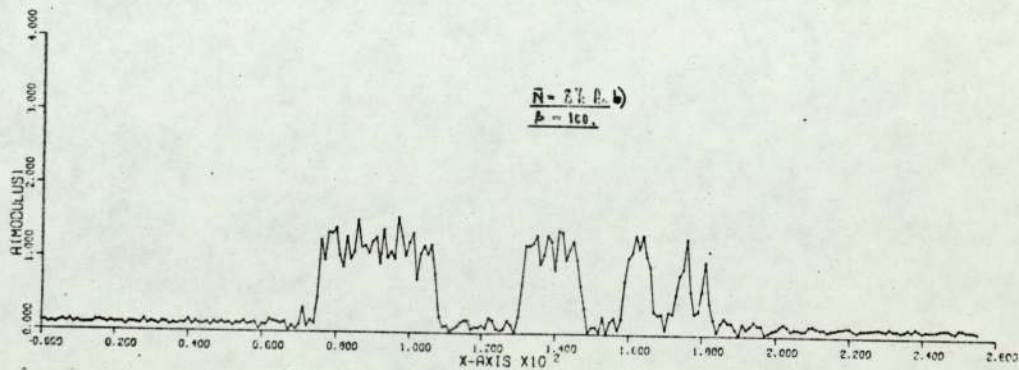
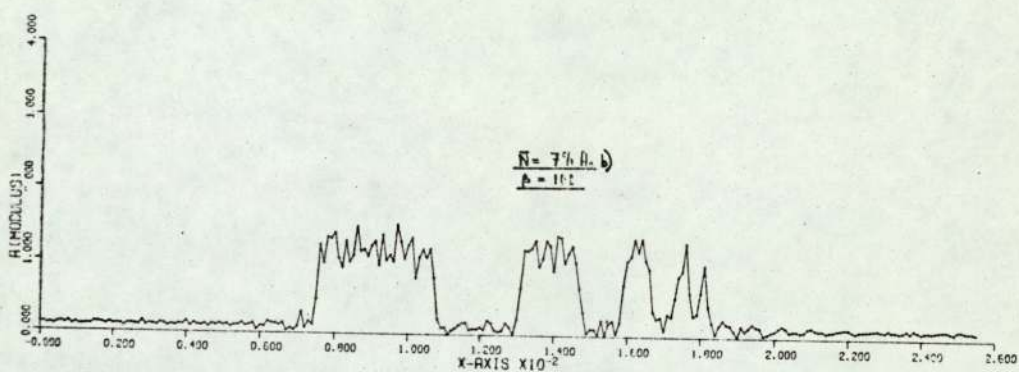
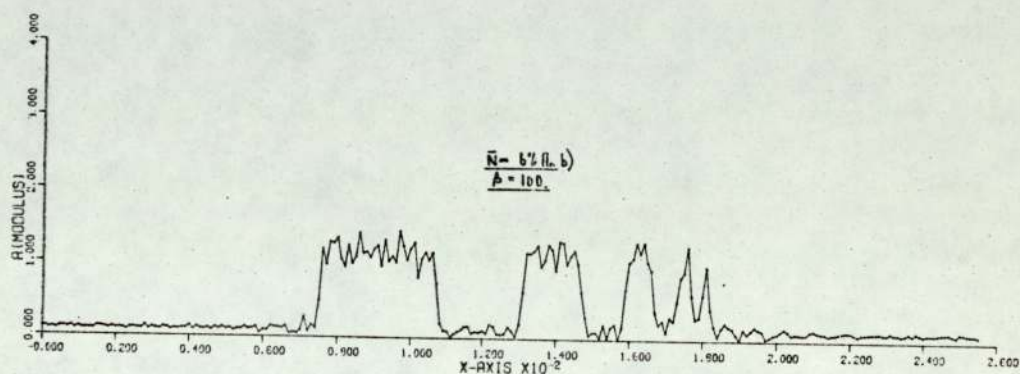
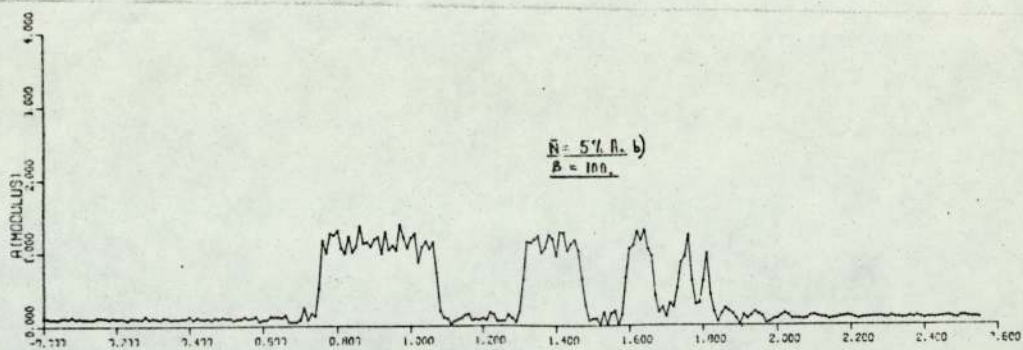


FIG. 2.16 b



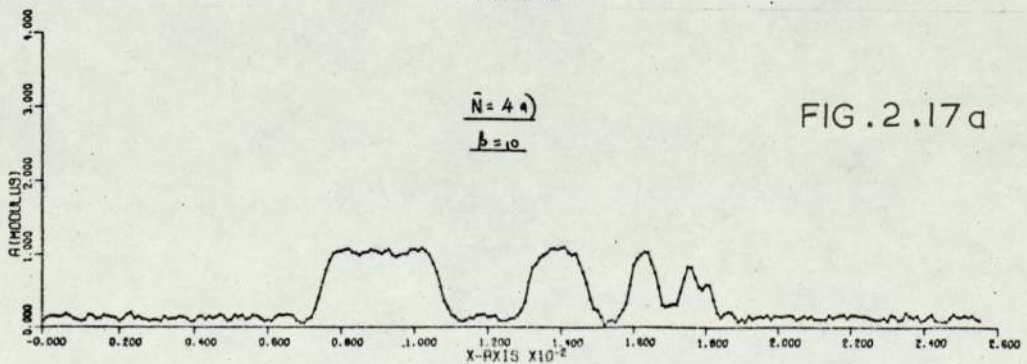
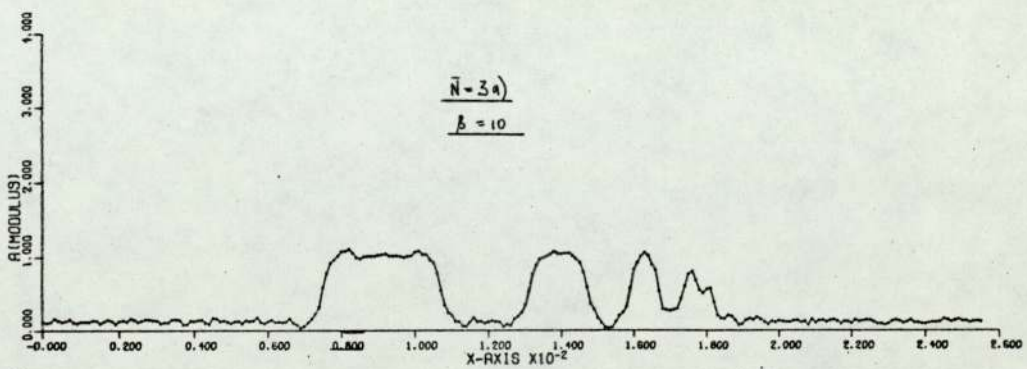
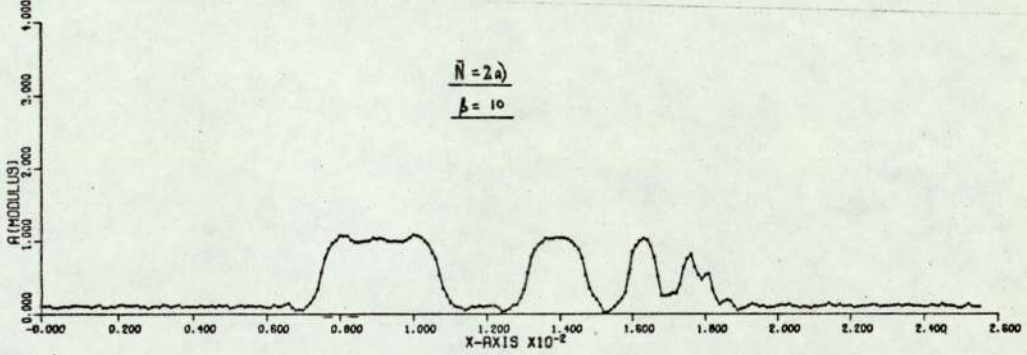
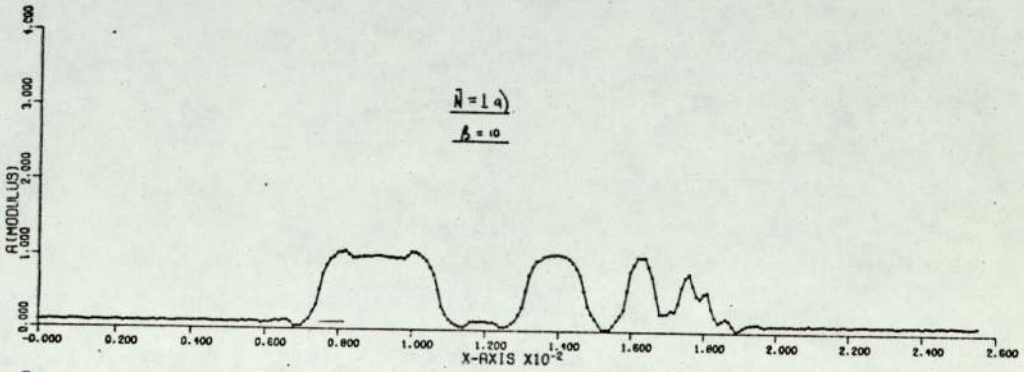
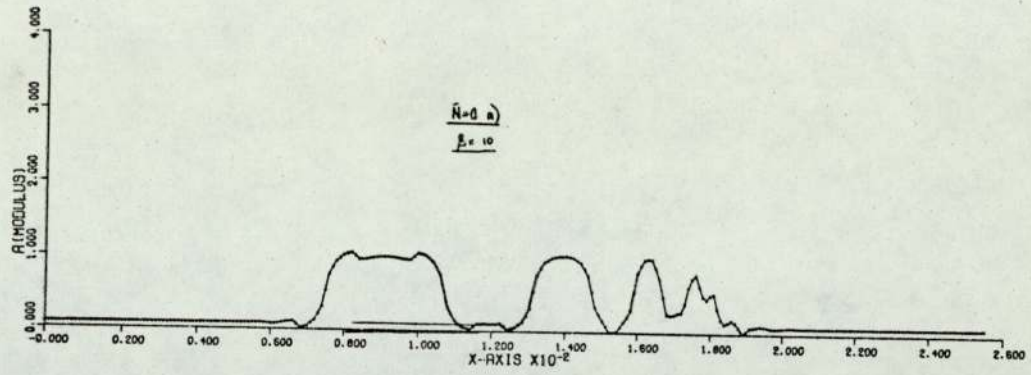


FIG. 2.17a

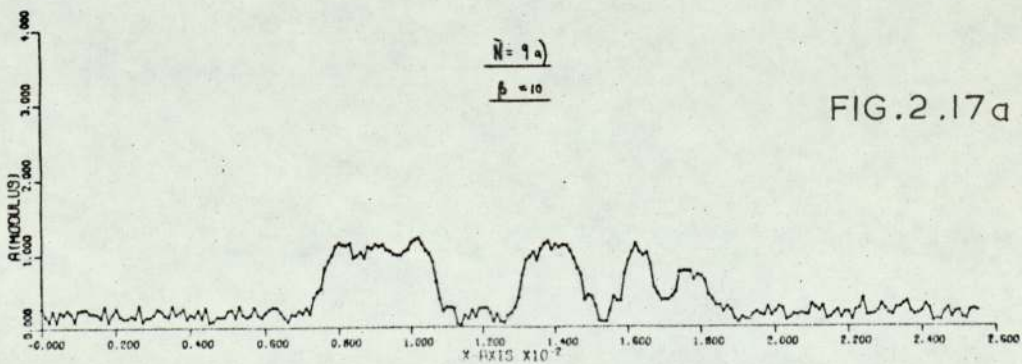
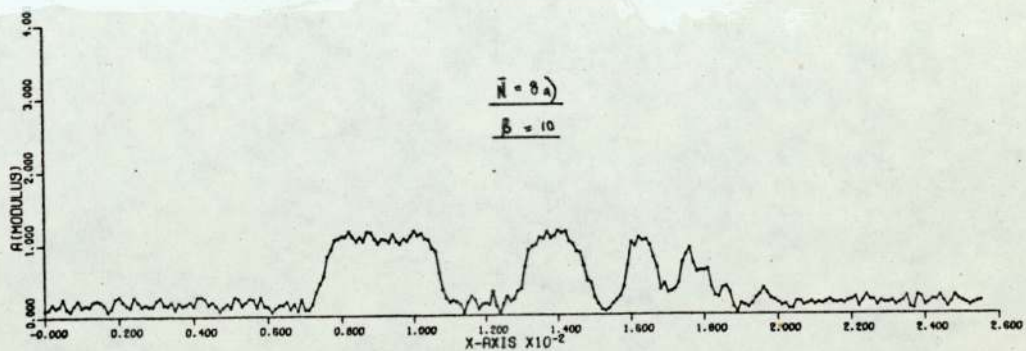
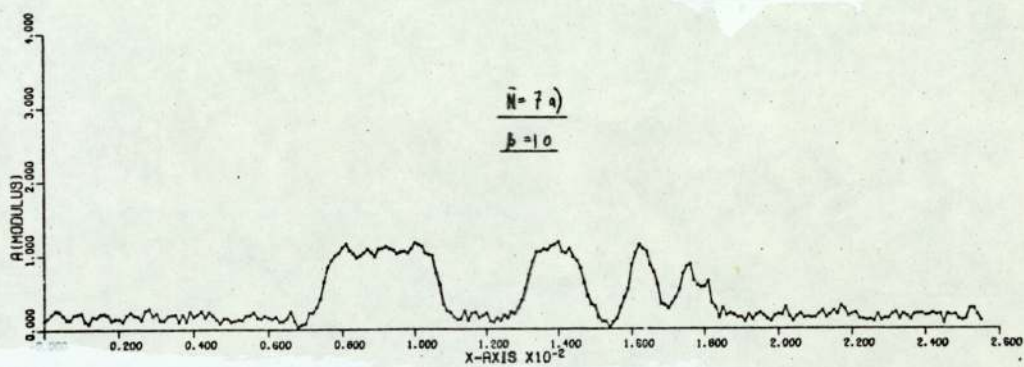
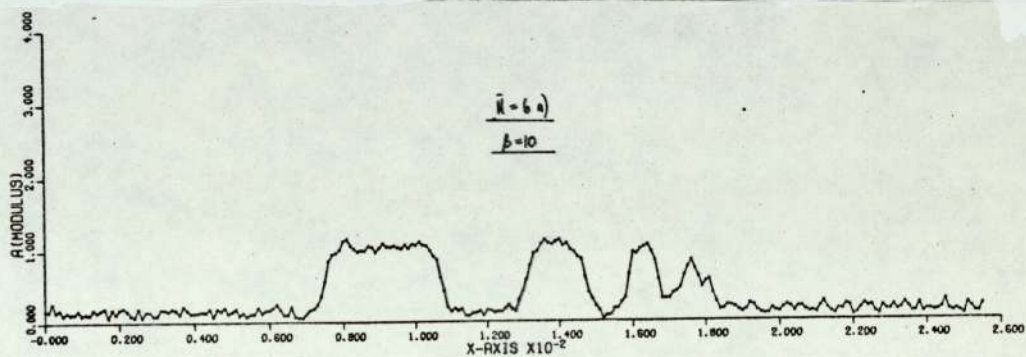
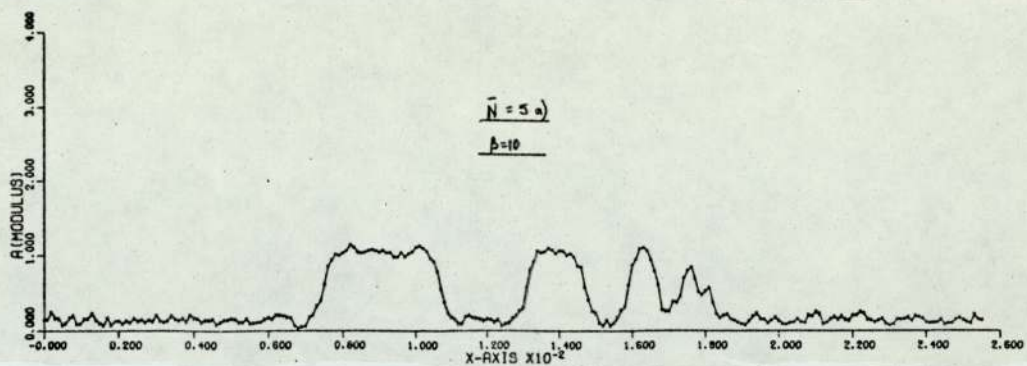


FIG. 2.17 a



76

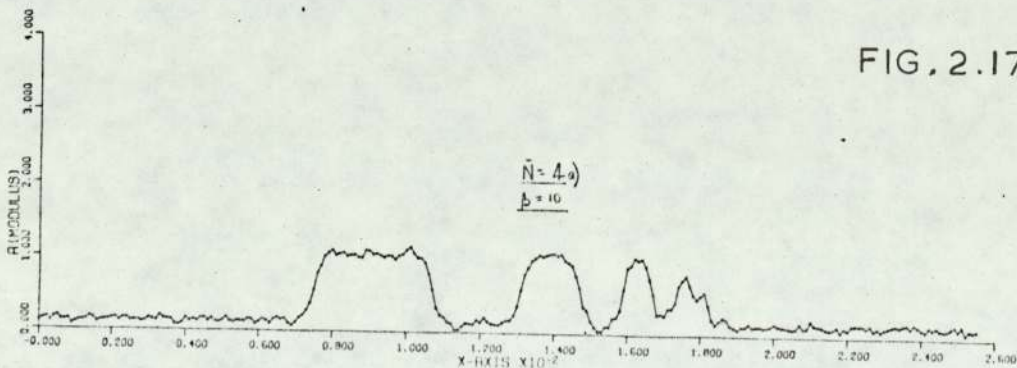
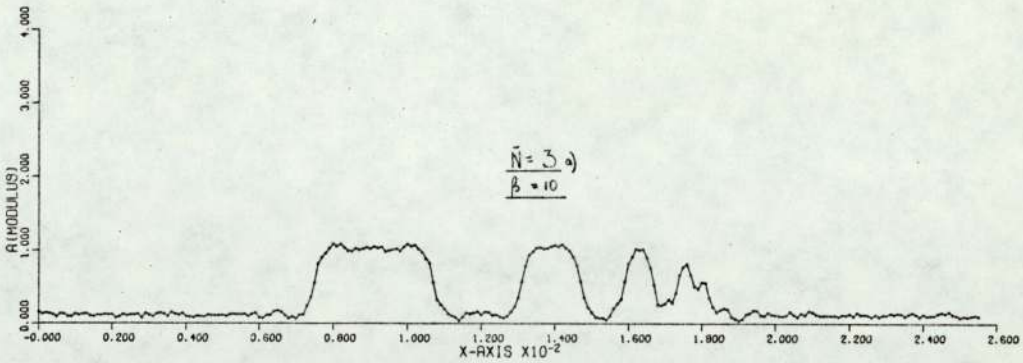
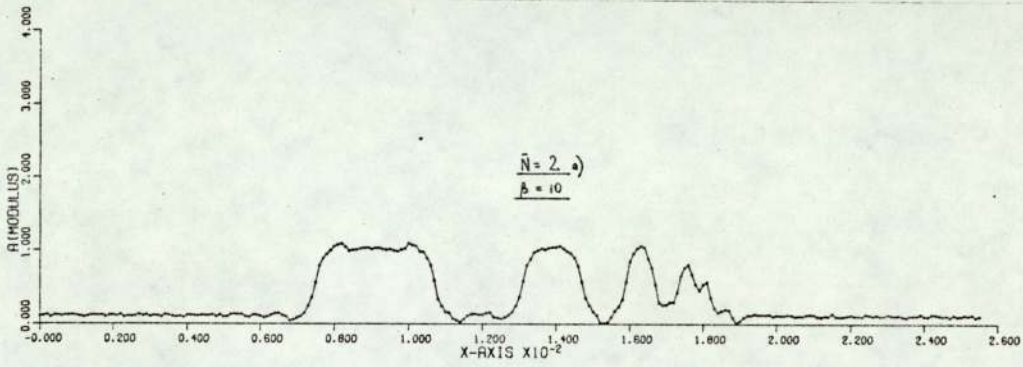
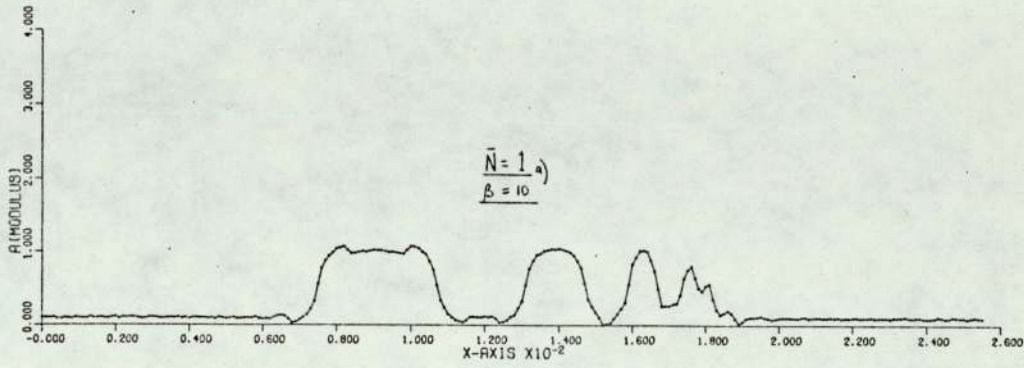
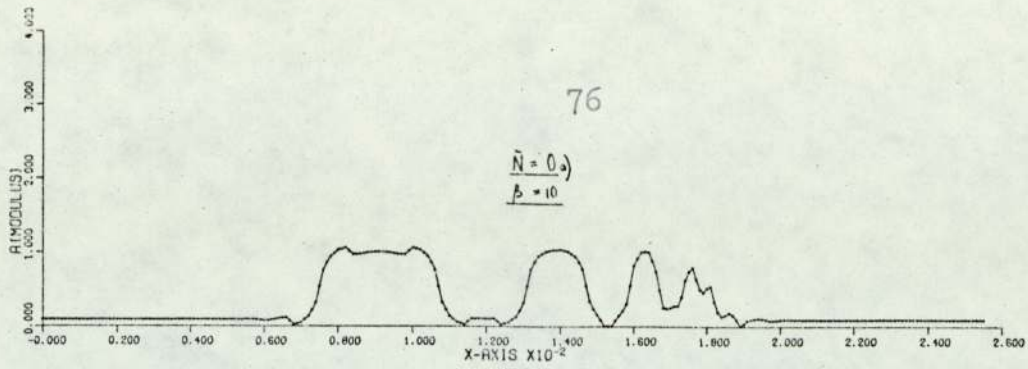


FIG. 2.17 a

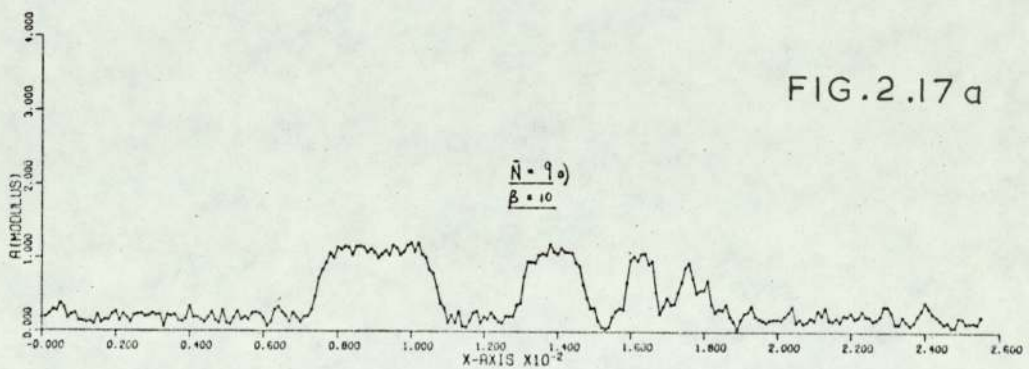
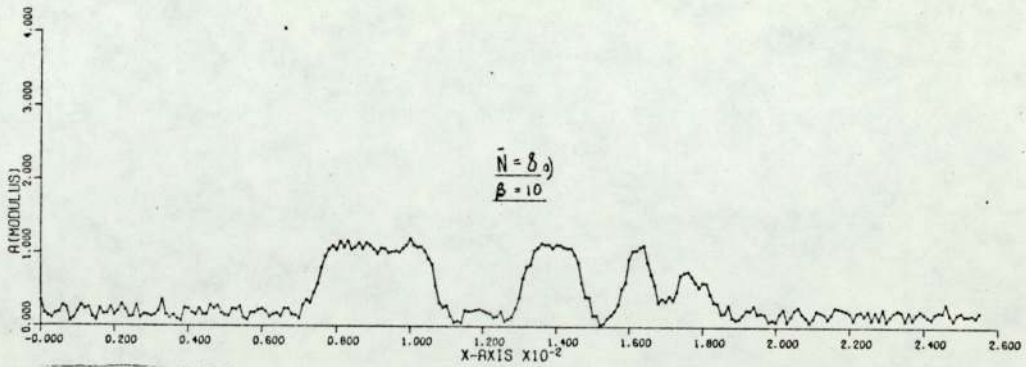
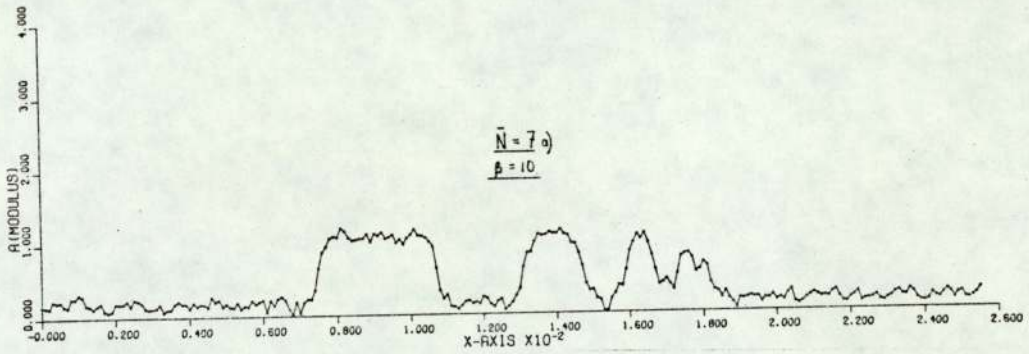
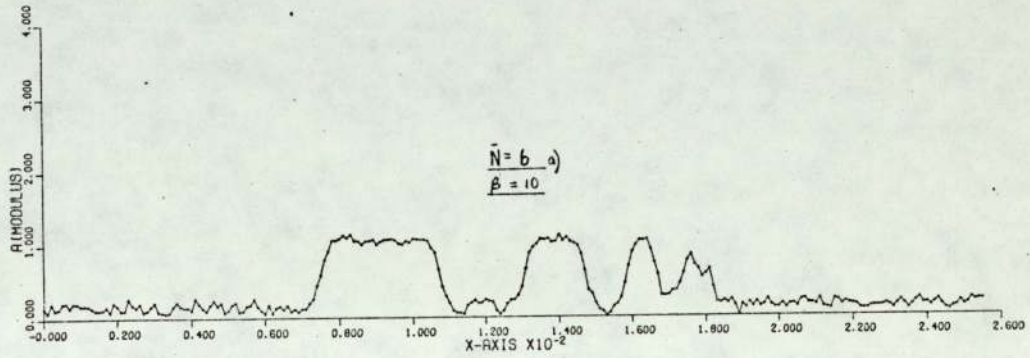
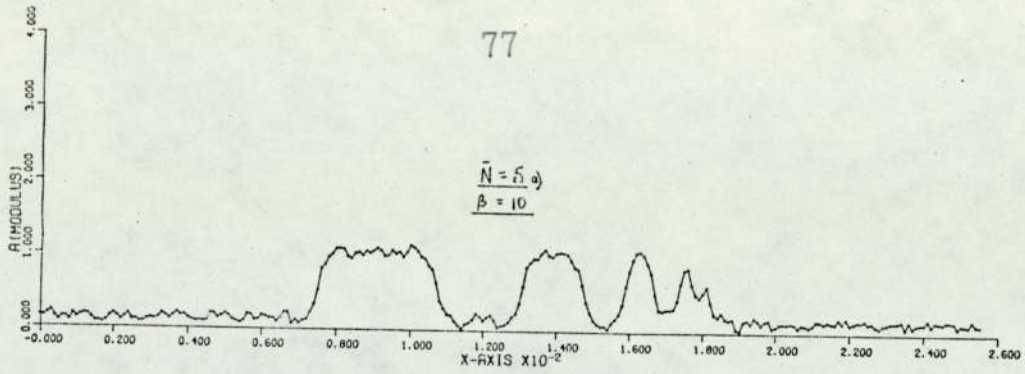


FIG. 2.17 a



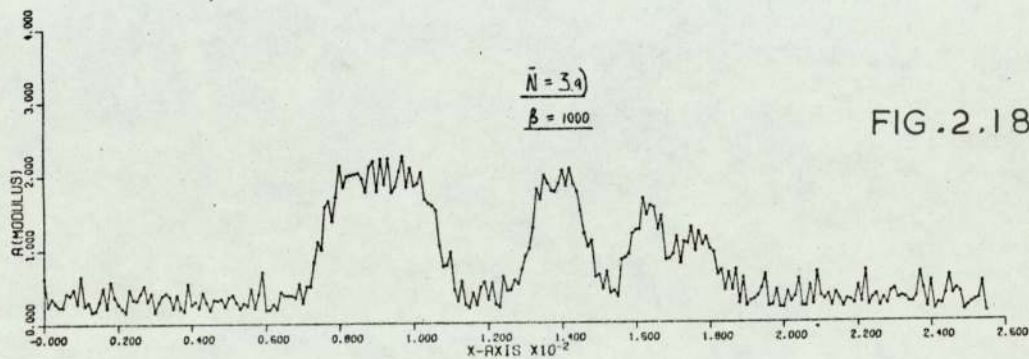
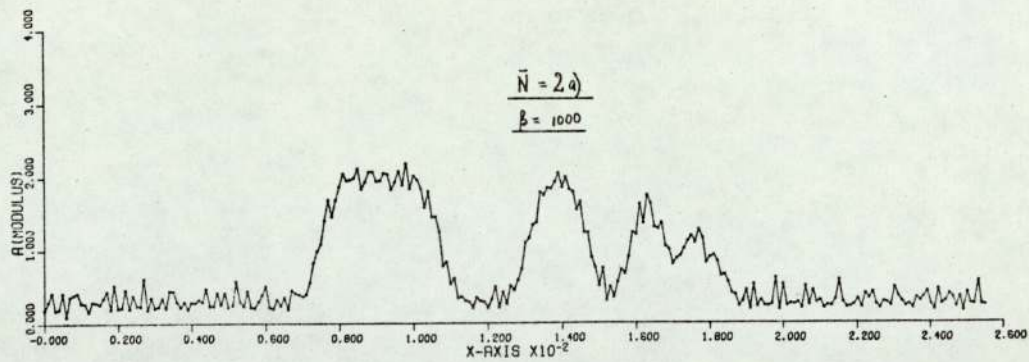
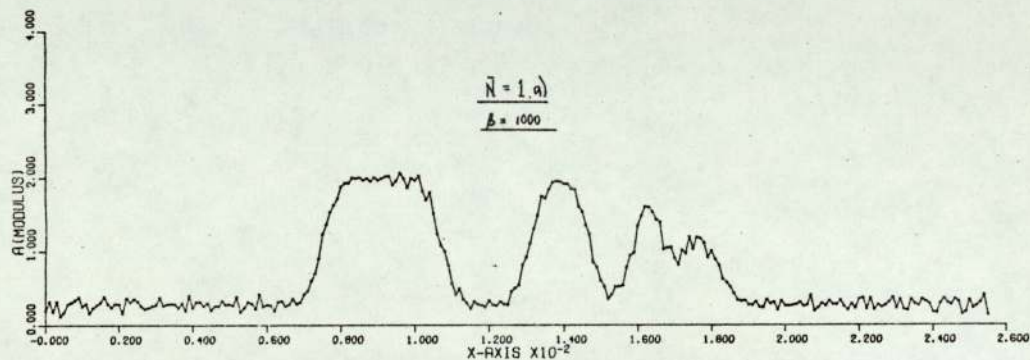
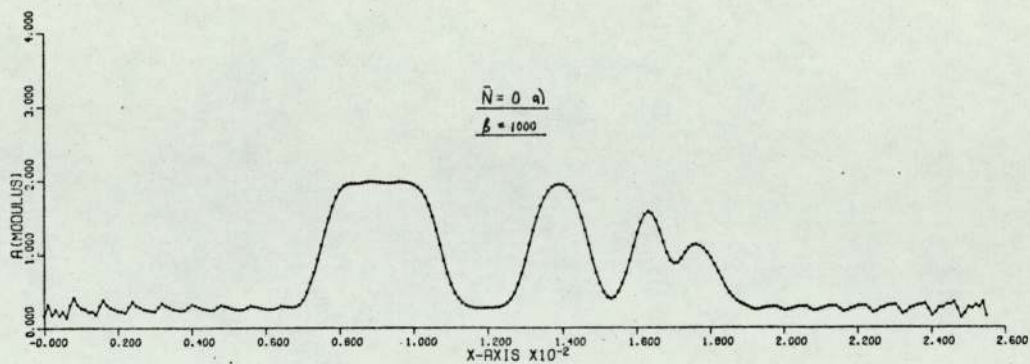


FIG. 2.18 a

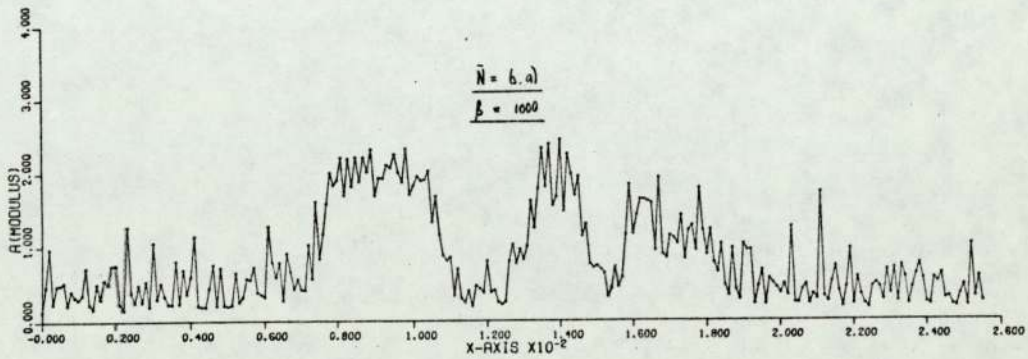
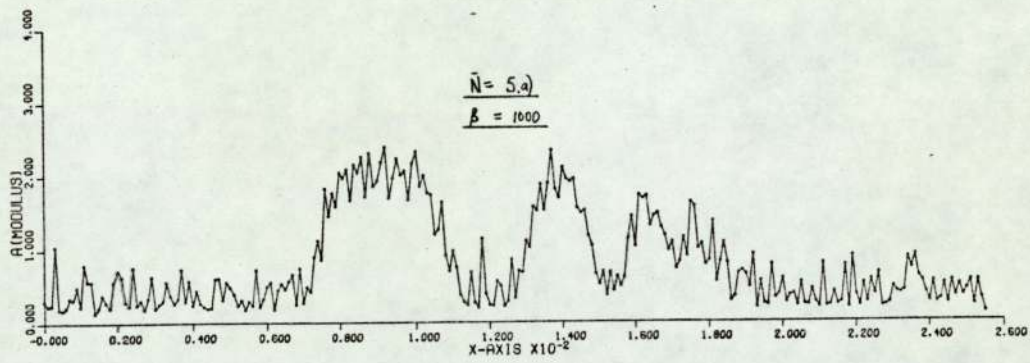
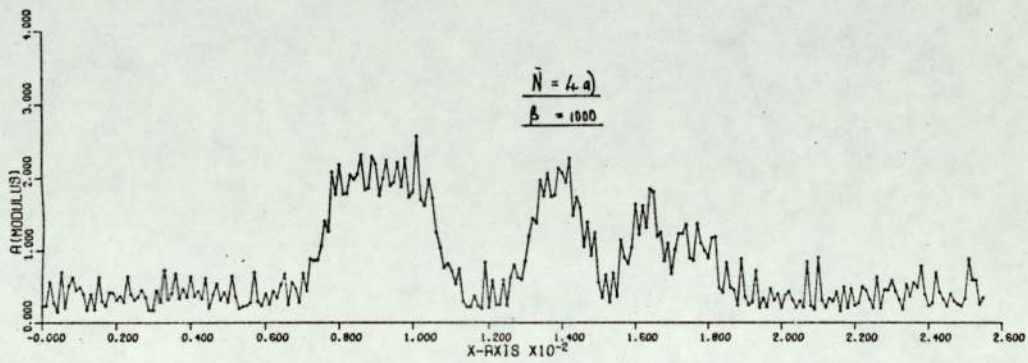
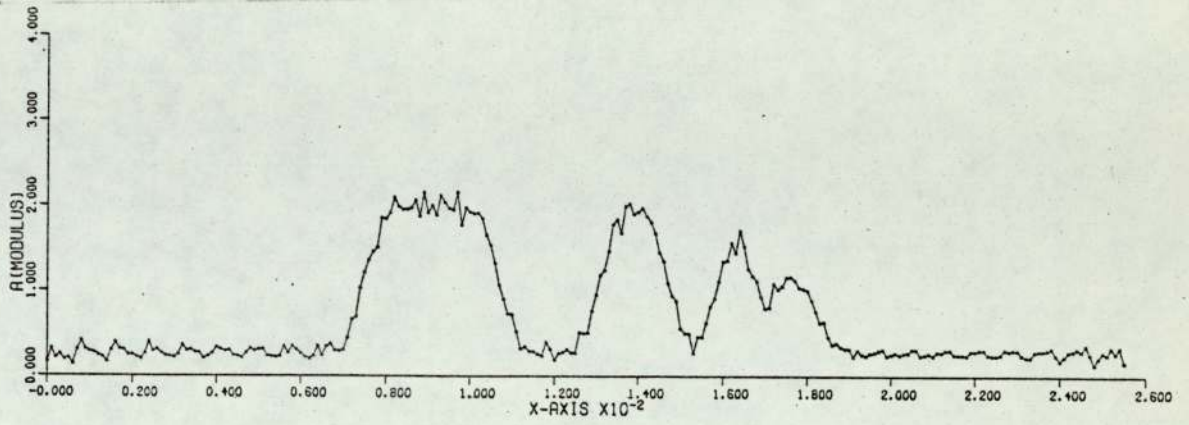


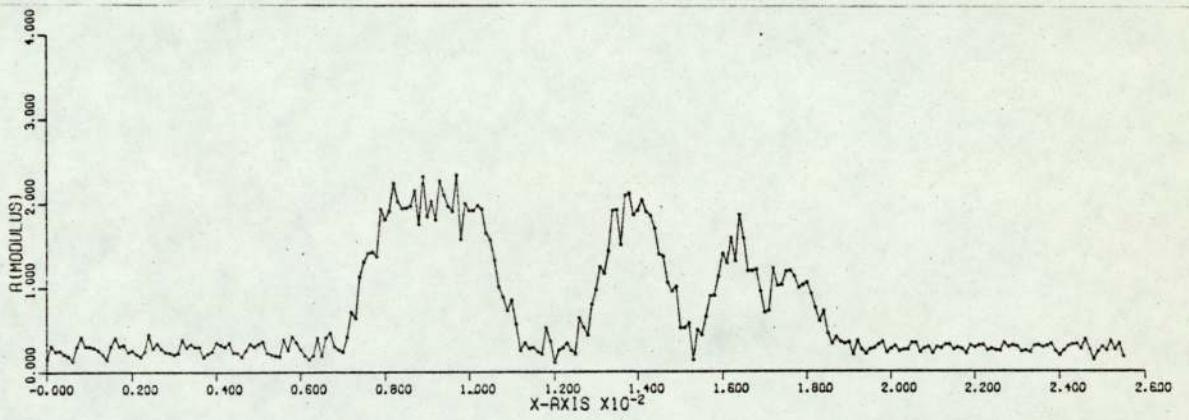
FIG. 2.18 a





F ⊕ G  $N_A = 1 b$

$\beta = 1000$



F ⊕ G  $N_A = 2 b$

$\beta = 1000$

FIG. 2.18 b

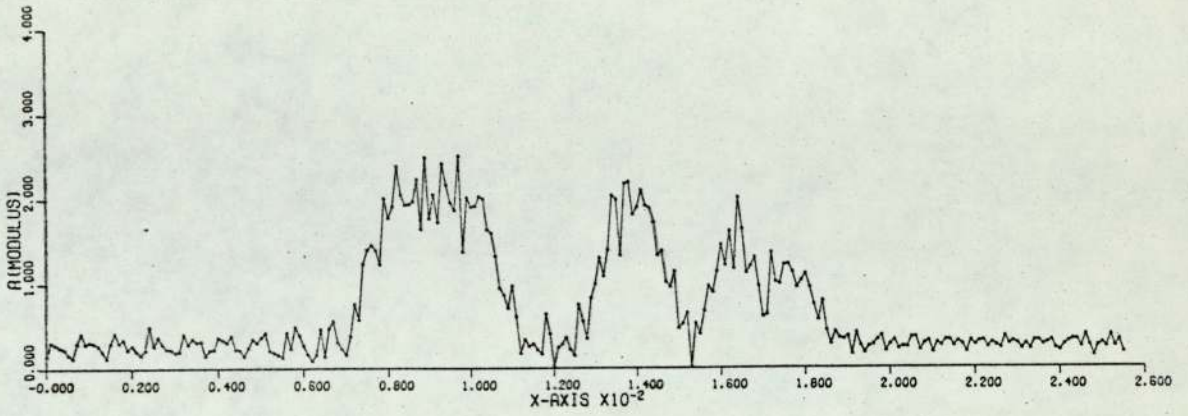
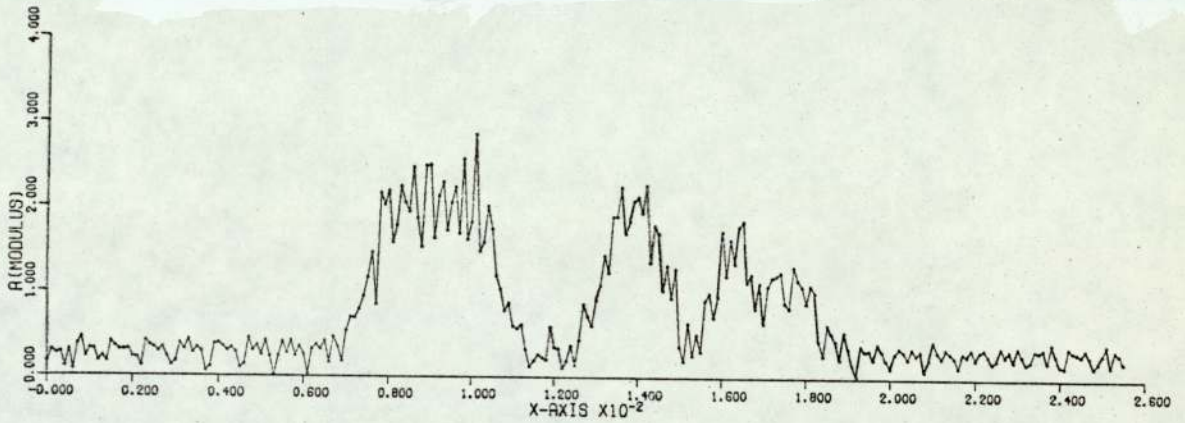
F ⊗ G  $N_A = 3$  b) $\beta = 1000$ F ⊗ G  $N_A = 4$  b) DS $\beta = 1000$ 

FIG. 2.18 b



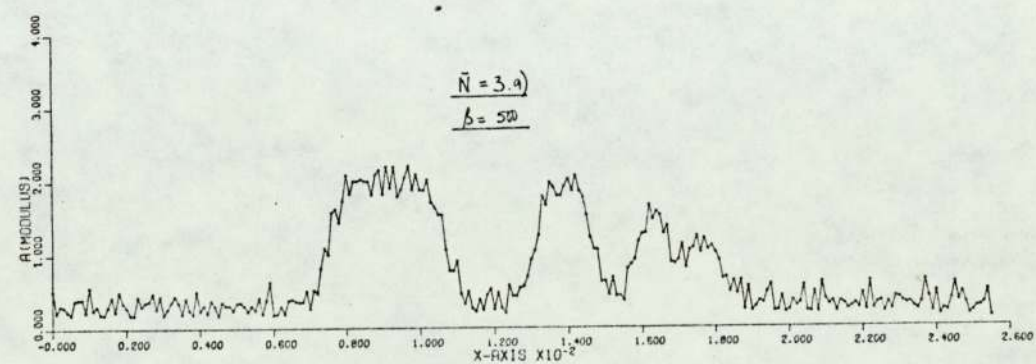
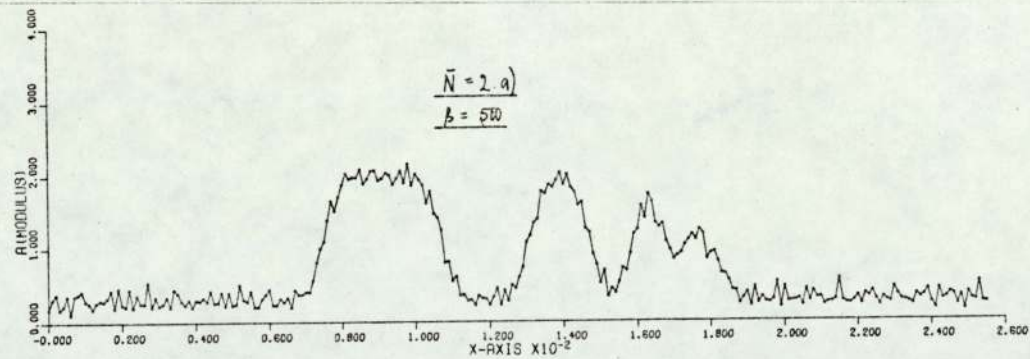
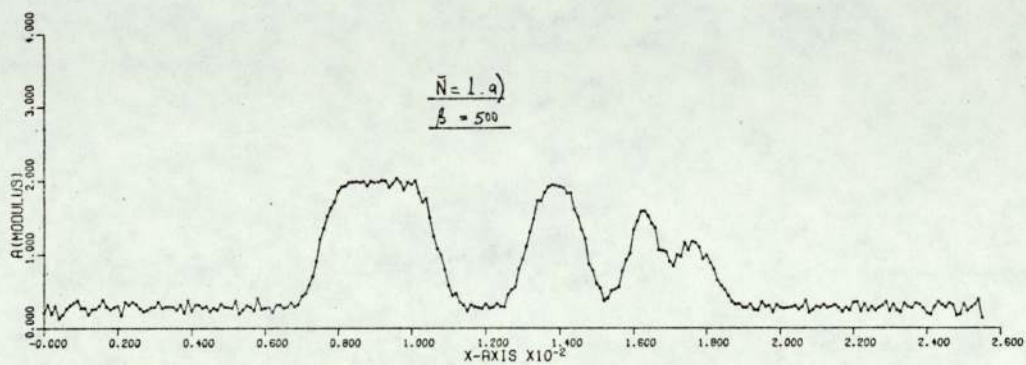
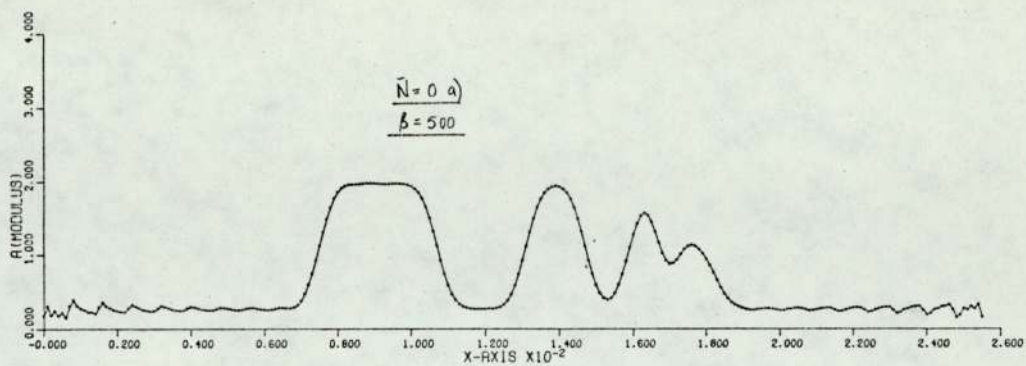


FIG. 2.19 a

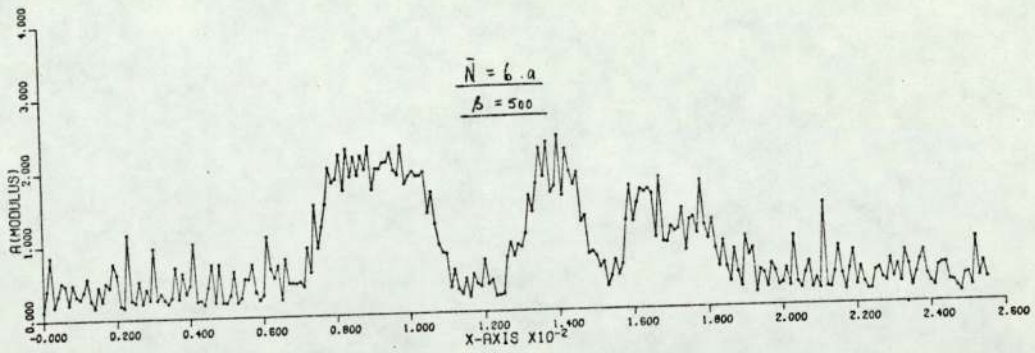
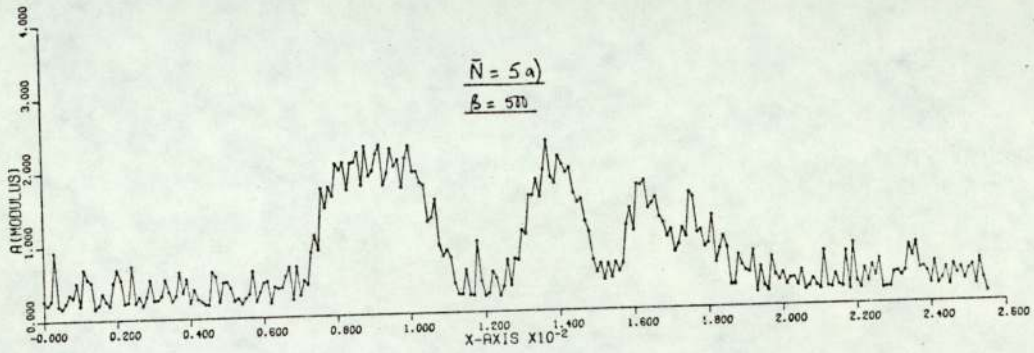
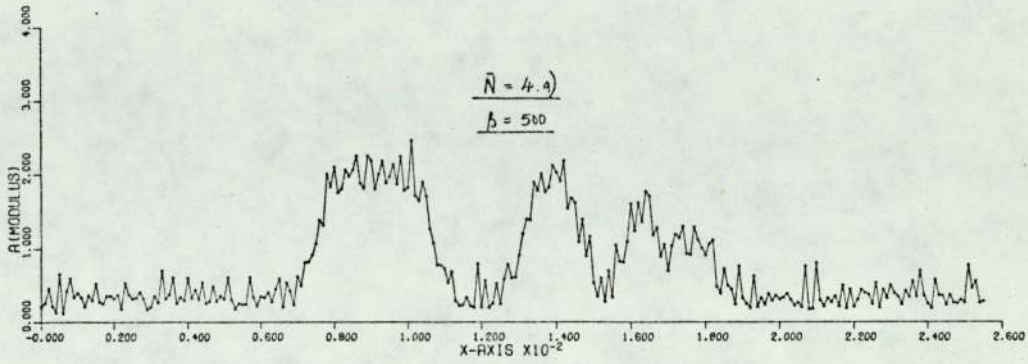
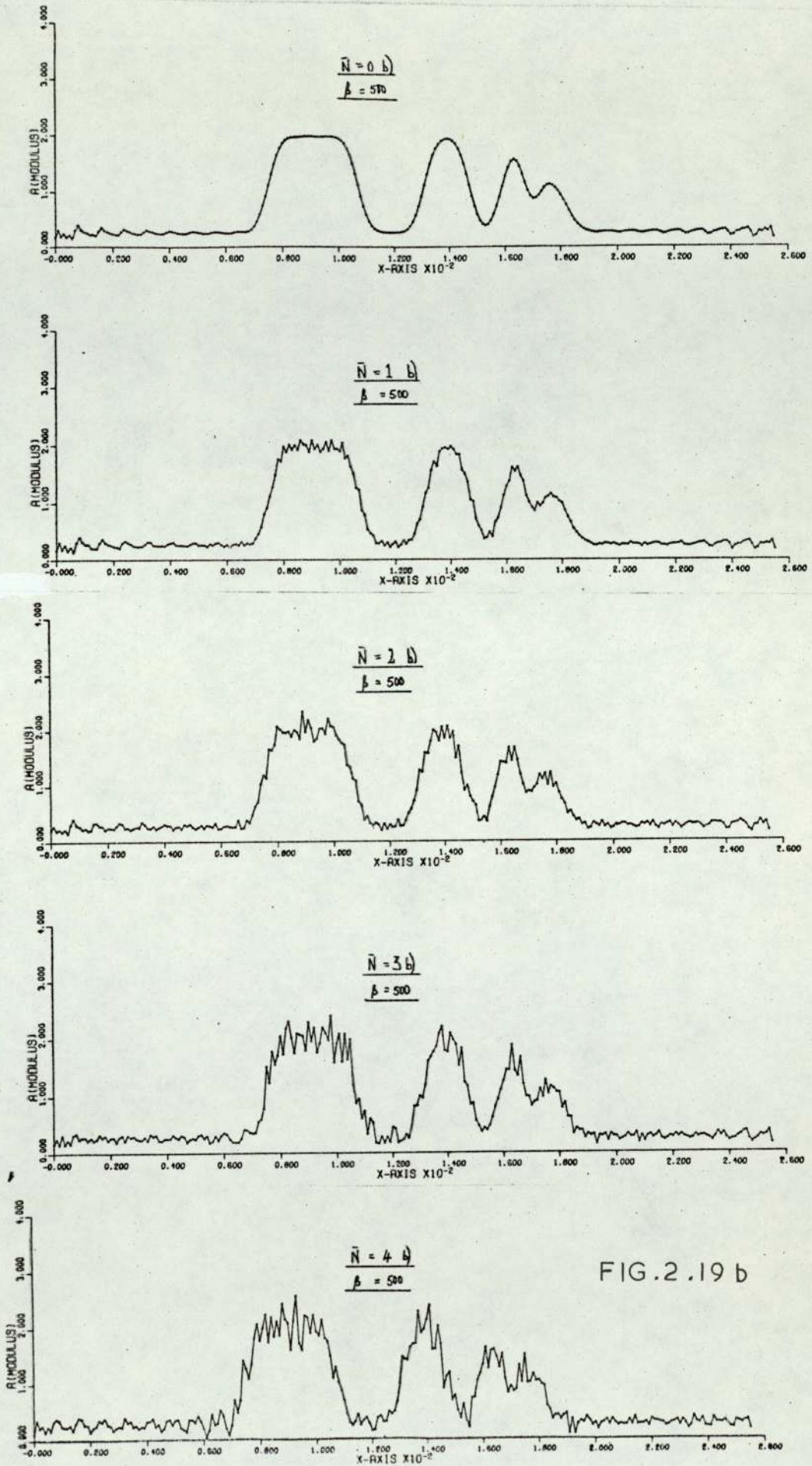


FIG. 2.19 a





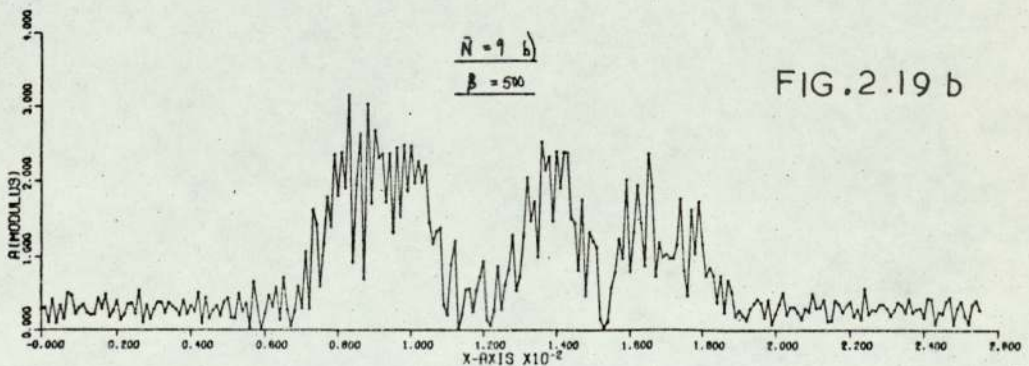
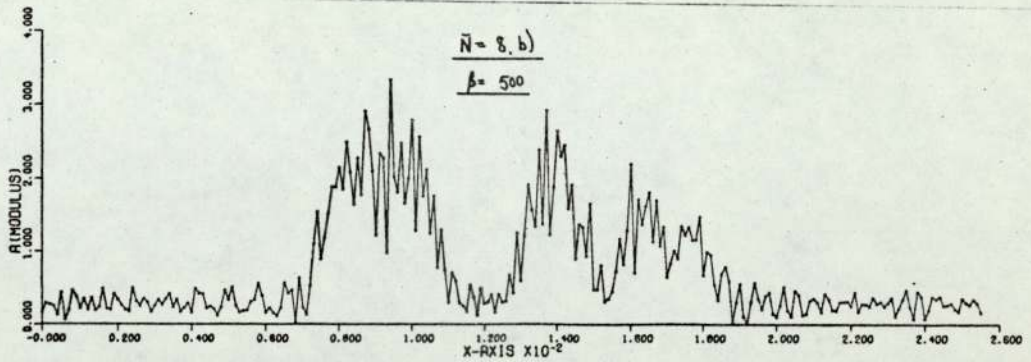
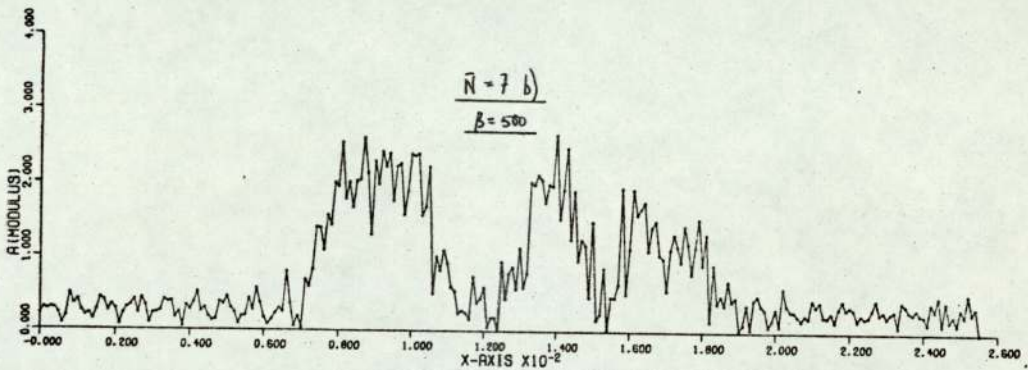
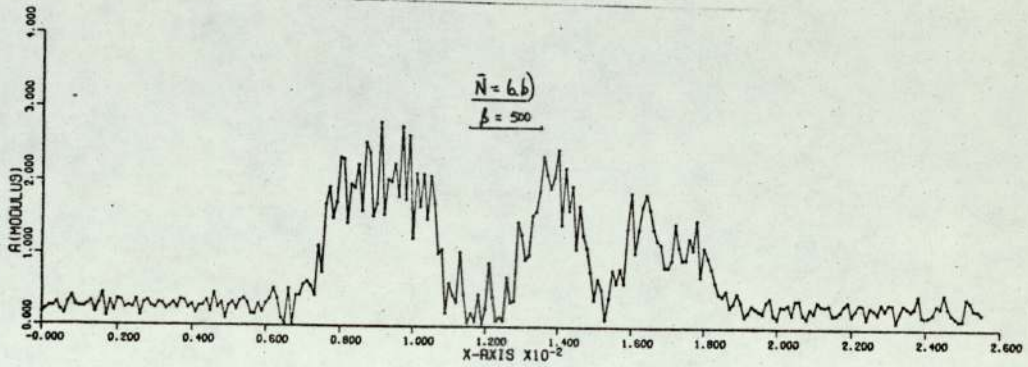
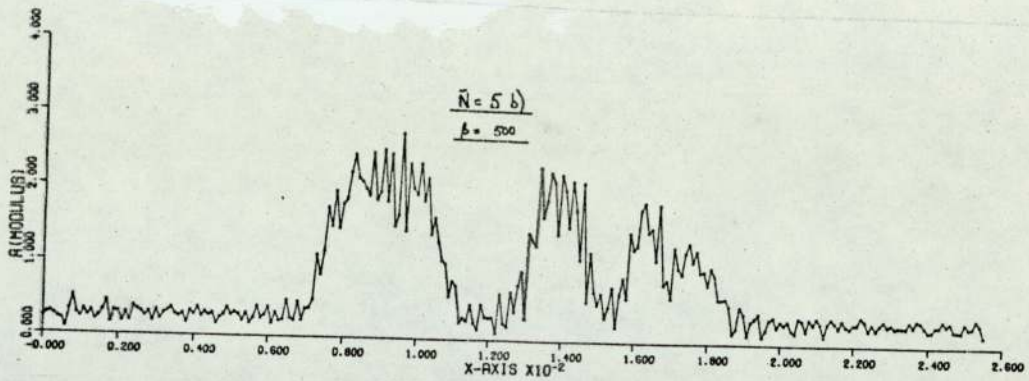


FIG.2.19 b



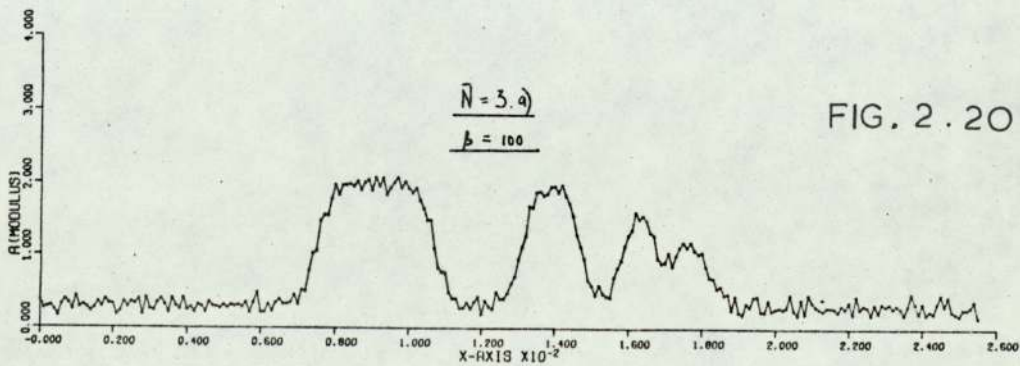
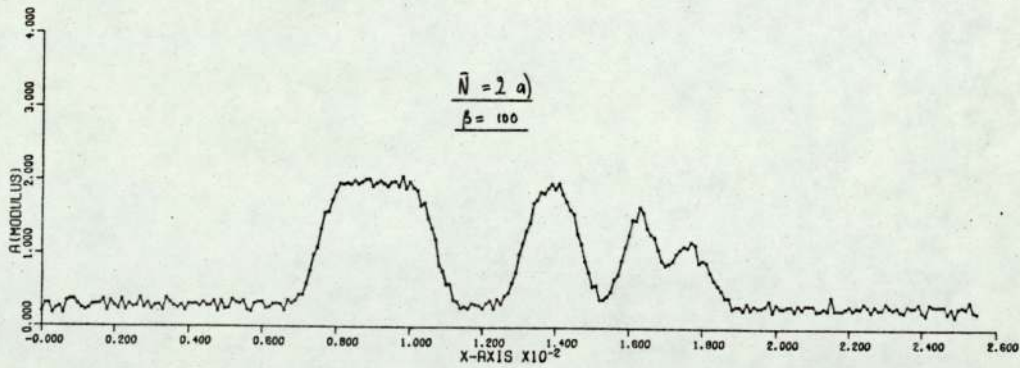
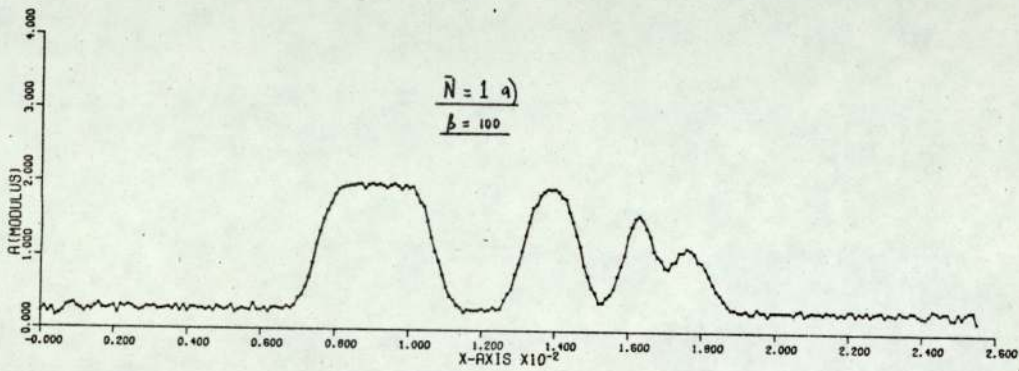
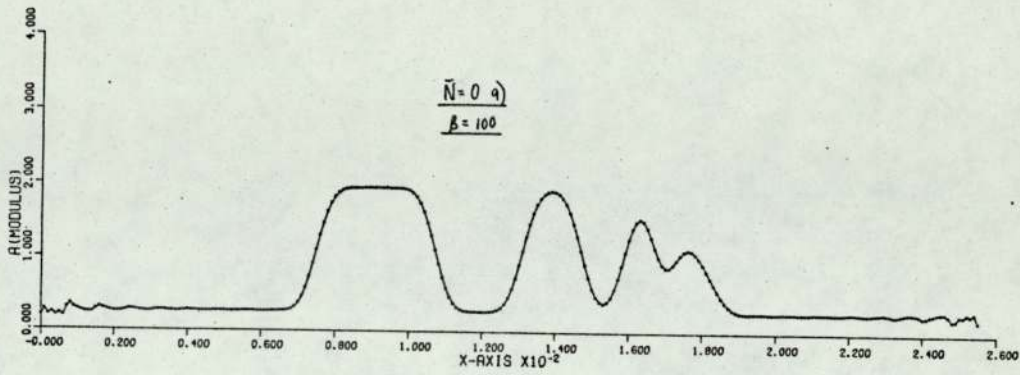


FIG. 2.20 a

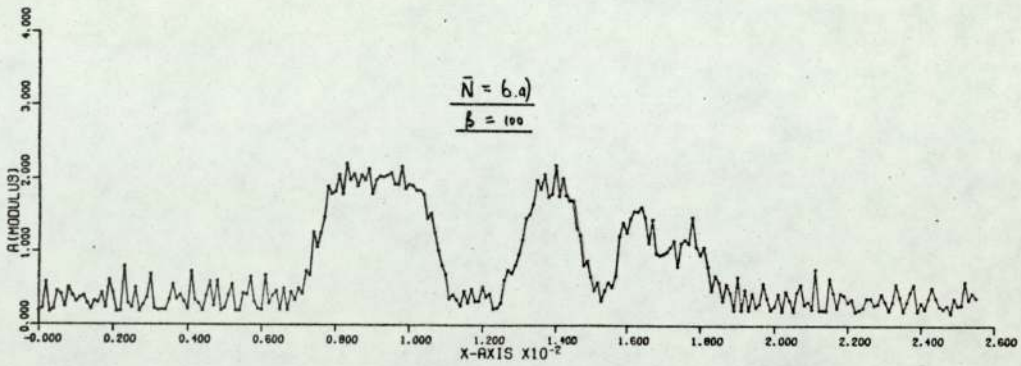
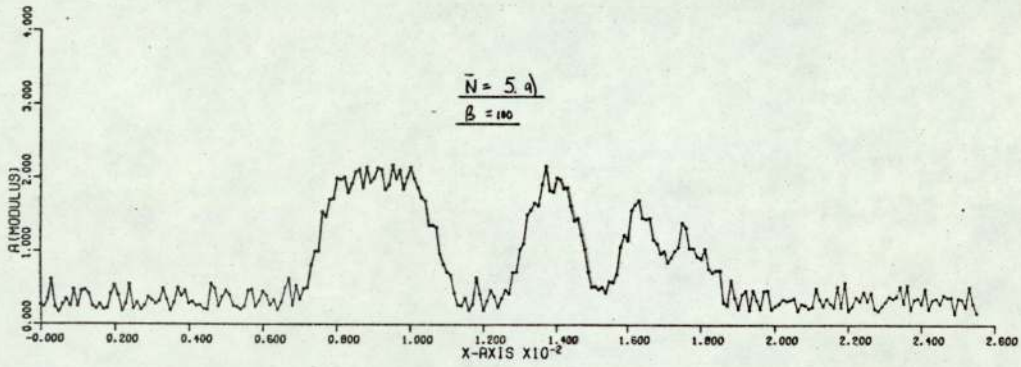
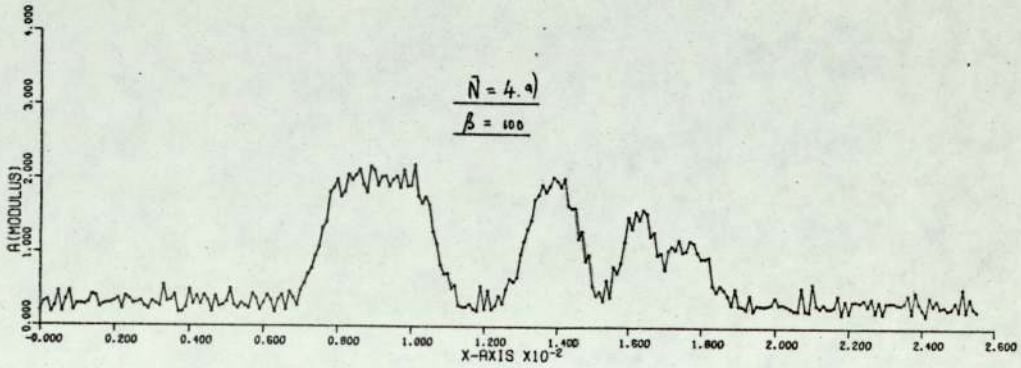


FIG.2.20 a



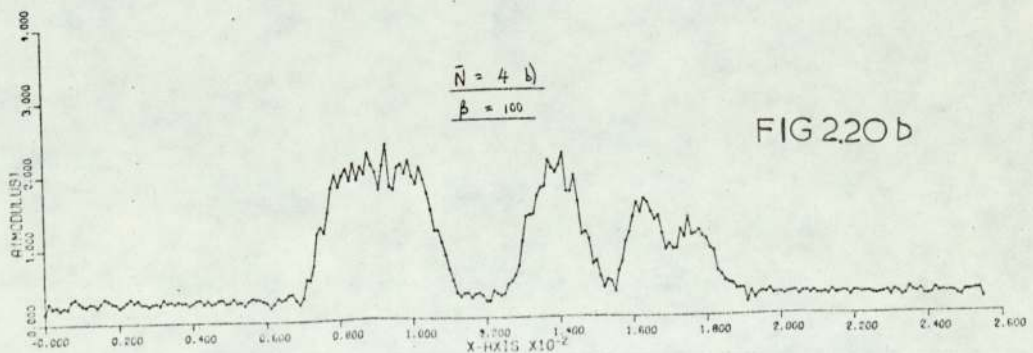
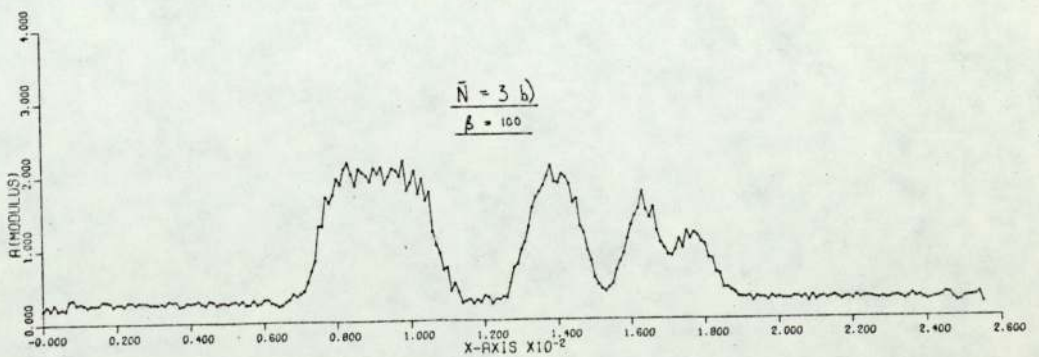
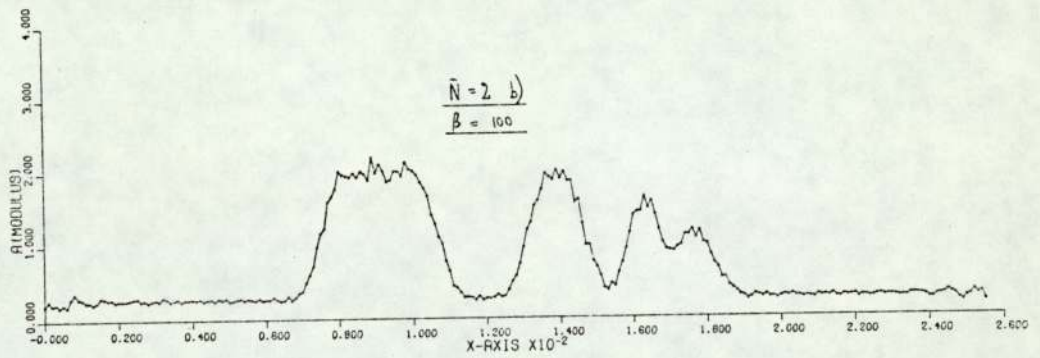
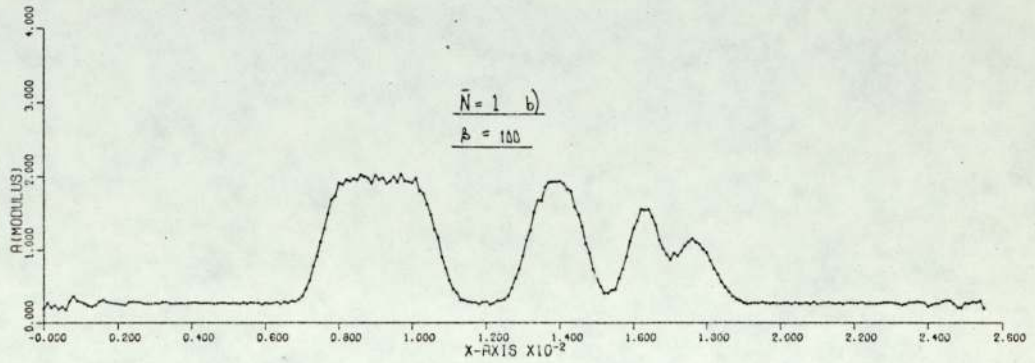
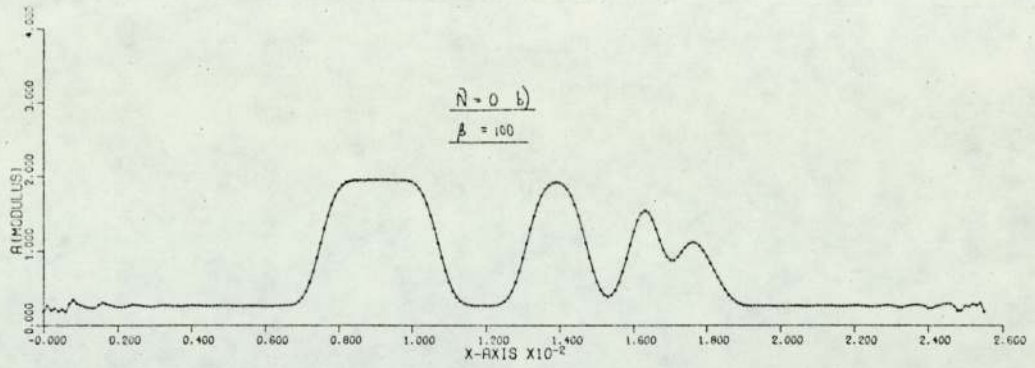
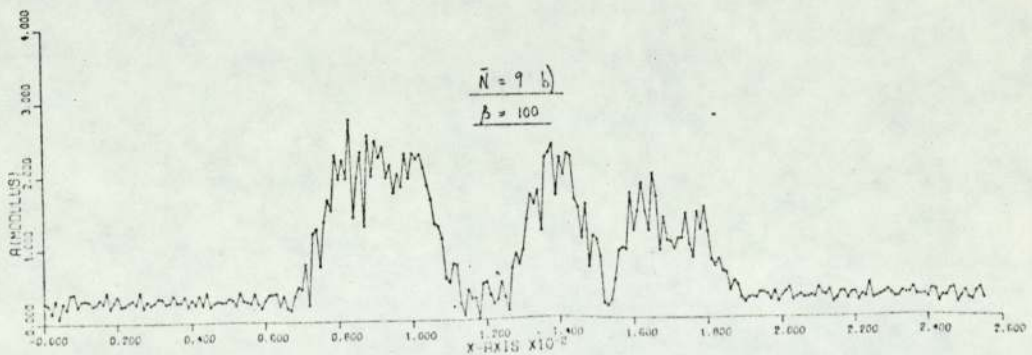
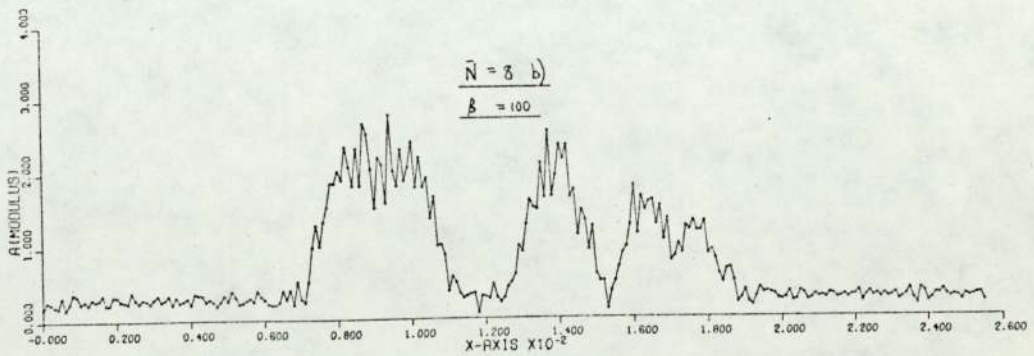
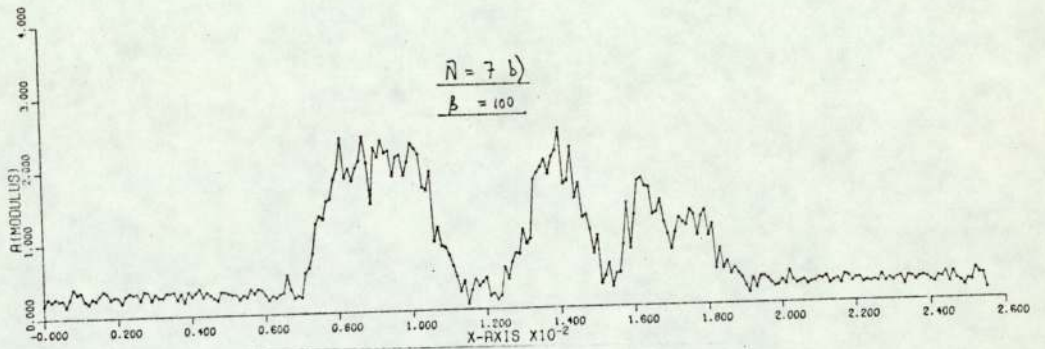
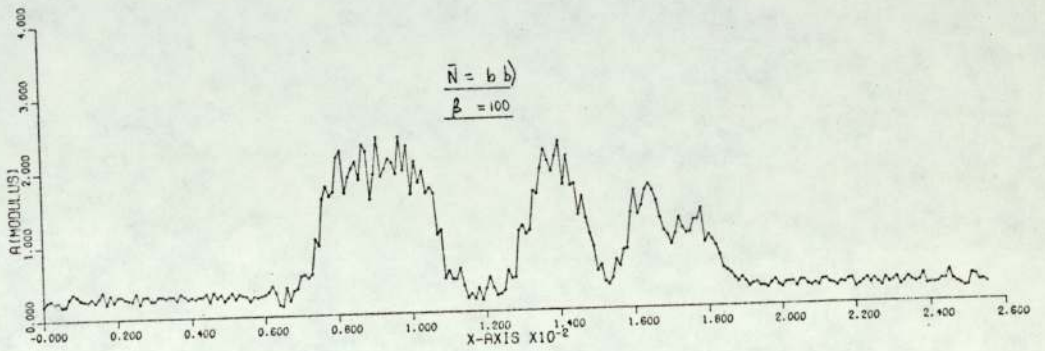
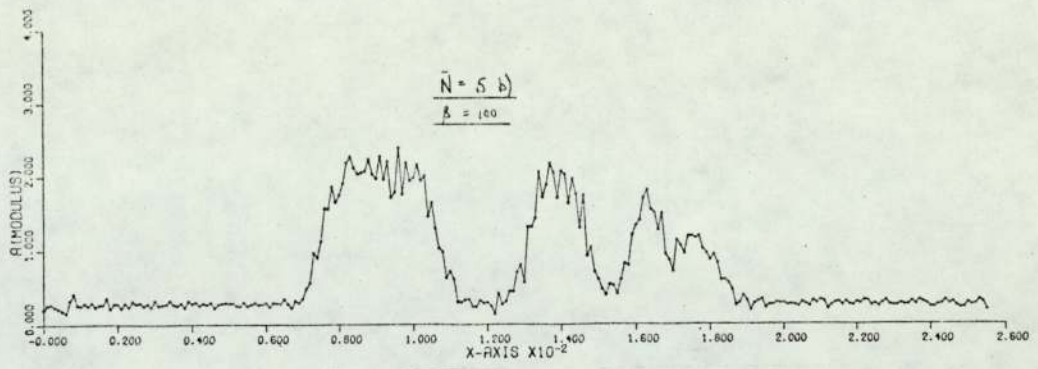


FIG 2.20b





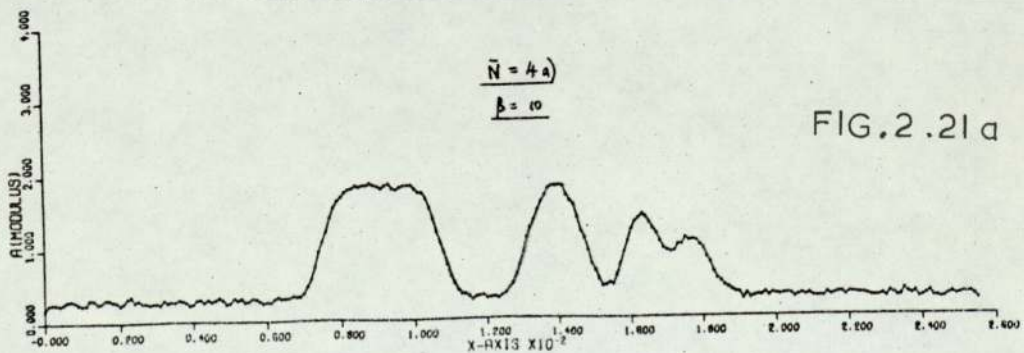
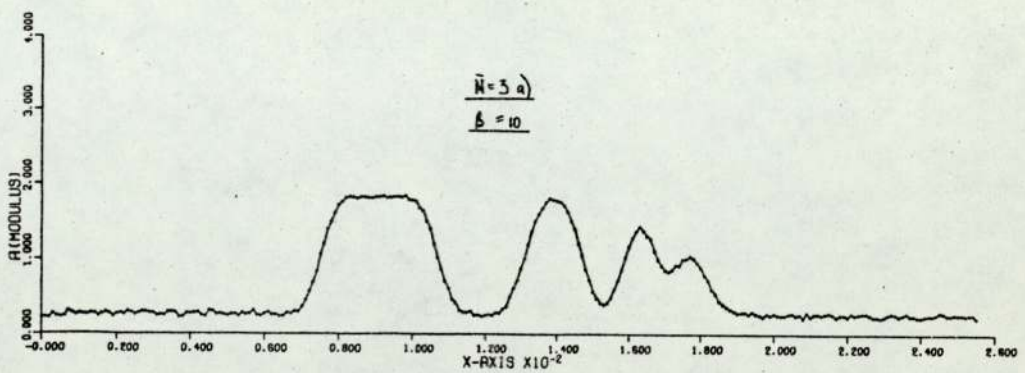
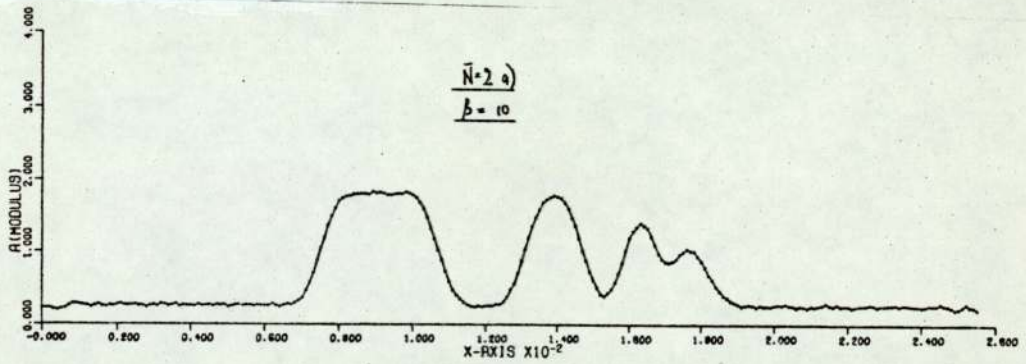
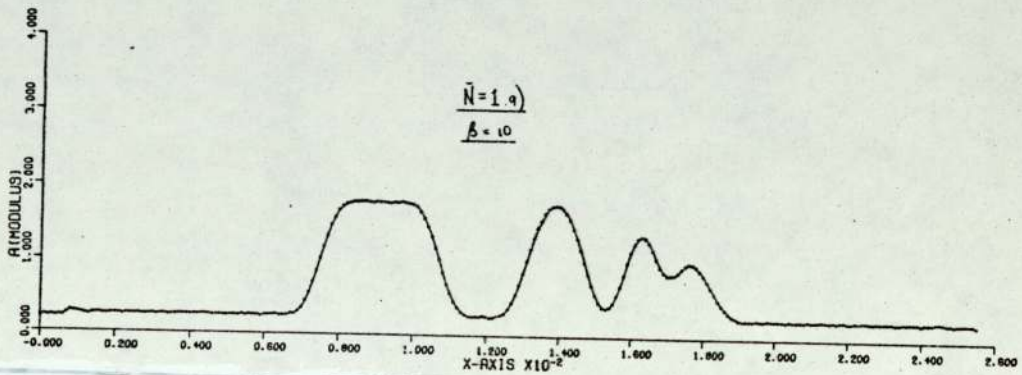
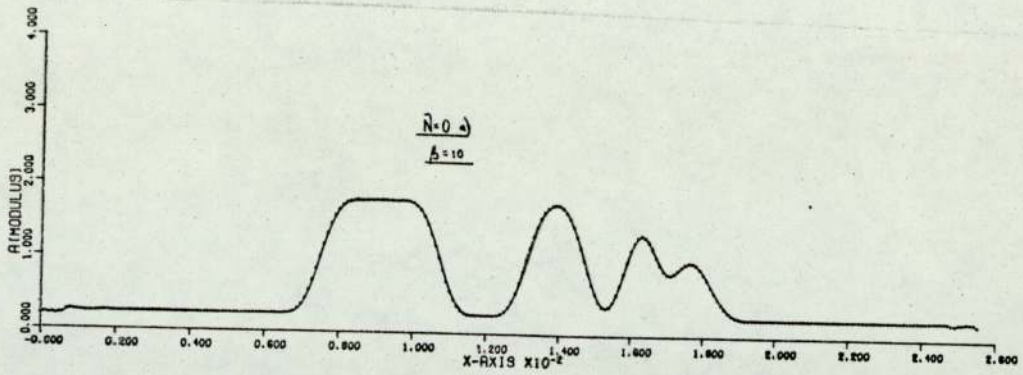
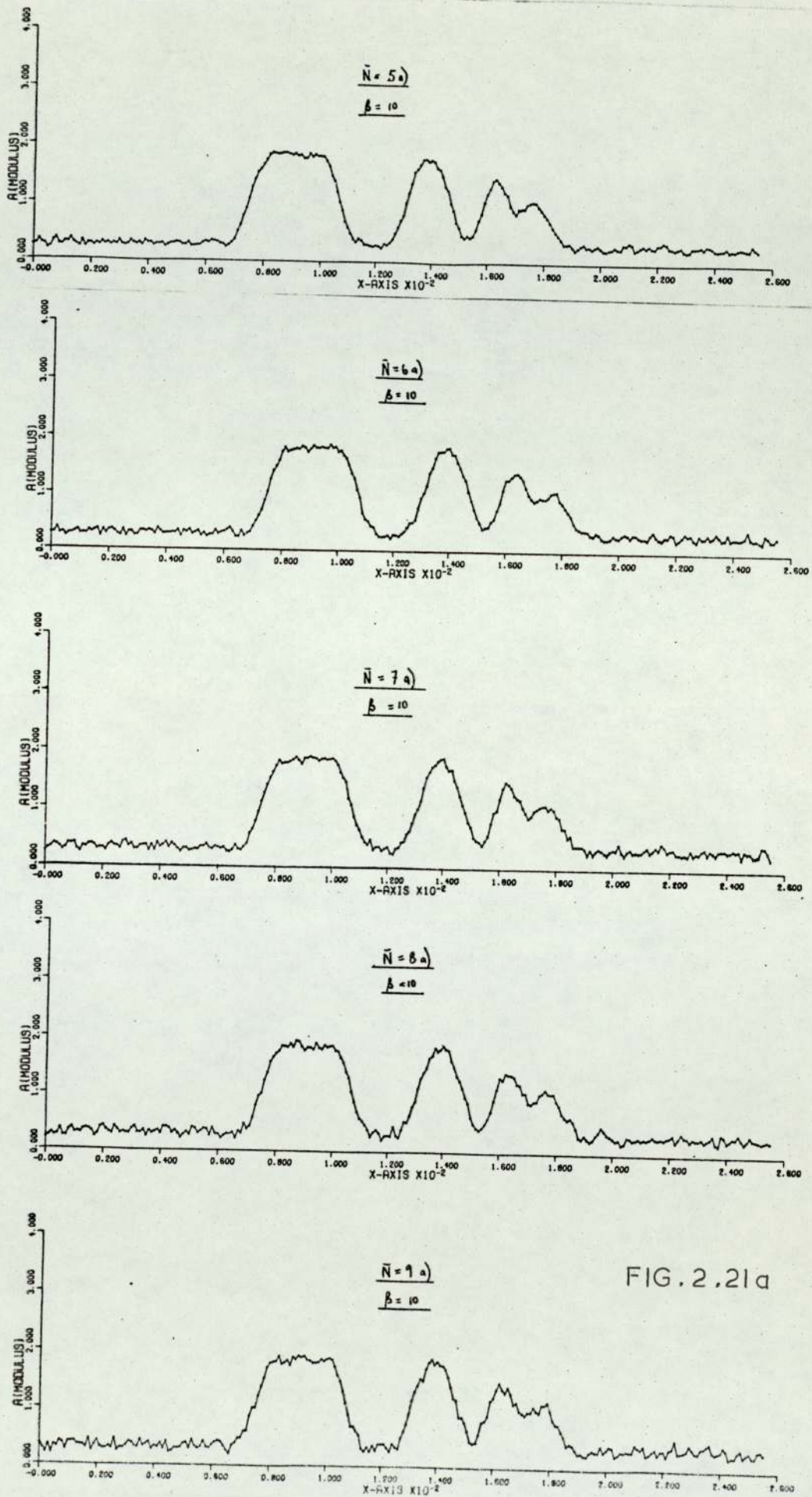
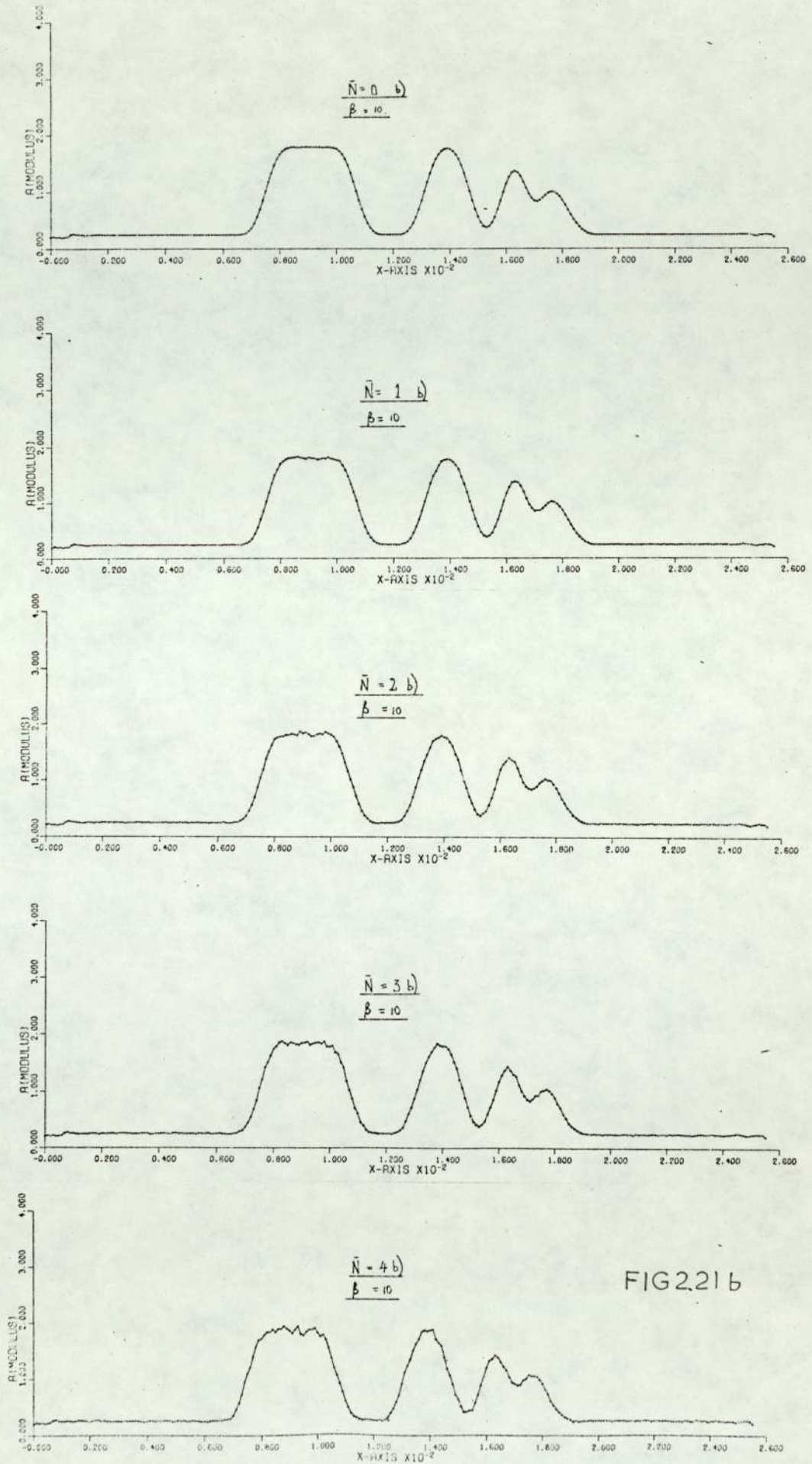
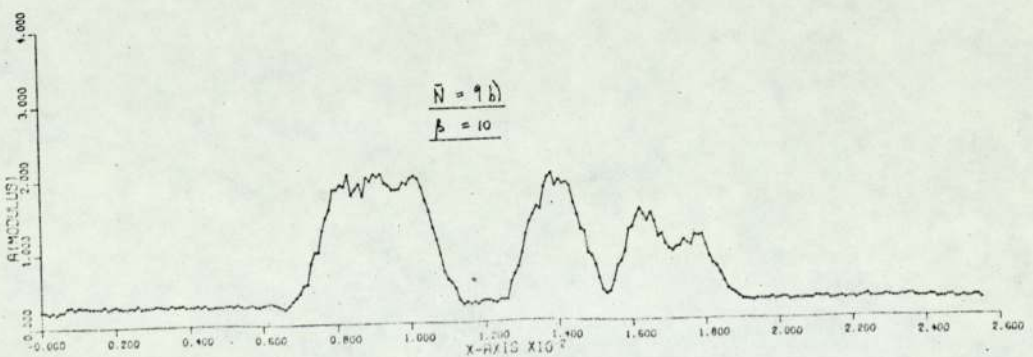
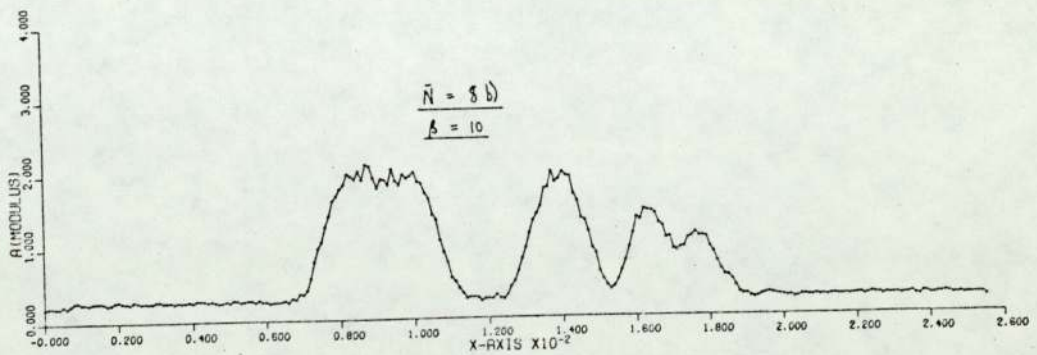
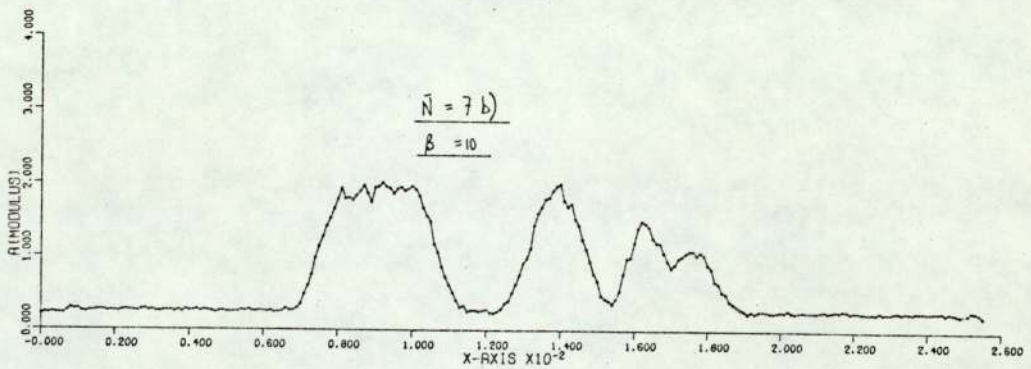
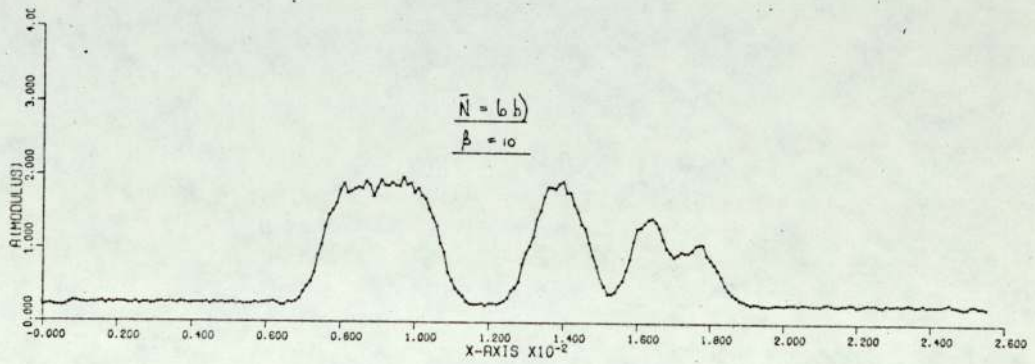
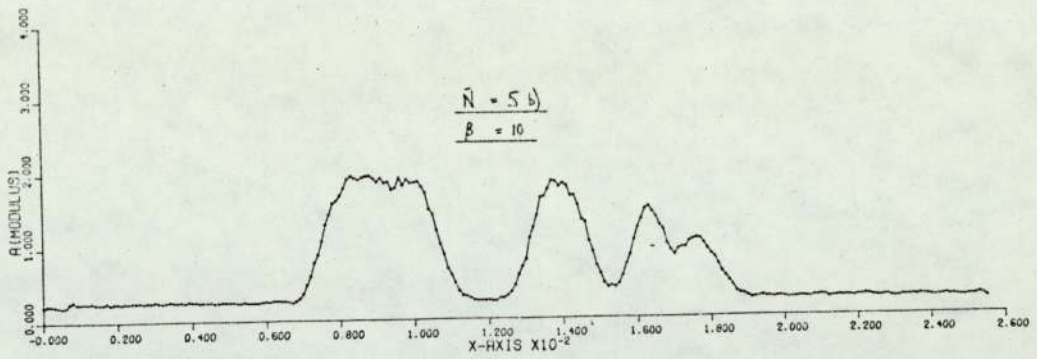


FIG. 2.21 a











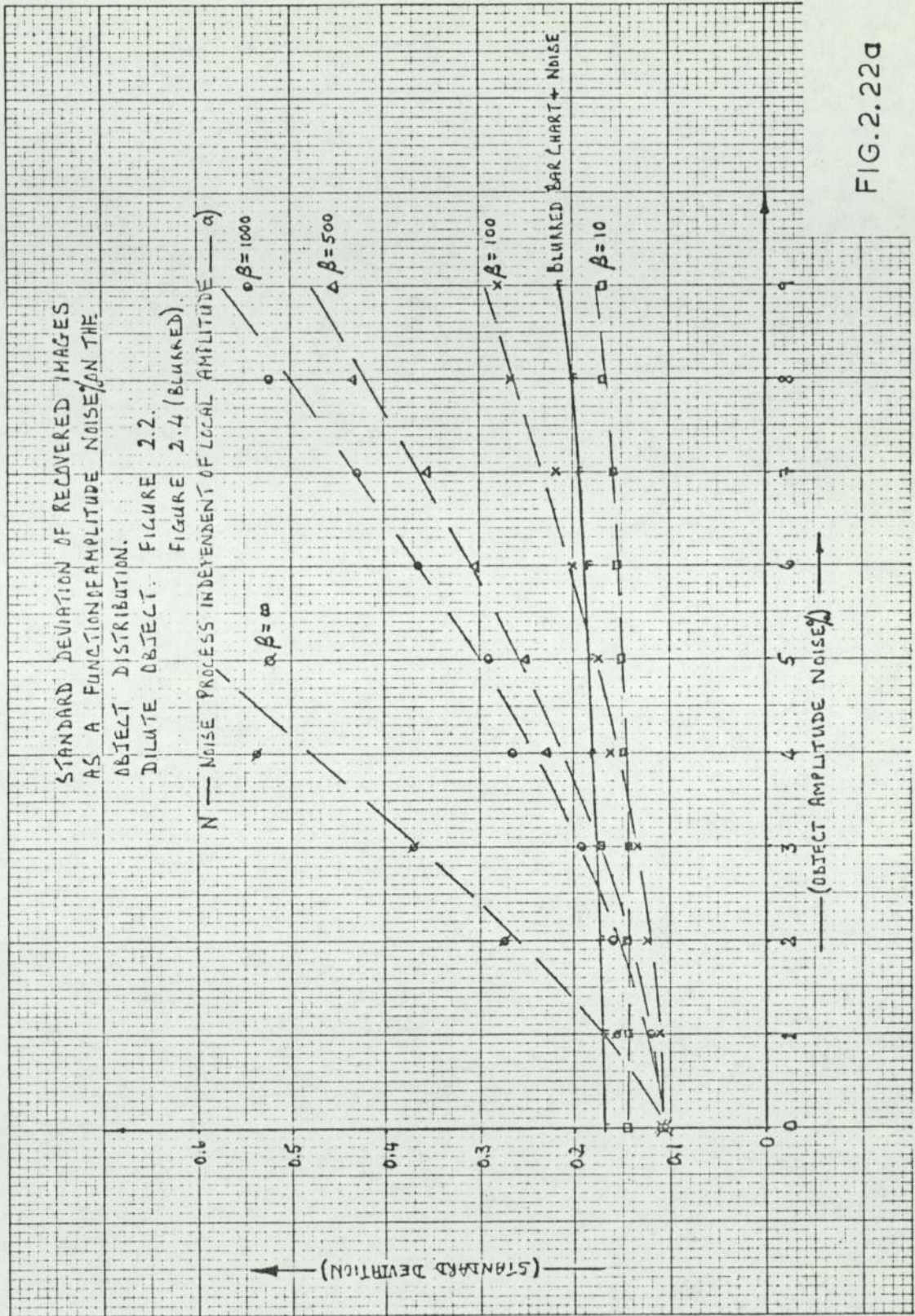


FIG. 2.22a



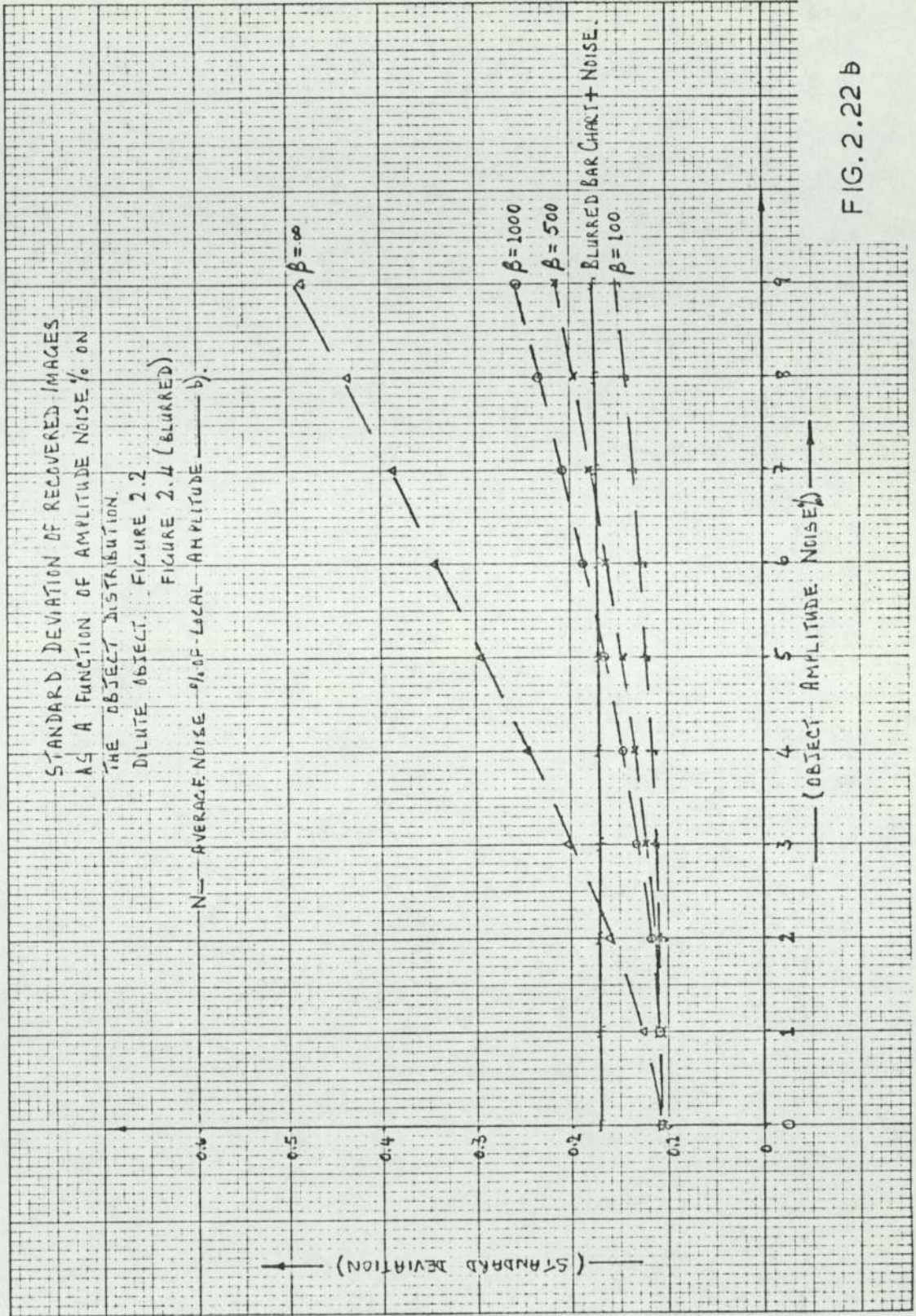


FIG. 2.22 b



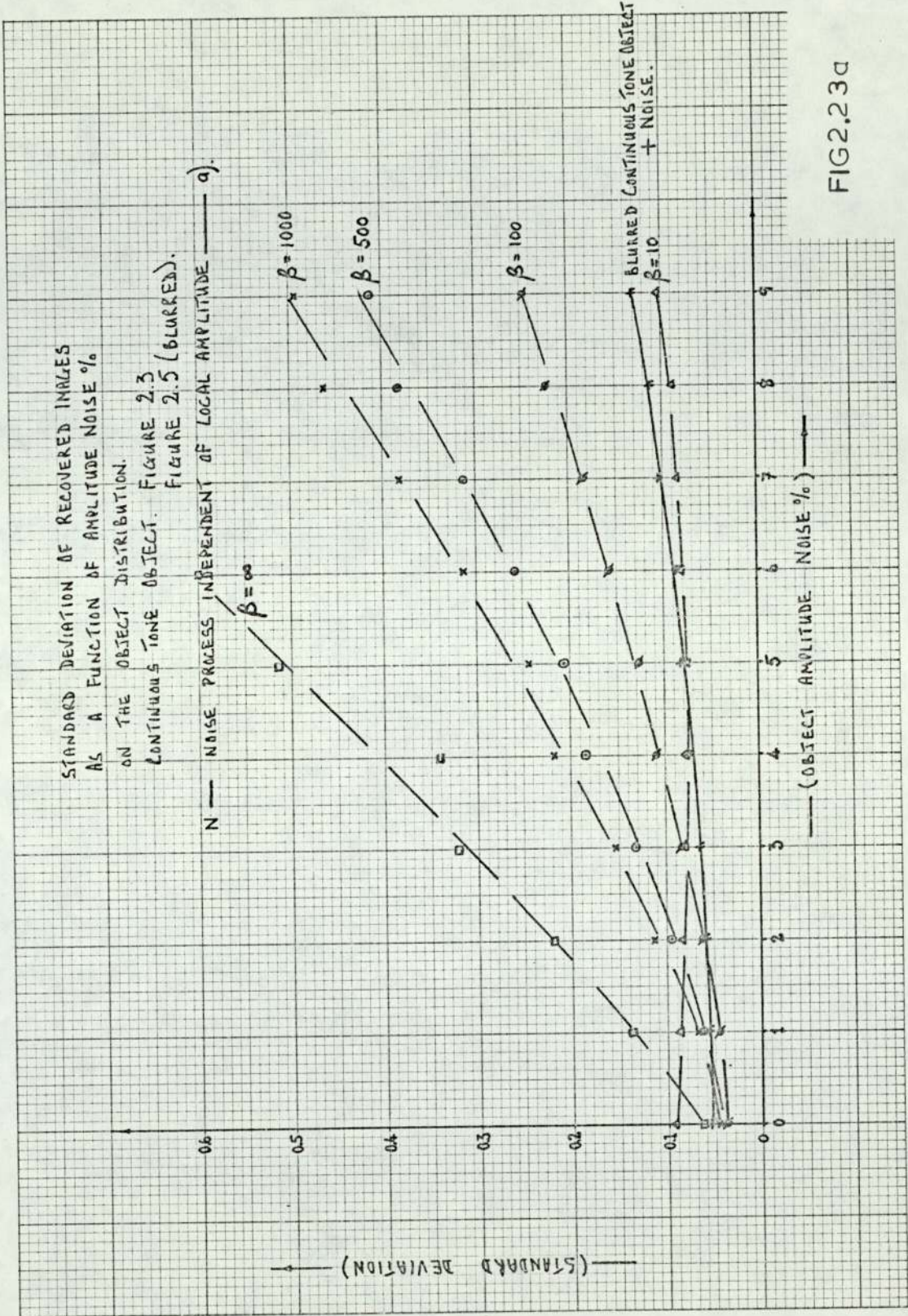


FIG2.23d



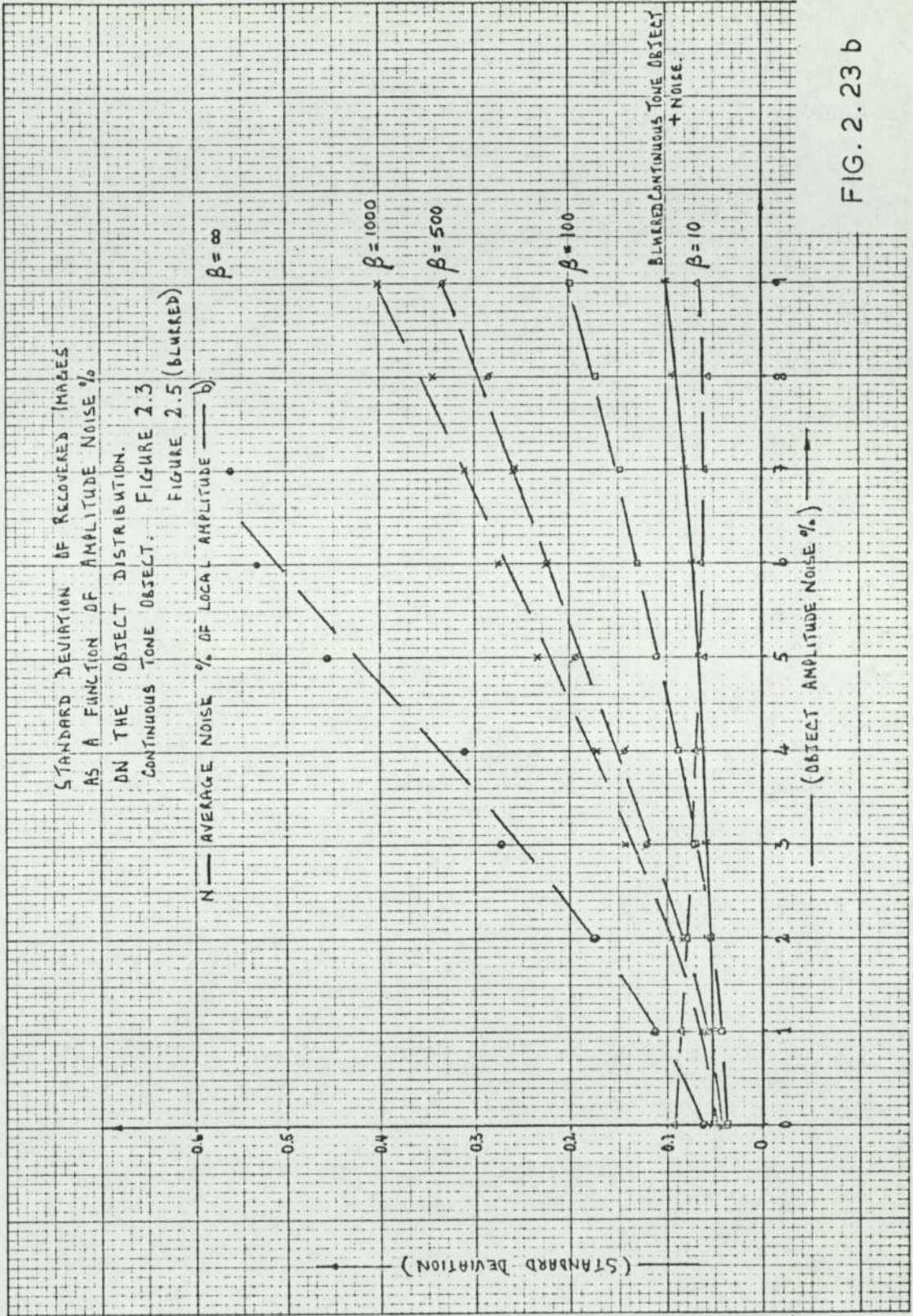


FIG. 2.23 b



Standard Deviations of Recovered Images

In order to assess the operation of the filters used, curves of standard deviation of the recovered images as a function of object noise were calculated for both objects, and both noise schemes. These curves are shown in Figures 2.22 a), b), for the binary object, and Figures 2.23 a), b), for the continuous tone object. The procedure was to calculate the normalized square root of the sum of the squares of the deviations of the recovered images from the original unblurred object distribution. As a measure of the statistical goodness of recovery, the standard deviations of the original blurred noisy objects were calculated, and are also shown in the figures. The significance of the curves is that when the standard deviation of a recovered image becomes greater than that of the blurred noisy object, the recovered image is, by a LMSE criterion, a poorer representation of the original object than is the blurred version. The noise level,  $\bar{N}_{\max}$ , at which this occurs, (when the two curves cross), represents the maximum noise tolerable in order to statistically recover the image according to a LMSE measure.

The curves of Figures 2.22 and 2.23 all show a general reduction in standard deviation for the recovered images as the filter signal to noise ratio is reduced. As an example, for the binary object and additive noise, a), the perfect filter results in an image with a standard deviation less than that of the original, blurred noisy object up to

a noise level of  $\bar{N}_{\max} \approx 1\%$ . For noise scheme b),  $\bar{N}_{\max} \approx 2\%$ . With  $\beta = 1000$ ,  $\bar{N}_{\max} \approx 2\%$  for a) and  $\bar{N}_{\max} \approx 5\%$  for b). It should be noted that these are only approximate values as the standard deviation at each value of  $\bar{N}$  will depend upon both the form of the object sequence and the noise impressed upon it. Strictly a value of standard deviation should be obtained for a given  $\bar{N}$  by calculating the ensemble average over all data sequences and noise processes. (The Central Limit Theorem suggests that the resulting standard deviations will tend to be normally distributed as the number of data and noise sequences considered is increased, (Ref. 33) ).

For each of the curves of Figure 2.22 b) different noise sequences were generated by computer and used with weightings,  $\bar{N}$ , on the object data. The resulting curves are thus smooth. For the Figures 2.22 a) and 2.23 a), b) different noise sequences were generated for each value of  $\bar{N}$  as well as between the individual curves. In this case the statistical scatter of the calculated standard deviations can be seen.

The computer time required to statistically analyse the variation of standard deviation with data and noise sequences is, of course, large as for each value of standard deviation the whole deconvolution process must be performed. The available computer facilities (ICL 1904S) prohibited such a study. Also, in view of the

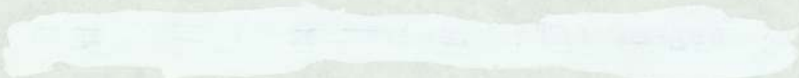


qualitative nature of the assessment of the recoveries, further statistical analysis of the variation of standard deviation was not pursued.

It is also worth pointing out that a certain degree of ringing of the filter is apparent which results in aliasing of the recovered images. It is most noticeable for the filters with large signal to noise ratios which have rapid amplitude changes resulting in impulse responses that do not decay to nearly zero at the edges of the image region,  $\pm \Delta X/2$  (see Figure 2.10). This aliasing is more obvious in recoveries of the noise free continuous tone object as the resulting amplitude ripples are then more apparent, see for example Figure 2.13 a) with  $\bar{N} = 0$ . In practice it is normal to apodise the filter in order to reduce image aliasing. In these simulations the filters were not apodised; the data field was, however, reduced from the six element bar chart extent of Figures 2.14 b) and 2.16 b), in which a fraction 219/256 of the object field was used, to 107/256 of the object field.

In terms of standard deviations the aliasing error results in the calculated values being slightly high with the error decreasing as  $\beta$  decreases. For  $\beta < 500$  the aliasing is negligible.

The case of a Kinoform was considered earlier and was seen to produce a predominantly low frequency image of poor fidelity. A similar effect is seen for filters with low



signal to noise ratios. The images are recovered with low standard deviations as a result of the suppression of progressively larger high frequency regions of the object spectrum. This can be seen in the form of the filters in Figures 2.10.

As a result of this, the calculated maximum tolerable noise levels,  $\bar{N}_{\max}$ , do not generally agree with those judged by an inspection of the recovered images. For example, the curve for  $\beta = 500$  of Figure 2.22 a) gives a value,  $\bar{N}_{\max} \approx 3\%$ , but the recoveries of Figure 2.15 a) suggest  $\bar{N}_{\max} \approx 5\%$ . More noticeable discrepancies occur for small values of  $\beta$  in which the standard deviation calculations show a high degree of tolerance to noise. Figure 2.22 a) shows that for scheme a) with  $\bar{N} > 4\%$  the image recovered by a filter with  $\beta = 10$  is the best estimate of the original bar chart object. This is not born out by an inspection of the recovered images of the blurred bar chart with 4% additive noise for the other LMSE filters. With  $\beta = 1000, 500$  and  $100$  all the recoveries exhibit a greater degree of image deconvolution than does the recovery with  $\beta = 10$ .

The discrepancy arises because deconvolution is an edge sharpening operation, enhancing the high frequency content of the image, and it is exactly this image structure which results in large values of standard deviation. In this sense, the LMSE criterion is a poor test of the success of deconvolution as it primarily measures image noise



rather than edge sharpness.

### Deconvolution in the Presence of Filter Amplitude Noise

The same two noise schemes were used to simulate amplitude noise on the filter element in the linear motion deconvolution system. In this case, however, only the ideal filter was considered. The results are shown in Figures 2.24 a) and 2.24 b) in which the Fourier plane resistance to noise is exhibited. The recoveries are quite different for the two noise schemes. This is because the filter has a large dynamic range. Hence, for scheme b), in which the average noise excursion is limited to a percentage,  $\bar{N}$ , of the local amplitude, the noise has its largest effect where the filter amplitude is maximum. The additive noise thus tends to boost the transmittance in these regions with the result that little image degradation occurs (Figure 2.24 b). This is clearly an unsatisfactory physical model.

The noise scheme in which the average noise excursions are limited to a percentage of the maximum amplitude, scheme a), results in an image with a large low frequency content due to the effective suppression of the filter's high frequency transmittance, (Figure 2.24 a).

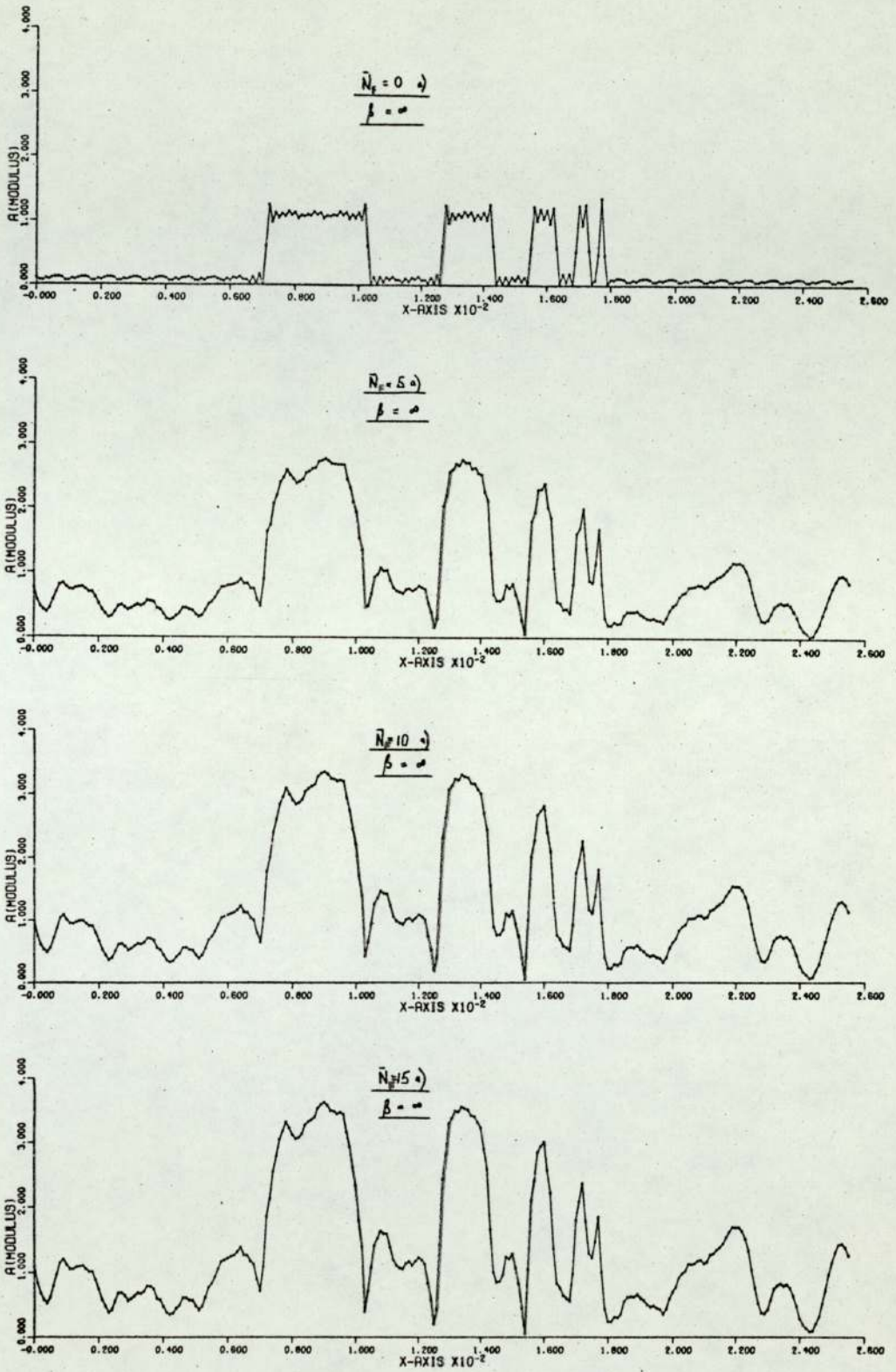


FIG.2.24 a



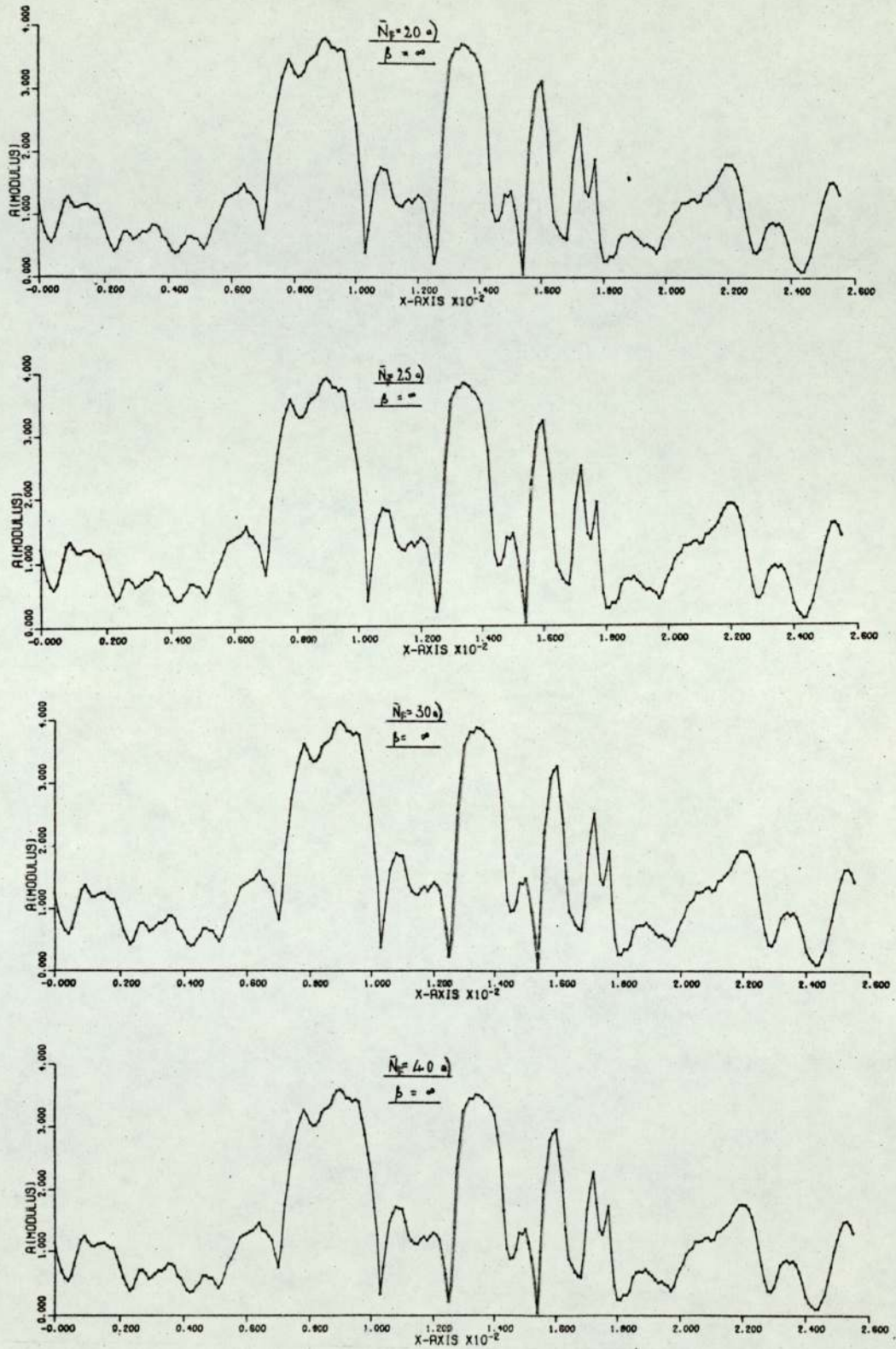


FIG. 2.24 a

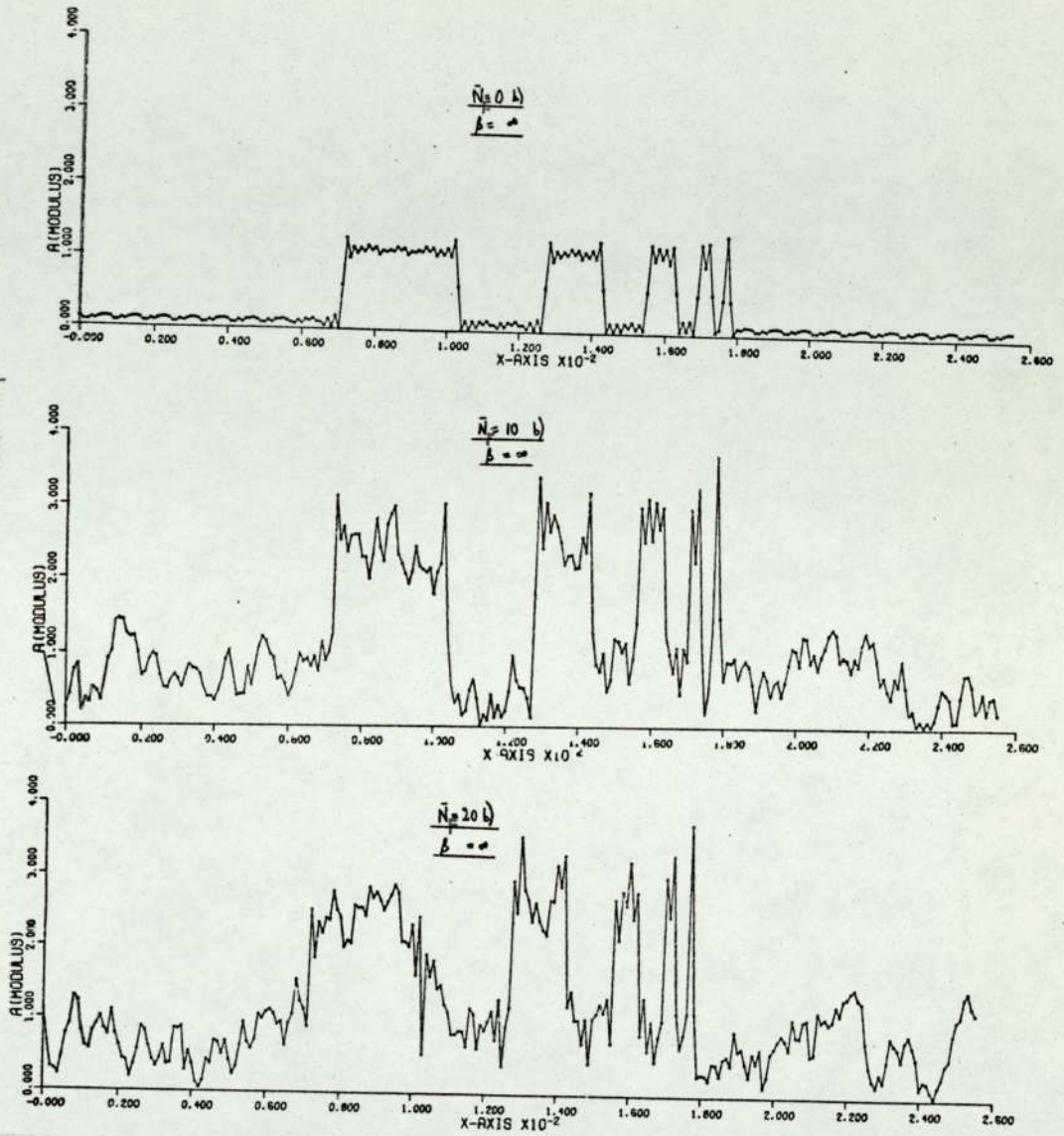


FIG.2.24 b



Deconvolution in the Presence of Filter Phase Noise

Finally we have simulated the effects of random variations in the phase of the filter element. The phase noise is assumed to be independent of the local phase values and is additive. Hence, the mean difference in phase between the different regions of the filter remains  $\approx \pi$  radians. Figure 2.25 shows the effects of random phase noise on the images recovered by a Kinoform filter. An average, additive excursion of  $\approx 20^\circ$  is tolerable. For the case of an ideal filter, the recoveries for which are shown in Figure 2.26, the resistance to phase errors is increased slightly by the improved fidelity due to the corrected amplitude transmittance.

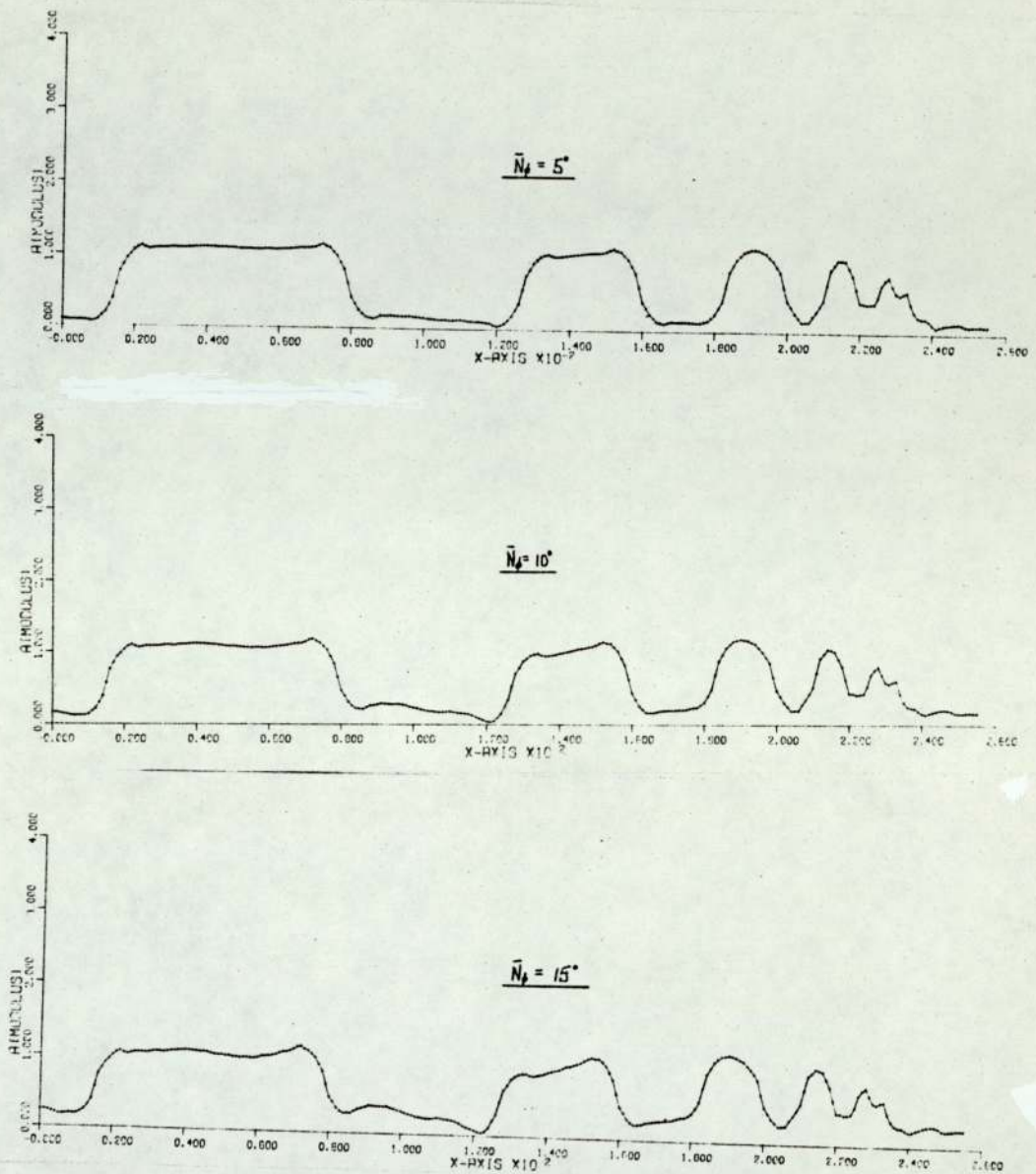


FIG. 2.25

Kinoform Recoveries With  
Filter Phase Errors.



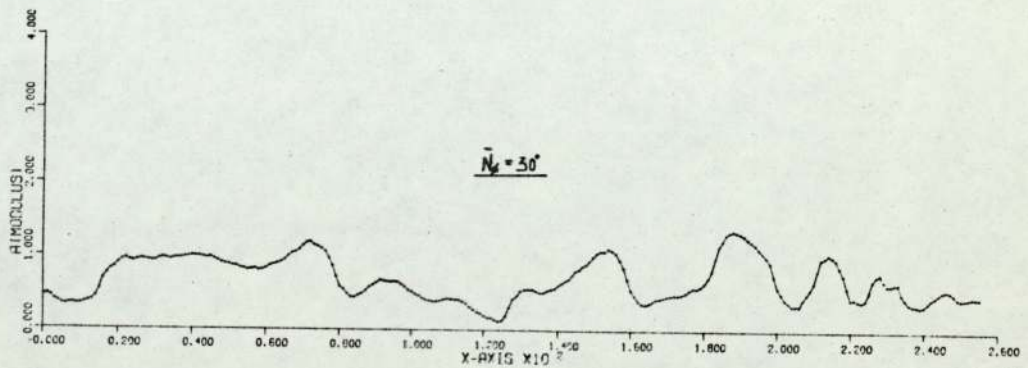
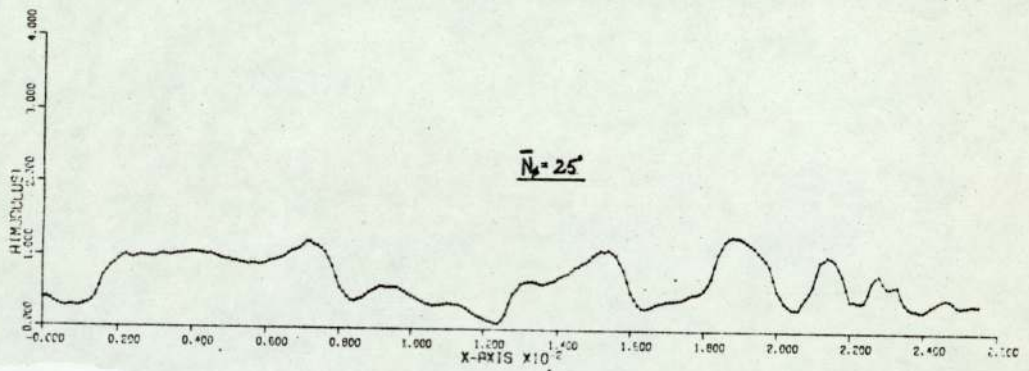
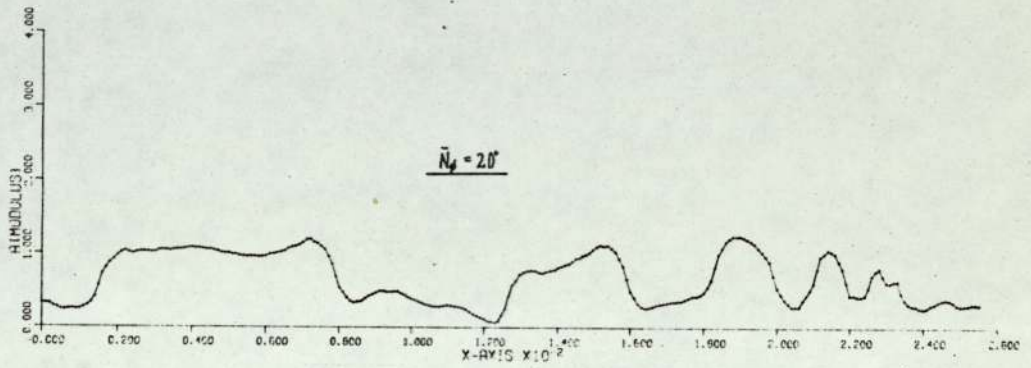
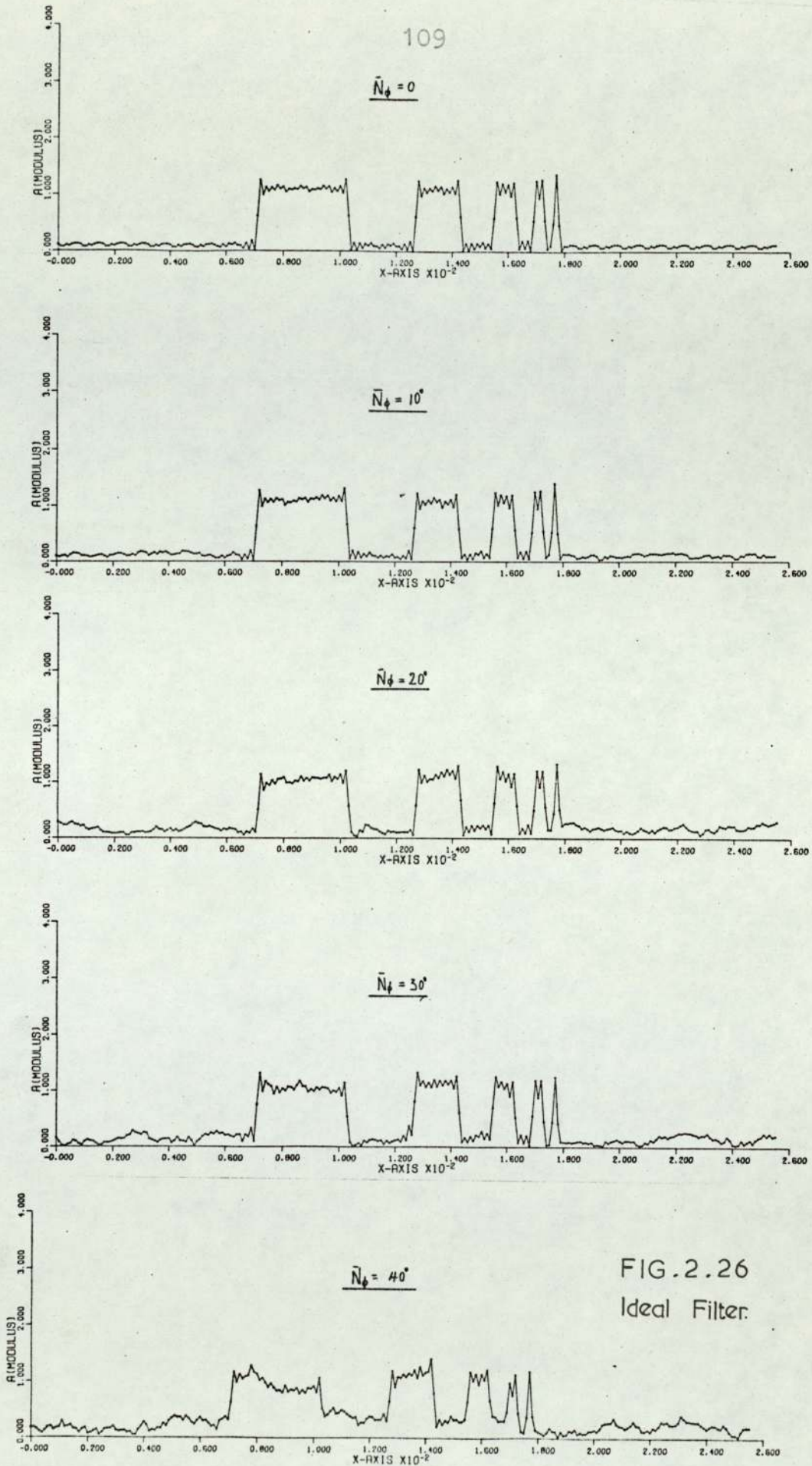


FIG. 2.25





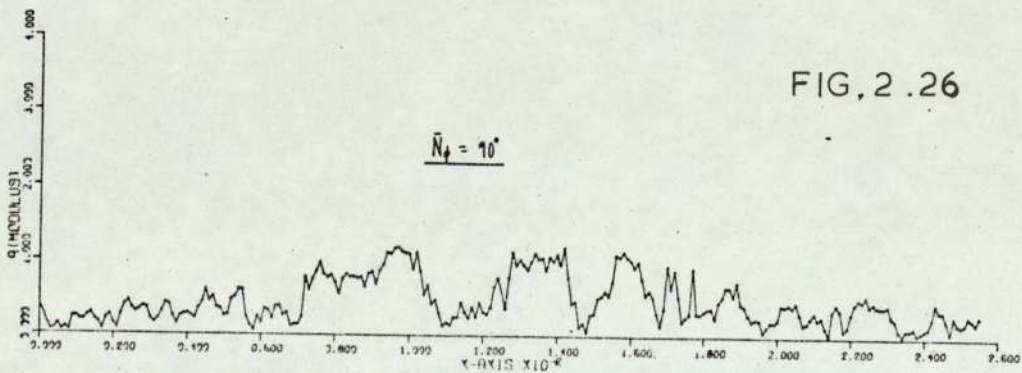
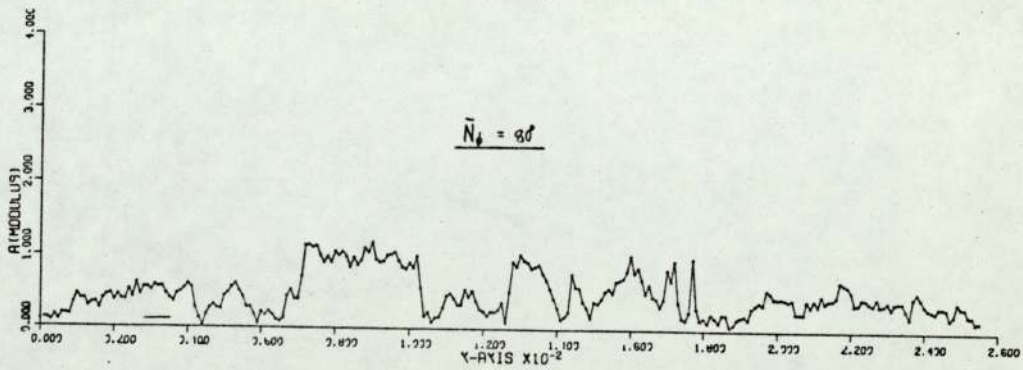
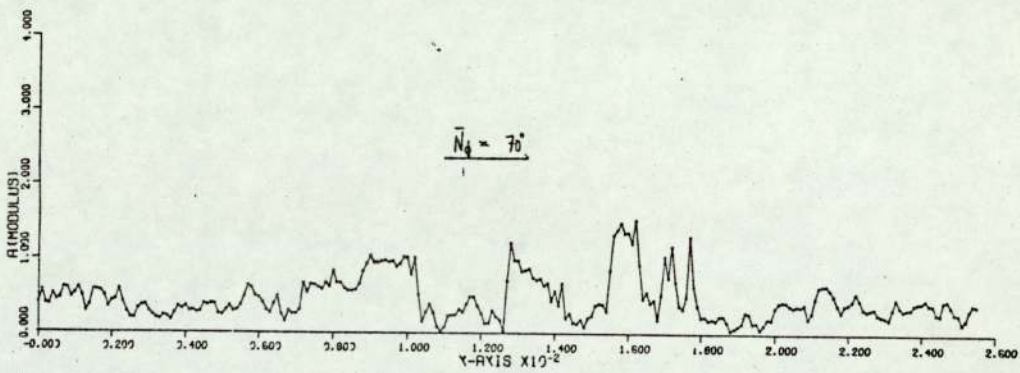
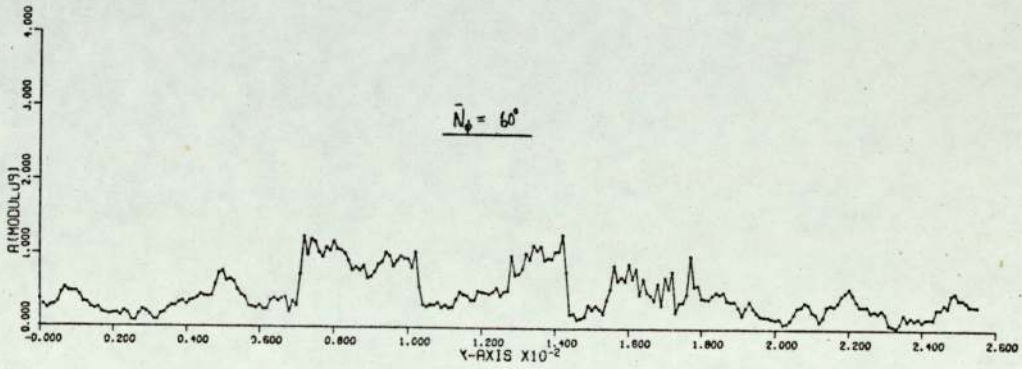
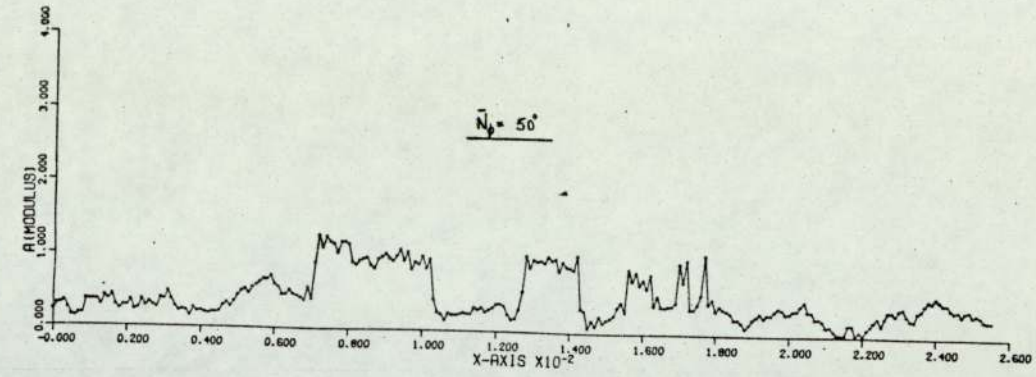


FIG. 2.26

CHAPTER 3

COMPUTER GENERATED HOLOGRAMS - ANALYSIS



### 3.1 INTRODUCTION

As the complex element's impulse response is not required for the synthesis of holograms by computer this method of production is very versatile. This chapter is devoted to the study of Fourier transform computer generated holograms. The restriction to Fourier transform holograms is imposed because of their particular importance. They have the following properties:

1. A lateral translation of the whole hologram produces no change in the intensity distribution of the image which remains stationary. This is a direct result of the property of the Fourier transform where translation in one space is accompanied by a linear phase shift in the other space, without affecting the modulus. This is, of course, the source of detour phase, but in the case of detour phase the translations are amongst the individual elements of the filter and not of the whole filter itself.

2. Localised disturbances in one space are distributed more or less uniformly in the other space. Hence, localised defects in the hologram due to scratches and dust particles do not result in localised blemishes in the image but rather produce a slight general loss of fidelity in the entire image.

3. If the Fourier transform is repeated a number of times side by side on the hologram, the image is not repeated, but approaches a sampled version and appears as a dot structure. This facilitates the use of detection devices such as photo-diodes and reduces interference between data elements. The repeating of the Fourier transform increases the redundancy, suppresses the speckle and increases the signal to noise ratio. Also the increased redundancy does not involve an accompanying increase in the number of detection devices in the image domain.

The Lohmann hologram is the simplest to make and as in its analysis many important characteristics of computer generated holograms are exhibited we shall study this case first.

A new class of computer generated holograms was developed recently by Severcan (Ref. 27 ) following earlier work on spectrum levelling by Chu and Goodman (Ref. 25 ).

Potentially the phase only filters which result have both high light efficiency and dynamic range. Two variations of these parity sequence filters are studied. An error



in the earlier analysis of these filters is corrected which results in a lower bound for the dynamic range.

A third phase only filter is also studied. This is the binary phase only filter (Ref. 20 ) in which the requirements of grey tone display and processing, necessary for the parity sequence filters, are relaxed as only two phase values are assigned to the  $(R \times R)$  subcells in each Fourier coefficient cell.

However, before analysing the Lohmann filter in detail we shall discuss the most important constraint on computer generated holograms - the limited number of addressable points on the display.

### 3.2 SAMPLING RATE LIMITATIONS

With the proviso of finite extent,  $\Delta X_0$ , the object distribution can be expanded as an infinite Fourier series of frequencies,  $H_n = n/\Delta X_0$ . Strictly, the Fourier series represents an infinite object distribution of periodicity  $\Delta X_0$ , so we must expect any subsequent image derived from this discrete spectrum to exhibit the periodicity  $\Delta X_0$ .

If in addition to its finite extent the object distribution is band limited, and contains  $N$  frequencies,  $n\Delta H$ , not higher than  $\frac{\Delta H}{2}$  then the Fourier series representing the object

distribution has a finite number of terms. The Whittaker-Shannon sampling theorem points out that the most efficient sampling of the object and its spectrum, in order that faithful Fourier transformations between the two spaces can be effected is when

$$H_n = n/\Delta X_0 = n\Delta H \quad 3.1$$

$$\text{i.e. } \delta H = 1/\Delta X_0 \quad 3.2$$

and hence when

$$\delta x = 1/\Delta H \quad 3.3$$

where  $\delta x$  is the sampling rate of the object. This is shown schematically in Figure 3.1.

The most efficient sampling thus occurs when,

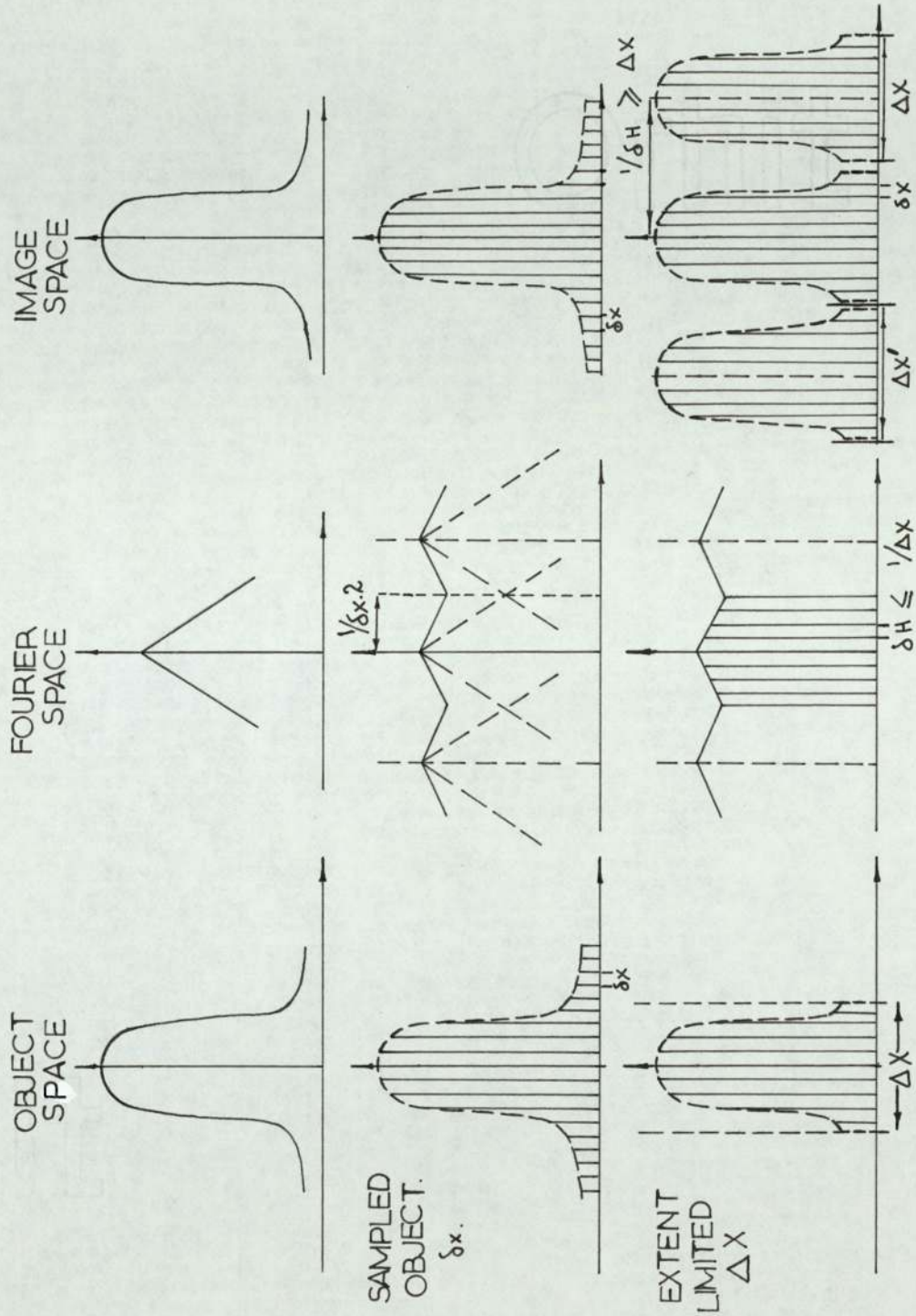
$$H/\delta h = N = \Delta X_0/\delta x \quad 3.4$$

Hence,  $\Delta H \cdot \Delta X_0 = N$

defines the minimum number of samples necessary to represent an object of extent  $X_0$  which contains no frequencies higher than  $\Delta H/2$ .  $N$  is the so called space-bandwidth product and in electrical engineering language  $\Delta H/2$  is the Nyquist frequency. In principle, then, the resolution cell size of a spatial filter,  $\delta H$ , is limited by the extent of its impulse response,  $\Delta H$ . Most holographic filters reconstruct with more than one image order. In particular, computer generated holograms, because of their square wave nature, reconstruct with many orders, see Figure 3.2.

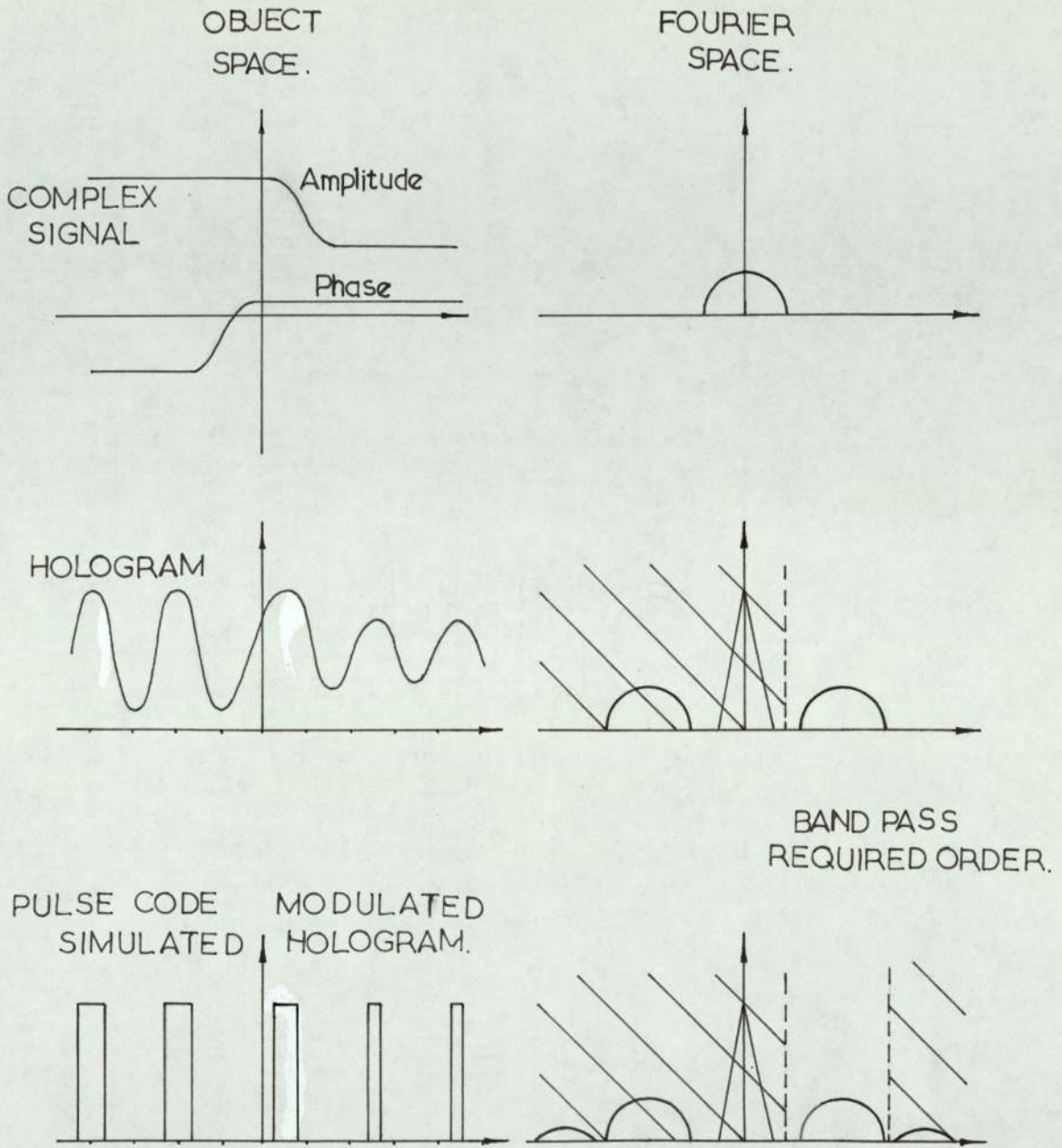
However, as the required image in the spatial filtering situation is the convolution of the filter's impulse





Sampling In Object , Fourier And Image Space

FIG .3.1



Pulse Code Modulation Of A Complex Signal,  
Showing The Associated Spectra

FIG. 3.2



response with an object distribution; and overlap (or aliasing) of the convolution of the object with different diffraction orders is to be avoided, the resolution cell size of the filter should be less than  $1/\Delta X_F$ . Specifically if the required image resolution is  $dx$ , and the object and filter impulse response is  $\Delta X_O$  and  $\Delta X_F$  respectively, the number of samples required to represent each is,

$$N_O = \frac{\Delta X_O}{dx} \quad \text{and} \quad N_F = \frac{\Delta X_F}{dx} \quad \text{where}$$

generally  $N_F \ll N_O$ .

In two dimensions, for a square object distribution of resolution equal in each direction, every resulting convolution term in the image has  $N_O^2 + N_F^2$  samples.

If there is to be no overlapping, adjacent orders should be separated by at least  $N_O + N_F$  samples. Thus, the filter must have at least  $(N_O + N_F)^2$  Fourier coefficient

cells. If there are  $R_H \cdot R_K$  subcells in each of these cells (e.g.  $R_H = 4$ ,  $R_K = 1$  for a Lee hologram) then a total of  $R_H \cdot R_K (N_O + N_F)^2$  addresses are necessary to avoid aliasing of the image orders.

### 3.3 HOLOGRAPHIC COPYING OF FILTERS

One solution to the problem of a limited number of display addresses is to holographically copy the computer generated

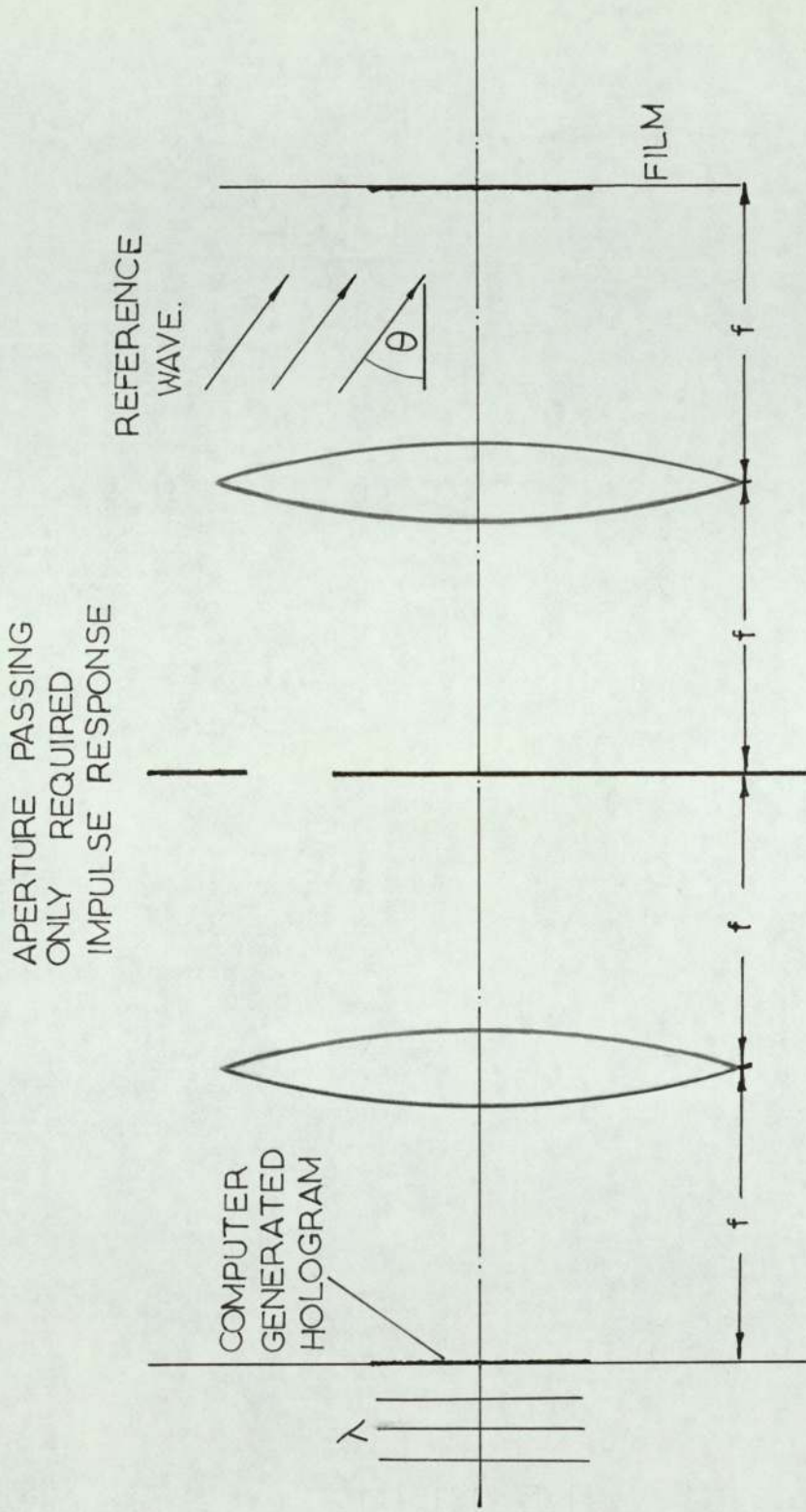
hologram. Illuminated coherently, the impulse response of the required filter is band passed and its Fourier transform recorded with an oblique reference wave, the angle of which can be adjusted to give the required resolution. The drawback to this method is that the resulting fringes are sinusoidal, and so the light efficiency is limited to that of a conventional hologram, as discussed in Chapter 1. Any dynamic range advantage of the original filter is, however, preserved. A typical holographic copying scheme is shown in Figure 3.3.

As the R.O.A.C.H. filter has only one on-axis image - the other orders being considerably attenuated - the required number of display locations,  $N_F$ , only depends on the impulse response size,  $\Delta X_F$  and the resolution  $\delta x$ . One of the two-channel phase only filters to be discussed also only needs this number of addresses. Higher space-bandwidth products are possible with these filters, but the price paid is that the grey tone display and processing is critical in both cases.

#### 3.4 LOHMANN BINARY HOLOGRAM - DIFFRACTION ANALYSIS

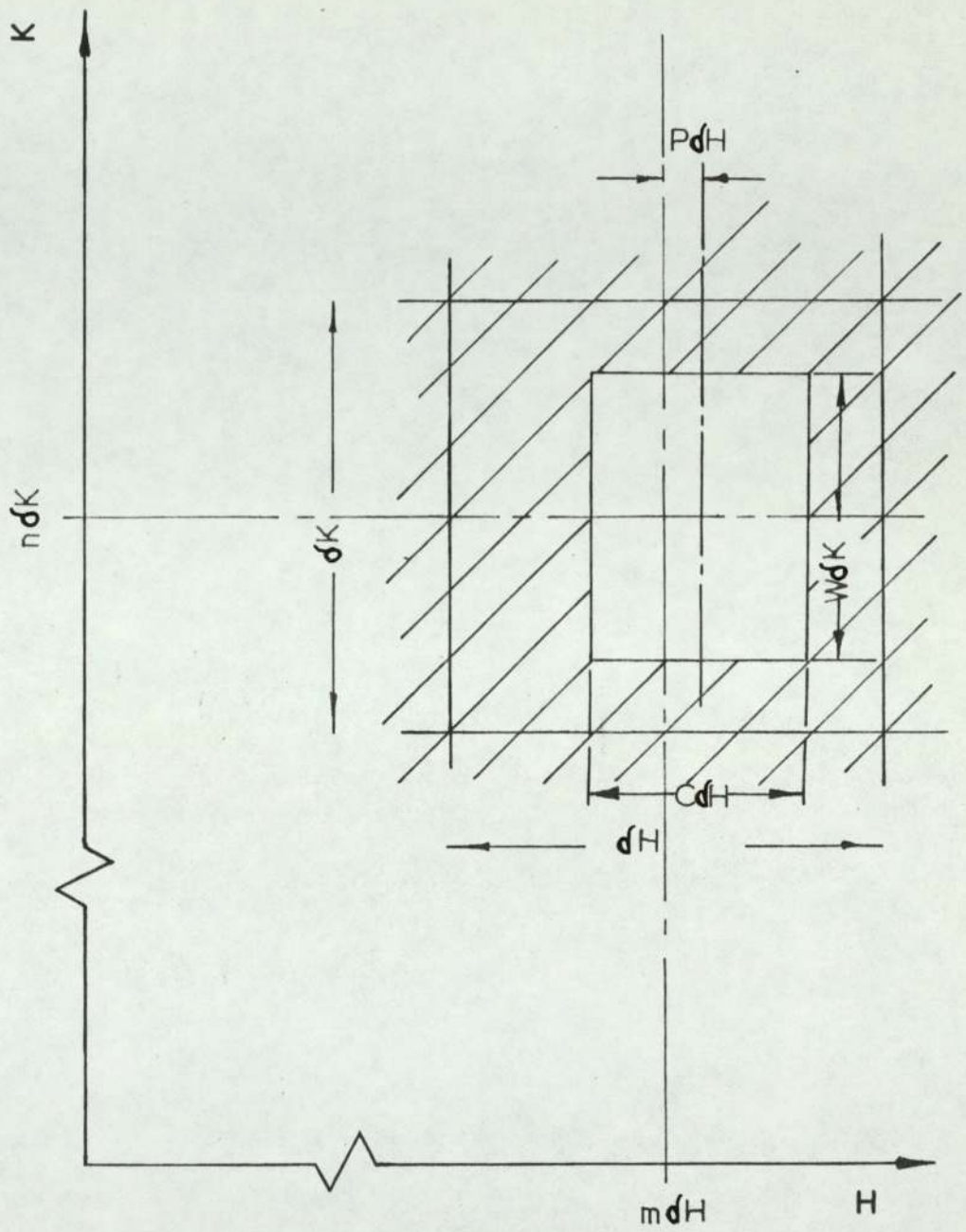
Consider the  $(m,n)^{th}$  cell, of dimensions  $\delta H \delta K$ , of a Lohmann hologram of total extent  $\Delta H \Delta K$  - as shown in Figure 3.4. If an aperture of size  $c \delta H \delta K$  is positioned a distance  $P_{mn} \delta H$  from the centre of the cell the amplitude





Holographic Copying Of A Computer Generated Spatial Filter

FIG. 3.3



Lohmann Coded Cell

FIG 3.4



transmittance of the cell is

$$F(m, n) = \text{Rect} \left\{ \frac{H - (m + P_{mn})dH}{cdH} \right\} \cdot \text{Rect} \left\{ \frac{K - ndK}{W_{mn}dK} \right\} \quad 3.5$$

The whole hologram has a transmittance

$$F(H, K) = \sum_{m=0}^{M-1} \sum_{n=0}^{N-1} \text{Rect} \left\{ \frac{H - (m + P_{mn})dH}{cdH} \right\} \text{Rect} \left\{ \frac{K - ndK}{W_{mn}dK} \right\} \quad 3.6$$

For a plane wave illuminating the hologram,

$$A(H, K) = e^{2\pi i (HX_0 + KY_0)} \quad 3.7$$

where  $(X_0, Y_0)$  is the object space point source of the plane wave the complex amplitude behind the hologram is

$$F(H, K) \cdot A(H, K) \quad 3.8$$

The Fourier transform of this complex amplitude distribution is formed in the image plane to give

$$I(x, y) = \iint F(H, K) \cdot A(H, K) e^{2\pi i (HX + KY)} dH dK \quad 3.9$$

$$\therefore I(x, y) = \int_{(m+P_{mn}-\frac{c}{2})dH}^{(m+P_{mn}+\frac{c}{2})dH} \int_{(n-\frac{W}{2})dK}^{(n+\frac{W}{2})dK} \sum_{m=0}^{M-1} \sum_{n=0}^{N-1} e^{2\pi i (H(x+Y_0) + K(y+Y_0))} dH dK \quad 3.10$$

Hence,

$$I(x,y) = \sum_{m=0}^{M-1} \sum_{n=0}^{N-1} c \delta H \delta K \operatorname{sinc}(\pi c(x+y_0) \delta H) W_{mn} \operatorname{sinc}(\pi W_{mn}(y+y_0) \delta K) \times e^{2\pi i((m+P_{mn})(x+x_0) \delta H + n(y+y_0) \delta K)} \quad 3.11$$

For illumination from a point on the X axis,  $Y_0 = 0$  and

$$I(x,y) = c \delta H \delta K \operatorname{sinc}(\pi c(x+y_0) \delta H) \sum_{m=0}^{M-1} \sum_{n=0}^{N-1} W_{mn} \operatorname{sinc}(\pi W_{mn} y \delta K) \times e^{2\pi i(m x \delta H + n y \delta K + P_{mn} x_0 \delta H + P_{mn} x \delta H + m y_0 \delta H)} \quad 3.12$$

There are thus  $2MN$  free parameters  $W_{mn}$  and  $P_{mn}$  and two constants  $X_0$  and  $C$  available. They can be adjusted so that  $I(x, u)$  is equal to the required impulse of the filter,  $I_p(X, V)$ , at least within an area  $\Delta X \cdot \Delta Y$  of the image plane. We have already discussed how the resolution and extent requirements in image space constrain the hologram resolution and extent. If the number of resolvable points is

$$N^2 = \frac{\Delta X}{\delta x} \cdot \frac{\Delta Y}{\delta y} = \left(\frac{\Delta X}{\delta x}\right)^2 \quad 3.13$$

for a square image, then at least  $N^2$  cells are needed in the hologram to reproduce the image distribution.

That is

$$\left(\frac{\Delta H}{\delta H}\right)^2 \geq \left(\frac{\Delta X}{\delta x}\right)^2 = N^2 \quad 3.14$$



and so

$$\delta H \leq \frac{1}{\Delta X} \quad 3.15$$

The equality in Equation 3.15 is the most efficient sampling condition of Whittaker and Shannon as in Equation 3.2.

If the required impulse response is  $I_p(x, y)$ , it is required to choose the available values  $W_{mn}$ ,  $P_{mn}$ ,  $Q$  and  $X_0$  such that within the region  $|x| < \frac{\Delta X}{2}$ ,  $|y| < \frac{\Delta Y}{2}$

$$I(x, y) \propto I_p(x, y) \quad 3.16$$

That is

$$\text{Rect}\left(\frac{x}{\Delta X}, \frac{y}{\Delta Y}\right) \iint F(H, K) A(H, K) \cdot e^{2\pi i(Hx + Ky)} dH dK \propto I_p(x, y) \quad 3.17$$

As we are limiting the region of interest to  $\Delta X^2$  in image space then  $I_p(x, y)$  can be expanded as a Fourier series with sampled coefficients  $\hat{I}_p(m\delta H, n\delta K)$  which can be used in the Fourier transform representation of  $I_p(x, y)$ .  
Hence

$$I_p(x, y) = \iint \hat{I}_p(m\delta H, n\delta K) e^{2\pi i(Hx + yK)} dH dK \quad 3.18$$

and

$$I_p(x, y) = \text{Rect}\left(\frac{x}{\Delta X}, \frac{y}{\Delta Y}\right) \sum_{m=0}^{M-1} \sum_{n=0}^{N-1} \hat{I}_p(m\delta H, n\delta K) e^{2\pi i (x m \delta H + y n \delta K)} \quad 3.19$$

Within the region ( $\Delta X$ ,  $\Delta Y$ )  $I_p(x, y)$  is represented as a Fourier series, Equation 3.8, the impulse response of the hologram, is almost a Fourier series and the two series could be made equal, equating term for term, if the following conditions are met,

$$1) \text{ sinc}(\pi c(x + x_0)\delta H) = \text{constant for } |x| < \frac{\Delta X}{2} \quad 3.20$$

$$2) \text{ sinc}(\pi W_{mn} y \delta K) = 1 \text{ for } |y| < \frac{\Delta Y}{2} \quad 3.21$$

$$3) e^{2\pi i (P_{mn} x_0 \delta H + P_{mn} x \delta H + m x_0 \delta H)} = e^{i\phi_{mn}} \quad 3.22$$

$$\text{where } F(m\delta H, n\delta K) = |F(m\delta H, n\delta K)| e^{i\phi_{mn}} \quad 3.23$$

$$4) W_{mn} = |F(m\delta H, n\delta K)| \quad 3.24$$

With these conditions satisfied the complex transmittance of the hologram can be controlled by the position,  $P_{mn}$ , and height,  $W_{mn}$ , of the  $M \times N$  apertures.

Condition 3 can be simplified if the illuminating point,  $x_0$  is chosen such that

$$x_0 \delta H = J \quad 3.25$$

where  $J$  is an integer. We then have



$$3) e^{2\pi i (P_{mn} \times dH + P_{mn} \times dH)} = e^{i\phi_{mn}} \quad 3.26$$

$$\text{that is } J \cdot P_{mn} + P_{mn} \times dH = \frac{\phi_{mn}}{2\pi} \quad 3.27$$

If

$$e^{2\pi i P_{mn} \times dH} = 1$$

$$J \cdot P_{mn} = \frac{\phi_{mn}}{2\pi} \quad 3.28$$

and  $P_{mn}$  directly controls the phase from the  $(m,n)^{\text{th}}$  cell into the  $J^{\text{th}}$  order.

As  $\phi_{mn}$  needs controlling over  $2\pi$  radians

$$|\phi_{mn}| \leq \pi$$

Hence  $|2\pi P_{mn} J| \leq \pi$

and

$$|P_{mn}| \leq \frac{1}{2J} \quad 3.29$$

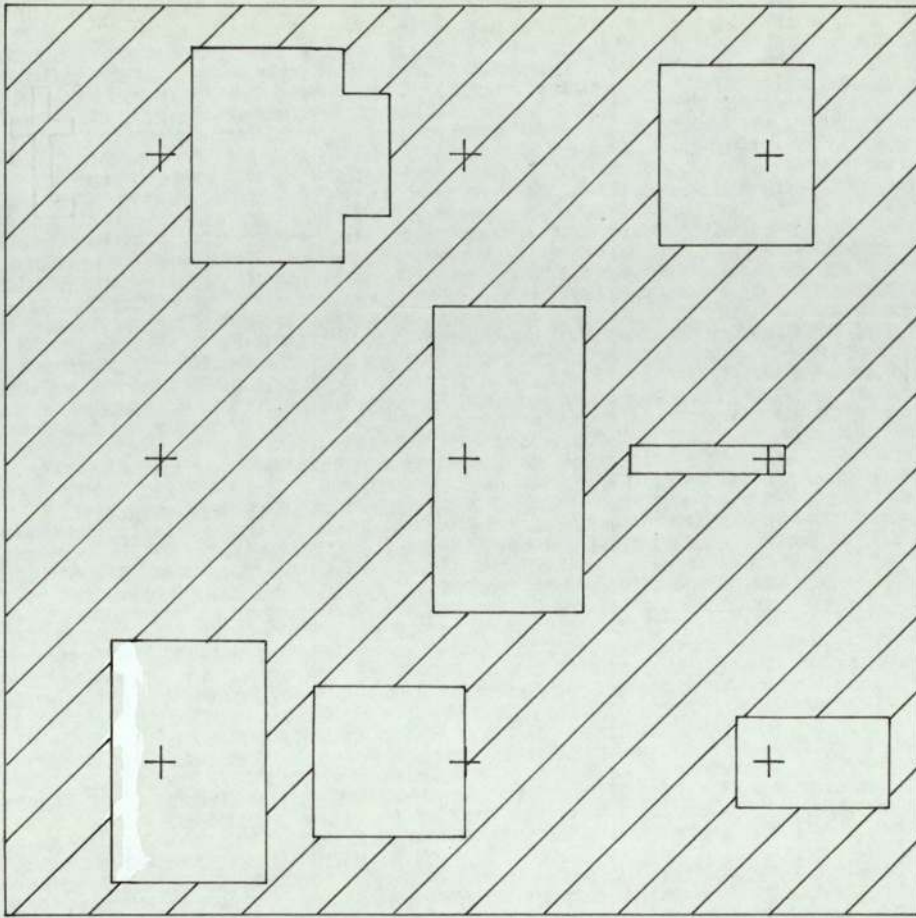
This follows intuitively from the detour phase discussion of Chapter 1. For a first order image

$$|P_{mn}| \leq \frac{1}{2} \quad \text{in order to}$$

control the phase in the region  $-\pi$  to  $+\pi$  radians. That is the aperture must be moved by  $\pm \frac{1}{2} dH$  for  $\pm \pi$  phase change.

We noted previously that this could lead to the problem of overlapping of adjacent cell apertures with a subsequent transmission error as shown in Figure 3.5. For an aperture of width  $cdH$ , in order to avoid overlap we require

$$P dH + \frac{C dH}{2} \leq \frac{dH}{2}$$



Region Of A Lehmann Filter Coded For First

Order Operation ,  $J=1$   $C=1/2$

FIG. 3.5



That is  $C \leq 1 - \frac{1}{J}$  3.30

follows from Equation 3.29.

Maximum brightness is to be expected when  $C = \frac{1}{2}$  (as  $C$  and  $1-C$  are equivalent by Babinet's principle.)

Hence, for no overlap with  $C = \frac{1}{2}$

$$J \gg \frac{1}{1-C}$$

$$\therefore J \gg 2$$

The image brightness is controlled by condition 3.20,

$$C^2 (\text{sinc}(\pi C(x+x_0)) \delta H)^2$$

On axis, at  $X=0$  this becomes

$$\left( \frac{\sin \pi C J}{\pi J} \right)^2$$

which is a maximum when

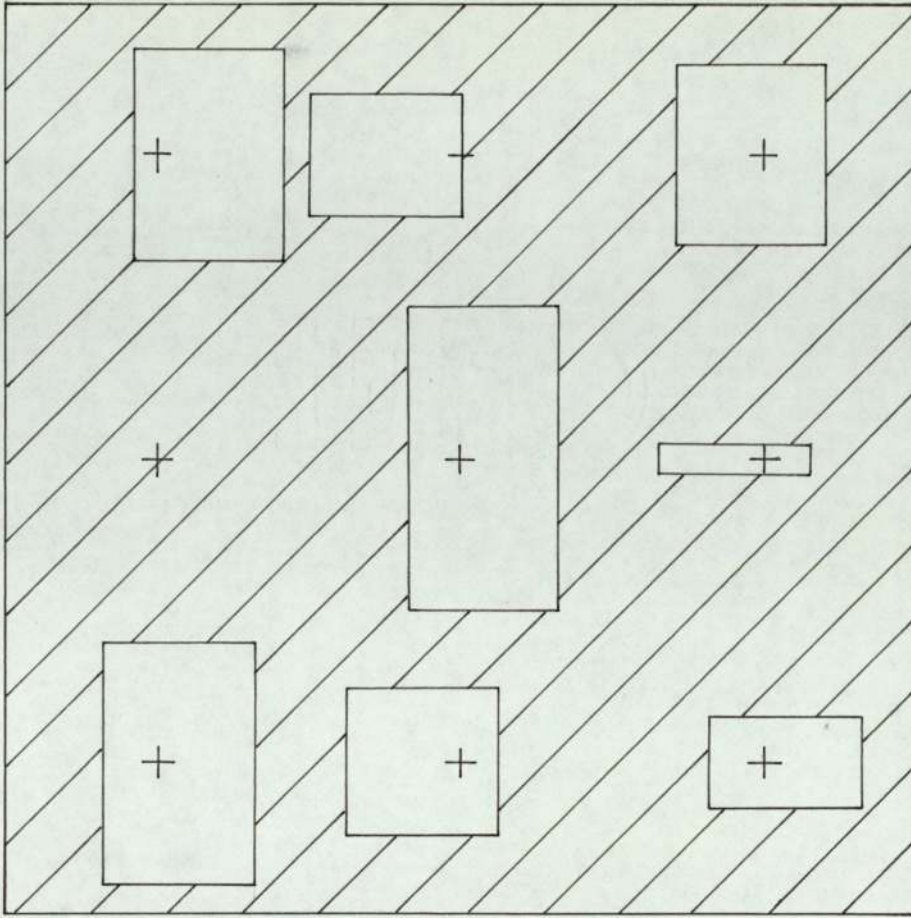
$$CJ = \frac{2k+1}{2}, \quad k = 0, 1, 2, \dots$$

The first maximum, when  $CJ = \frac{1}{2}$ , yields a brightness term

$$\left( \frac{1}{\pi J} \right)^2$$

This is maximum for  $J = 1$ .

Hence, a maximum brightness occurs when overlap error is possible with  $J = 1$  and  $C = \frac{1}{2}$ . If this is avoided by invoking Equation 3.30, and using the next available order,  $J = 2$ , the image brightness is reduced by a factor of 4. The cells of Figure 3.5 are shown again in Figure 3.6 for the same image in the  $J = 2$  order, avoiding the overlap error.



Regional Of A Lohmann Filter Coded Identically

TO Fig.3.5 , Coded For Second Order Operation

$$J=2 \quad C=1/2$$

FIG. 3.6



The first condition, equation 3.20, which controls the image brightness imposes a wide "sinc" function over the whole extent of the image. This is common to all computer generated holograms and is a result of the assumption that the sampled complex amplitude, at point  $(m\delta H, n\delta K)$ , is constant over the whole cell  $(\delta H\delta K)$ . As the width of the aperture  $c\delta H$  is reduced the "sinc" becomes broader and the approximation of Equation 3.20 improves. The brightness of the image does, however, decrease. The "sinc" function has extreme values at the edges of the image  $X = \pm \frac{\Delta X}{2}$  given by

$$\text{sinc} \left( \pi C \left( J \pm \frac{\Delta X \delta H}{2} \right) \right)$$

where we have used Equation 3.25.

As  $\Delta X \delta H = 1$  the image brightness changes over the image by the ratio of

$$\left( \frac{\text{sinc}(\pi C (J + 1/2))}{\text{sinc}(\pi C (J - 1/2))} \right)^2$$

For  $CJ = \frac{1}{2}$  the change in brightness over the first order image is 9 : 1.

In practice if the field of the image is restricted to less than  $\Delta X, \Delta Y$  the image brightness variation will be less than this.

Equation 3.21 also imposes a "sinc" over the image in the Y direction, but this varies as the height of the aperture,  $W_{mn}$ , varies. The most severe case is when  $Y = \pm \frac{\Delta Y}{2}$

and  $W_{mn} = 1$ . Then the "sinc" function drops to 0.64 of its value at  $Y = 0$ . If the heights of the apertures,  $W_{mn}$ , are all reduced this variation is also reduced. However, this will lower the image brightness and also restrict the dynamic range.

The final approximation to be considered is that of Equation 3.27 that

$$e^{2 \pi P_{mn} X d / h} = 1$$

This describes the variation in detour phase (due to an aperture offset by  $P_{mn} d$ ) as the observer moves about in the image plane.

$P_{mn}$  has the extreme values  $\pm \frac{1}{2J}$  and  $X$  can vary over the whole image plane area of interest  $\pm \frac{\Delta X}{2}$

Hence, the phase term varies by  $\pm \frac{\pi}{2J}$  across the image - a total change of  $\frac{\pi}{J}$  radians which decreases as higher image orders are used.

### 3.5 SPECTRUM SHAPING WITH PARITY SEQUENCES

The Lohmann hologram has a dynamic range restricted by the number of display addresses per cell,  $R_H \times R_K$ , and has a low coding efficiency. The Kinoform, however, has a maximum coding efficiency, requiring a single display address per cell, but suffers from poor image quality.



Although having maximum coding efficiency like the Kinoform, the ROACH has limited dynamic range due to its absorption amplitude control. Recently a technique has been developed (Ref. 26) which has high light efficiency like the Kinoform, but retains image quality. The coding efficiency is between that of the Kinoform and the Lohmann filters. The method is a development of the spectrum levelling techniques first described by Chu and Goodman (Ref. 25).

Instead of simply using the phase information which is obtained by Fourier transforming the data (for the case of a deblurring filter the data would be the impulse response - the phase of its Fourier transform being the Kinoform) a sequence of phase terms is generated which are the transform phase terms modulated by terms derived from the transform amplitudes. A particular version of this scheme was realised by Kirk et al (Ref. 34) when they obtained a phase only filter containing amplitude information modulating a phase term added to any periodic carrier. The retransformation of the resulting uniform transmittance phase only element cannot exactly reconstruct the impulse response of the filter because of the differences introduced into the original spectrum. However, it is possible to choose the phase modulating amplitude terms in such a way that the resulting image consists of the required distribution spatially separated from the distribution due to the spectrum levelling terms - the so called parity sequence. There are many ways of coding the Fourier

transform to achieve a flat spectrum and parity and data separation in the image.

If the function to be coded has a transform

$$F(H,K) = |F(H,K)| e^{i\phi(H,K)}$$

then for each Fourier space point  $(H,K)$  a complex vector can be drawn on an Argand diagram as in Figure 3.7. The radius of the circle defines the maximum value of  $F(H,K)$  and thus the dynamic range. For a Lohmann hologram there are  $R_H \cdot R_K + 1$  complex points within the circle that can be reached by the coded vector  $F(H,K)$ . These addressable points are located on  $R_K$  concentric, equally spaced circles at angular intervals of  $2\pi/R_H$  radians for a Lohmann cell of  $R_H \cdot R_K$  display points per Fourier cell.

If for each complex vector,  $F(H,K)$  one vector,  $P_1(H,K)$ , is added and another vector  $P_2(H,K)$  is subtracted, two resultant vectors  $T_1(H,K)$  and  $T_2(H,K)$  will be generated,

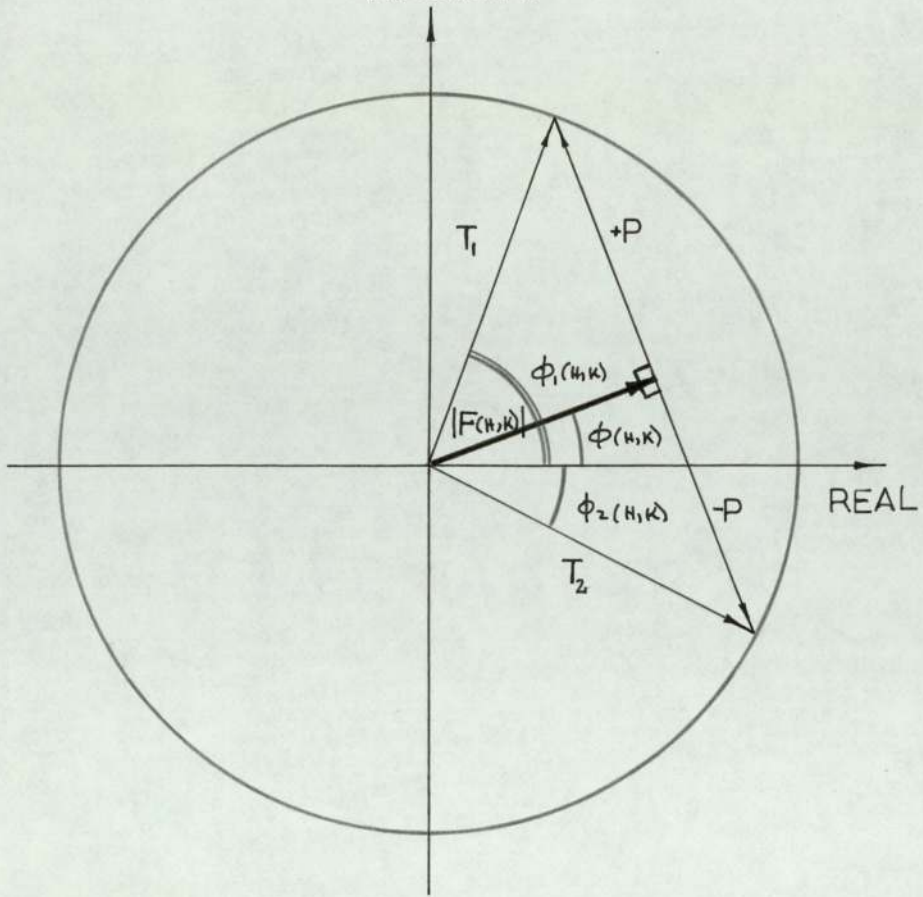
$$T_1(H,K) = F(H,K) + P_1(H,K) \quad 3.31$$

$$T_2(H,K) = F(H,K) - P_2(H,K) \quad 3.32$$

In order to convert the complex coefficients,  $F(H,K)$ , into wholly phase terms it is required that

$$T_1(H,K) = e^{i\phi_1(H,K)} \quad 3.33$$





Scheme For Spectrum Levelling With Parity Sequences

FIG 3.7

and

$$T_2(H,K) = e^{i\phi_2(H,K)} \quad 3.34$$

Hence, the vectors  $T_1(H,K)$  and  $T_2(H,K)$ , having unity (that is levelled) transmittances will reach to the circumference of the circle in Figure 3.7. Clearly there are many ways of choosing  $P_1(H,K)$  and  $P_2(H,K)$ . However, if it is desired to spatially separate the resulting Fourier transform terms of the filter transmittance,  $T_1(H,K) + T_2(H,K)$ , into data,  $f(x,y)$ , and parity,  $p(x,y)$  terms it is necessary to constrain  $P_1(H,K)$  and  $P_2(H,K)$  further.

If  $|P_1(H,K)| = |P_2(H,K)| = |P(H,K)|$  and the Fourier space parity terms are made orthogonal to the filter coefficients,  $F(H,K)$ , then this separation can be achieved with a particularly simple relationship between the terms,

$$|P(H,K)| = \left\{ 1 - |F(H,K)|^2 \right\}^{\frac{1}{2}} \quad 3.35$$

and

$$\phi_1(H,K) = \phi(H,K) \pm \cos^{-1} |F(H,K)| \quad 3.36$$

$$\phi_2(H,K) = \phi(H,K) \mp \cos^{-1} |F(H,K)| \quad 3.37$$

where each pair of signs are available for every  $(H,K)$ . The complex vector,  $F(H,K)$ , can thus be replaced by two phase only elements  $\exp(i\phi_1(H,K))$  and  $\exp(i\phi_2(H,K))$ , each of which transmits  $\frac{1}{2}$  of the total light which would be incident upon the corresponding Fourier coefficient cell.



### 3.6 PARITY SEQUENCE FILTERS

To construct a phase only filter with its spectrum flattened by parity sequence terms it is necessary to replace each Fourier space coefficient,  $F(H,K)$ , by the two phase terms of equations 3.36 and 3.37. This requirement arises because the  $2(M \times N)$  free parameters representing the modulus and phase of  $F(H,K)$  need at least  $2(M \times N)$  free parameters to code them.

The spatial parity and data separation in image space is a result of the cosine like addition of the data terms accompanied by a sine like addition of parity terms for each coded Fourier coefficient. The relative locations of the two phase elements,  $\phi_1(H,K)$  and  $\phi_2(H,K)$  determines exactly how the spatial separation will occur.

For a one dimensional Fourier sequence,  $F(H)$ , if each Fourier space cell is divided into two subcells and  $\phi_1(H)$  located in one half and  $\phi_2(H)$  located in the other, then on Fourier transforming the resulting distribution, the data terms will be multiplied by a broad cosine fringe - a period  $\propto 2/dH$  - and the parity terms will be multiplied by sine fringe of the same period. Consequently around the origin of image space the parity terms will be suppressed to zero and will only appear at the edges of the image region (which is of twice the extent of the original data field). The available image area is thus limited to the region in which the parity terms are

satisfactorily suppressed in an analogous way to the aliasing restrictions on other computer generated holograms.

An alternative scheme avoids this and removes the constraint on the image extent which can be operated upon in the deconvolution system.

If, instead of locating the phase elements,  $\phi_1(H)$  and  $\phi_2(H)$ , in adjacent subcells, they are again put into separate parallel channels, but the channels are separated by  $\Delta H$  - the extent of the data (or parity) sequence Fourier transform - then retransformation will result in high frequency cosine data and sine parity sequence fringes. The fringes in image space will have periods  $\propto 1/\Delta H$  and the data and parity terms will thus be interleaved.

The object extent which can be operated upon for deconvolution does not, in this case, determine the required filter sampling rate in Fourier space.

This is determined only by the required filter resolution.

Both types of parity, phase only filters, which require grey tone display and careful processing, have been realised by Severcan (Ref. 26), for both deblurring and matched filtering operations. The second type of parity filter described above involves diffracting the object



spectrum into two separate channels. This can be achieved using a suitable grating but does result in the light efficiency being limited due to the 1st order diffraction efficiency of a practical grating being  $< 50\%$ .

### Dynamic Range

The dynamic range, defined as the ratio of maximum to minimum amplitude transmittance depends on how finely the phase can be controlled. This in turn is limited by the number of available intensity display levels. If  $N_p$  display intensities are available then the smallest change in phase,  $\delta\phi$ , that can be produced is  $2\pi/N_p$  radians. Severcan (Ref. 26) calculated the resulting dynamic range to be  $8/\delta\phi^2$  with a value of  $\approx 2000$  for a display of  $N_p = 100$  intensity levels. However, such a dynamic range can only be achieved if a phase error is associated with the Fourier coefficient being coded.

With reference to Figure 3.8. The smallest change in  $F(H,K)$  is  $\delta F$  and occurs when either  $T_1(H,K)$  or  $T_2(H,K)$  changes by  $|\delta\phi|$ . The resulting complex vector, however, is shifted in phase by  $\phi_\epsilon$  as well as in amplitude by  $\delta F$  and becomes

$$(|F(H,K)| + \delta F) e^{i(\phi(H,K) + \phi_\epsilon)} \quad 3.38$$

In order to preserve the phase of the Fourier coefficient





$F(H,K)$  while changing its modulus both phase only channels must be shifted by  $\delta\phi$  at the same time.

\* For a wholly real component,

$$\phi(H,K) = 0 \quad 3.39$$

and

$$\phi_1(H,K) = \pm \cos^{-1} |F(H,K)| \quad 3.40$$

$$\phi_2(H,K) = \mp \cos^{-1} |F(H,K)|$$

If both  $\phi_1$  and  $\phi_2$  are shifted in phase by the quantised amount  $\delta\phi$  - resulting in a change in the modulus of  $F(H,K)$  of  $\delta A$  - then if

$$\begin{aligned} \phi_1' &= \phi - \delta\phi, \\ \phi_1' &= \cos^{-1} |F + \delta A| \end{aligned} \quad 3.41$$

Hence,

$$\cos \phi_1' - \cos \phi_1 = \delta A \quad 3.42$$

Expanding the left hand side and simplifying gives

$$\delta A = \sin \phi_1 \sin \delta\phi - 2 \cos \phi_1 \sin^2 \frac{\delta\phi}{2} \quad 3.43$$

When  $\phi_1 = \delta\phi$ ,

$$\delta A = \sin^2 \delta\phi - 2 \cos \delta\phi \sin^2 \frac{\delta\phi}{2}$$

and for small values of  $\delta\phi$ ,

$$\sin^2 \delta\phi \approx \delta\phi^2$$

and  $\cos \delta\phi \approx 1$  giving

$$\delta A \approx \delta\phi^2/2 \quad 3.44$$

Hence, the modulus of a Fourier coefficient can be changed while keeping its phase constant in steps of  $\frac{\delta\phi^2}{2}$  - a reduction of  $4x$  in the dynamic range calculated by Severcan, (Ref. 26).

The addressable locations of the Lohmann hologram, like those of the sandwich type holograms (including ROACH) are uniformly distributed in the complex plane. Equation 3.43 shows that this is not true of the parity sequence filters as the dynamic range,  $1/\delta A$ , is a function of  $\phi_1$  as well as  $\delta\phi$ . It should be remembered that in deriving equation 3.43 it was assumed  $\phi(H,K) = 0$ . Hence,  $|\phi_1| = |\phi_2| = \cos^{-1} |F|$ . The dynamic range thus varies with  $|F|$  and the value calculated above is a maximum - achieved by putting  $\phi_1 = \delta\phi$ . This occurs for values of  $F \approx 1.0$ . The minimum value of dynamic range is when  $\delta A$  is a maximum and  $|F|$  is  $\approx 0$ . It can be calculated by putting  $\phi_1 = \frac{\pi}{2}$  in Equation 3.43.

Then 
$$\delta A_{\max} = \sin \delta\phi$$

Hence, for small values of  $\delta\phi$

$$\delta A_{\max} \approx \delta\phi$$

and the minimum dynamic range is

$$\frac{1}{\delta A_{\max}} \approx \frac{1}{\delta\phi} \quad 3.45$$



The dynamic range thus changes by a factor of  $2/\delta\phi$  over the complex plane.

Again, for  $\delta\phi = 2\pi/100$  the minimum dynamic range has a value of  $\approx 17$  and changes by  $\approx 28x$  across the complex mapping plane.

It is not always desirable to have equally spaced quantization levels. Powers and Goodman (Ref. 35) have shown that the reconstruction error rates for a holographic state may be minimised by particular schemes for the bounds of the quantization levels.

For the deconvolution system it is desirable to have fine quantization in the regions of highest transmittance and this is automatically achieved by the parity schemes discussed above. This is analogous to the technique of companding of data in communication systems for more efficient use of available addresses during pulse code modulation (Ref. 36).

For a generalised detour phase hologram (Ref. 47) the subcells are not constrained to opening in sequence. The result is that many more addressable points are made available in the complex plane. Each addressable point is reached by the complex summation of up to  $R_H \cdot R_K$  complex vectors - each of maximum length  $1/R_H R_K$ . Severcan (Ref. 26) considered a binary phase version of this generalised detour phase hologram in which each subcell

has associated with it both a detour phase, due to its relative position in the cell, and also a local phase - restricted to two values, 0 or  $\pi$  radians, to relax the processing constraints.

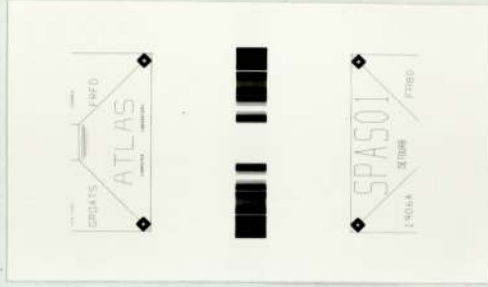
As each of the  $R_H \cdot R_K$  subcell can have 2 phase values there are in this case  $2^{R_H \cdot R_K}$  available addressable points, again reached by the complex addition of vectors of transmittance  $1/R_H \cdot R_K$ . In this case, however, as all subcells transmit, the summation is over all  $R_H \cdot R_K$  subcells for each addressable point. In general some addressable points will be located by several different summations and the total number of separate points in the complex plane will be less than  $2^{R_H \cdot R_K}$ . A computer search is required to map these complex points, and the routes required to reach them must be stored in order to be able to address a given complex transmittance to the nearest available complex location.

As for the case of the parity phase filters, it is misleading to define the dynamic range only in terms of the smallest available change in amplitude transmittance as this will generally be accompanied by an associated phase change.

### Conclusions

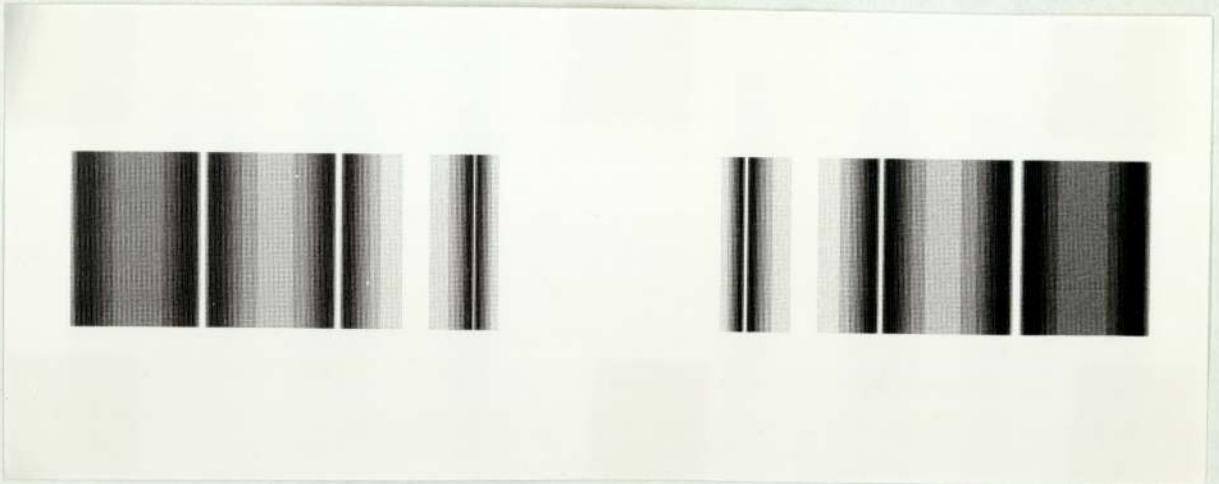
The Lohmann hologram is the simplest to generate, two examples are shown in Figures 3.9 and 3.10 for first and





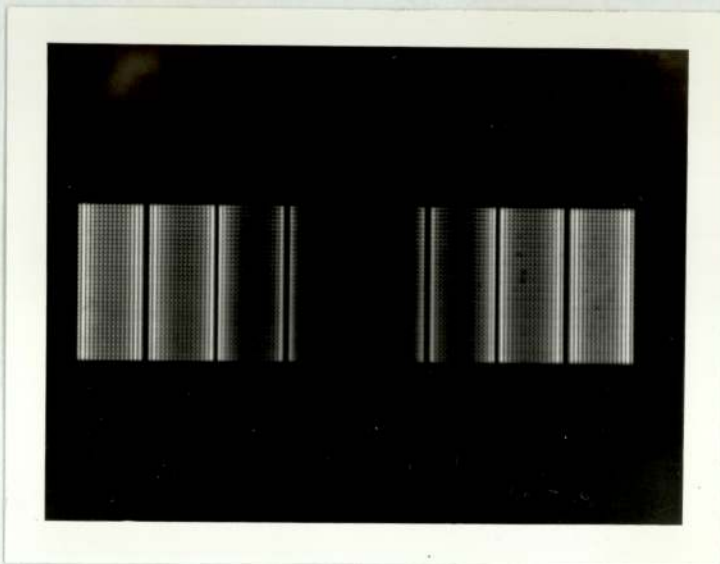
Negative of Lohmann Linear Motion  
Deblurring Filter. Full Size. (by FR80).

$$J=1 \quad C=\frac{1}{2}$$



Detail of Above.

FIG3.9



Positive Of Lohmann Linear Motion  
Deblurring Filter (by Graphplotter)  
Enlarged.

$$J = 2 \quad C = \frac{1}{2}$$

FIG3.10



second order linear motion deblurring filters ( $\beta = 1000$ ). Figure 3.9 was produced using a microfilm plotter writing directly onto 35 mm film and consists of 641 cells across the  $\pm 4$  side lobes of the filter with a dynamic range of 20 giving an image order separation of  $\approx 20$ mm. Clearly to operate with this filter on an object of extent larger than a few mm would be holographically copied.

Figure 3.10 is a positive of a photoreduction of a filter drawn by graphplotter. This realises 129 cells across the whole filter with a dynamic range of 30. For the deblurring filter, as detour phases of  $+\pi$  and  $-\pi$  are identical the adjacent cell overlap problem can be avoided by suitable choice of the phase shifts at the poles of the filter.

The impulse response of the filter produced on the Atlas Computer Laboratories' FR80 Microfilm plotter, Figure 3.9, is shown in Figure 3.11 along with a microdensitometer tracing of its distribution.

The phase only filters - particularly the two channel parity phase device which circumvents the image overlap problem - look attractive because of their potentially high dynamic range. Even the reduced value calculated is a large overall increase compared with that of the Lohmann filter. The price paid for this is the difficulty of continuous tone control and, for the <sup>two</sup> channel parity device, the difficulty of satisfactorily locating the two

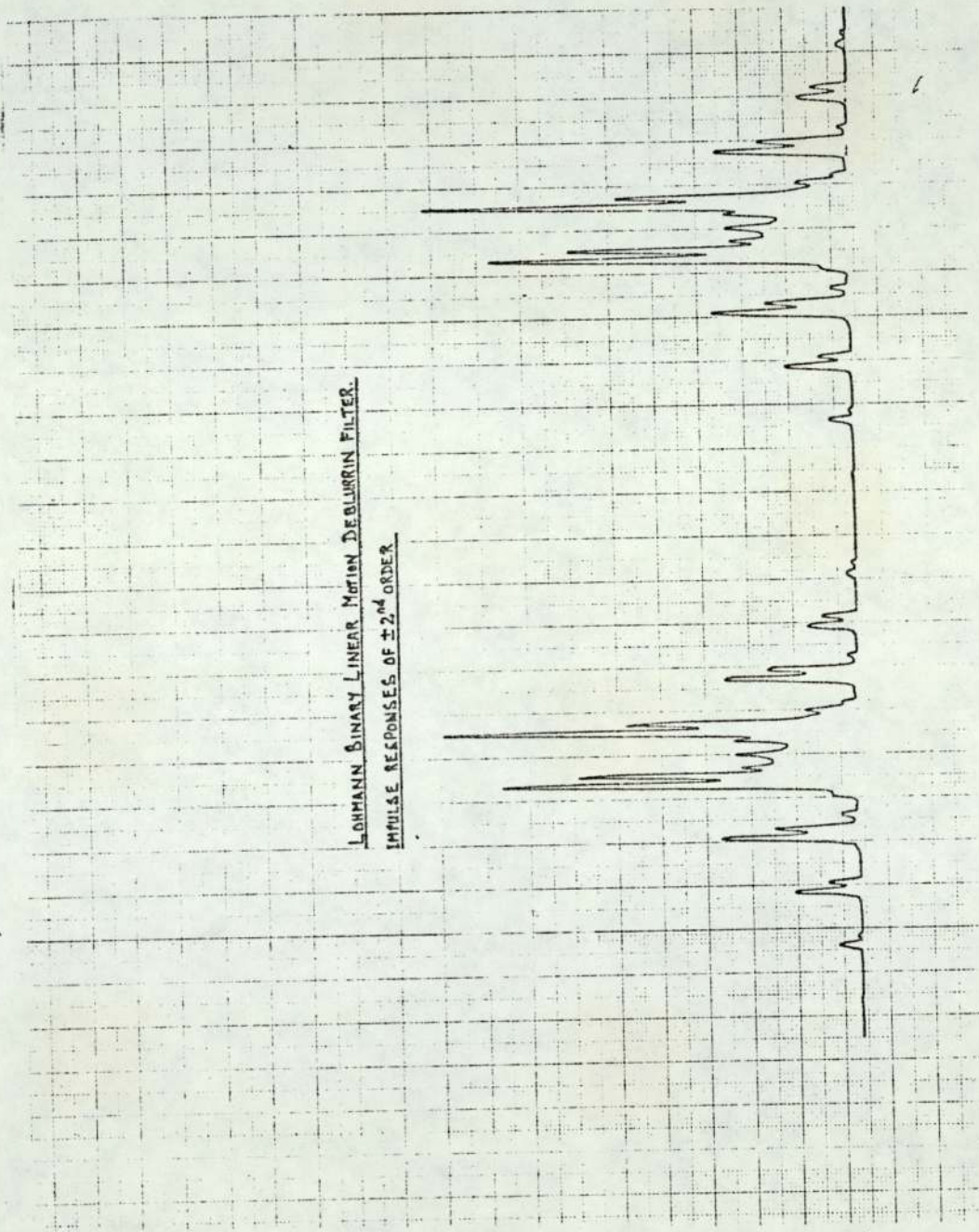


FIG 3.11



diffracted Fourier space channels and of detecting the resulting data amongst the parity terms of the images. It is possible with the parity filters to trade-off some of the perfect image fidelity by reducing the number of available quantization levels, and so gain an increase in the amount of light scattered to each data point.

This is achieved by putting

$$\phi_1(H,K) = \phi(H,K) \pm \cos^{-1} \left[ \frac{|F(H,K)|}{D} \right]$$

$$\phi_2(H,K) = \phi(H,K) \mp \cos^{-1} \left[ \frac{|F(H,K)|}{D} \right]$$

where  $D$  is a constant and the term

$$\cos^{-1} \left[ \frac{|F(H,K)|}{D} \right] \quad \text{is suppressed to zero if}$$

$$D < |F(H,K)|$$

When  $D = |F|_{\max}$  ( $= 1$ ) maximum fidelity of the data is obtained, but a considerable amount of light may be diffracted towards the parity terms. As  $D$  tends to zero more light is diffracted to the data terms at the expense of the parity terms, until the limiting case of  $D = 0$  is reached when maximum efficiency and minimum fidelity is obtained. The hologram is then simply a Kinoform.

The generalised detour phase holograms (both binary absorption and phase only) require many subcells per Fourier coefficient and are thus not as efficiently coded as a Kinoform or ROACH.

However, for the same number of subcells as a Lohmann coded hologram, although the coding efficiency is the same, the generalised detour phase holograms achieve finer complex quantization.



CHAPTER 4

COMPUTER SIMULATION OF A COHERENT OPTICAL SPATIAL  
FILTERING SYSTEM

#### 4.1 INTRODUCTION

In an earlier chapter we studied, by computer simulation, the effects of random processes on the deconvolution operation. The filters used were LMSE constrained. In this chapter we present the results of a more general computer simulation of a coherent deconvolution system. In particular we look at the effects of the filter being computer generated and hence being of limited and quantised dynamic range.

A prerequisite for deconvolution is a knowledge of the blurring function or its optical transfer function, (OTF). In some cases the degrading system is available and direct measurements of the OTF can be made, Nathan (Ref. 37 ). In cases where there are zeros in the OTF the Fourier transform of a blurred image may allow these zeros to be found, provided the noise level is low enough. Along with any exhibited symmetries this can be used to identify the OTF if it is one of the common forms, e.g. linear blur



or defocus, Gennery (Ref. 38 ). Other techniques have also been suggested for determining the form and degree of degradation, Huang et al. (Ref.39 ), by taking measurements of the blurred image.

#### 4.2 OPTICAL TRANSFER FUNCTION ERROR IN BLUR EXTENT

With this OTF recognition problem in mind simulation results are presented showing the effects of deconvolving a linear blur for the situation in which the filter is not matched exactly to the degree of blurring. The one dimensional variable frequency bar chart used in the simulations in Chapter 2 was again used as the unblurred object, Figure 4.1. As no noise was present in the object data the perfect "inverse-sine" deconvolution filter was used. The bar chart was convolved with rectangle functions of varying extents to simulate linear motion blurs of different degrees - as would result from taking photographs with different exposure times of an object executing linear motion. The filter used was the ideal filter for a linear blur of 8 units (in units of  $X_0/256$ ). The bar chart object was blurred by different amounts,  $b = 2$  units to  $b = 16$  units in integer unit steps and the resulting distributions Fourier transformed by F.F.T., operated upon by the  $b = 8$  filter and inverse transformed and displayed. The results are presented in the form of the recovered deconvolved images Figures 4.2 to 4.5. There are several points worth noting.

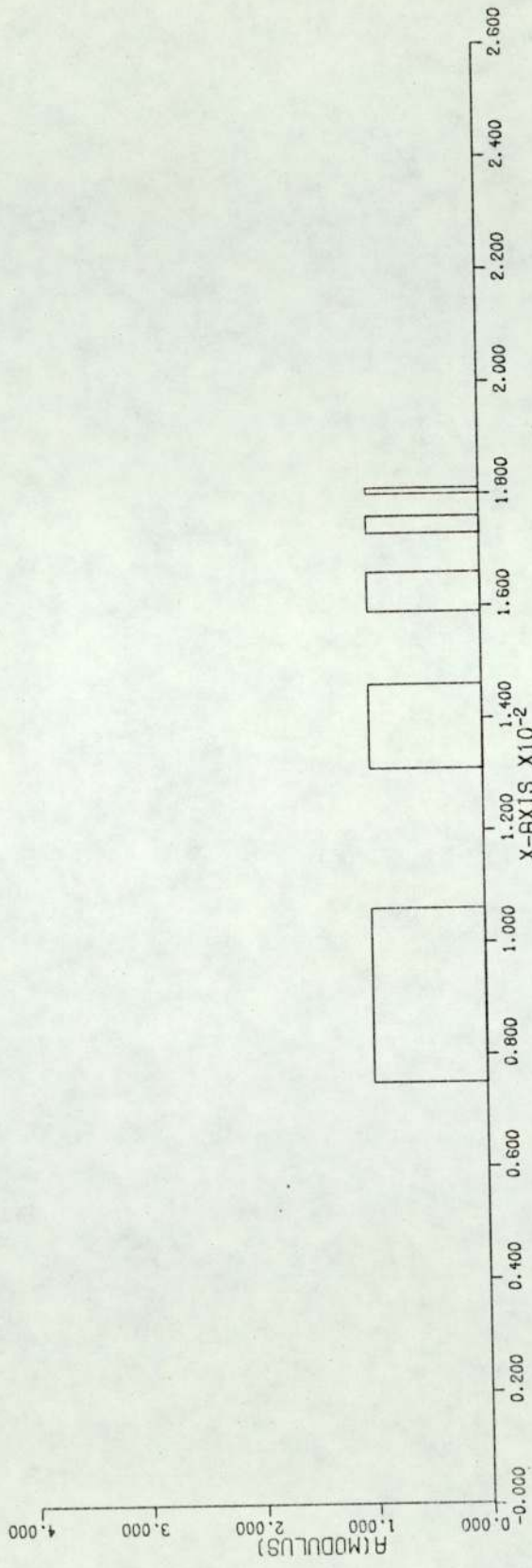


FIG 4.1



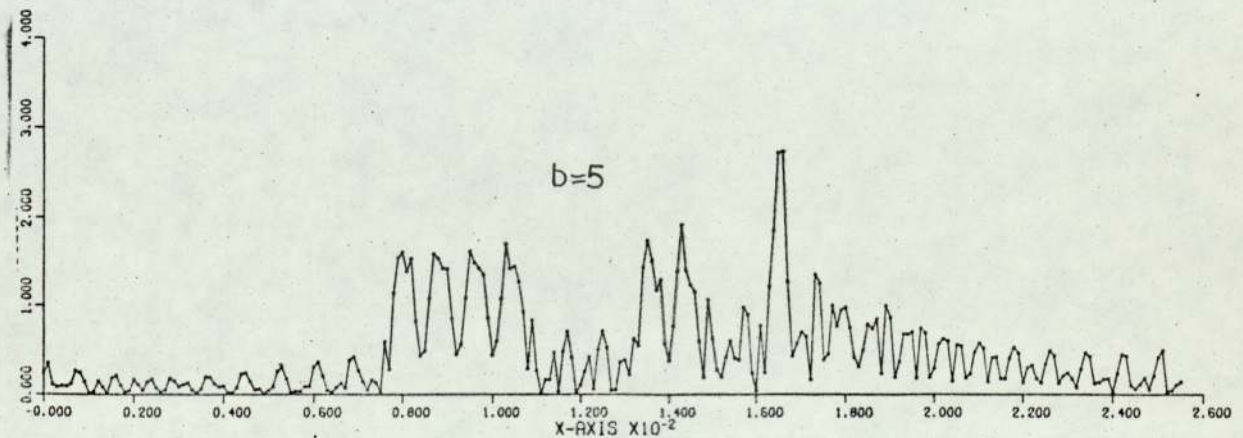
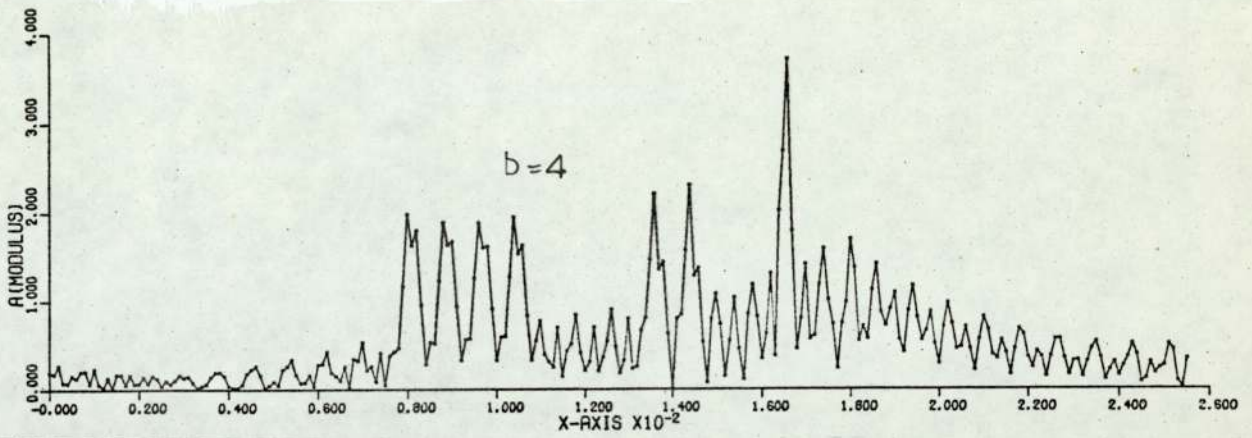
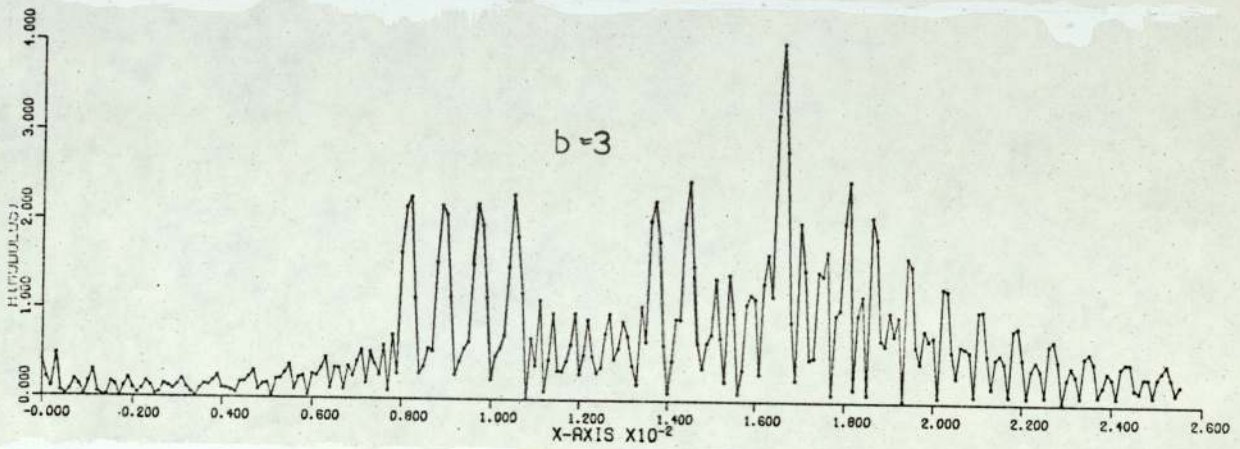
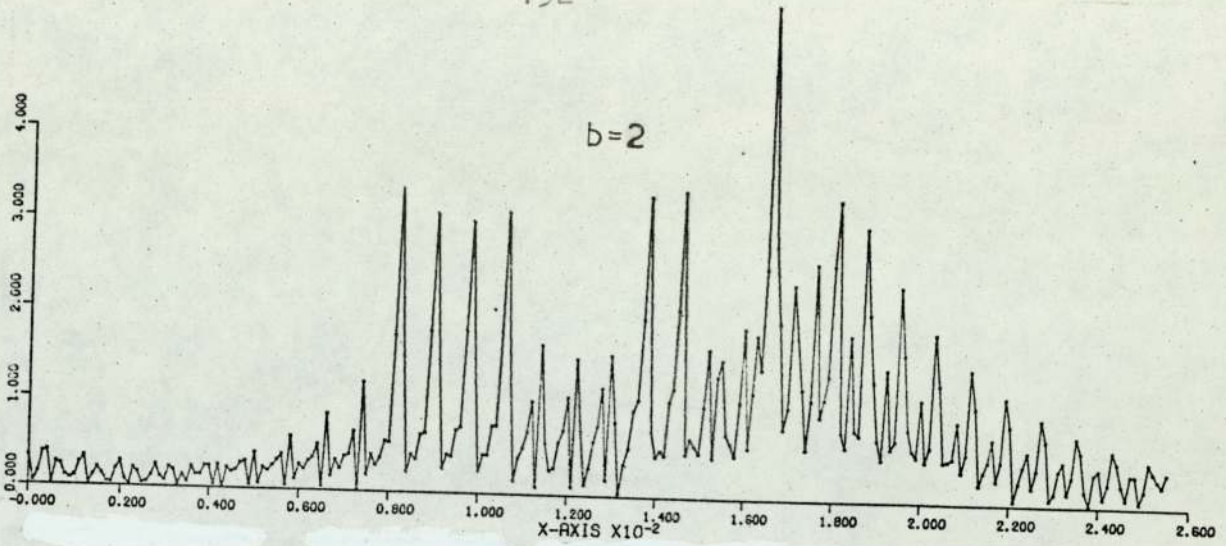


FIG 4.2

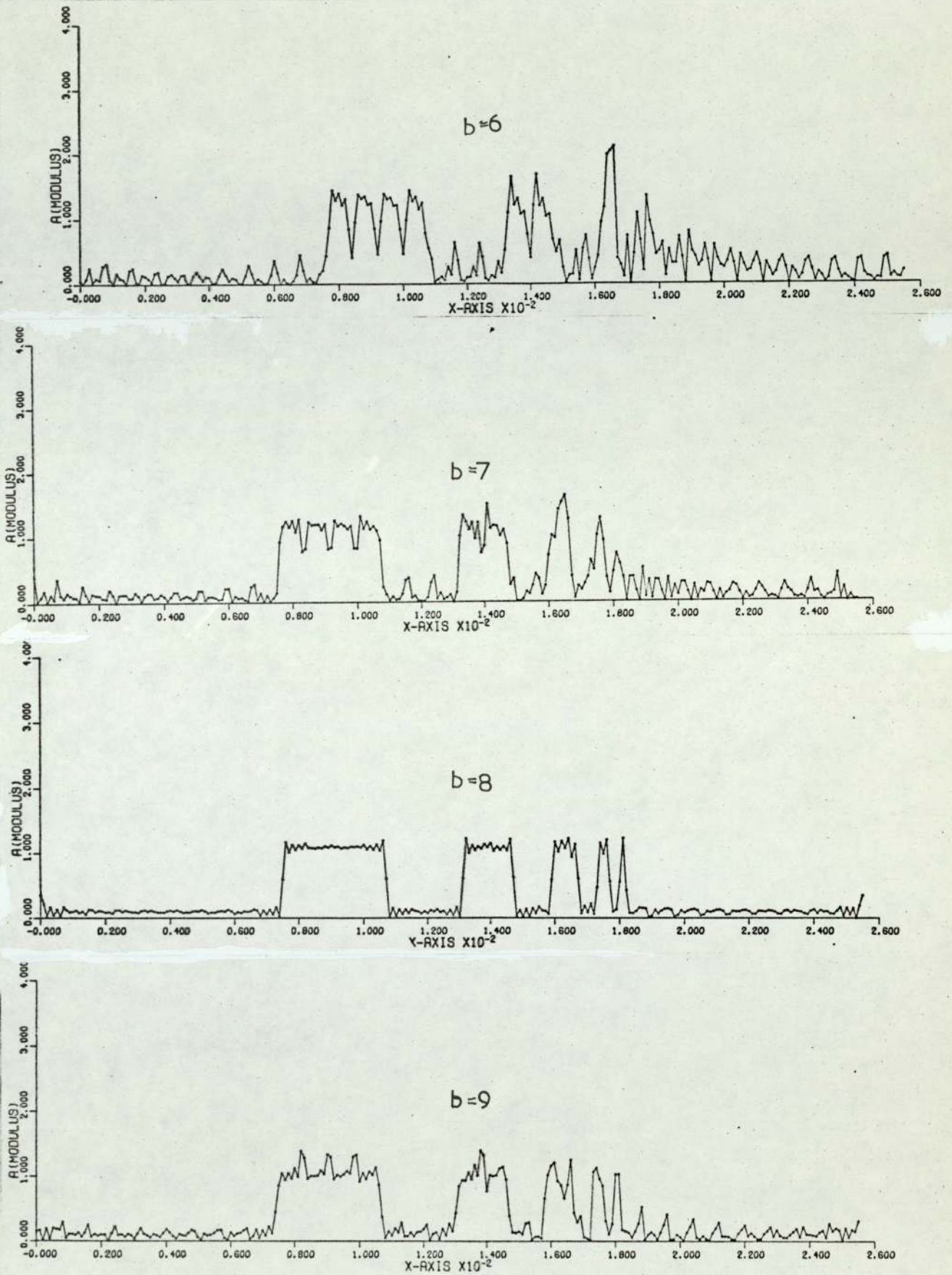


FIG 4.3



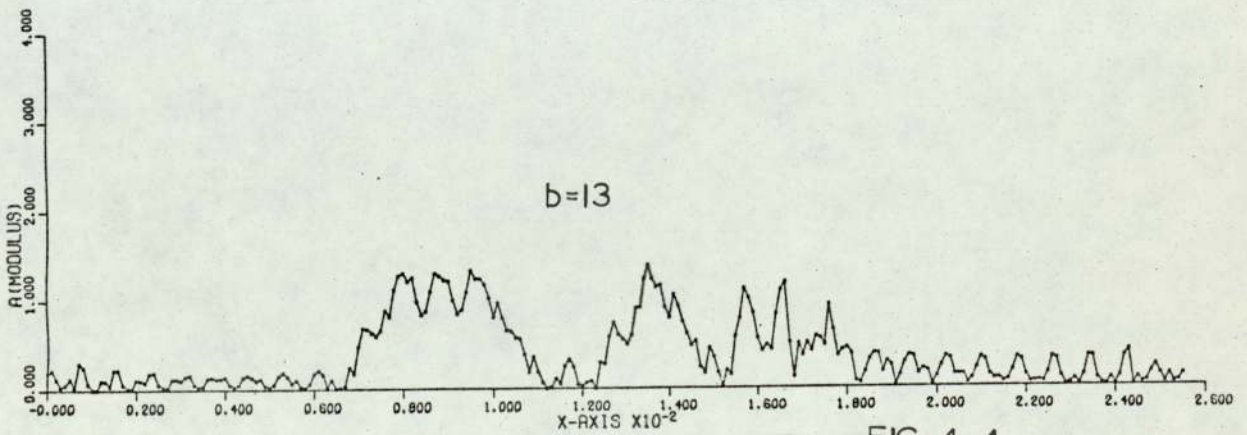
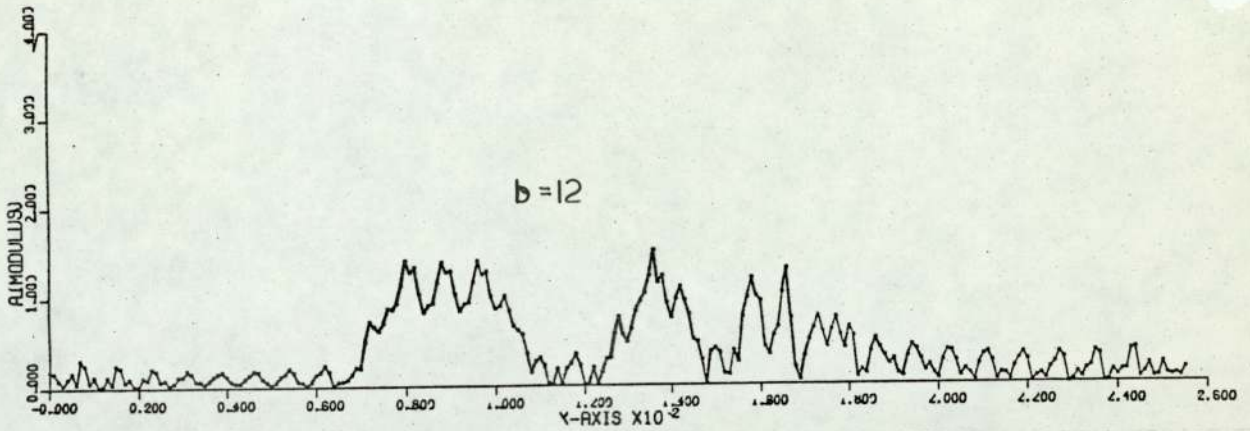
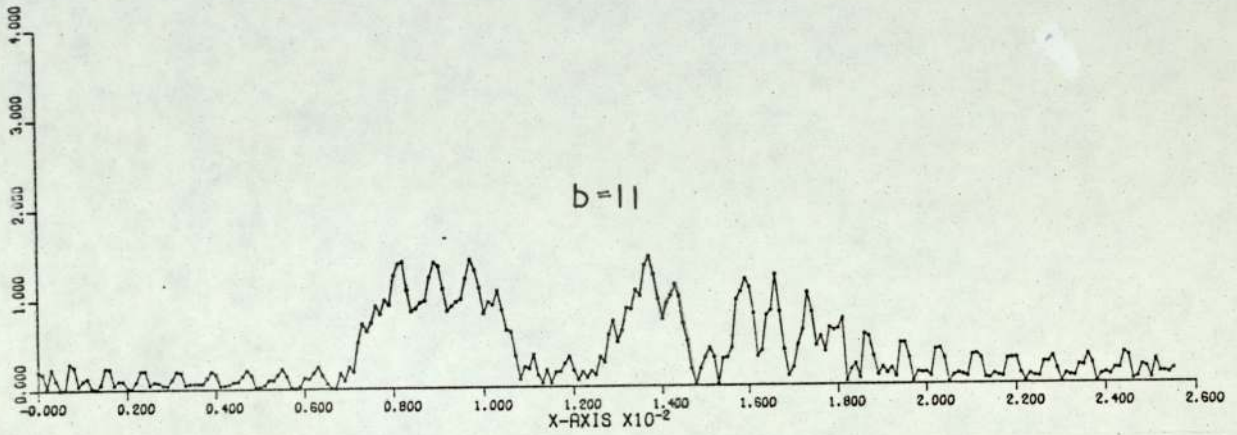
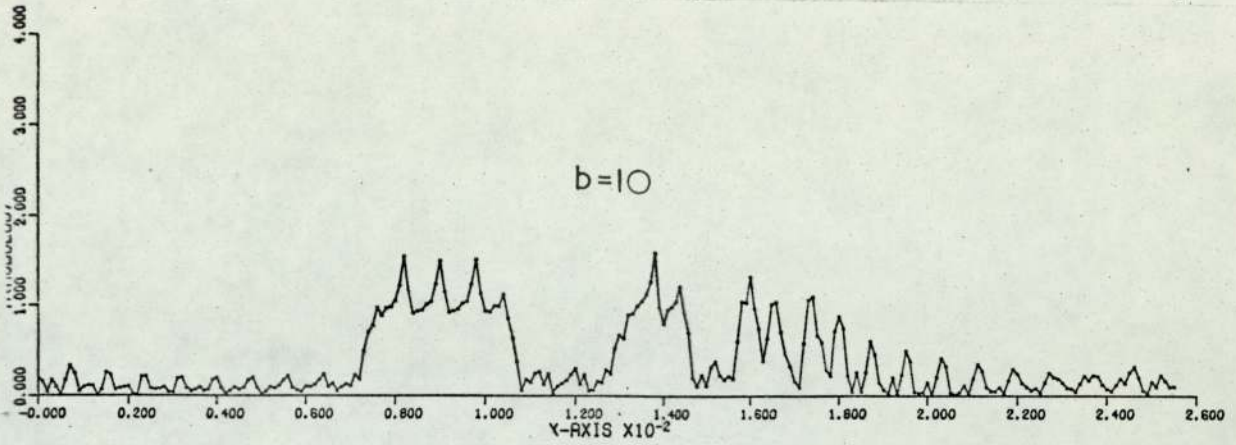


FIG 4.4

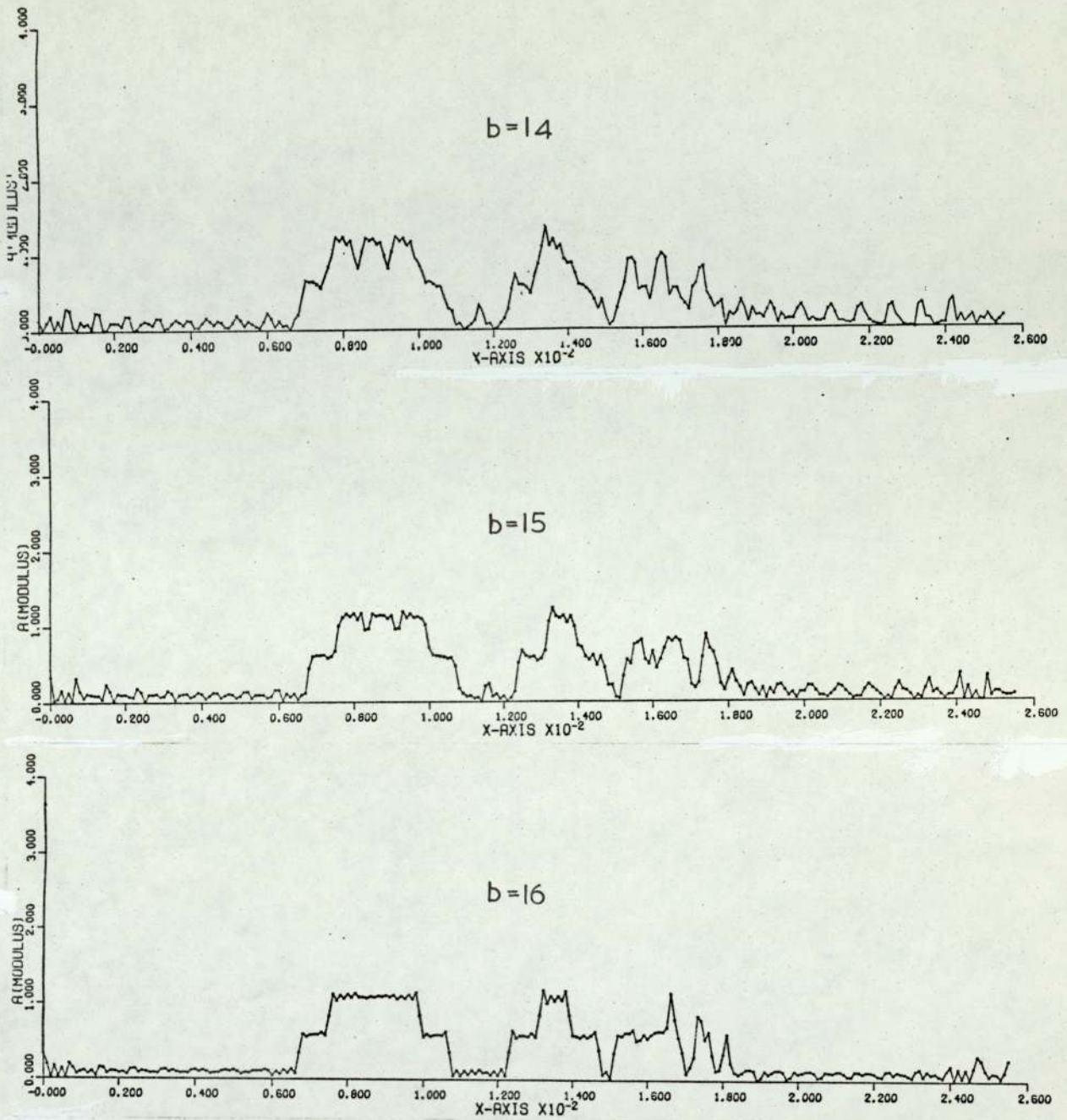


FIG 4.5



### 4.3 RESULTS OF COMPUTER SIMULATION

The maximum tolerable error in matching the filter to the degree of blur,  $b$ , is one unit if the highest frequency information is to be recovered - see Figure 4.3.

One noticeable feature of the images is the general difference between the recoveries for  $b < 8$  and  $b > 8$ . The former are far noisier than the latter which also show a lack of sharp edges at the bars. The reason for this is not difficult to discover. The number of positive frequency side lobes of the OTF describing the linear blur is equal to half the blur extent,  $b$ . For a blur of  $b = 8$  there are thus the 4 side lobes shown in Fig. 1.6. As the blur extent increases the correcting filter must realise more side lobes and thus operate with a larger dynamic range. A filter designed for a smaller blur than is present in the object will thus not enhance the high frequencies sufficiently, as shown in the Figures for  $b > 8$ . In contrast, for a blur,  $b < 8$ , the filter will over amplify the high frequencies and produce a noisy image. This is not the only effect however, as the filter will also produce erroneous phase corrections in the spectra of the blurred charts. The recovered image for blur  $b = 16$  units exhibits a greater degree of sharpening than do other images with  $9 < b < 16$ . This is because although the amplitude is not amplified sufficiently at high frequencies, half

of the total spectrum is, in fact, phase shifted correctly by the  $b = 8$  filter, as every filter pole coincides with every other zero of the OTF of the blur. As a measure of the goodness of recovery of the images, variances were calculated for each degree of blur. That is, each recovered image point was subtracted as an amplitude from its corresponding object point, the result squared and the squares summed across the image extent and normalised to form,

$$\text{Variance, } V(b) = \frac{1}{N} \sum_{x=0}^{N-1} (s_b(x) - c_b(x))^2 \quad 4.1$$

for  $b = 1$  to  $19$ ,

where  $b$  is the extent of the blur in units of  $X$ . The resulting curve of  $V(b)$  as a function of  $b$  is shown in Figure 4.6. The trend of a reduction in variance with increasing blur due to insufficient high frequency amplification by the filter is clear. The slight image recovery of Figure 4.5 for a blur,  $b = 16$ , is also apparent as a secondary minimum of variance.

#### 4.4 LATERAL MISREGISTRATION OF THE FILTER ELEMENT

Although in a Fourier transform system both the image position and its intensity are invariant to translations of Fourier plane elements, for a deblurring operation the filter still has to be aligned to register correctly with the diffraction pattern being operated upon. Figures 4.7 to 4.8 are the computed deblurred images of a linear



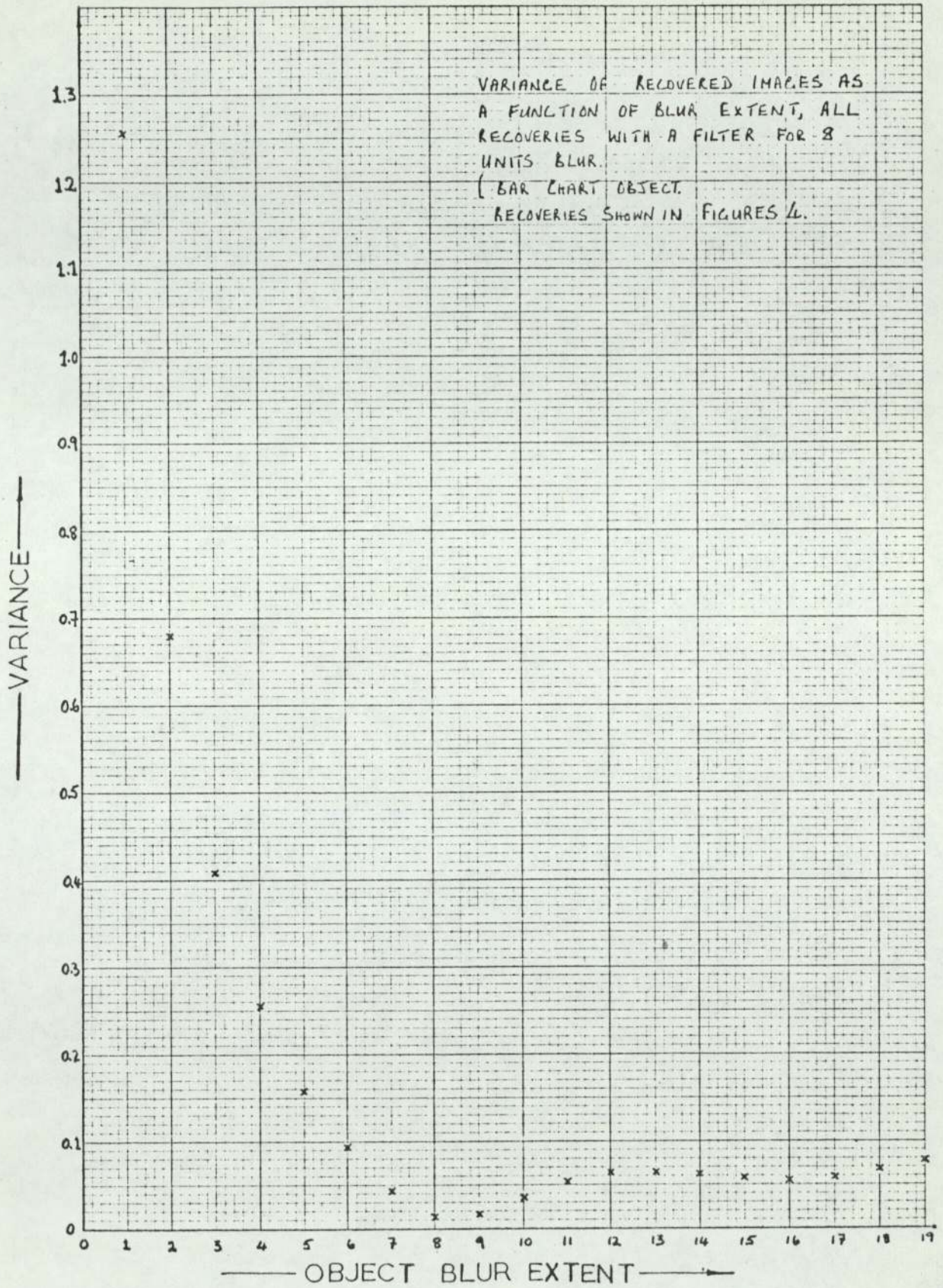


FIG 4.6

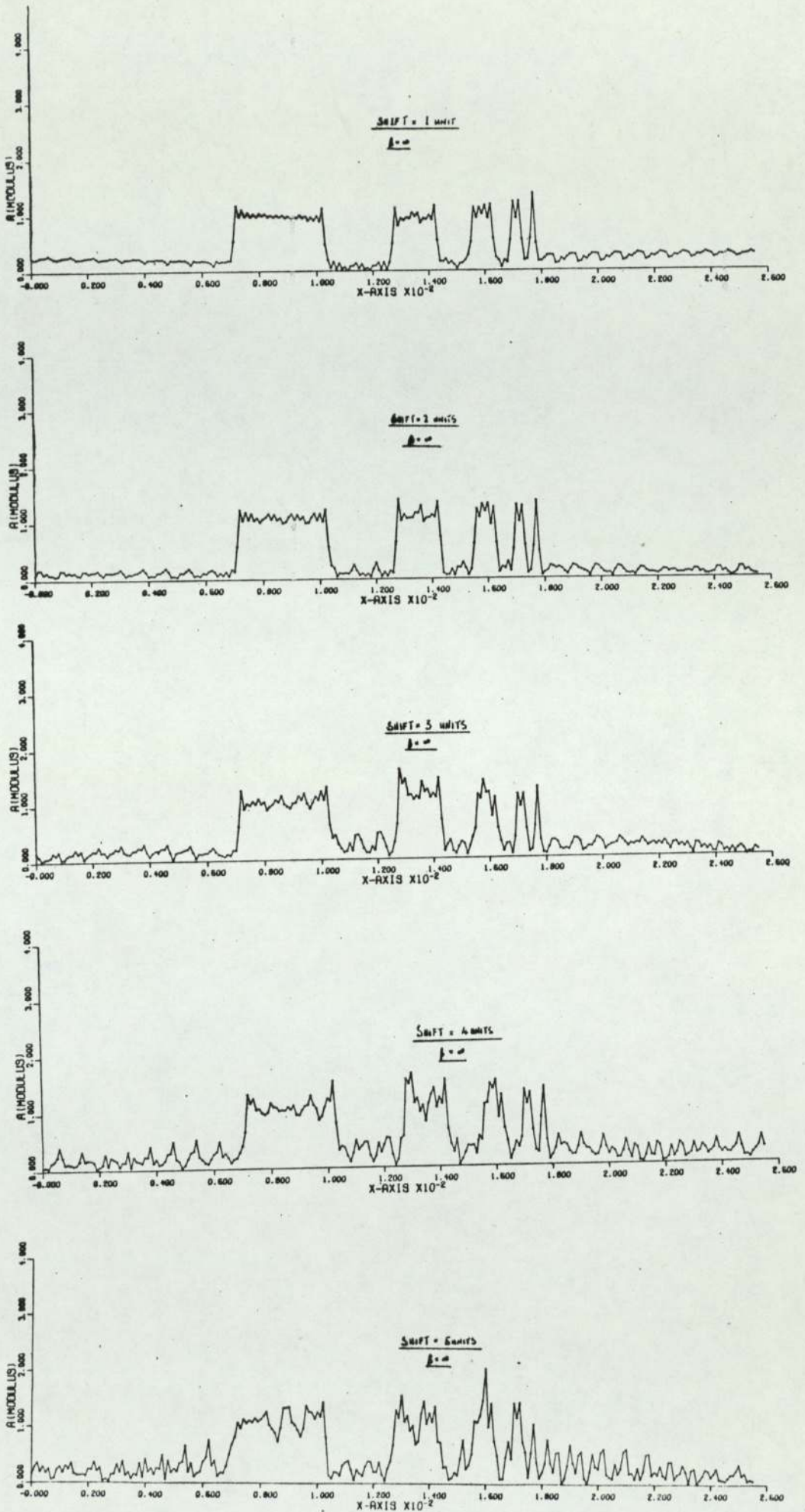


FIG 4.7



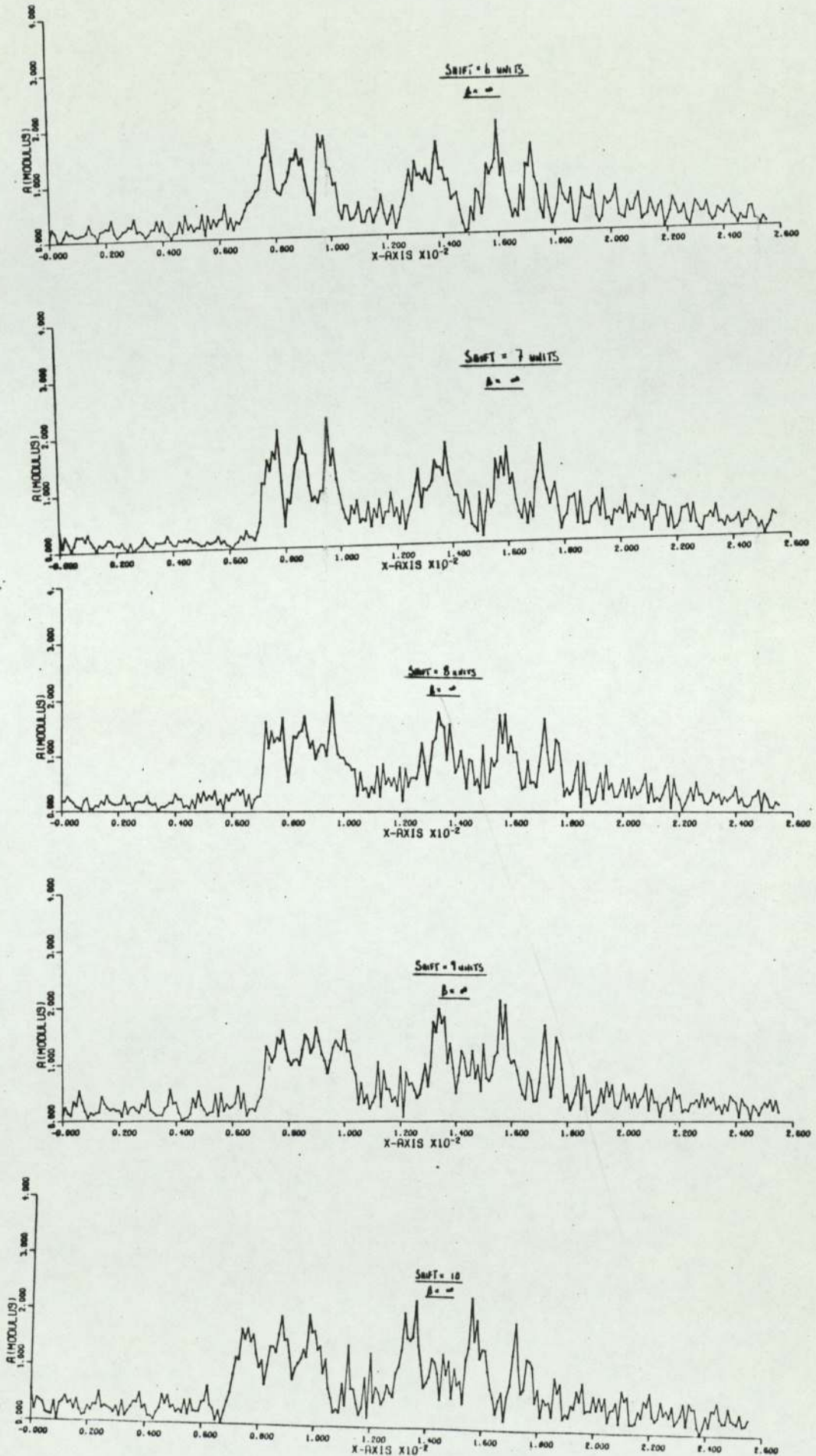


FIG 4.8

blurred bar chart, (Figure 4.1), which has been deconvolved with a filter laterally shifted so as to misregister with the diffraction pattern of the blurred bar chart.

As for the simulation of blurs of different extents in section 4.2, the misregistrations are constrained to at least integer frequency changes because of the finite number of terms in the calculated spectrum.

The most noticeable effect is the asymmetry of the images. This is due to regions of the spectrum being assigned incorrect phases by the filter. These regions of phase error are of the same extent as the misregistration and first appear around the poles of the filter. They strongly influence the form of the image, even for small misregistrations, as it is in pole regions that the filter is most strongly amplifying.

#### 4.5 QUANTIZATION AND DYNAMIC RANGE

The space bandwidth product relates the image and spectrum extents. If the address density is constant, as it is for a typical computer display device, then an increase in image order separation, obtained by a reduction in the Fourier coefficient cell sizes, is gained at the expense of a reduction in the number of addresses in each cell. Hence, for Lohmann coding the image order separation is inversely proportional to the dynamic range which in turn



determines the number of side lobes of a deblurring filter that can be realised. For the filter system we have simulated by computer, a dynamic range of 15 is required to realise 4 side lobes on either side of the zero frequency axis of a deblurring filter with  $\beta = 1000$ . Thus,  $15 \times 15$  addresses are required in each square Fourier cell. The coding efficiency,  $\eta$ , is defined as

$$\eta = \frac{\text{Total number of values to be coded}}{\text{Total number of addresses required to code them}} \quad 4.2$$

For this case then, 
$$\eta = \frac{N^2}{N^2 R^2} \quad 4.3$$

$$\text{and } \eta < 5 \times 10^{-3}.$$

For an absorption filter, in which the amplitude is controlled by the film density, a continuous range of transmittance values are available within the dynamic range constraints. That is from a transmittance of 1 down to  $1/DR$ . However, for the Lohmann hologram, excluding the case of zero transmittance, the number of available amplitude transmittance values is equal to the dynamic range,  $DR$ . For a square cell this is also the number of available phase values.

Like all pulse-code modulated (PCM) systems, these holograms thus suffer from quantisation error as a result of the analogue to digital conversion. With  $R_H \times R_K$  addresses per Fourier cell the dynamic range (including zero transmittance) is  $R_K + 1$  and there are  $R_H$  values of phase available to the 1st image order. The amplitude

transmittance can change in  $1/R_K$  steps and the phase can change by  $J.2 \pi / R_H$  radians for  $R_H$  even, and  $J.2 \pi / (R_H - 1)$  radians, for  $R_H$  odd, as seen from the  $J^{\text{th}}$  order.

In Chapter 3 it was noted that in order to obtain maximum image brightness and at the same time ensure that apertures of adjacent cells do not overlap it is necessary to use an image order  $J \gg 2$ . However, as the phase is only to be controlled over  $2\pi$  radians, the use of a high order image reduces the number of available phase quantization levels by approximately  $1/J$  and has the effect of increasing the phase quantization noise.

The deblurring filter is a special case of a wholly real element. As the phase needs controlling with only two values, 0 or  $\pi$  radians, the filter does not suffer from phase quantization errors, unless an image order,  $J$ , is chosen so large that  $J.2 \pi / R_H$  radians.

#### 4.6 AMPLITUDE QUANTIZATION IN A DEBLURRING FILTER

The results of quantizing the amplitudes of different LMSE deblurring filters are shown in Figures 4.10 to 4.27, (even numbers) along with their associated calculated impulse responses (odd numbers). The amplitude quantization error is the difference between the amplitude of the ideal and coded filters. An example of its variation is shown in Figure 4.28 for  $DR = 10$ ,  $\beta = 1000$ . The maximum



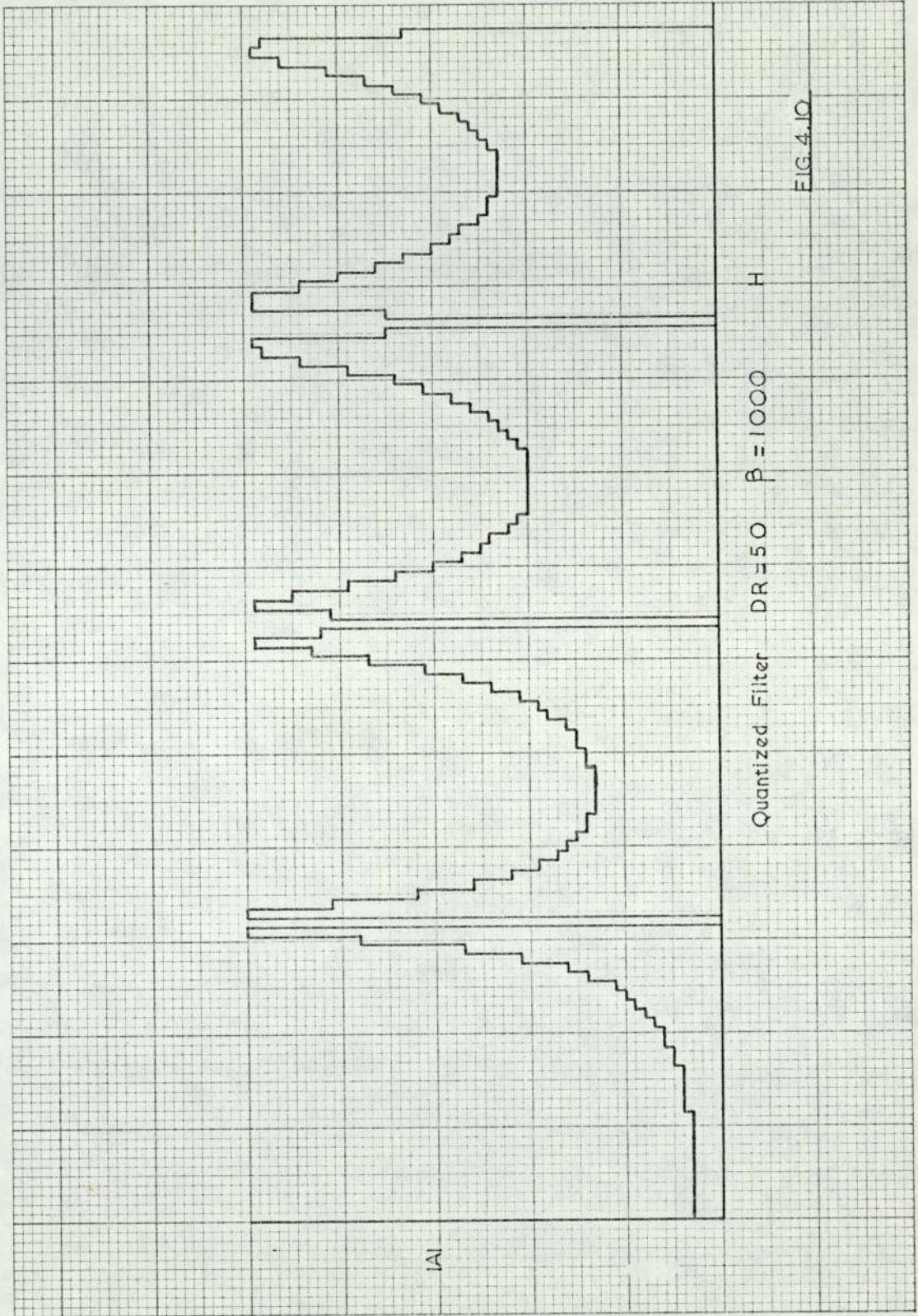
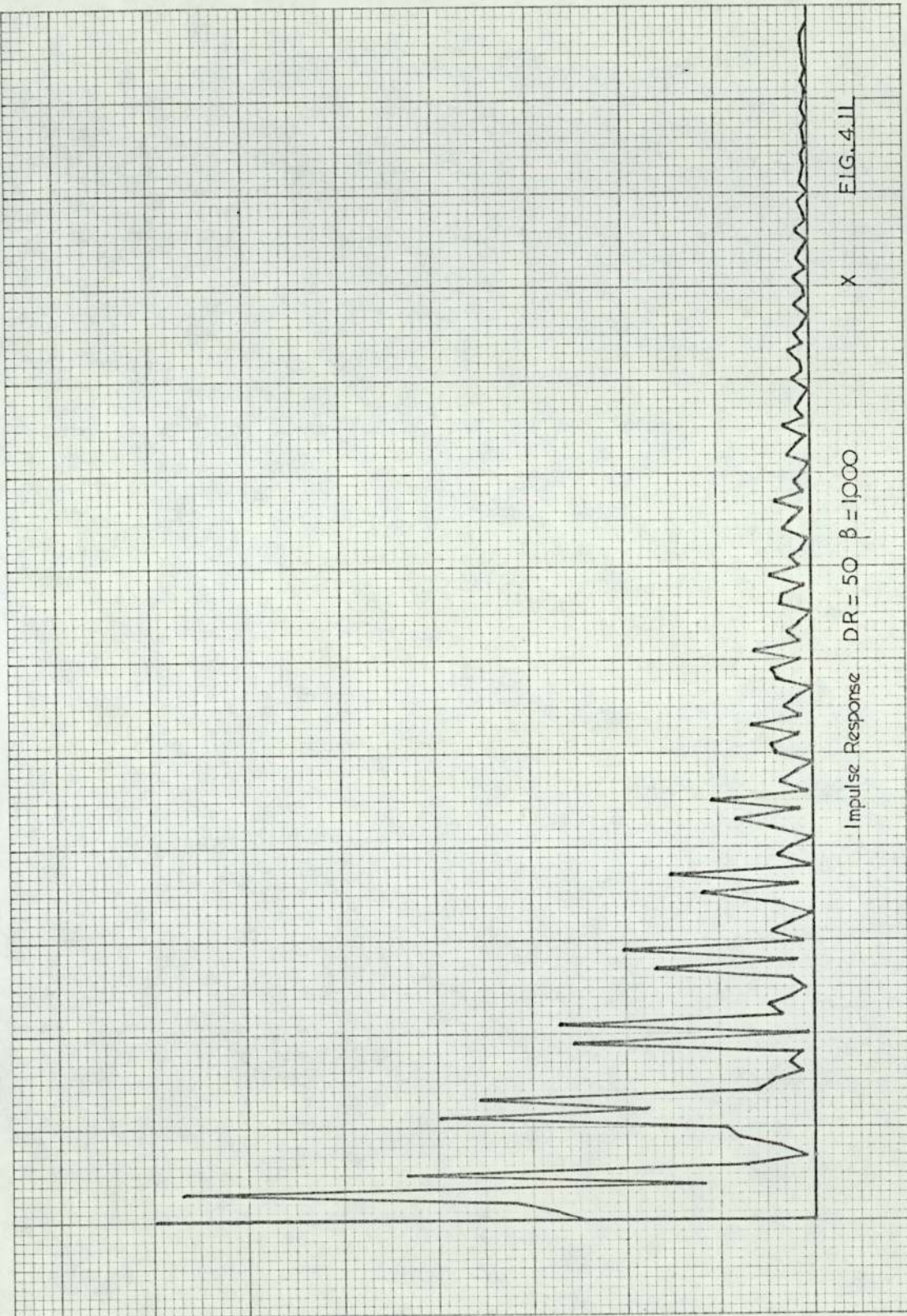
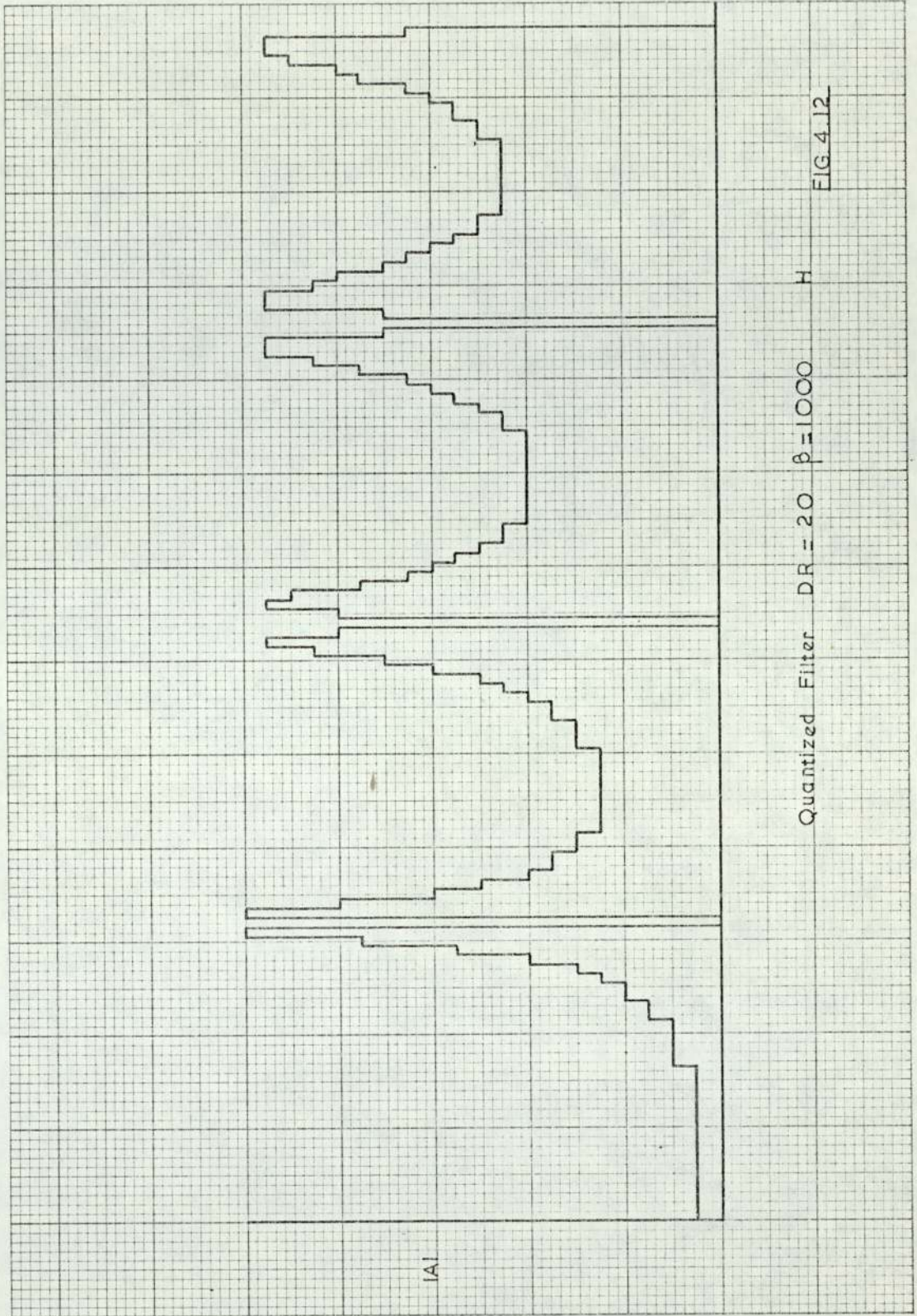


FIG. 4.10











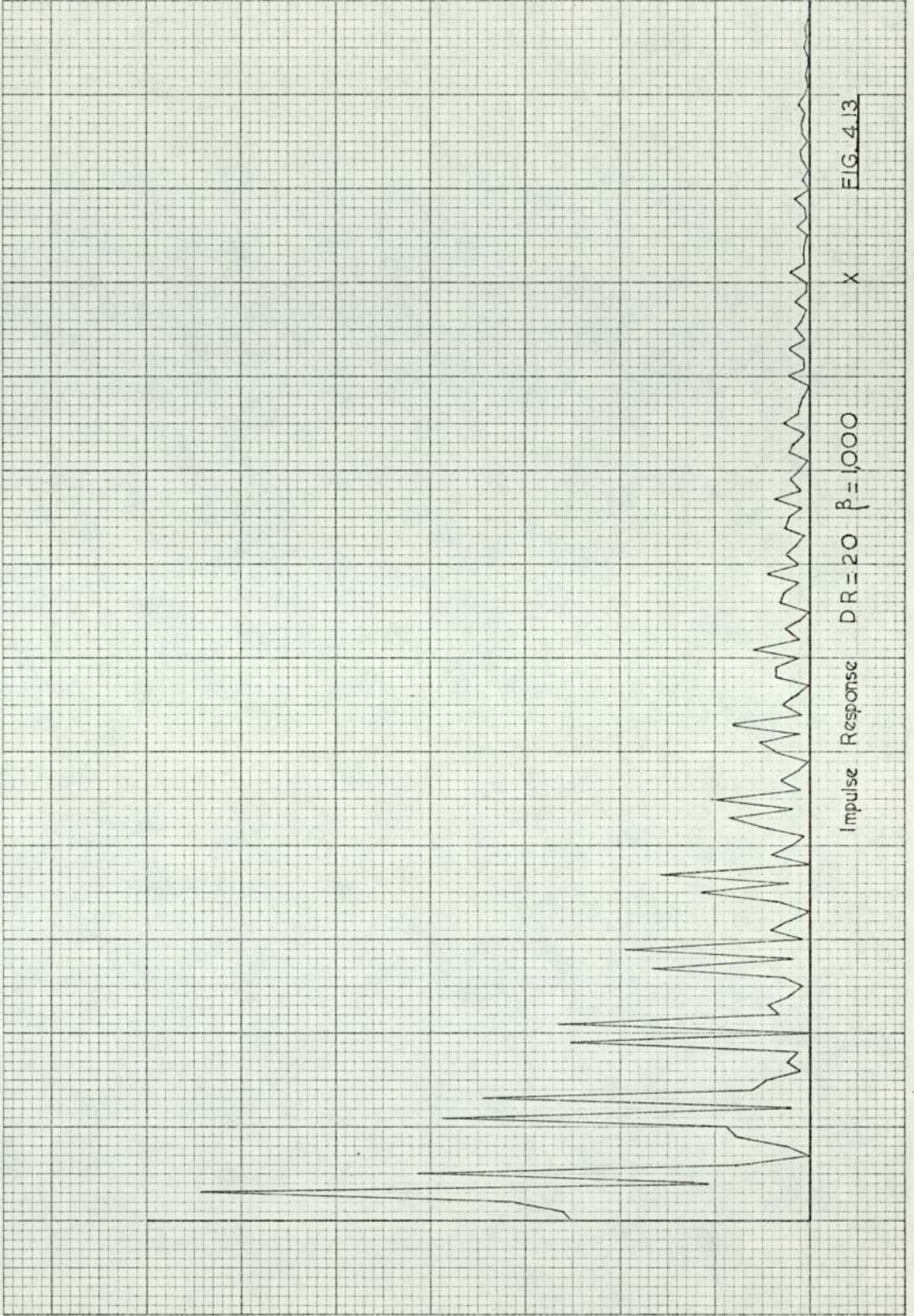


FIG. 4.13

x

DR = 20  $\beta = 1000$

Impulse Response



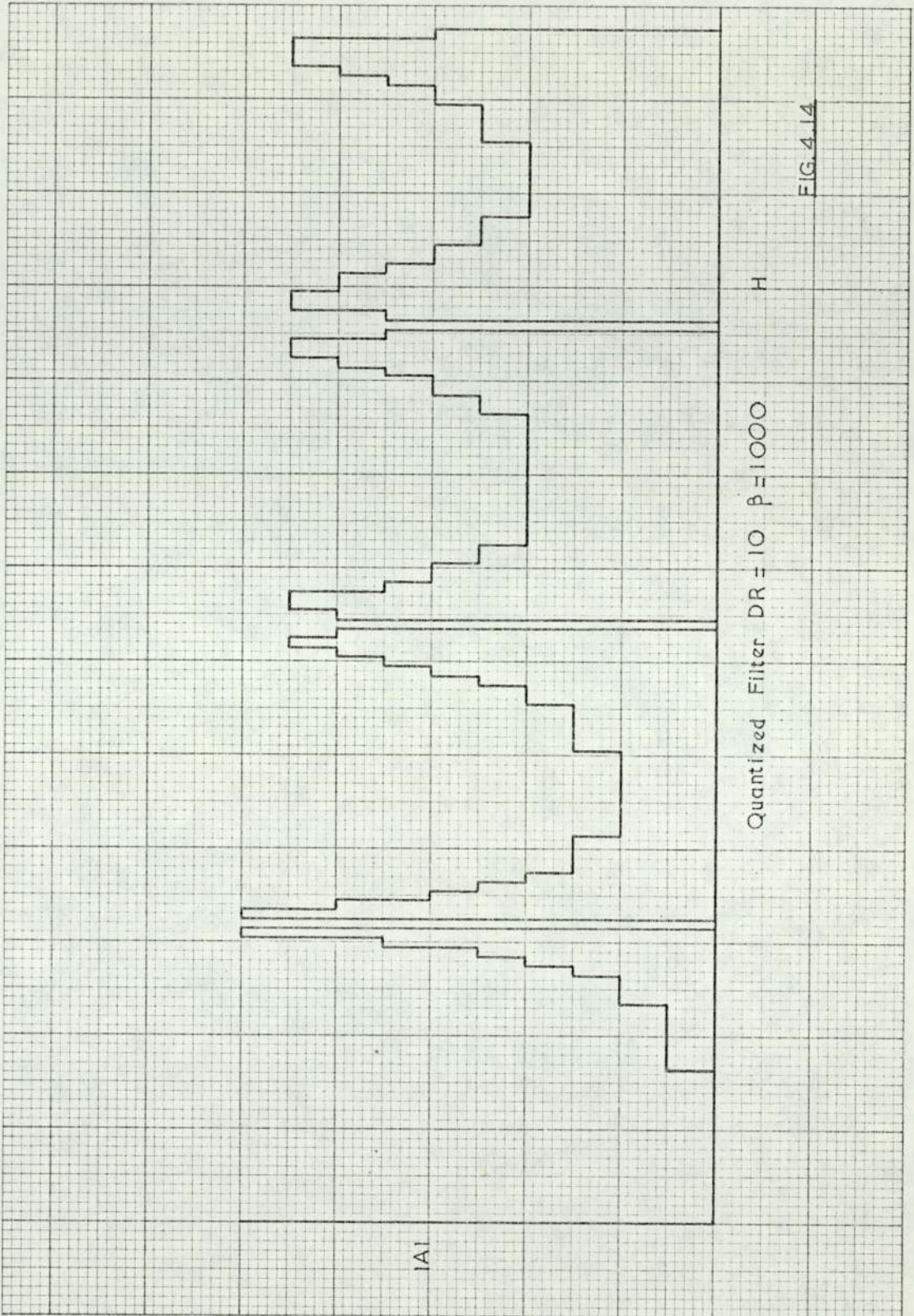


FIG. 4.14



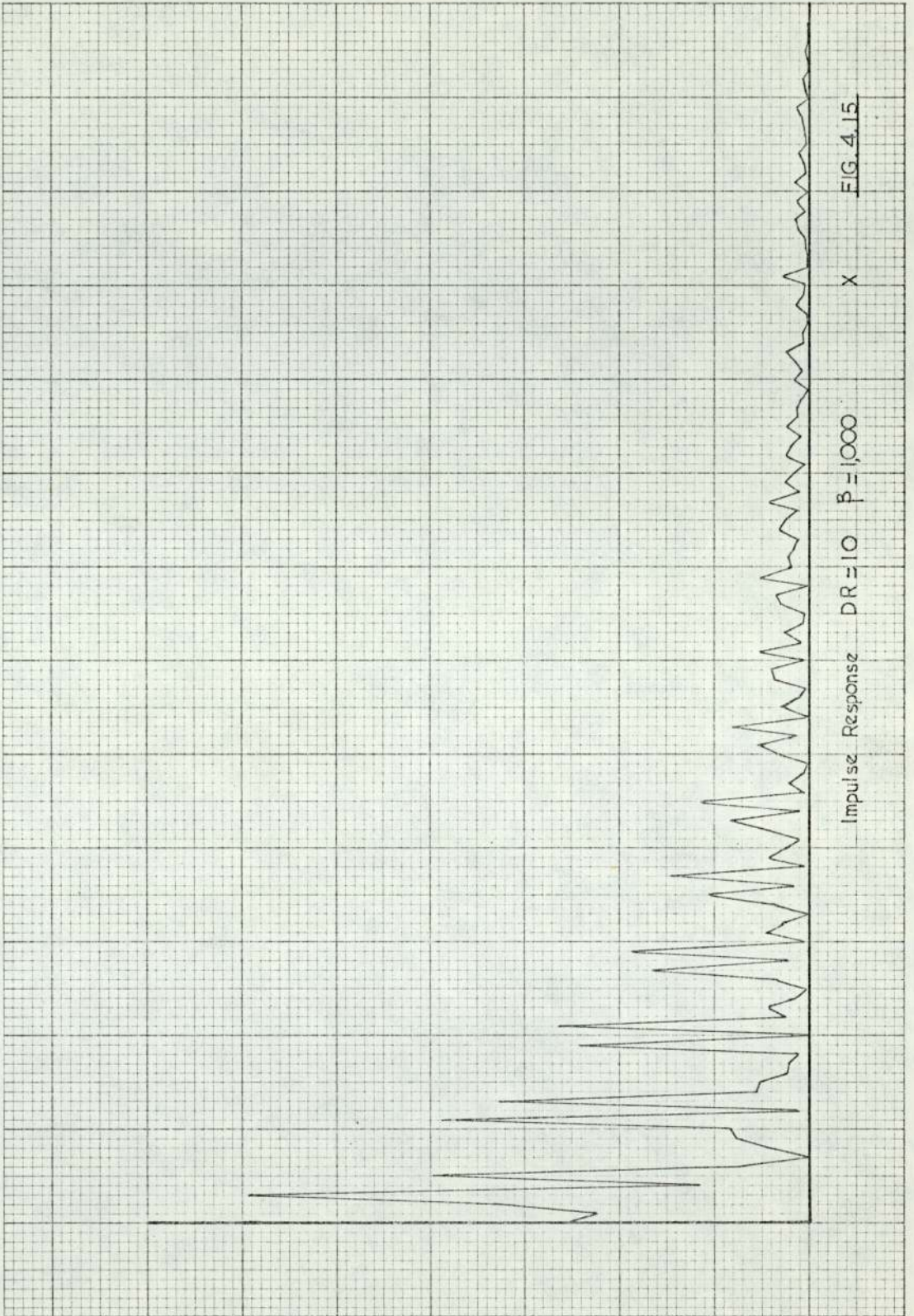


FIG. 4.15

X

$\beta = 1,000$

DR = 10

Impulse Response



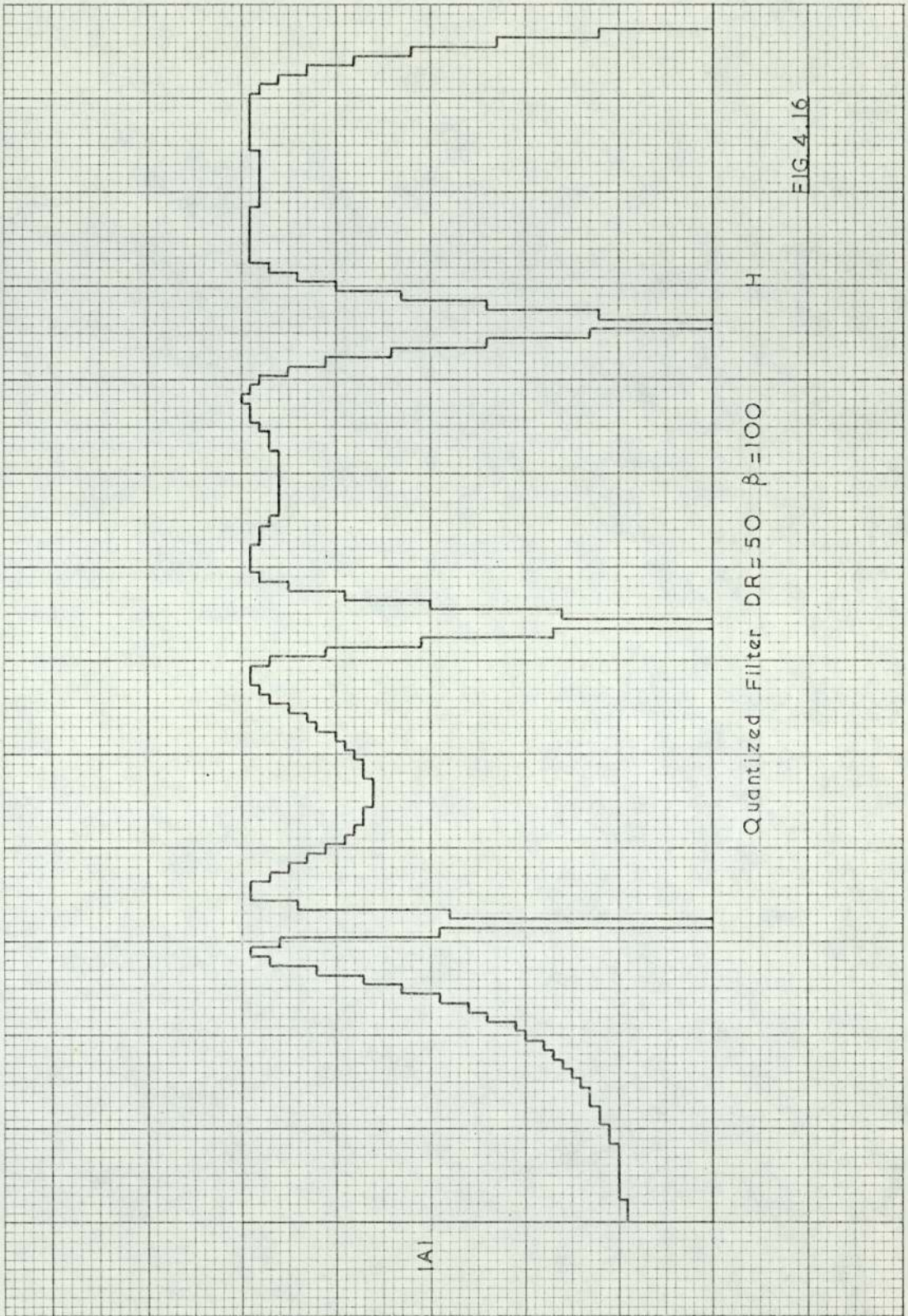


FIG. 4.16



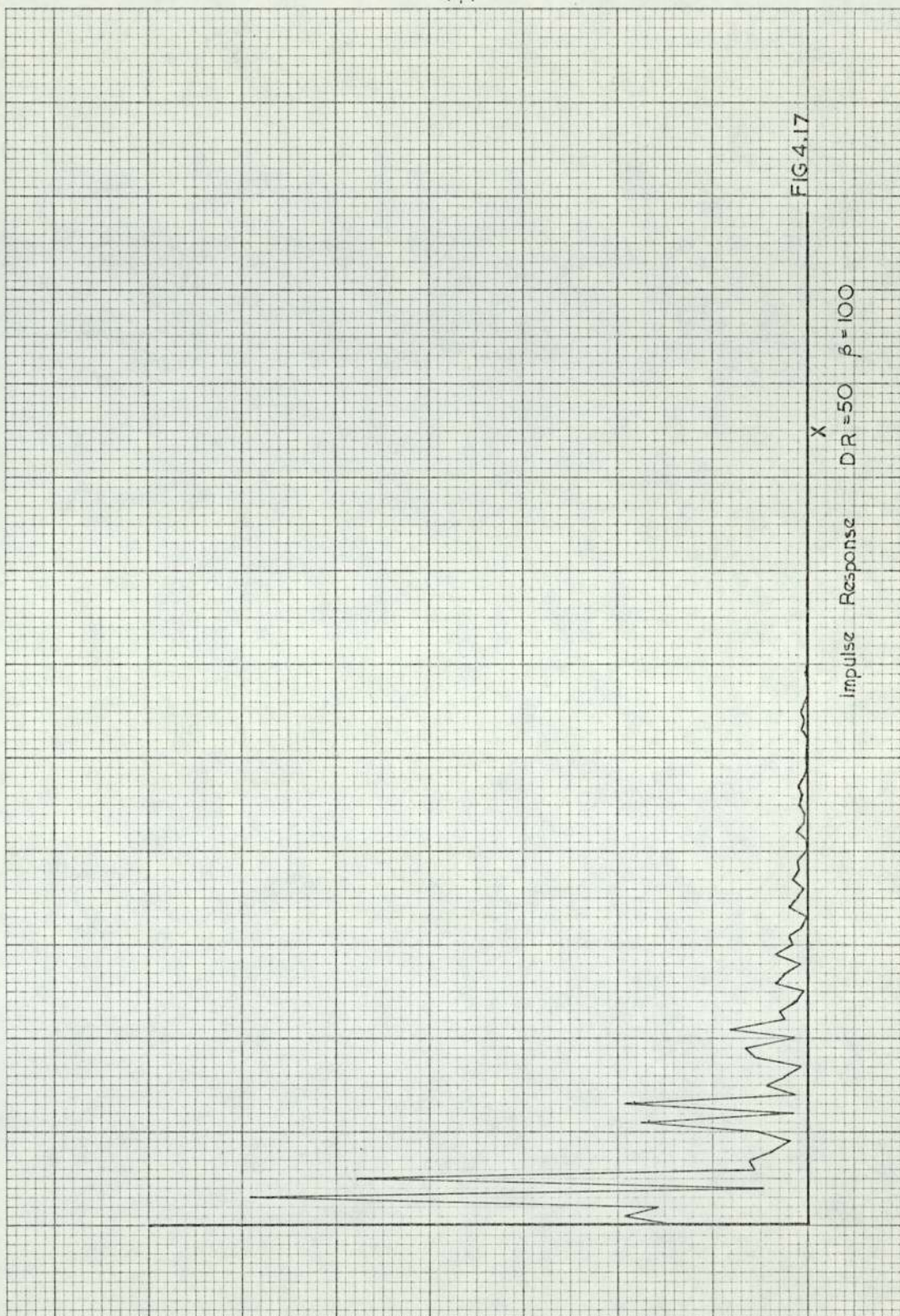


FIG 4.17



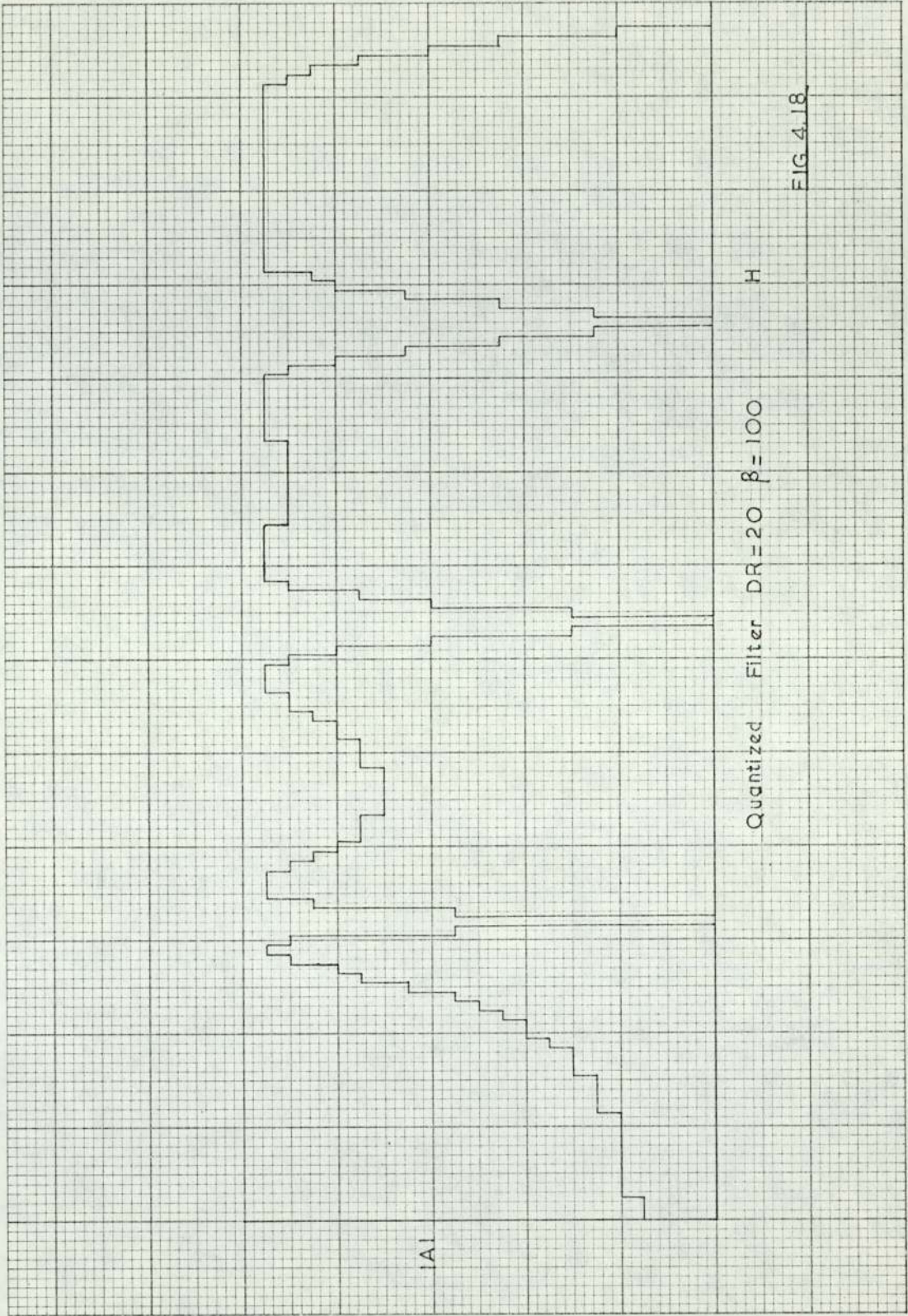
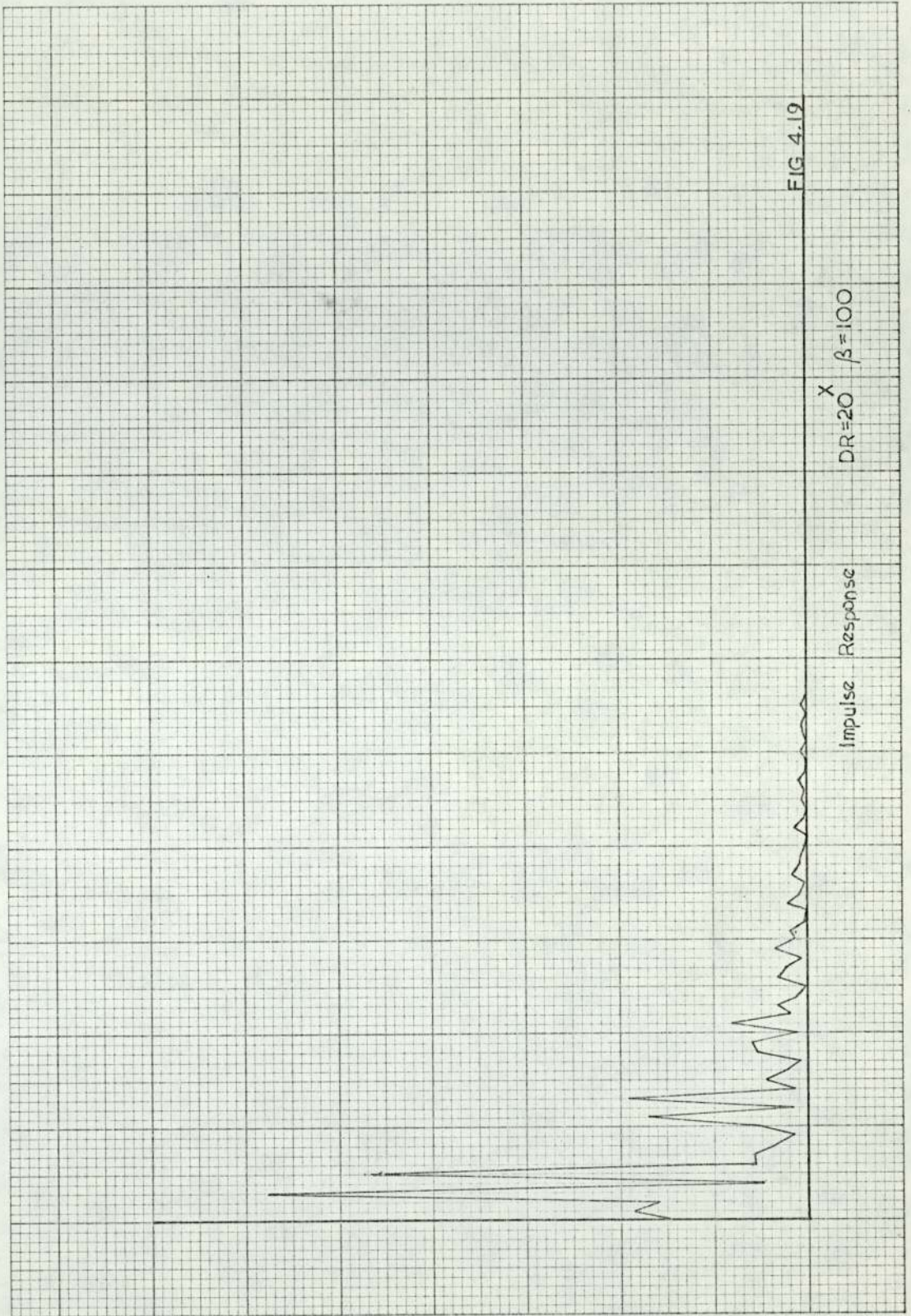


FIG. 4.18







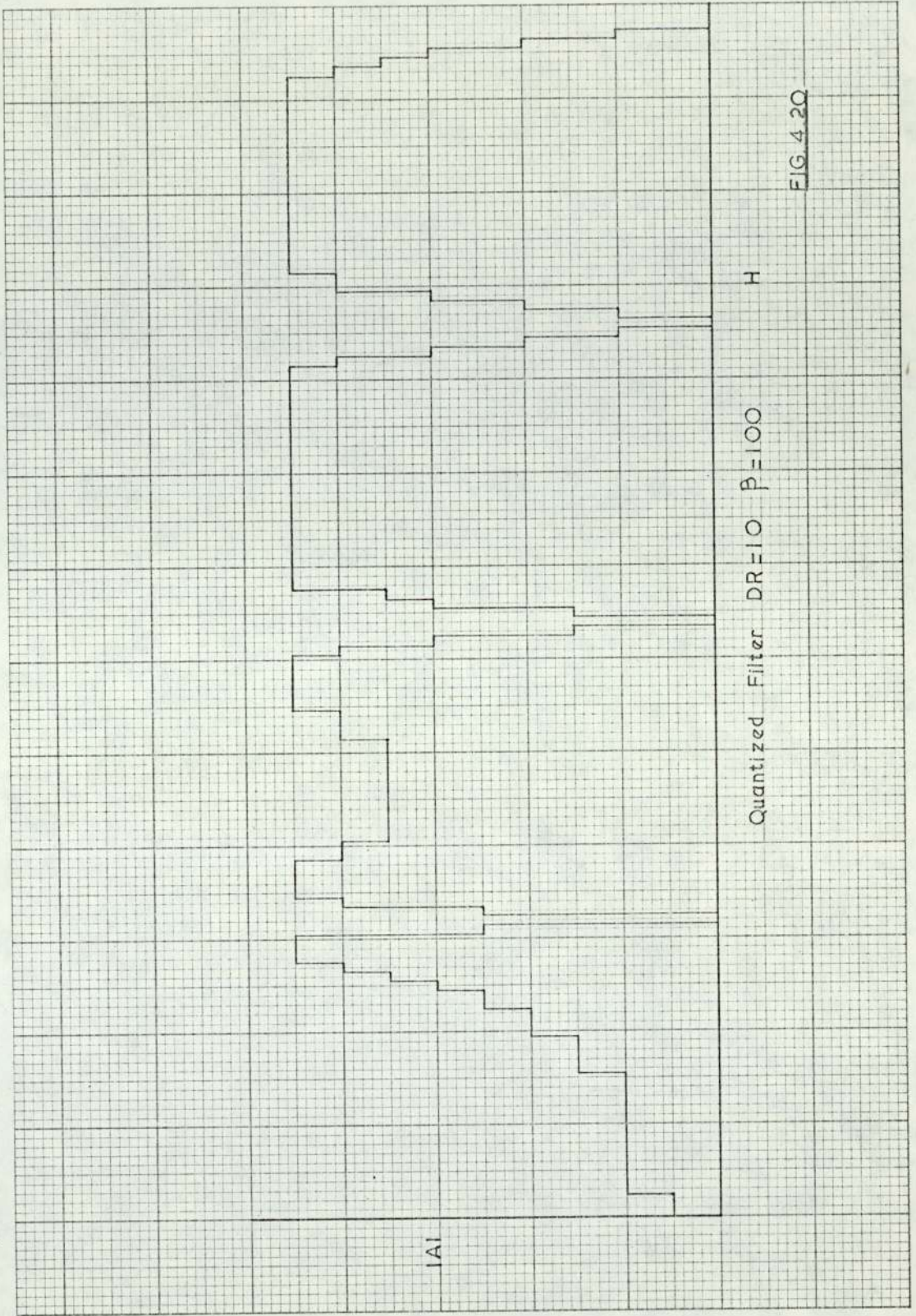


FIG. 4.20



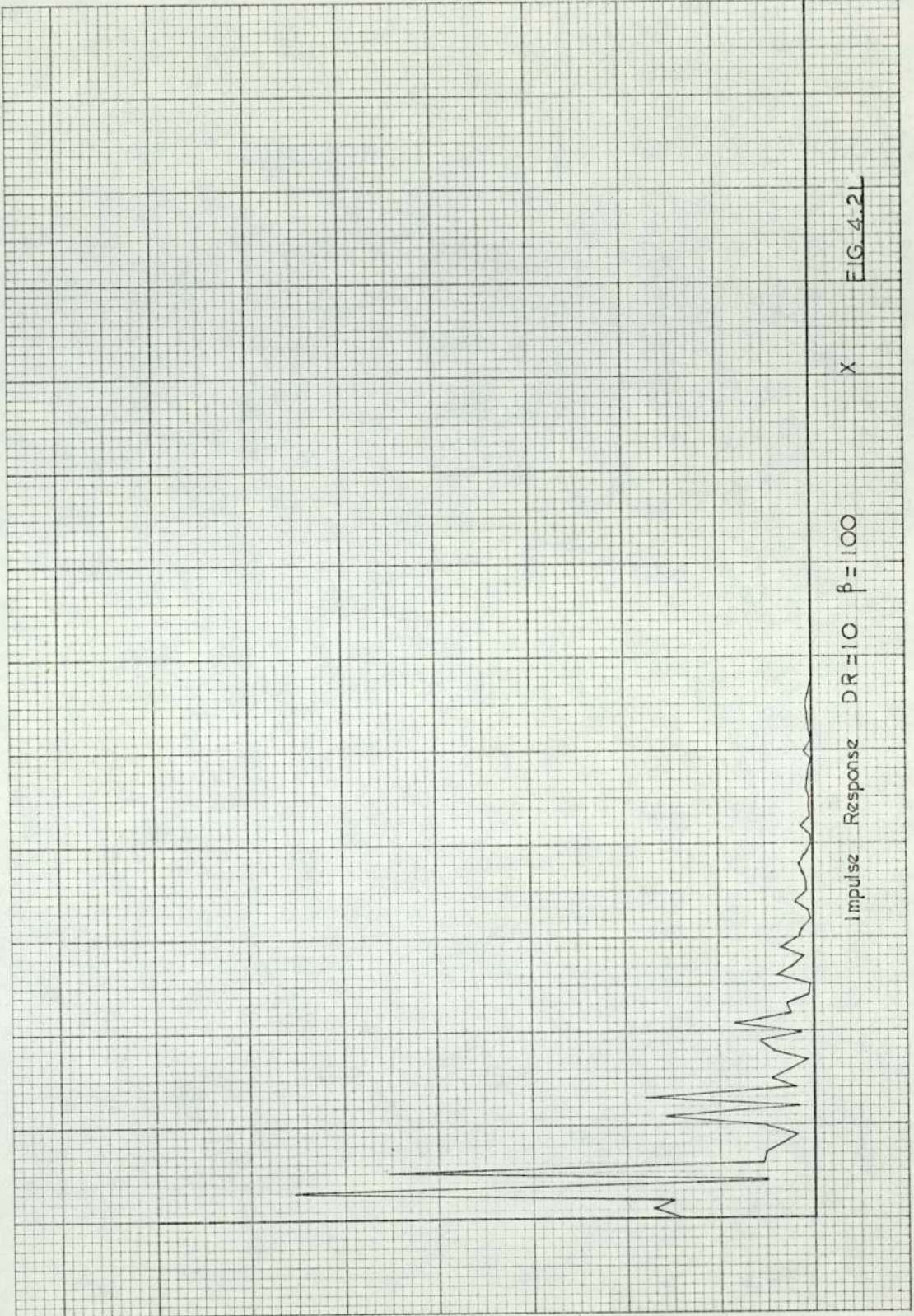


FIG. 4.2L



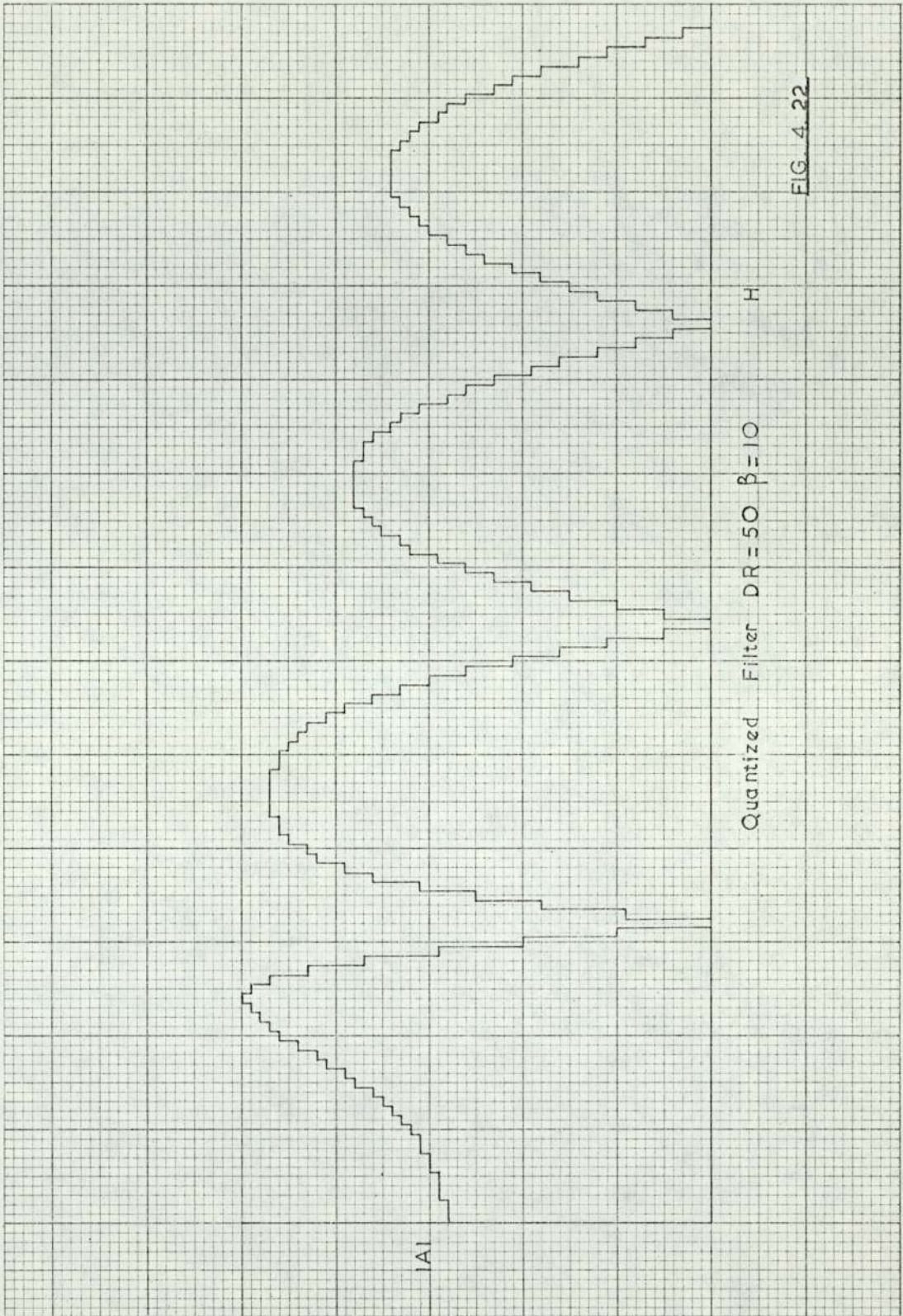
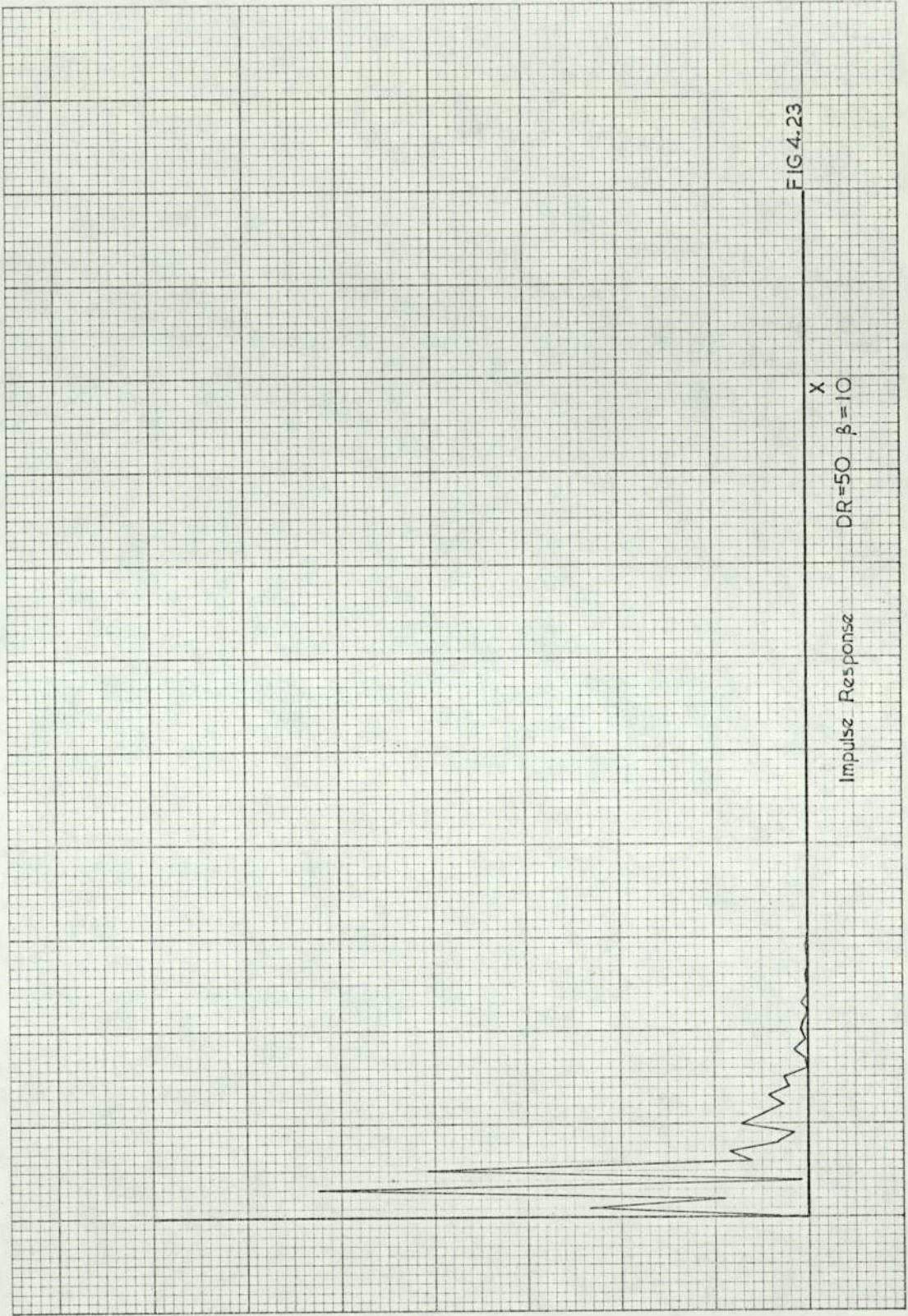


FIG. 4.22







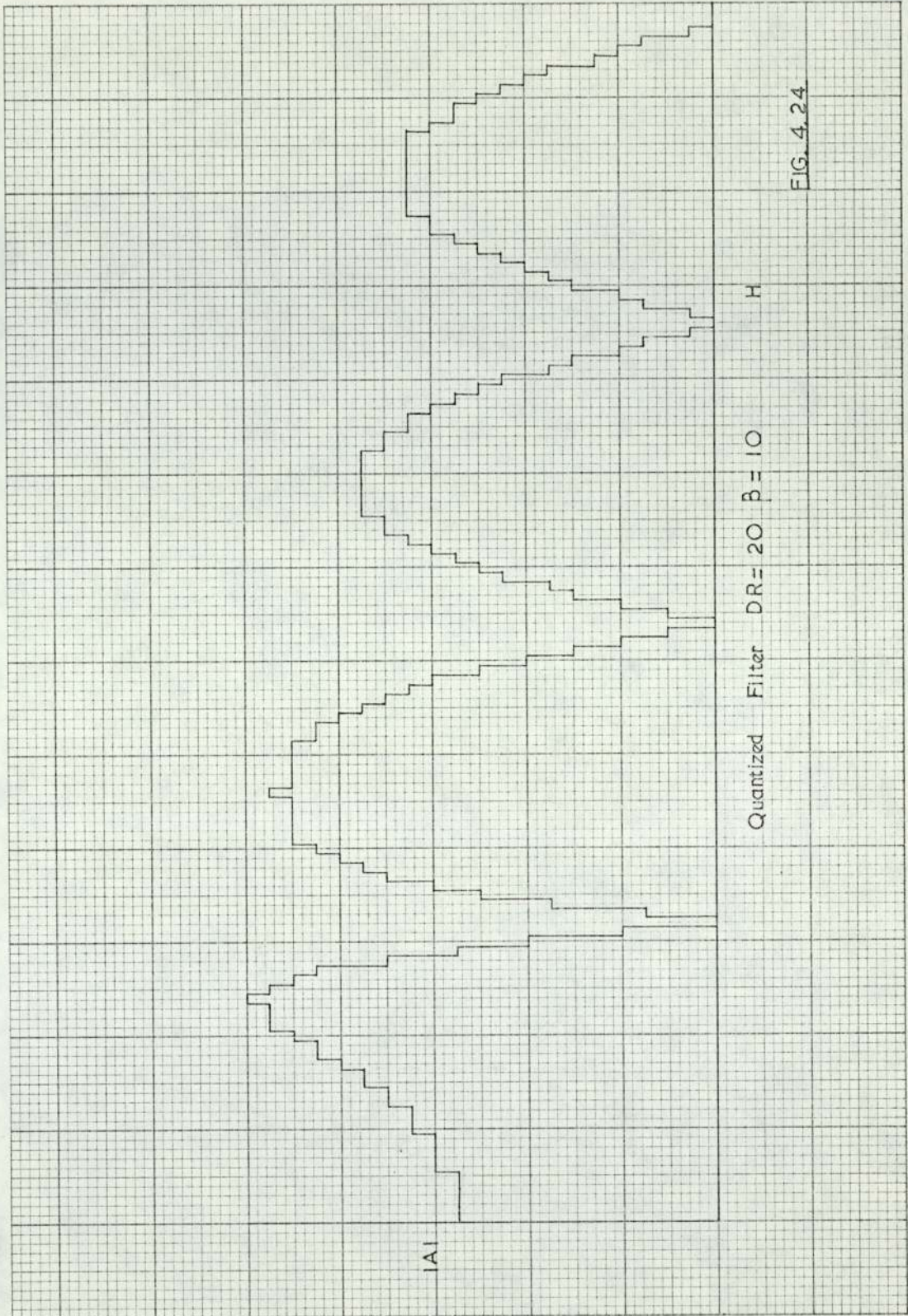


FIG. 4.24



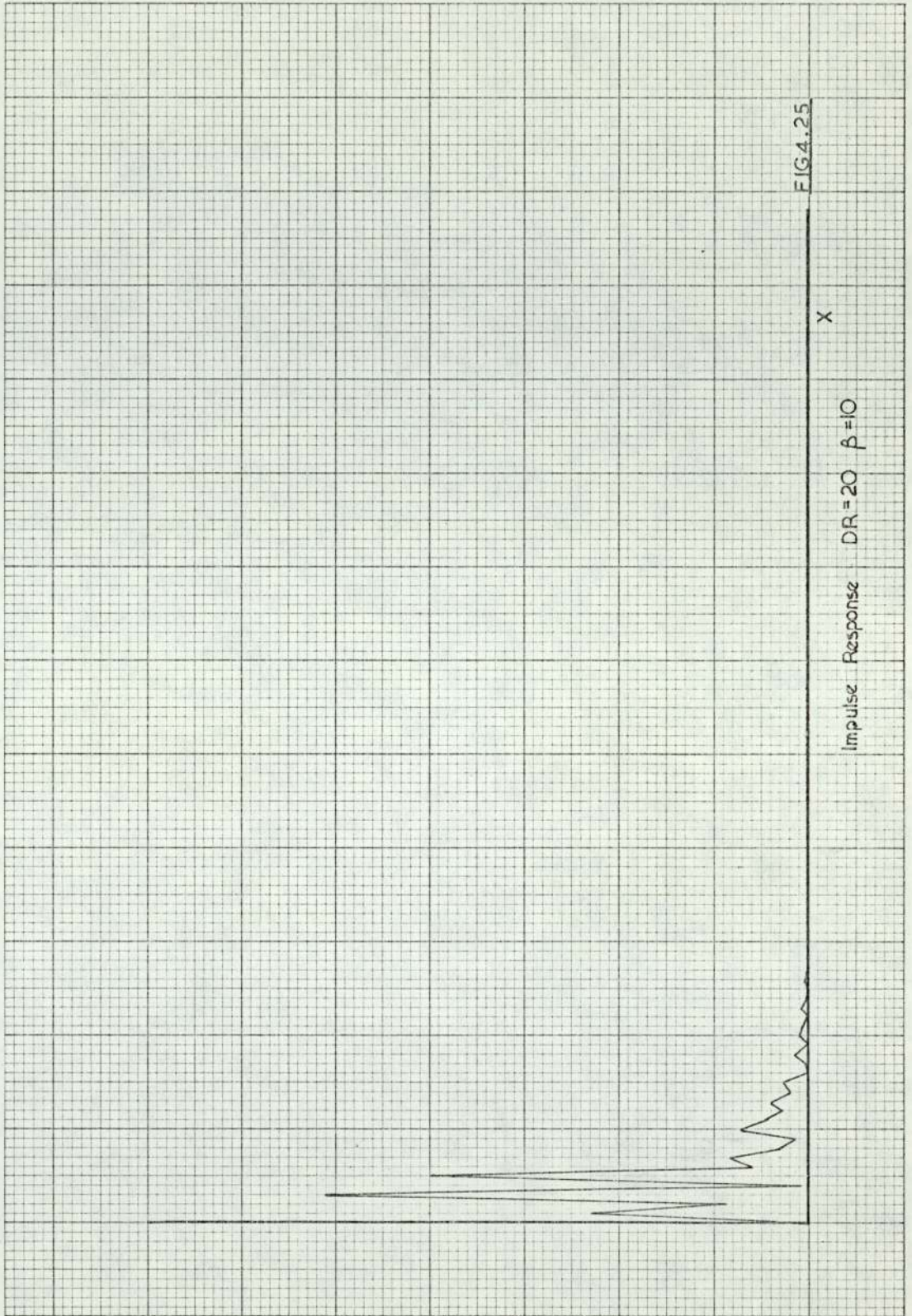
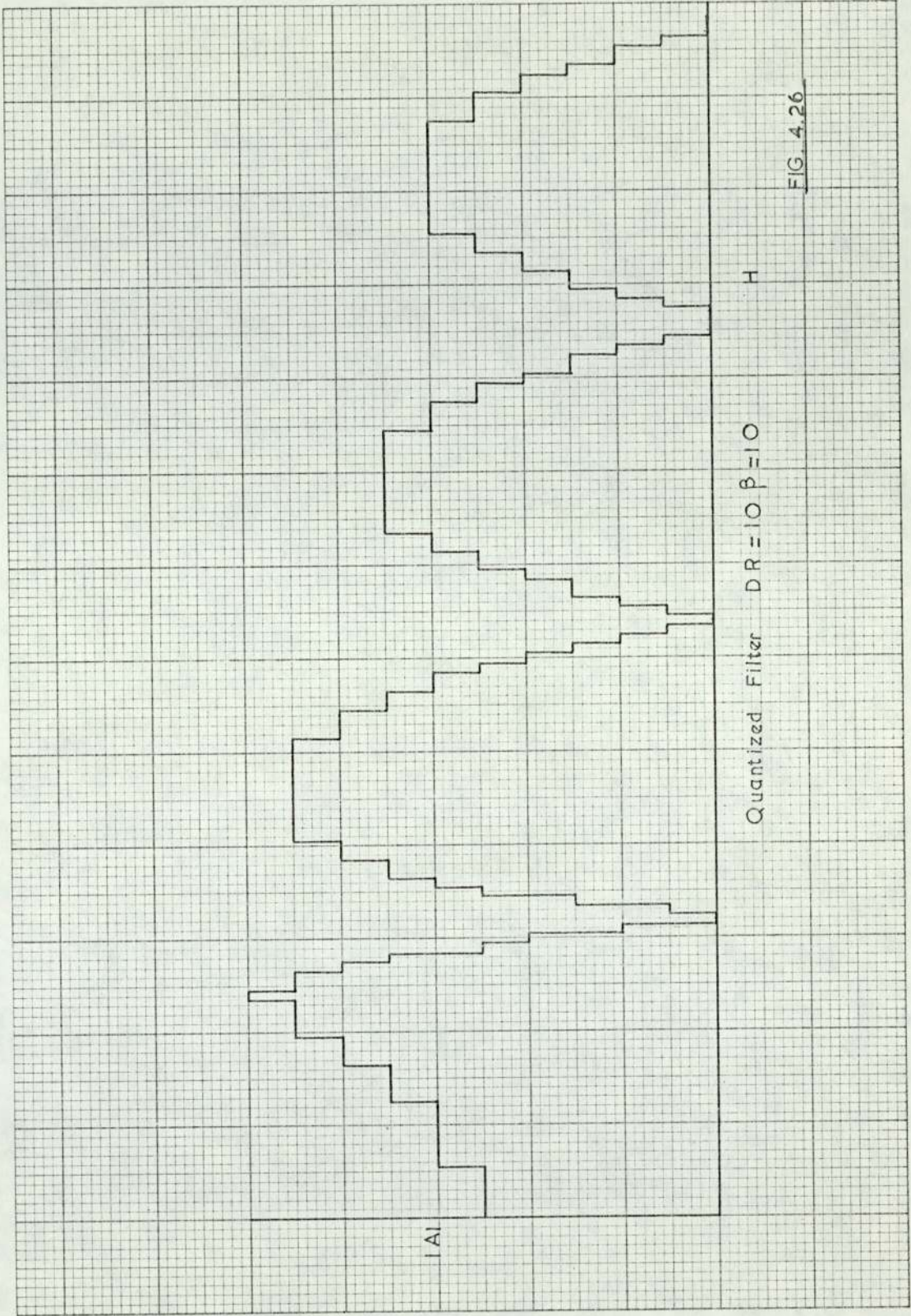
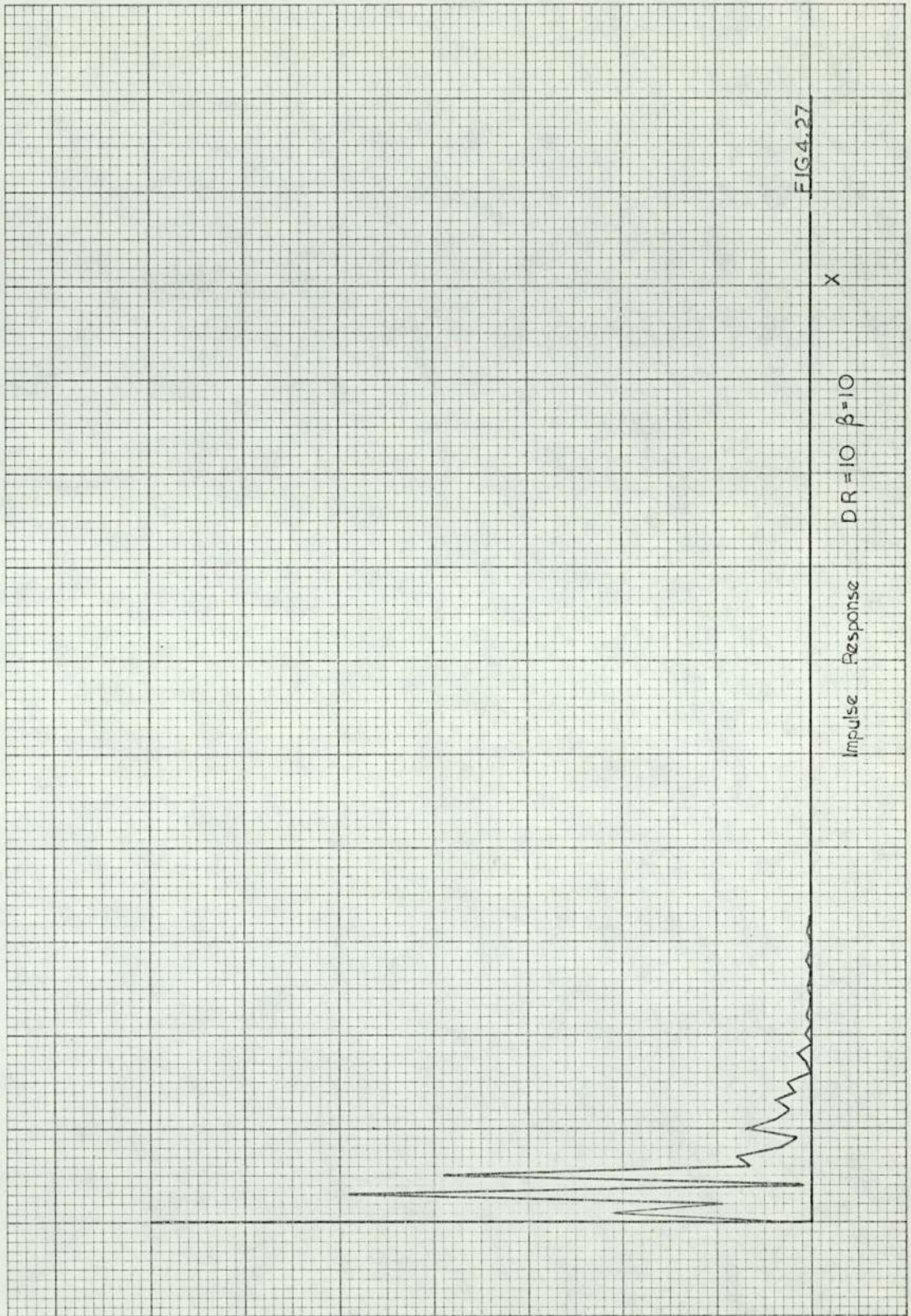


FIG. 4.25











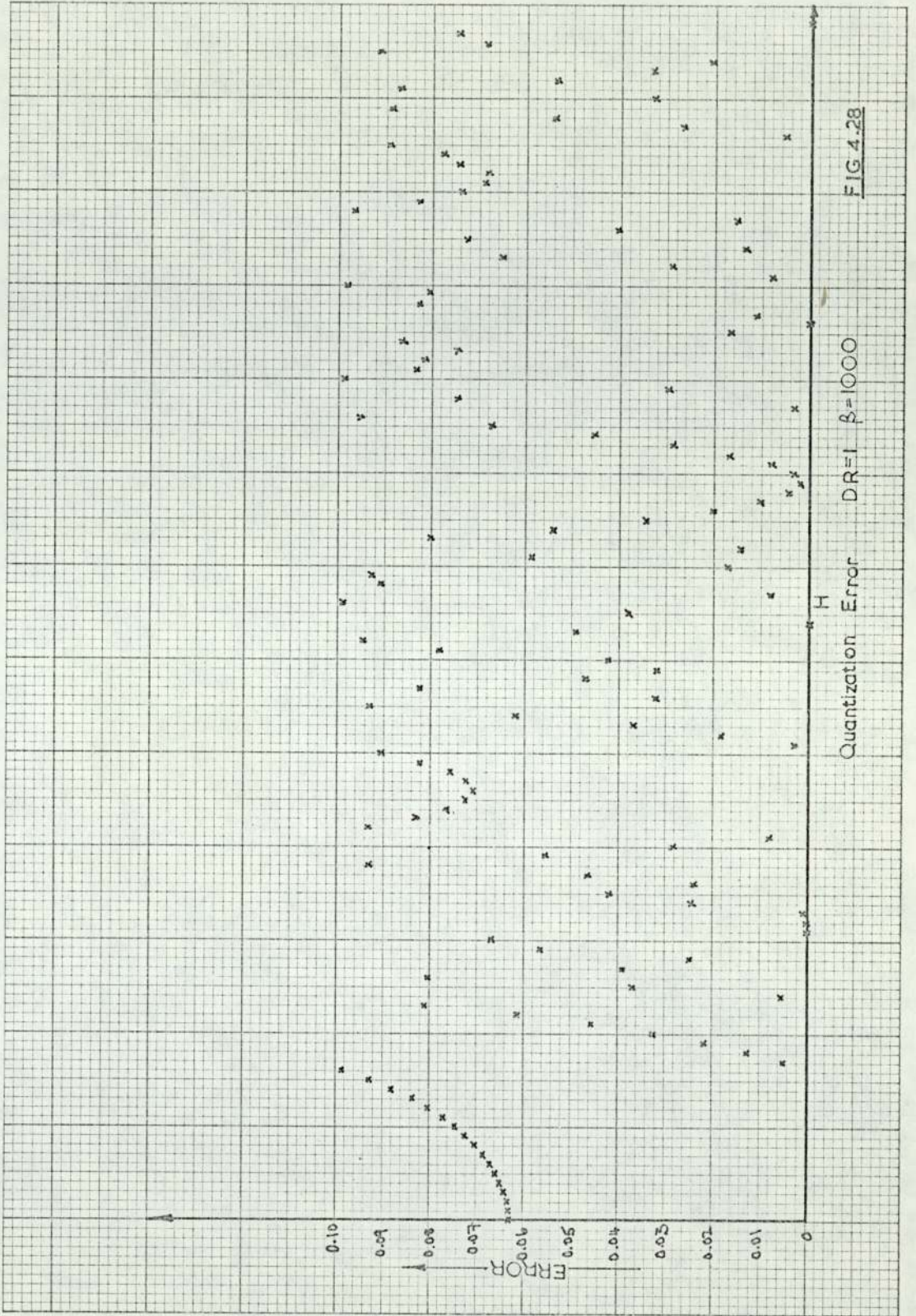


FIG 4.28

Quantization Error DR=1  $\beta=1000$

quantization error is, of course,  $50/DR\%$ . For a dynamic range  $DR = 50$  then, the modulus of the amplitude of the filter is everywhere within 1% of its value for a continuously variable amplitude system.

The effects of amplitude quantization can be judged by comparing the impulse responses of the quantized filters (odd numbered Figures 4.11 to 4.27) with those for the corresponding continuously variable amplitude filters shown in Chapter 2, Figure 2.10. Their close similarity shows the deblurring filter's insensitivity to quantization noise. This is to be expected in view of the results of Chapter 2 in which it was shown that the recovered images were not very sensitive to random noise modifying the modulus of the filter amplitude. A value of about 40% of the maximum filter amplitude was tolerable for the maximum excursion of the random amplitude noise - approximately equivalent to a dynamic range of  $DR = 4$ . This is in agreement with the quantization noise bounds calculated analytically and numerically by Naidu (Ref. 40).

The Kinoform (Ref. 23) represents the most extreme form of amplitude quantization as the modulus of its amplitude transmittance can take only one value of unity. The Kinoform for a deblurring filter is shown in Figure 2.4 and is simply the phase part of a "sinc" filter. It is similar to the quantized filter  $\beta = 100$ ,  $DR = 20$  except at the low frequency region of the spectrum which the Kinoform transmits, along with all other frequencies,



with unity amplification. This low frequency transmittance is responsible for the slowly varying form of the recovered image of Chapter 2, Figure 2.5.

The Kinoform is not, of course, used as a deblurring element because of this inability to conserve image fidelity. It is used specifically as a coding device as it has a maximum coding efficiency,  $\eta = 1$ , only requiring one address per cell. Like ROACH, which is also capable of maximum coding efficiency, the Kinoform does require continuous phase control to obtain this value of  $\eta = 1$ .

Orbit

CHAPTER 5

NONCOHERENT DECONVOLUTION

Orbit

Orbit



## 5.1 INTRODUCTION

The process of image formation is most frequently thought of in terms of the two stages of diffraction discussed in the previous chapters. The Fourier transform description linking the object plane, back focal plane and image plane of an imaging system is satisfactory only with the proviso that the object is transparent and coherently illuminated by a source of very limited size.

A more general approach views the image as the re-transformation of the partial coherence pattern of the object. In this case the object generates a partial coherence pattern in the entrance pupil of the imaging system. This partial coherence pattern is then taken in whole or part by the imaging system which forms a whole series of Young fringes of appropriate visibility, period and orientation in the image plane of the system. The exact form of the image depends on the way in which the entrance pupil of

the imaging system samples the partial coherence pattern. This chapter describes how a mask of suitable weighted image depends on the way in which the entrance pupil of the imaging system samples the partial coherence pattern. This chapter describes how a mask of suitable weighted apertures positioned in the entrance pupil plane can be used to sample the partial coherence pattern in such a way that some degree of deconvolution can be effected. The description of the imaging process followed here has been developed in some detail by Rogers (Ref. 41 ) after a similar treatment by Hopkins (Ref. 42 ) and Born and Wolf (Ref. 43 )

## 5.2 IMAGE FORMATION AS A SUPERPOSITION OF YOUNG FRINGES

As a preliminary to discussion the operation of non-coherent filter consider a Young fringes type experiment shown schematically in Figure 5.1. A monochromatic point source of wavelength,  $\lambda$ , situated on the optic axis coherently illuminates a pair of small pin holes positioned a distance  $P$  apart in the entrance pupil plane of a lens. The resulting Young fringes in the image plane of the system subtend an angle  $\lambda/P$  at the lens and are for the case of the source point plane and image plane being conjugate cosine fringes being symmetrical about the optic axis. The fringes are invariant to a translation of the pin holes but move in the opposite sense to a translation of the point source along the direction of a line parallel



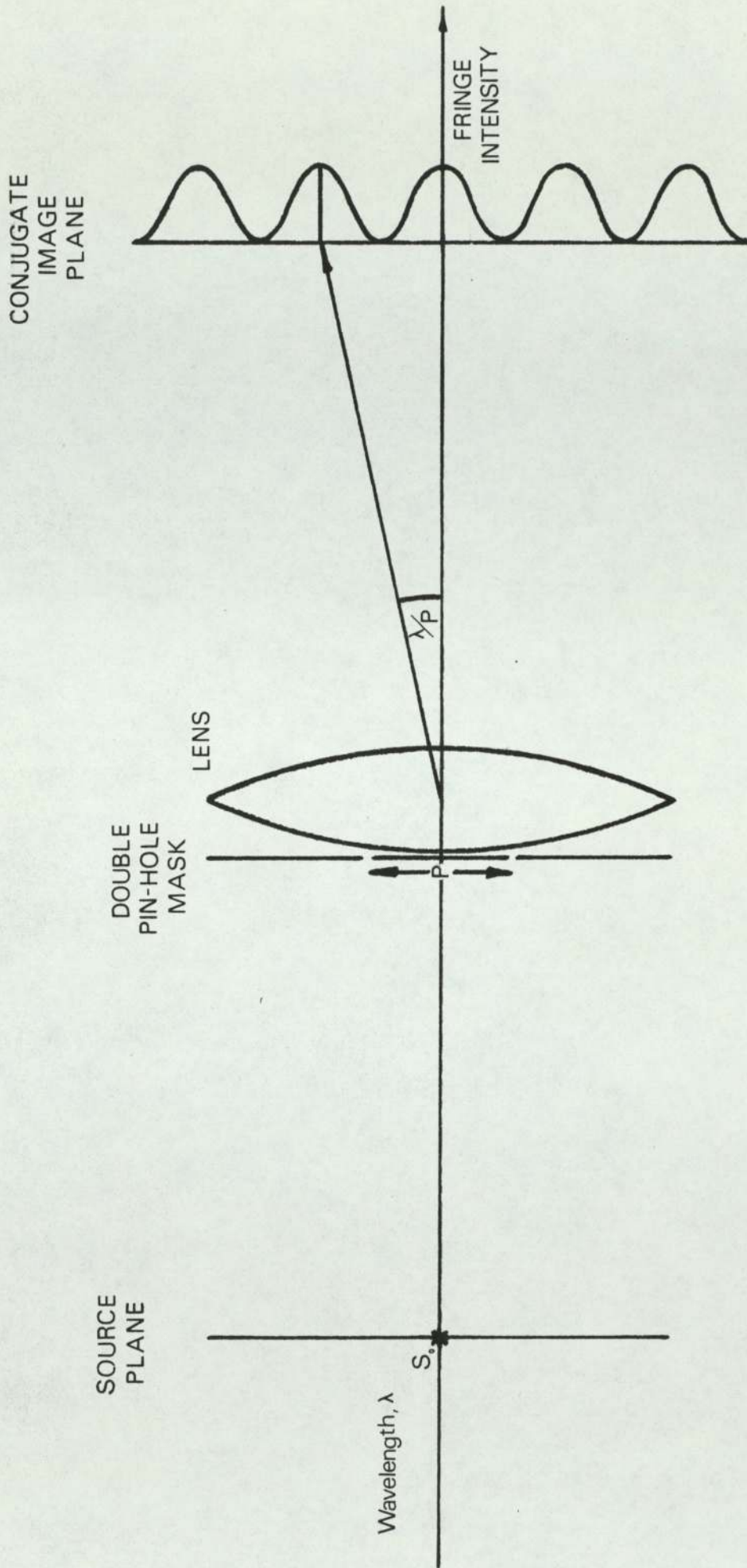


FIG 5.1

to that joining the pin holes. Consider now more point sources positioned along this line adjacent to the first point source. If they have an angular separation of  $\lambda/P$  at the lens then the sets of fringes produced by each will be in exact register and will add noncoherently to give maximum visibility. Point sources at intermediate positions will produce fringes which are out of register and these will tend to reduce the visibility as shown in Figure 5.2.

For an extended source, composed of a large number of noncoherent point sources, the visibility of the fringes it forms will decrease as the angular size of the source increases.

As the fringe period varies inversely as the separation of the pin holes the fringes of highest frequency containing information about the fine detail of the source are formed by pin holes of maximum possible separation. A mask of  $N$  pin holes separated by distances  $P_K$  will thus form  $\frac{1}{2}N(N-1)$  sets of fringes in the image plane. If the  $P_K$  are selected at random and  $N$  is sufficiently large a good image of the source will be produced. h

This suggests that it is possible to sample the partial coherence pattern with a mask of suitably sized and positioned apertures so as to modify the frequency content of the image in some desired way. However, the ways in which the frequency spectrum of a source can be modified



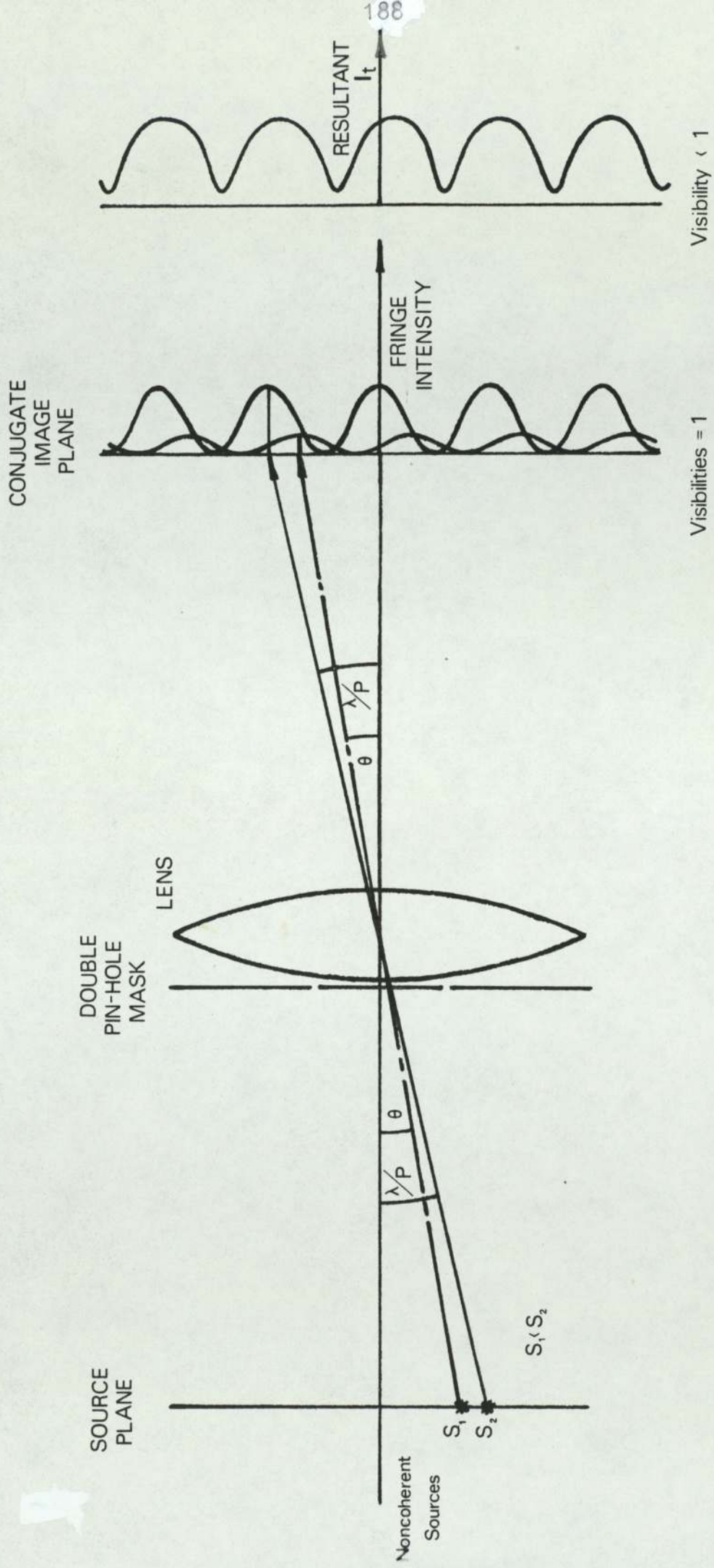


FIG 5.2

by such a sampling mask are severely limited. As the phases of the diffracted amplitudes from the source cannot easily be modified the mask can only operate as a real, positive frequency filter. Any phase changes produced at the apertures of the mask will laterally shift the sets of fringes and in general ruin the image in a similar way to inserting a diffuser in the entrance pupil of a lens.

### 5.3 DECONVOLUTION OF A GAUSSIAN FUNCTION

For convenience in this section a brief restatement of the deconvolution operation is given.

For a one dimensional source intensity distribution,  $s(x)$ , convolved with a blurring function,  $g(x)$ , resulting in a distribution,  $b(x)$ ,

$$b(x) = s(x) \otimes g(x) \quad 5.1$$

in Fourier space we have, denoting the frequency space functions by capitals,

$$B(u) = S(u).G(u) \quad 5.2$$

We can thus recover  $s(x)$  from  $b(x)$  (provided we know the form of the blurring function,  $g(x)$ ,) by multiplying the the frequency distribution,  $B(u)$ , by a filter,  $F(u)$ , such that

$$F(u) = D/G(u) \quad 5.3$$

where  $D$  is a constant less than 1.



If  $g(x)$  is such that its frequency spectrum is positive definite then noncoherent deconvolution may be attempted using a pupil plane mask constructed to transmit the various frequencies as required by equation 5.3.

A blurring function of Gaussian form

$$g(x) = \exp(-C^2x^2) \quad 5.4$$

is suitable for noncoherent deconvolution as its Fourier transform is also of Gaussian positive definite form,

$$G(u) = A \exp(-C^2u^2) \quad 5.5$$

The filter must operate so as to weight the frequencies reaching the image plane as

$$F(u) = A^{-1} \exp(C^2u^2) \quad 5.6$$

where  $c$ ,  $C$  and  $A$  are constants.

#### 5.4 THE NONCOHERENT DECONVOLUTION MASK

Consider a pupil plane mask of  $N$  apertures. Each of the  $\frac{1}{2}N(N-1)$  pairs of apertures will transmit a frequency which is inversely proportional to the separate of the pair  $P_k$ . If the mask operates only in say the  $x$  direction as a frequency filter then the weighting of the transmitted frequencies can be controlled by the lengths of the apertures perpendicular to the  $x$  direction.

The problem in making a filter is one of finding the weighted lengths of  $y_n$ , of the  $N$  apertures for a chosen set of

spacings,  $P_K$ , such that the resulting  $\frac{1}{2}N(N-1)$  frequencies are transmitted in the proportions of equation 5.6.

Formulated as a set of highly redundant simultaneous equations the best solutions are easily found by standard numerical methods (Ref. 44 ). One of the twice redundant difference series (Ref. 45 ) was found to be satisfactory when the solutions were based on the lowest 24 differences only. The filter then takes the form

$$y_1 \quad 8 \quad y_2 \quad 10 \quad y_3 \quad 1 \quad y_4 \quad 3 \quad y_5 \quad 2 \quad y_6 \quad 6 \quad y_7 \quad 8 \quad y_8$$

where the numbers denote the separations of  $P_K$  of the apertures of length  $y_n$  in arbitrary units.

At the expense of further overweighting the redundant frequency corresponding to spacing  $P_K = 8$  the lengths of the apertures  $y_1$  and  $y_8$  were increased by 30% and 60% respectively in order to produce a higher powered filter. Table 5.2 shows the solutions of the redundant equations for the  $y_n$  and the modified solutions after increasing  $y_1$  and  $y_8$  and Figure 5.3 shows the form of the filter after modification and the inverse Gaussian filter to which it approximates.

## 5.5 CONSTRUCTION AND OPERATION OF THE NONCOHERENT FILTER

In practice a filter was made to the above specifications by photoreducing onto Ortho-Lith type 3 film from an original made of suitable lengths of black tape mounted on white card



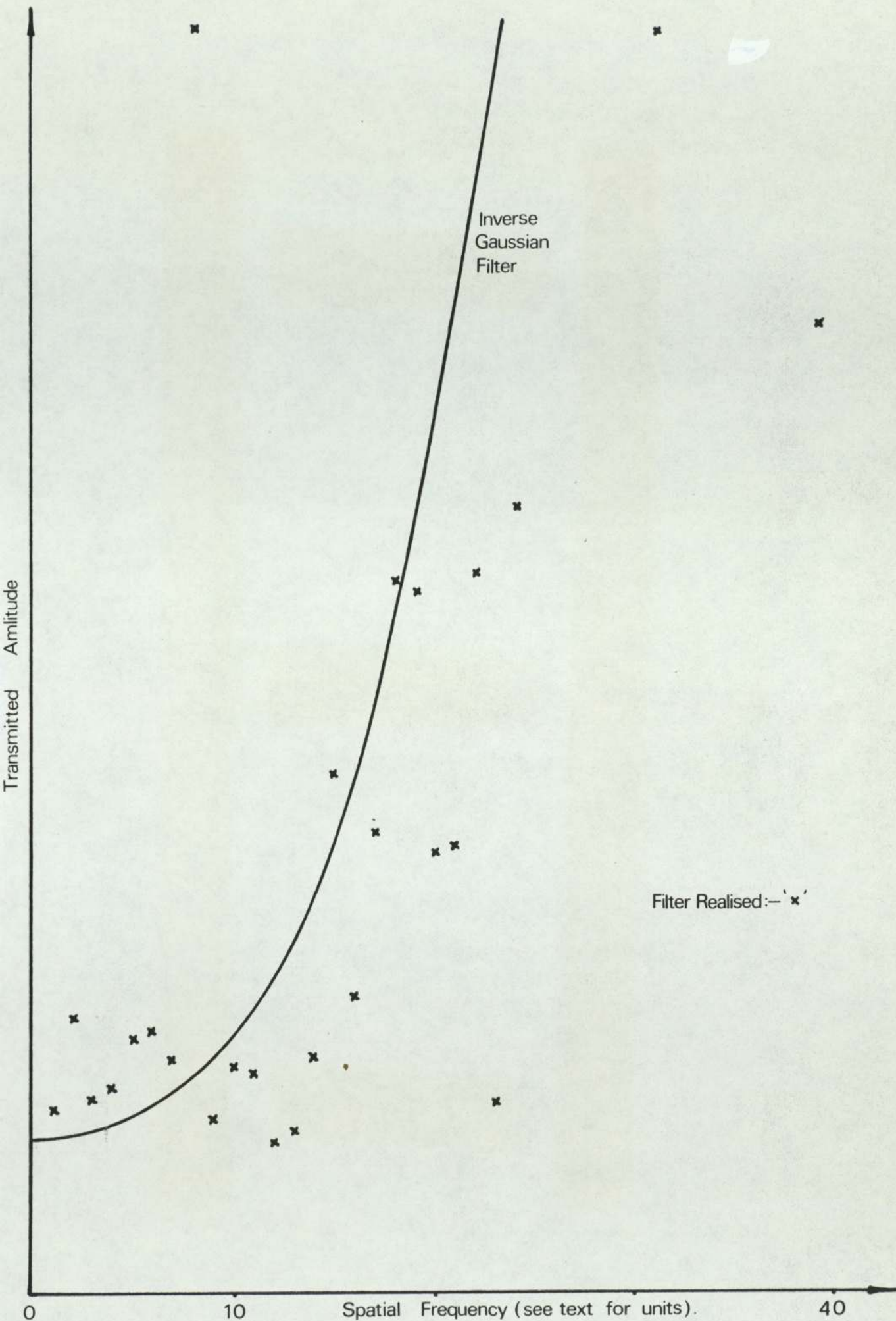


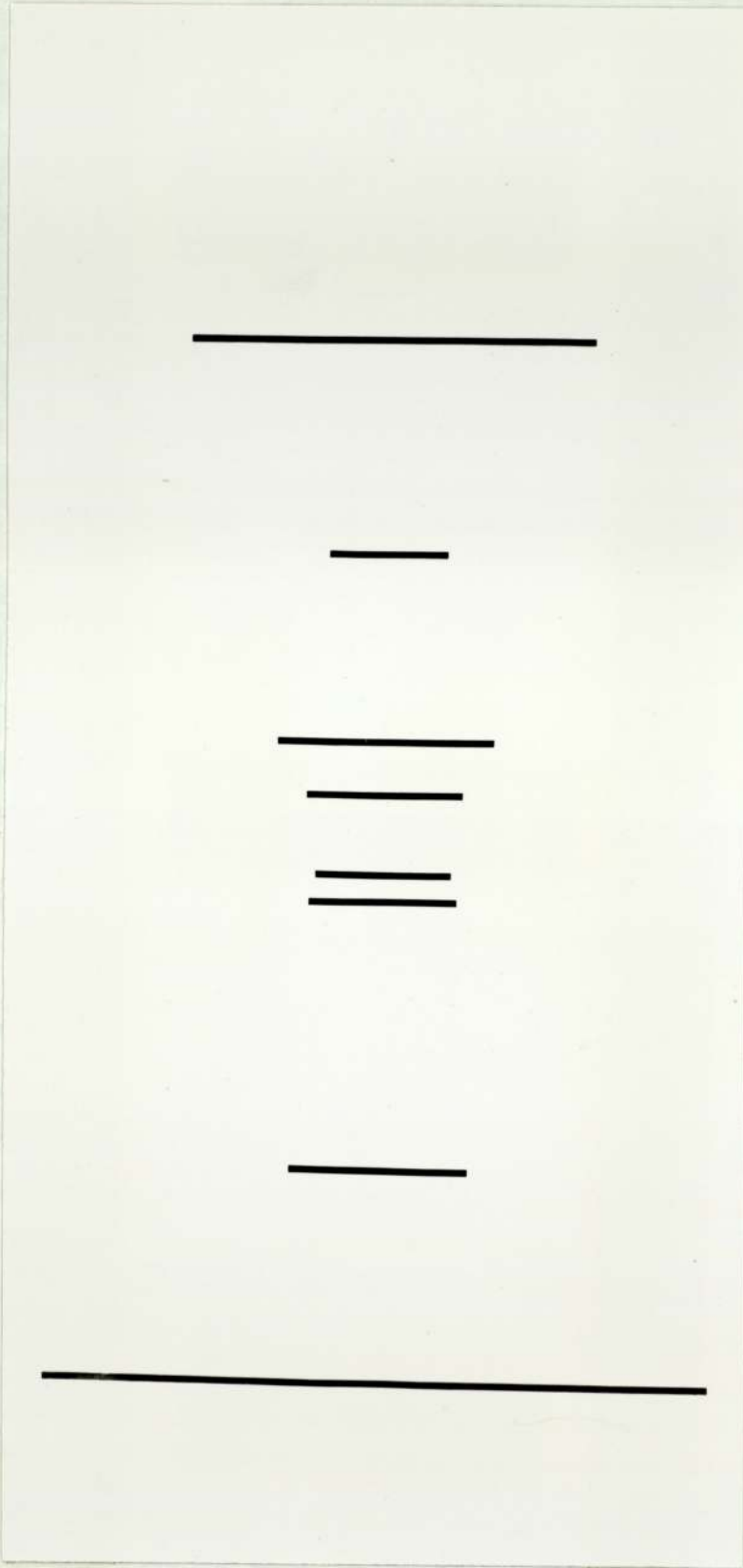
FIG 5.3

as shown in Figure 5.4. The object used,  $s(x)$ , was a five element variable frequency bar chart which was numerically convolved with a Gaussian distribution,  $g(x)$ , having a full width at half maximum height of 8 times the width of the smallest bar. The resulting distribution,  $b(x)$ , was displayed as a graph of  $y = b(x)$  and the region between the curve and the line  $y = 0$  was blackened. The bar chart, Gaussian blurring function and the resulting convolved function are shown in Figure 5.5. The variable area input function was converted to a variable density record corresponding to  $b(k)$  by imaging the display onto a continuous tone photographic plate using a cylindrical lens (Ref. 46). The resulting unblurred and Gaussian blurred bar chart objects are shown in Figures 5.6 and 5.7.

The optical system used to perform the deconvolution is shown schematically in Figures 5.8. It consists of a sodium lamp and diffuser illuminating the object distribution  $b(x)$ , with a collimating lens  $L_1$  throwing a parallel beam into the camera lens  $L_2$ . The filter  $F$  is mounted in a Xylene liquid gate to remove any phase changes between the apertures which would produce unwanted lateral shifts in some of the fringes, and the liquid gate is positioned between the lenses  $L_1$  and  $L_2$ .

The scaling of the system is such that the maximum solved spacing of the filter,  $P_{\max} = 24$  units, is related to the angle,  $\theta_{\min}$ , subtended at the lens by the smallest bar,  $T_{\min}$ , by





Enlarged Negative Of Noncoherent Filter

FIG 5.4

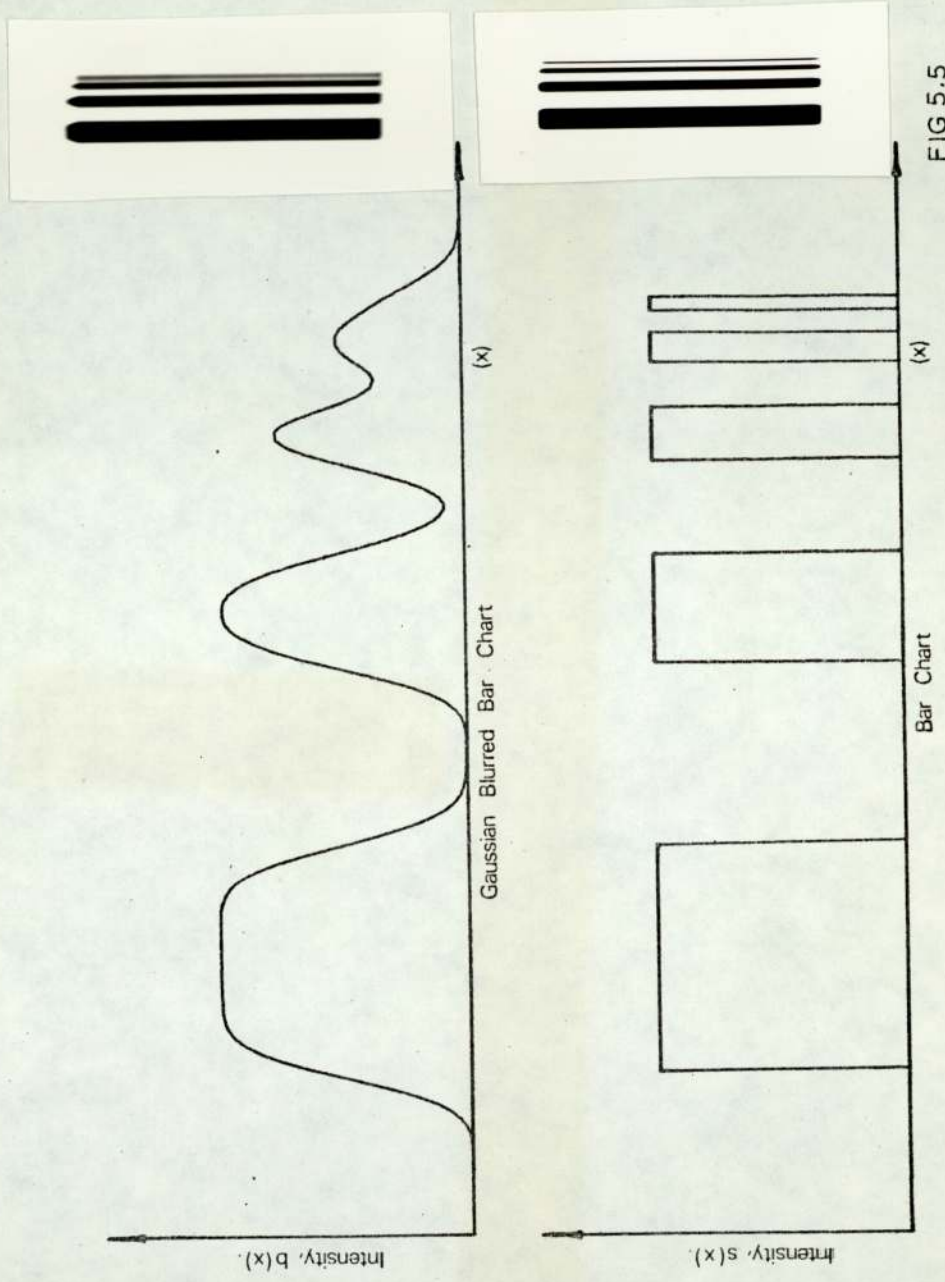


FIG 5.5





Negative Of Bar Chart..

FIG5.6



Negative Of Gaussian Blurred Bar Chart.

FIG5.7

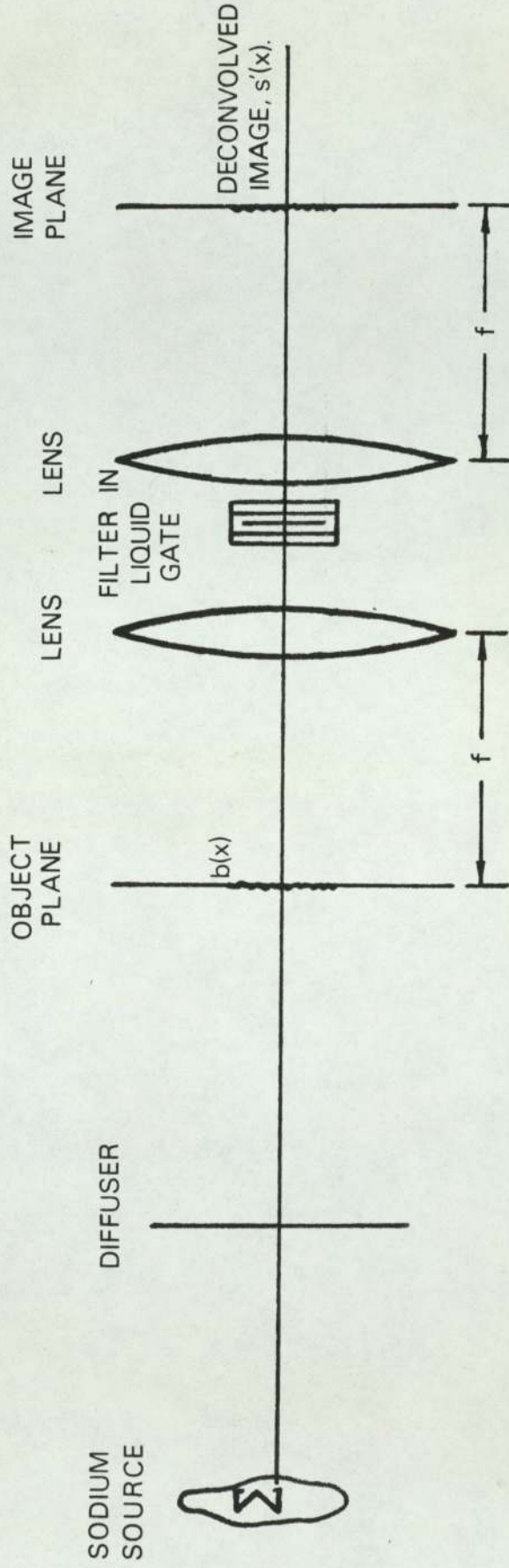
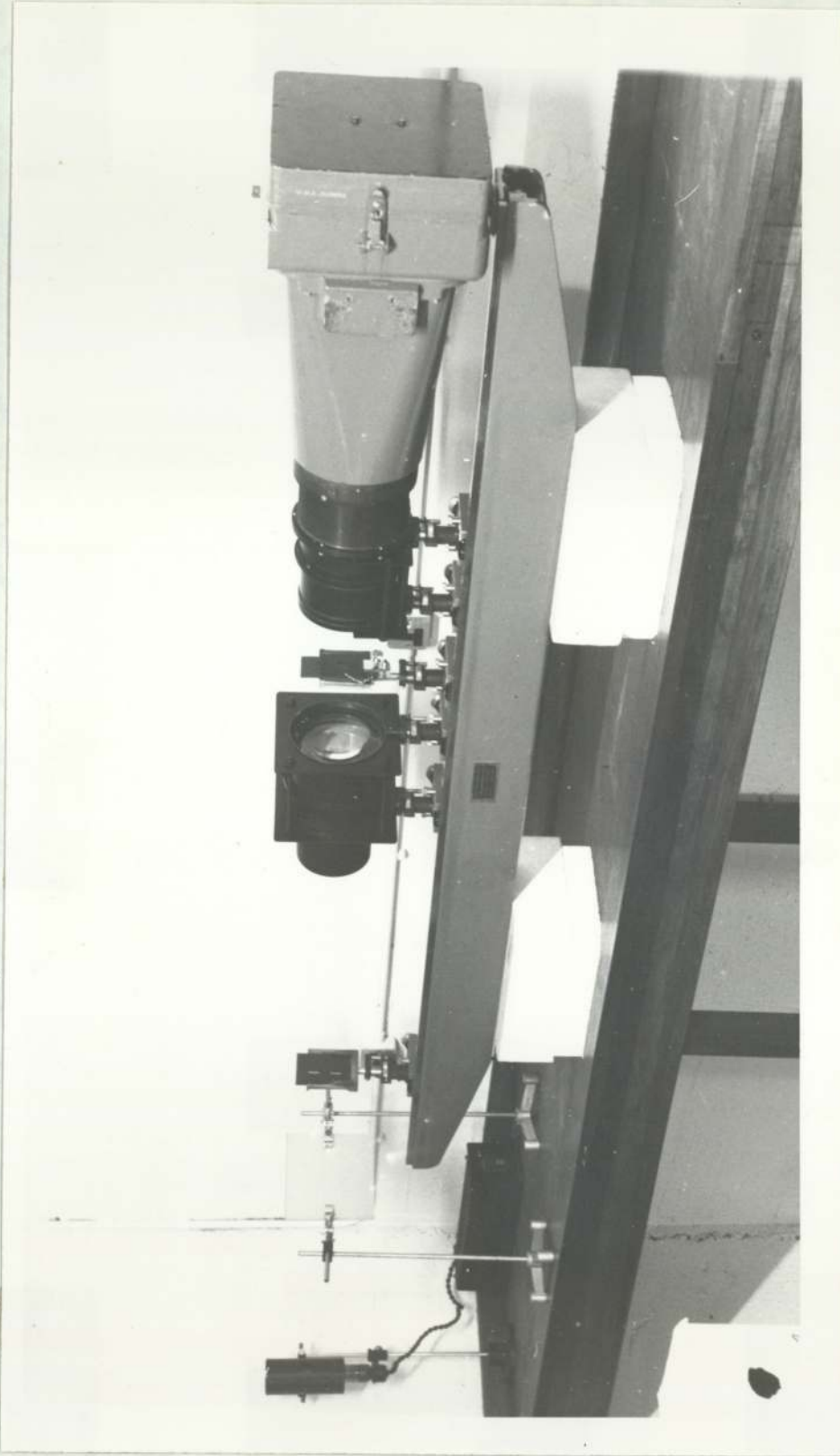


Diagram Of Optical System.

FIG 5.8.





Photograph Of Optical System.

FIG 5.8a

$$\theta_{\min} = \frac{\lambda}{P_{\max}} \quad (8)$$

where  $\lambda$  is the wavelength of sodium light. For a lens  $L_1$  of focal length  $f_1$

$$T_{\min} = \frac{\lambda f_1}{P_{\max}} \quad (9)$$

In practice reasonable scaling was produced by a pair of 914 mm focal length lenses used with a filter having a minimum spacing of 0.103 mm and an object with a minimum bar of 0.217 mm.

## 5.6 EXPERIMENTAL DECONVOLUTION RESULTS

A microdensitometer trace of the image of the deconvolved bar chart is shown in Figure 5.9 along with a trace of the image of the blurred bar chart. The latter was obtained with an aperture stop limiting the maximum frequency transmitted to the highest filter frequency corresponding to  $P = 39$  units. The measured slopes of the bar edges and the relative heights of the bars are tabulated in Table 5.1. There is some sharpening of the edges and a slight peak height enhancement. On the right hand side of the recovered image it is just possible to pick out the first order image separated from the zero order image by the beat frequency period. This can be clearly seen in the recoveries shown in Figures 5.10 and 5.11.

The analysis has assumed that the filter operates on the



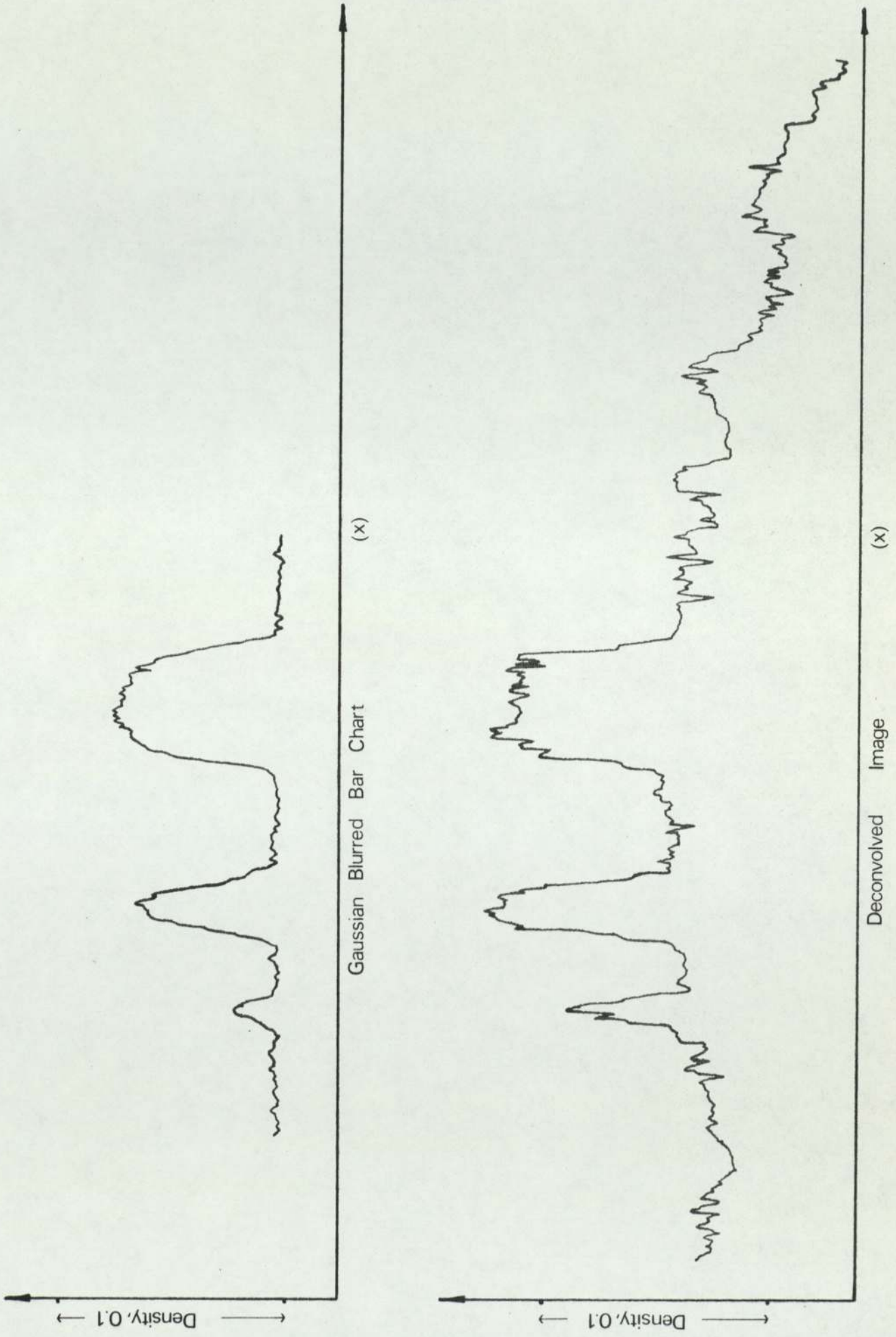


FIG 5.9

TABLE 1

Angles included by peak edges (leading and trailing)

from microdensitometer traces : Figure 7

<u>Peak Width</u>	<u>Blurred</u>	<u>Deblurred</u>
32	81.83	86.85
16	81.81	85.85
8	71.72	83.82

Peak heights normalized to peak width 32 units

from microdensitometer traces : Figure 7

<u>Peak Width</u>	<u>Blurred</u>	<u>Deblurred</u>
32	1.00	1.00
16	0.97	1.09
8	0.34	0.82

TABLE 2(Gaussian Filter)<sup>-1</sup> solutions for 24 simultaneous equations.

<u>Aperture</u>	<u>Aperture Length</u>	<u>(Modified)</u>
Y <sub>1</sub>	33.06	43.06
Y <sub>2</sub>	11.49	11.49
Y <sub>3</sub>	9.32	9.32
Y <sub>4</sub>	8.73	8.73
Y <sub>5</sub>	10.01	10.01
Y <sub>6</sub>	13.87	13.87
Y <sub>7</sub>	7.41	7.41
Y <sub>8</sub>	16.00	26.00



discrete frequencies 1 to 24 units only. In practice there is a spread of  $\pm \frac{1}{4}$  frequency units about each frequency as each aperture has a width of  $\frac{1}{4}$  of the smallest aperture separation. There is also a zero to  $\frac{1}{4}$  frequency units contribution from each aperture acting individually. Although solved for 24 frequencies, as Figure 5.4 shows the system transmits frequency 31 (which is redundant and receives contributions from 2 pairs of apertures) and frequency 39. Inclusion of these two highest frequencies in the equations to be solved resulted in both positive and negative solutions for the aperture lengths  $Y_K$ . The phases of the apertures have to be held equal by using the filter in a liquid gate and to avoid the further complications of phase shifting some of the apertures by  $\pi$  radians to produce the required negative contributions a set of all positive solutions were pursued. Basing the equations on the lowest 24 frequencies resulted in the positive solutions shown in Figure 5.3. It should be pointed out that removal of the constraint on the sign of the solutions does result in a slightly better fit.

## 5.7 DISCUSSION AND CONCLUSIONS

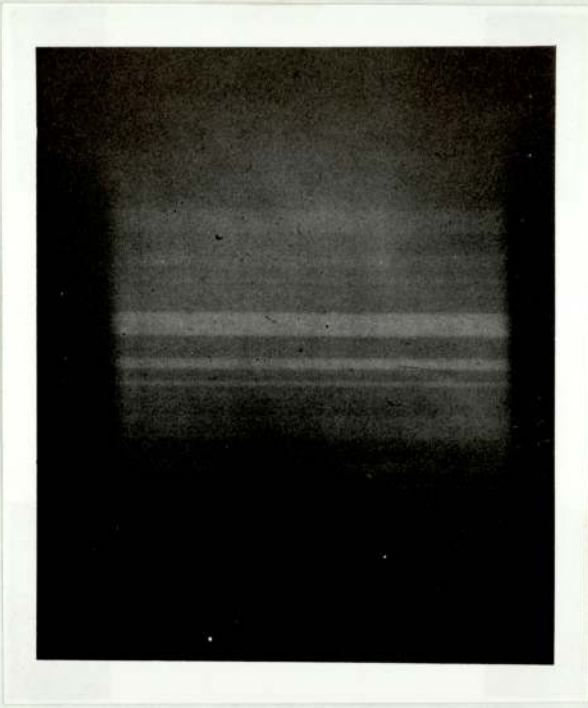
The difficulty of finding good solutions to the filter function arises because the  $N$  apertures operate in parallel, each one contributing to  $(N-1)$  frequencies. A highly over determined set of simultaneous equations is the

result. For the filter considered and the difference series chosen 24 equations were solved for only 8 variables.

An alternative scheme would be to operate with suitably sized and space apertures exposed to give the correct frequency weighting but used sequentially in pairs. This would allow an exact fit to the filter function for each frequency and at the same time would remove the difficulty of redundant frequencies. We have considered the image to be built up from the noncoherent addition of sets of cosine fringes from each source point. More correctly each source point produces in the image plane an intensity distribution which is the coherent summation of the contributions from each aperture of the mask. It is weighted versions of this whole pattern which are added noncoherently for each noncoherent source point. This process is not modelled by the sequential use of pairs of apertures which adds all the individual cosine fringes noncoherently. The image produced by this operation will thus have low visibility even though the frequencies will have been corrected more accurately.

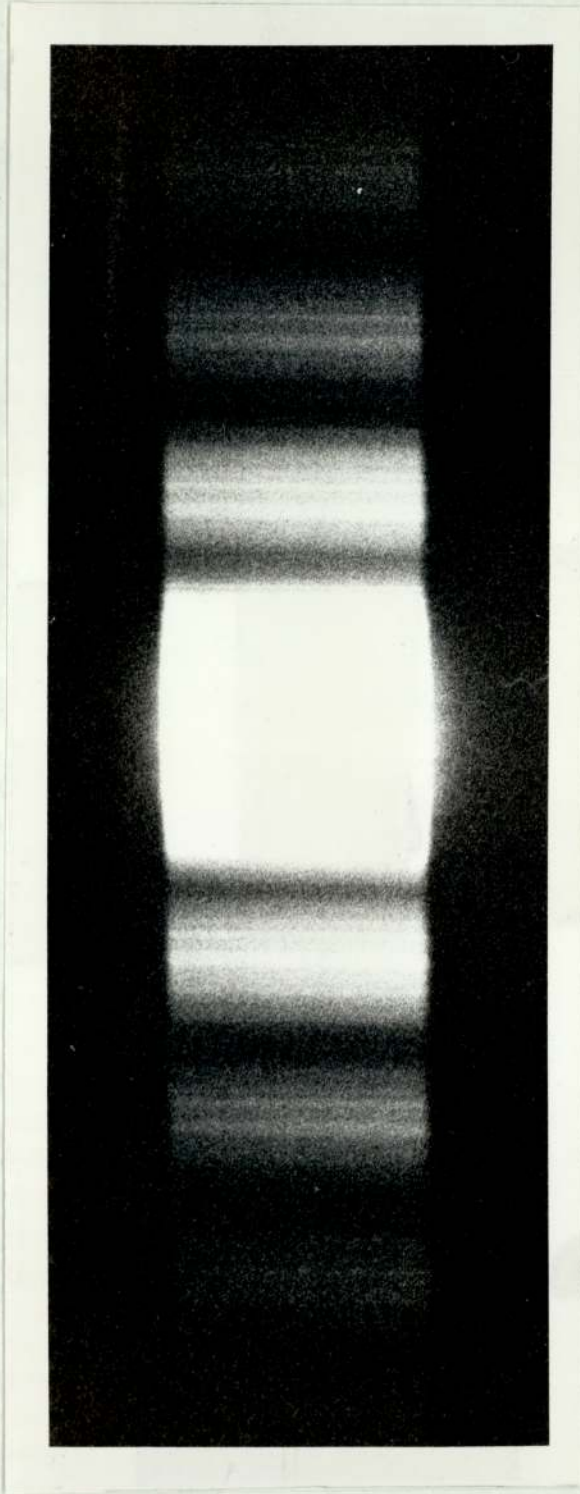
Finally, to end on a practical note, as the effective aperture of a system with a mask is very small the exposure times necessary are rather long, typically several hours using HP3 film.





Non-coherent Deconvolution Of Gaussian Blurred Barchart

FIG 5.10



Enlarged Deconvolution Showing High  
Order Images.

FIG 5.11



CHAPTER 6

CONCLUSIONS

We have simulated a deconvolution system and demonstrated the breakdown of the LMSE criterion as a measure of the quality of deconvolved images. This incompatibility is a result of deconvolution being a process which primarily produces increases in edge slopes. This is inevitably accompanied by high frequency noise which produces a large mean squared error. This effect is particularly noticeable in binary objects as a large amount of image energy occurs in the high frequencies of the spectrum and is suppressed by the convolution process. In the continuous tone object there is little change in the spectrum due to the convolution operation and consequently little change in the form of the object distribution.

The maximum tolerable noise levels for the dilute object recovered by filters optimised using a LMSE criterion for various levels of signal to noise ratio,  $\beta_F$ , are summarised in Table 6.I for both noise independent of and proportional to the local object amplitude. Visually estimated maximum tolerable average noise percentages,  $N_V$ , are compared with statistically calculated maximum tolerable average



noise percentages,  $N_s$ . The latter,  $N_g$ , are the intercepts of the curves of recovered image variance with the curve of blurred object variance shown in Fig 2.22a) and Fig 2.22b).

Although the high  $\beta_F$  filters amplify signal and noise throughout the spatial frequency spectrum, there is initially a good signal to noise ratio throughout which allows a tolerable level of noise to be added.

A similar statistical and visual comparison of maximum tolerable noise levels for the case of the simulated continuous tone object is given in Table 6.2. The values of  $N_v$  are in this case the intercepts of the curves of recovered image variance with the curve of blurred object variance deduced from Fig 2.23a) and Fig 2.23b). In this case, however, the visual estimation of tolerable recoveries is more difficult due to the lack of easily identifiable features. For the binary, bar chart object recovery can be judged by an inspection of the sharp edges of the bars. Such features are not generally to be expected in continuous tone objects and this difficulty highlights the role of recognition of information in an optical signal processing system.

Consequently in Table 6.2 the maximum tolerable noise level is that for which the general structure of the object can still be seen, irrespective of the degree of recovery. Hence, Tables 6.1 and 6.2 can not be compared directly.

The use of high  $\beta_F$  filters with the continuous tone object results in very noisy images. This is because, although they correct the spectrum as required, the high  $\beta_F$  filters transmit strongly in the high frequency regions of the spatial frequency spectrum where the signal to noise ratio is low, even when the object is distorted by

very modest amounts of noise. A low  $\beta_F$  filter can be used to reduce this sensitivity to noise but the resulting image, although having a low statistical variance, will then show little restoration.

For the case of amplitude noise added to an ideal filter such that the noise is independent of the local amplitude a mean noise level of 10% was found by computer simulation to be tolerable. Similarly, for noise proportional to the local amplitude a mean noise level of 20% was tolerable.

A maximum random phase excursion of  $20^\circ$  about the correct phase value was acceptable in the case of a Kinoform element used to recover a dilute bar chart object and for a similar recovery using an ideal filter a maximum phase excursion of  $50^\circ$  about the correct phase value was tolerable. In both cases no other sources of noise were present in the computer simulations.

The operation of computer generated holograms has been discussed and some details of their operation studied. In particular the dynamic range of parity phase only filters has been analysed in terms of its variation over the complex plane. It has been noted that the dynamic range with the constraint of a constant Fourier coefficient phase is 4X less than that obtained if a slight phase change is allowed in the coefficient. The dynamic range of a parity phase only filter was found to vary by a factor of  $2/\delta\phi$  across the complex plane, where  $\delta\phi$  is the quantised phase interval of the phase only element.

In general the complex addressable points will have to be mapped (most



conveniently by computer search) in order to ascertain the characteristics of generalised detour phase holograms.

The effects of deconvolving with a misregistration of the filter element and with the filter element mismatched to the degree of object blurring were studied and maximum tolerable errors estimated. For misregistration this was  $\sim 12\%$  in the simulation (measured in terms of the maximum tolerable filter misregistration from the correct position as a percentage of the distance off-axis of the first filter pole- the point at which the first phase inversion occurs).

For the mismatched filter an error of  $\sim 12\%$  could be tolerated in matching the size of the blur for which the filter was designed to the actual size of the blur which occurred in the object being deconvolved (calculated as:  $\left| \frac{\text{Correct blur} - \text{Tolerable blur}}{\text{Correct Blur}} \right| \times 100\%$ ).

In the case considered a filter designed for a blur of 8 units would just operate satisfactorily on objects blurred both by 7 units and 9 units as well as the filter's optimum of 8 units. The recovered images are considerably more sensitive in terms of calculated standard deviation to filtering with an element designed for a larger blur than occurred, than to filtering with an element designed for a smaller blur than occurred. This is because in the former case high frequencies are over amplified and these contribute heavily to the variance of the resulting image. Whenever the blur extent is an integer multiple of the blur for which the filter is designed, a subsidiary minimum is formed in the image variance against blur extent curve. When scanning for a minimum of variance in order to determine the extent of a blur it is thus better to scan out, starting from a filter matched for a small blur in order to miss the subsidiary minima.

For the deblurring system the filter is insensitive to filter amplitude noise and a comparison of the impulse responses of amplitude quantised filters - simulating dynamic range limited computer generated holograms - and an ideal filter shows that the low dynamic range elements are permissible. This is in agreement with the measured impulse responses of a Lohmann binary filter generated by microfilm plotter and having a dynamic range of 20.

The results of a non-coherent deconvolution show that some degree of image sharpening can be produced but the analysis shows that this is only to be expected for dilute objects which have suffered blurs which can be expressed as positive definite functions. It may be possible to produce improved noncoherent deconvolution by using phase shifted elements in the mask as this results in a better solution to the filter function, and consequently a slightly more powerful element. An alternative approach of using a sequential filter to build up the image would eliminate redundancies in the filter frequency response, and at the same time increase its dynamic range. However, this would probably be offset by an overall reduction in image visibility due to the extra, highly non-coherent additions involved.



TABLE 6.1

## BINARY BAR CHART OBJECT

MAXIMUM AVERAGE TOLERABLE NOISE PERCENTAGE,  $\bar{N}\%$ 

Noise scheme a).                      Noise scheme b).  
 (Noise independent of                (Noise proportional to  
 the local amplitude).                the local amplitude).

Filter	Statistical	Visual	Statistical	Visual
Signal/Noise Ratio, $\beta_F$	Measure, $\bar{N}_S\%$ (see Fig 2.22a)).	Estimate, $\bar{N}_V\%$	Measure, $\bar{N}_S\%$ (see Fig 2.22b)).	Estimate, $\bar{N}_V\%$
$\infty$	1.0	3.0	2.5	6.0
1000	2.5	5.0	5.5	7.0
500	3.0	5.0	6.6	8.0
100	5.0	7.0	>9	>9
10	>9	8.0	>9	/

Comparison of statistically calculated with visually estimated maximum tolerable average noise levels resulting from the computer simulations of the deconvolutions of a dilute binary bar chart object using LMSE filters having different signal/noise ratios,  $\beta_F$ .

Although high  $\beta_F$  filters amplify both signal and noise throughout the spatial frequency spectrum, there is initially a good signal/noise ratio throughout which allows a tolerable level of noise to be added, see Figs 2.2 to 2.11.

TABLE 6.2

## CONTINUOUS TONE OBJECT

MAXIMUM AVERAGE TOLERABLE NOISE PERCENTAGE,  $\bar{N}\%$ 

Noise scheme a).

Noise scheme b).

(Noise independent of  
the local amplitude).(Noise proportional to  
the local amplitude).

Filter	Signal/Noise Ratio	Statistical Measure, $\bar{N}_S\%$ (see Fig 2.23a)).	Visual Estimate, $\bar{N}_V\%$	Statistical Measure, $\bar{N}_S\%$ (see Fig 2.23b)).	Visual Estimate, $\bar{N}_V\%$
	$\infty$	0	2.0	0	2.0
	1000	0.4	3.0	0.4	3.0
	500	0.7	4.0	0.7	5.0
	100	1.8	5.0	2.1	8.0
	10	>5	8.0	>5	>9

Comparison of statistically calculated with visually estimated maximum tolerable average noise levels resulting from computer simulations of the deconvolutions of a continuous tone object using LMSE spatial filters having different signal/noise ratios,  $\beta_F$ .

The high  $\beta_F$  filters produce strong distortion (resulting in low  $\bar{N}_S$  values) because there is a low signal/noise ratio at the high frequency end of the spatial frequency spectrum which causes distortion with very little additional noise, see Figs 2.12 - 2.21.



REFERENCESRef.No.

1. Shannon, C.E. and Weaver, W.  
"The Mathematical Theory of Communication"  
Univ. of Illinois Press, Urbana, 1962.
2. Wiener, N.  
"Extrapolation, Interpolation, and Smoothing  
Time Series".  
Technology Press and Wiley, New York, 1949.
3. Codey, J.W. and Tukey, J.W.  
"An Algorithm for the Machine Calculation  
of Complex Fourier Series."  
Math.Comp. v.19, 297, 1965.
4. Beauchamp, K.G.  
"Walsh Functions and their Applications".  
Academic Press, 1975.  
(Techniques of Physics Series, No.3).
5. Davis, H.F.  
"Fourier Series and Orthogonal Functions".  
Allyn and Bacon, Boston, 1963.
6. Beauchamp, K.G. et al.  
"The BOON System - a Comprehensive Technique  
for Time Series Analysis."  
Proceedings: COMPSTAT Symposium, University  
of Vienna, Vienna, 1974.
7. Gold, B., Lebow, I.L., McHugh, P.G. and  
Roder, C.M.  
"The FDP, a Fast Programmable Signal Processor."  
IEEE Trans. (Comput.), vol.c-20, pp.33-38  
Jan.1971.
8. Goodman, J.W.  
"Introduction to Fourier Optics."  
McGraw-Hill, New York, 1968.
9. Zernicke, F.  
"Das Phasenkontrastverfahren bei der  
Mikroskopischen Beobachtung."  
Z.Tech.Phys., v.16, 454, 1935.

10. Abbe, E.  
Archiv.Mikroskopische Anat.  
vol.9, 413, 1873.
11. Marechal, A and Croce, P.  
Comptes Rendus, v.237, 607, 1953.
12. Tsujiuchi, J.  
    in Wolf, E. (Editor).  
Progress in Optics, vol.II.  
North Holland Publishing Co., Amsterdam,  
1963.
13. Vander Lugt, A.B.  
"Signal Detection by Complex Spatial  
Filtering."  
Radar Lab.Report No.4594-22-T,  
Institute of Science & Technology,  
Univ. of Michigan, 1963.
14. Stroke, G.W., and Zech, R.G.  
Phys.Lett, vol.25A, 89, 1967.
15. Lohmann, A.W., and Werlich, H.W.  
Phys.Lett, vol.25A, 570, 1967.
16. Stroke, G.W., and Halioua, M.  
Phys.Lett, vol.39A, 269, 1972.
17. Brown, B.R., and Lohmann, A.W.  
IBM J.Res.Develop., vol.13, 160, 1969.
18. Burch, J.J.  
Proc.IEEE, vol.55, 599, 1967.
19. Brown, B.R., Thohmann, A.W.  
"Complex Spatial Filtering with Binary  
Masks."  
Appl.Opt., vol.5, 967, 1966.
20. Lohmann, A.W.  
"How to make Computer Holograms."  
Proc.Soc. of Photo-Optical Engineers  
Seminar on Developments in Holography,  
Boston, April 14-15, 1971.
21. Kozma, A., and Kelly, D.L.  
Appl.Opt., vol.4, 37, 1965.
22. Lee, W.H.  
Appl.Opt., vol.9, 639, 1970.



23. Lesem, L.B., Hirsch, P.M., and Jordan, J.A.  
 "The Kinoform: a New Wavefront Reconstruction Device."  
IBM J.Res.Develop., vol.13, 150, 1969.
24. Chu, D.C., and Goodman, J.W.  
 "Spectrum Shaping with Parity Sequences."  
Appl.Opt., vol.11, 8, 1972.
25. Chu, D.C., and Fienup, J.R.  
 "Recent Approaches to Computer-Generated Holograms."  
Optical Engineering, vol.13, 3, 1974.
26. Severcan, M.  
 "Computer Generation of Coherent Optical Filters with High Light Efficiency and Large Dynamic Range."  
Technical Report No.6415-6, Information Systems Laboratory, Stanford Electronic Laboratories, Stanford University, December, 1973.
27. Chu, D.C., Fienup, J.R., and Goodman, J.W.  
Appl.Opt., vol.12, 1386, 1973.
28. Middleton, D.  
 "An Introduction to Statistical Communication Theory."  
 McGraw Hill Book Co., New York, 1960.
29. Wolton, W.P., and Redman, J.D.  
 "Enhancement of Blurred Pictures by Spatial Filtering."  
10th. International Congress on High Speed Photography, Nice, September 1972.
30. Huang, T.S.  
 "Some Notes on Film Grain Noise."  
Woods Hole Summer Study, 105, 1966.
31. Helstrom, C.W.  
 "Image Restoration by the Method of Least Squares".  
Journal of the Optical Society of America, vol.57, 3, 1967.
32. Yu, F.T.S.  
 "Introduction to Diffraction, Information Processing and Holography" Chapter 8, p.186.  
 MIT Press, Cambridge, Mass. 1973

33. Pearlman, W.A.  
"Error Rates in Computer Generated Holograms."  
Ph.D.Thesis - Stanford University,  
Stanford, California, 1974.
34. Kirk, J.P., Jones, A.L.  
J.Opt.Soc.Am., vol.61, 1023, 1971.
35. Powers, R.S., Goodman, J.W.  
"Error Rates in Computer-Generated Holographic Memories."  
Applied Optics, vol.14, 7, 1975.
36. Betts, J.A.  
"Signal Processing, Modulation and Noise."  
English Universities Press, 1970.
37. Nathan, R.  
"Picture Enhancement for the Moon, Mars, and Man" in  
Pictorial Pattern Recognition, Washington DC  
Thompson, 1968.
38. Gennery, D.B.  
"Determination of Optical Transfer Function by Inspection of Frequency-Domain Plot."  
Jnl. of the Optical Society of America,  
vol.63, 12, 1973.
39. Huang, T.S. et al  
"Image Processing",  
Proc.IEEE, vol.59, 11, 1971.
40. Prabhakar, S.N.  
"Quantization Noise in Binary Holograms."  
Optics Communications, vol.15, 3, 1975.
41. Rogers, G.L.  
Proc.Phys.Soc. vol.81, pp.323, 1963.
42. Hopkins, H.H.  
Proc.Roy.Soc., vol.A208, pp.263, 1957.
43. Born, M. and Wolf, E.  
"Principles of Optics" Chapter 10.  
Pergamon Press, Oxford, 1959.



44. Nottingham Algorithms Group Library  
(Lib Nag)  
Procedure FO4AMAM, 1973.
45. Leech, J.  
Proc.Math.Soc., London, v.32, pp.169, 1955.
46. Rogers, G.L.  
Proc.Roy.Soc., Edinburgh, 1952.